Coventry University

DOCTOR OF PHILOSOPHY

A new non-linear k model with enhanced near-wall treatment of turbulence anisotropy

Fadhila, Hasna Nur

Award date:
2020

Awarding institution:
Coventry University

Link to publication

General rights
Copyright and moral rights for the publications made accessible in the public portal are retained by the authors and/or other copyright owners and it is a condition of accessing publications that users recognise and abide by the legal requirements associated with these rights.

- Users may download and print one copy of this thesis for personal non-commercial research or study
- This thesis cannot be reproduced or quoted extensively from without first obtaining permission from the copyright holder(s)
- You may not further distribute the material or use it for any profit-making activity or commercial gain
- You may freely distribute the URL identifying the publication in the public portal

Take down policy
If you believe that this document breaches copyright please contact us providing details, and we will remove access to the work immediately and investigate your claim.

Download date: 18. Feb. 2021

A new non-linear $k - \omega$ model with enhanced near-wall treatment of turbulence anisotropy

Hasna Nur Fadhila

September 2019

A thesis submitted in partial fulfilment of the University's requirements for the Degree of Doctor of Philosophy

Content removed on data protection grounds

Certificate of Ethical Approval

Applicant:

Hasna Fadhila

Project Title:

Development of a new non-linear eddy-viscosity turbulence model for anisotropic flows

This is to certify that the above named applicant has completed the Coventry University Ethical Approval process and their project has been confirmed and approved as Low Risk

Date of approval:

20 July 2018

Project Reference Number:

P72933

To my parents

'Where under this beautiful chaos can there lie a simple numerical structure?'

— J Bronowski

Abstract

A new quadratic $k-\omega$ turbulence model with enhanced treatment for near-wall turbulence anisotropy is developed, implemented, and validated in this work. The model abandons the linear Boussinesq approximation and employs an expanded tensor polynomial formulation for the Reynolds stress tensor, or its corresponding anisotropy, applying it to the standard $k-\omega$ formulation. The original transport equations for the turbulence scales are retained. The modification for the near-wall turbulence anisotropy uses a novel approach which considers how anisotropic turbulence effects are manifested in different regions of the boundary layer. This is achieved using damping functions that rely only on local variables, specifically turbulence quantities and velocity gradients. The formulation is incorporated into the developed non-linear $k-\omega$ framework through its anisotropy expansion coefficients.

Initially, the model predictions on simple boundary layer flows, namely a fully-developed plane channel flow at various Reynolds numbers and a flow over a flat plate, are analysed to validate the formulation and implementation of the model. The performance of the model on a configuration that involves streamline curvatures and internal shear layers, specifically a curved channel flow, is also examined. The model is subsequently applied to more complex configurations that exhibit features such as separation, recirculation, impingement, and swirl: a planar diffuser with a downstream monolith and a swirling flow through a sudden expansion. The model shows to be effective in returning improved predictions, relative to the standard $k-\omega$ model, for many aspects of the flows presented. For example, on the prediction of pressure losses on the curved channel and on the prediction of reattachment points on the sudden expansion. The maximum increase in computation time associated with the model is around 40% compared to the linear $k-\omega$ model. Nevertheless, the new model is shown to be robust in the configurations tested, i.e. stable and converged solutions are obtained and no change in the numerical or computational setup is needed. Based on the cases considered, the model is expected to be particularly advantageous in applications involving internal flows in which the abovementioned flow features (e.g. separation, recirculation, and impingement) are present, for example, for modelling flows in automotive exhaust catalytic converters, fuel systems, or turbochargers. While room for further development is identified, for example by adding an explicit rotational correction, the general conclusions of this work are encouraging.

Acknowledgements

First and foremost, I would like to express my deepest appreciation to Dr Humberto Medina for the guidance, advice, time, and encouragement that he has given me in the past four years. He showed tremendous knowledge and fascination in the field, and trained me to be a researcher through all the insightful and stimulating discussions. I would also like to express my gratitude for my other supervisors, Dr Svetlana Aleksandrova and Prof Steve Benjamin, for all the invaluable advices and for often giving me a much-needed fresh perspective and reminding me of the bigger picture.

The financial support from the Faculty of Engineering, Environment, and Computing at Coventry University is gratefully acknowledged.

I would also like to thank my PhD colleagues, Ijhar, Suzzy, Abhi, Marco, Dimitar, Gianluca, and others, for making the day-to-day in the office more enjoyable. My sincere thanks to Tom for the support and kindness when I needed it. I also very much appreciated having my friend Tifa, with whom I shared the ups and downs of the PhD life since before it even started. I am forever grateful for my friendship with Ankitha, who helped me stay sane throughout and beyond. And my love and thanks go to my boyfriend, Benji, for the cheering me up, supporting me, and caffeinating me towards the end.

Massive love and heartfelt gratitude go to my parents, Istuti and Dwi, my sister, Arin, and my brother, Fariq, for the continuous love, support, and encouragement that they have given me throughout my life. A special thank you to Kieran who, without even realising it, never fails to put a smile on my face when I need it the most. I am grateful to have a family who are always supportive of everything that I do. I owe everything I am to them.

Contents

List of Figures

List of Tables

Nomenclature

CFD	Computational Fluid Dynamics	
DNS	Direct Numerical Simulation	
EARSM	Explicit Algebraic Reynolds Stress Model	
LES	Large-Eddy Simulation	
RANS	Reynolds-Averaged Navier-Stokes	
RSM	Reynolds Stress Model	
β_n	Anisotropy expansion term	$[s^{-2}]$
δ_{ij}	Kronecker delta	
ν	Laminar kinetic viscosity	$[m^2/s]$
ν_T	Eddy viscosity	$[m^2/s]$
Ω	Magnitude of vorticity rate tensor: $\sqrt{2\Omega_{ij}\Omega_{ij}}$	$[s^{-1}]$
ω	Specific dissipation rate	$[s^{-1}]$
Ω_{ij}	Vorticity rate tensor: $\frac{1}{2}\left(\frac{\partial U_i}{\partial x_j} - \frac{\partial U_j}{\partial x_i}\right)$	$[s^{-1}]$
$\tilde{\Omega}$	Vorticity rate tensor invariant: $\frac{1}{\omega}\sqrt{2\Omega_{ij}\Omega_{ij}}$	
ε	Dissipation rate	$[m^2/s^3]$
$\overline{u_i' u_j'}$	Reynolds stress tensor	$[m^2/s^2]$
$\tilde{S}$	Strain rate tensor invariant: $\frac{1}{\omega}\sqrt{2S_{ij}S_{ij}}$	
a_{ij}	Anisotropy tensor	
C_μ	Eddy viscosity coefficient	
C_f	Skin friction coefficient: $\frac{\tau_w}{1/2\rho U_\infty^2}$	
C_p	Pressure coefficient	
$C_{\beta,n}$	Anisotropy expansion coefficient	

k	Turbulent kinetic energy	$[\mathrm{m}^2/\mathrm{s}^2]$
P_k	Production of k	$[\mathrm{m}^2/\mathrm{s}^3]$
Re	Reynolds number: $\frac{U_\infty L}{\nu}$	
Re_τ	Wall shear Reynolds number: $\frac{u_\tau L}{\nu}$	
Re_T	Turbulence Reynolds number: $k/(\nu\omega)$	
S	Magnitude of strain rate tensor: $\sqrt{2S_{ij}S_{ij}}$	$[\mathrm{s}^{-1}]$
S_{ij}	Strain rate tensor: $\frac{1}{2}\left(\frac{\partial U_i}{\partial x_j} + \frac{\partial U_j}{\partial x_i}\right)$	$[\mathrm{s}^{-1}]$
Tu	Turbulence intensity: u'/U_∞	
U	Mean velocity	$[\mathrm{m/s}]$
$u_i'u_i'^+$	Dimensionless Reynolds stress components: $u_i'u_i'/u_\tau^2$	
u_i'	Fluctuating velocity vector	$[\mathrm{m/s}]$
$u'v'$	Turbulent shear stress	$[\mathrm{m}^2/\mathrm{s}^2]$
u'	Streamwise fluctuating velocity	$[\mathrm{m/s}]$
u_τ	Wall shear velocity	$[\mathrm{m/s}]$
U_θ	Tangential velocity	$[\mathrm{m/s}]$
U_x	Axial velocity	$[\mathrm{m/s}]$
U_y	Wall-normal velocity	$[\mathrm{m/s}]$
v'	Wall-normal fluctuating velocity	$[\mathrm{m/s}]$
w'	Spanwise fluctuating velocity	$[\mathrm{m/s}]$
x	Streamwise coordinate	$[\mathrm{m}]$
y	Wall-normal distance	$[\mathrm{m}]$
y^+	Dimensionless wall-normal distance: $u_\tau y/\nu$	
∞	Refers to freestream condition	

Chapter 1

Introduction

The non-linear nature of the partial differential equations that govern fluid flows, the Navier-Stokes equations, for which a global solution has not been discovered, continues to make the numerical prediction of fluid flows a challenging task. Computational Fluid Dynamics (CFD) has been extensively used in the past five decades, especially in recent years, due to the growth of the power of digital computers. Turbulence modelling to this day continues to be a major challenge faced by CFD developers and users alike. To appreciate the intricacies involved in turbulence modelling, we first have to understand the characteristics of turbulence. Turbulent flows are chaotic and inherently three-dimensional and anisotropic. They consist of eddies, which can be thought of as coherent 'patches' of swirling fluid moving seemingly at random generally following the mean direction of motion. These eddies generally break down to exhibit a range of length and time scales, a process that is captured by the non-linearity of the Navier-Stokes equations. It is very expensive computationally to solve for all these scales of motion (using Direct Numerical Simulation, DNS). Therefore, turbulence modelling is used.

In the context of turbulence modelling, the approach known as Reynolds-Averaged Navier-Stokes (RANS), in which the flow quantities are split into their average and fluctuating parts, is the most commonly used due to its relatively low cost for modelling flows of engineering interest. This decomposition process, known as Reynolds-Averaging, results in a new unknown term which all RANS-based turbulence models aim to approximate, that is, the Reynolds stress tensor. The most widely used approach to model this term is based on the Boussinesq hypothesis, which uses an approximation analogous to Newton's law of viscosity. This hypothesis is the cornerstone of most turbulence models used in the present day (known as eddy-viscosity models). However, the Boussinesq hypothesis has been known to fail in many cases. For example, in the case of practical flows that involve complex characteristics such as: transitional flows, impinging flows, swirling flows, and separated flows. Flow separation in particular is one of the flow features that is heavily determined by the development and characteristics of the local boundary layer, which means an accurate prediction of boundary layers

is crucial. Of particular importance is when dealing with internal flows, which are effectively wall-bounded, since boundary layers are present in a large extent of the domain and, hence, influence the overall development of the flow. However, boundary layers exhibit highly anisotropic and non-linear behaviour, which means they are particularly difficult to predict using a linear approximation, such as the Boussinesq hypothesis.

Intuitively, the obvious approach to overcome the limitations of using a linear approximation is to model the Reynolds stress tensor directly. This approach is known as Reynold Stress Modelling. However, this is costly and difficult to implement since it requires solving six additional highly-coupled non-linear partial differential equations. Therefore, an alternative class of models exists: the non-linear eddy-viscosity models. Non-linear eddy-viscosity models aim to improve the representation of turbulence anisotropy while still retaining the simplicity of eddy-viscosity models. They achieve this by extending the classic formulation of the Boussinesq hypothesis to include higher order terms using a general, expanded tensor polynomial for the Reynolds stress tensor.

Although a large number of non-linear eddy-viscosity models have been proposed in the past few decades, there are only a few non-linear eddy-viscosity models that use the specific dissipation rate, ω, as the turbulence scale. This is curious since there is strong evidence in the literature suggesting that models that use ω (instead of turbulence dissipation rate, ε) generally show improved predictions in the near-wall regions, particularly for flows under adverse pressure gradient conditions. Therefore, a new non-linear $k-\omega$ turbulence model is proposed in the present work. The standard $k-\omega$ formulation is extended using a non-linear representation for the Reynolds stress tensor. The original transport equations for the turbulence scales are retained in order to avoid the need for a recalibration of a formulation that is commonly used, as well as to provide ease of implementation into existing CFD codes. Furthermore, a novel formulation for the enhanced treatment of turbulence anisotropy in near-wall regions is proposed. This is motivated by a shortage of non-linear $k-\omega$ models that include an explicit correction for near-wall anisotropy, which has been found to be underpredicted in existing models. To ensure that the near-wall formulation proposed here is applicable to complex geometries, only local variables are used.

The overall performance of the new model is examined using a number of canonical and complex internal flow configurations. Simple boundary layer flows such as fully-developed plane channel flows and flows over a flat plate are useful for validating the formulation and implementation of a new model. Meanwhile, curved channel flows are widely used for assessing the performance of a turbulence model against the effects of streamline curvatures and internal shear layers. Therefore, these configurations are considered here. Additionally, the model is applied to more complex cases, namely a planar diffuser with a downstream monolith and a swirling flow through a sudden expansion, to ensure that it can be robustly applied to engineering configurations.

1.1 Thesis outline

This thesis consists of 9 chapters:

Chapter 1 provides a succinct background to CFD, RANS, and turbulence modelling. This is followed by a brief explanation of the motivation behind the current work.

Chapter 2 presents the literature review which examines the performance of existing linear and non-linear eddy-viscosity models. The motivation of the current work is further highlighted, followed by the aim and objectives.

Chapter 3 provides a background to turbulence modelling. It begins with an introduction to turbulence and wall-bounded turbulence in particular. The formulation of eddy-viscosity models is presented. Reynolds stress models are described briefly, followed with the anisotropy formulation of non-linear eddy-viscosity models.

Chapter 4 describes the methodologies used in the computations presented in this work. This includes numerical methods within CFD: the finite volume method, interpolation schemes, and pressure-velocity coupling. The implementation of a new turbulence model in OpenFOAM is also described.

Chapter 5 presents the development of a new quadratic $k-\omega$ formulation. The calibration and initial assessment of the resulting formulation is also presented.

Chapter 6 describes the new approach and formulation for modelling turbulence anisotropy near the wall. The resulting modification is applied to the initial formulation developed in Chapter 5. The final formulation, the NL $k-\omega$ model, is validated on canonical cases and the results are presented.

Chapter 7 discusses an application of the NL $k-\omega$ model on a complex configuration, which is a planar diffuser with a downstream monolith. The first part of the chapter describes the porous medium modelling methodology for the monolith. An evaluation of two porous medium modelling approaches is then discussed. The performance of the model is subsequently presented and analysed.

Chapter 8 presents an application of the NL $k-\omega$ model on a complex three-dimensional configuration that involves rotational effects, namely a swirling flow through a sudden expansion.

Chapter 9 describes the conclusions drawn from the results presented in this work as well as the main contributions. Some suggestions for future work are also mentioned.

Chapter 2

Literature review

Reynolds-Averaged Navier-Stokes (RANS) continues to be the cornerstone of turbulence modelling for complex engineering flows due to the inevitable compromise between accuracy and cost. The RANS equations can be used to find steady-state solutions of the flow field where the effects of turbulence are represented as a loss of momentum by the term known as the Reynolds stress tensor. This introduces additional unknown quantities and results in the 'closure problem', i.e. there are more unknown variables than equations. Turbulence models are used to close the system of equations by providing a means to approximating the Reynolds stress tensor.

The Boussinesq hypothesis is the most widely-used approach to model this extra tensor. It assumes a linear relation between the Reynolds stress tensor and the mean strain rate by introducing a new scalar, the 'eddy' viscosity or turbulent viscosity. Turbulence models which use this approximation as their foundation are called the eddy-viscosity models. While eddy-viscosity models have been shown to be able to predict simple flows closely in regards to the mean fields, they have been found to struggle in capturing the second-order moments accurately, such as the velocity fluctuations and dissipation. A well-known example is the performance of eddy-viscosity models on a simple shear flow, in which they have been known to incorrectly predict the Reynolds stress components to be isotropic [1–3]. A correct prediction of anisotropic Reynolds stress components is a major deficiency of eddy-viscosity models. Anisotropy refers to the property of a variable to exhibit variation along different directions. Modelling Reynolds stress tensor using the linear Boussinesq approximation results in a formulation which consists two parts: an isotropic part that is proportional to the turbulent kinetic energy, and an anisotropic part which is linearly dependent on the mean velocity field. This assumption presents a limitation for some flow cases. The simple shear flow is a simple example. It can be shown that the incorrect predictions of isotropic Reynolds stresses are directly caused by this linear dependence on the mean strain rate, since there is only one component of velocity gradient in this case.

In addition, this assumption is not representative of most turbulent flow situations since turbulence

is naturally three-dimensional, i.e. anisotropic. This can result in incorrect predictions for not only the Reynolds stress components, but also on the mean fields for more complex cases. One example is the presence of secondary flows in a rectangular duct which is the result of the anisotropic nature of the normal Reynolds stresses and cannot be reproduced using a linear model [4]. This deficiency has also been observed in cases with rapid changes in the mean strain rates, for example flows over curved surfaces [5–7] or flows with strong swirl [8, 9]. In flows over curved surfaces, the Reynolds stresses change at a non-linear rate to the mean-flow processes [10] and there is a marked influence that wall-normal velocity fluctuations have on the structure of the boundary layer [11]. Furthermore, it is observed that there exists a transfer of kinetic energy between the normal and streamwise directions that changes the Reynolds stress components but leave the total kinetic energy unaffected [12], which indicates strong anisotropy. In a swirling flow, it has been found that the effects of the system rotation on isotropic turbulence affect the mean field only through non-linear interactions [13]. Additionally, flow features such as separation and reattachment are primarily driven by the distribution of turbulent stresses in the three-dimensional space [14]. Near a wall, turbulence is highly anisotropic and this anisotropy needs to be captured closely for an accurate prediction of the shear stress, which in turn dictates the prediction of separation. This is observed on a U-bend case where some eddy-viscosity models overpredict the shear stress over the convex wall and underpredict the separation as a result [6]. In an asymmetric diffuser, eddy-viscosity models are also found to fail in reproducing the separation and recirculation observed in the experiments [15]. These observations highlight the deficiencies of the eddy-viscosity assumption, which results in inaccurate flow predictions in complex cases, e.g. where high mixing rates, recirculation, separation, and stagnation regions are present.

A direct test of the validity of the Boussinesq hypothesis, which is the cornerstone of eddy-viscosity models, is consequently proposed [16, 17]. The test is based on the aforementioned approach of the eddy-viscosity approximation to linearly relate the anisotropic part of the Reynolds stress tensor, a_{ij}, and the mean strain rate tensor, S_{ij}, which means that it approximates the two tensors to be proportional. This proportionality is tested by introducing an indicator, ρ_{RS}, that is calculated from the double inner product between the two tensors:

$$\rho_{RS} = \frac{\mid a_{ij} : S_{ij} \mid}{\parallel a_{ij} \parallel \parallel S_{ij} \parallel} \tag{2.1}$$

This ratio is calculated to be a number between 0 and 1, with the value of 1 signifying a valid approximation. This test is applied on several DNS, LES, and experimental results for a number of cases. One example is the test performed using an experimental data of a double annular turbulent jet flow by [18]. A map of ρ_{RS} is obtained [16] and is shown in Figure 2.1. The area in which the Boussinesq approximation is valid is represented by $\rho_{RS} = 1$, i.e. the white region; although Schmitt [16, 17] suggests that since equation (2.1) is analogous to the cosine of an angle between two vectors, an alignment can be considered valid for angles smaller than $\pi/6$, corresponding to a value of ρ_{RS} larger than 0.86. It can be observed that the extent of the area is very limited throughout

the domain. Comparable behaviour is also observed for a flow past a rectangular cylinder based on the LES data in [19]. A similar test is also proposed for quantifying the non-linearity of the Reynolds stress tensor [20]. The methodology is based upon decomposing the anisotropic part of the Reynolds stress tensor into parts that are in-phase and out-of-phase with the strain rate tensor. Applying this to DNS database for a fully-turbulent plane channel flow [21] and turbulent rectangular channel flow [22, 23], the investigation shows that the Boussinesq hypothesis is not suitable even in regions of local equilibrium [20].

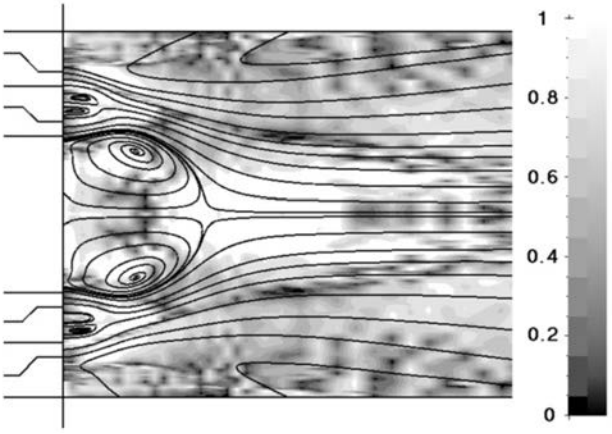

Figure 2.1: A map of ρ_{RS} for the experimental double annular jet data [16]

These findings show the limitations of the eddy-viscosity aproximation. As a remedy, a number of techniques have been proposed. The simplest is to apply corrections to a specific model for which the weaknesses are known. By correcting known deficiencies, it is expected that the error in predicting future unknown conditions will decrease. An example of this approach is the curvature correction proposed for the $k-\omega$ model [12] and the $k-\varepsilon$ model [24–26]. The correction is found to bring the model predictions for flows over curved surfaces to closer agreements with experimental data. However, while relatively easy to implement, this type of corrections, and other corrections similar to this such as [27, 28] are case-specific *ad hoc* modifications that are not universal and cannot be generalised for arbitrary flows. Therefore, there is a need to improve turbulence model predictions in a more generalised fashion. An approach exists which is to abandon the Boussinesq approximation altogether and solve the closure problem by directly approximating the Reynolds stress tensor. This is known as Reynolds Stress Modelling (RSM) [1, 29–32]. In RSM, transport equations for the Reynolds stress tensor are employed. This translates to the introduction of six additional highly-coupled, non-linear partial differential equations, which makes this modelling approach difficult and costly [33]. In addition, it involves a number assumptions and approximations that are required to solve it [34], which leads to an offset in the physical gain of this approach. Therefore, an alternative group of turbulence models exists which does not belong precisely in the eddy-viscosity models or Reynolds stress models. This is referred to as non-linear eddy-viscosity models.

The term 'non-linear' refers to a non-linear relation between the Reynolds stress tensor and the mean flow field. This is in contrast to the Boussinesq approximation (which assumes a linear relation) on which the eddy-viscosity models previously discussed rely. The aim of non-linear eddy-viscosity models is to capture some of the physical effects that are missed by linear eddy-viscosity models, while still retaining their low computational cost and simplicity in formulation and implementation. This is achieved by introducing a more general, non-linear formulation for the Reynolds stress anisotropy. Originally proposed by Lumley [2] and Pope [3], it is defined as a tensor polynomial consisting of higher-order functions of the mean strain and rotation rates. The formulation is derived using theory of matrix polynomials [35,36] and the Cayley-Hamilton theorem [37–39], which results in a polynomial consisting of ten tensor functions with a maximum degree of five. A number of non-linear eddy-viscosity models have been proposed using this general relation, retaining the terms in the polynomial up to a degree decided by the developers.

One of the earliest non-linear eddy-viscosity formulations is the quadratic $k-\varepsilon$ model of Nisizima and Yoshizawa [40]. The model is obtained by retaining the functions in the general anisotropy tensor formulation up to the quadratic terms. The results demonstrate the effectiveness of the non-linear Reynolds stress formulation in producing the correct anisotropic turbulence intensities in a fully-developed channel flow and a Couette flow. These results are also observed from the quadratic models of Rubinstein and Barton [41], Myong and Kasagi [42], and Shih *et al.* [31]. Speziale [4] proposes a quadratic $k-\varepsilon$ model that includes an Oldroyd convective that satisfies the frame indifference. The model is tested using a rectangular channel flow and it is found to be able to capture the turbulent secondary-flow streamlines while the corresponding linear $k-\varepsilon$ model has been found to miss this feature. This model has also been found to outperform the $k-\varepsilon$ model predictions for separated turbulent flows [4]. Applying this to a backward-facing-step problem, and comparing it to the experimental data of Kim *et al.* [43] shows that the model improves the prediction of flow separation and reattachment compared to the linear model [4]. Another quadratic $k-\varepsilon$ formulation is developed by Heschl *et al.* [14] using the anisotropy tensor approach of Gatski and Speziale [44]. It is tested on planar diffuser jet case experimentally done by Gutmark and Wygnanski [45] and a turbulent wall jet studied by Abrahamsson [46] and results show that it captures the recirculation zone in the domain better than the linear version.

Craft *et al.* [8] propose a cubic constitutive relation which retains the anisotropy polynomial terms up to the cubic level, coupled with the classic $k-\varepsilon$ model. The results on the curved channel flow experimentally done by [47] show that model returns improved predictions of the asymmetric velocity profile, quantified using the shear stress ratio between the inner and the other walls. In an impinging jet case, the model shows improvements in predicting the stress field, particularly in the impingement region, compared to the linear $k-\varepsilon$, resulting in the mean velocity peaks being captured more accurately. The later version of the model [48], which includes an added transport equation for a stress anisotropy invariant, also shows an improvement on the level of shear stress near the stagnation point of an impinging jet, where linear models overpredict. Suga and Abe [49] include a

transport equation for Lumley's stress parameter [50], which is also calculated using an invariant of the anisotropy, in their cubic $k-\varepsilon$ model and show encouraging performance in capturing anisotropic turbulence near both wall and shear-free boundaries. A cubic $k-\varepsilon$ model by Apsley and Leschziner [51] also gives more accurate predictions of the asymmetry of the velocity and turbulent stress profiles in the plane asymmetric diffuser flow of [52] compared to the linear $k-\varepsilon$. They later [15] investigate the isolated effects of the linear, quadratic, and cubic terms in the formulation to the flow prediction and find that in a non-equilibrium shear flow, the inclusion of the quadratic terms increases anisotropy, and therefore the second-order velocity gradients, which leads to a greater tendency to separation. This is consistent to the observation of Obi *et al.* [52] that for a realistic calculation of the turbulent separating process in the asymmetric plane diffuser, it is of principal importance to represent the anisotropy of the Reynolds stress tensor.

Overall, it has been observed that there is a general trend of improvement in the predictions of flow features in complex flows gained by extending the formulation for the Reynolds stress tensor to a non-linear form. This has been reviewed above, as well as in [53–57]. Conclusion can be drawn that the aim to improve eddy-viscosity models predictions can be achieved by abandoning the Boussinesq-type modelling and using a more general relation for the Reynolds stress tensor, or its corresponding anisotropy. This gives confidence in adopting this approach in this work. Although there is a large number of non-linear eddy-viscosity models that have been proposed in the past few decades, it is interesting to see that, to the knowledge of the author, with the exception of the works of Larsson [58], Song *et al.* [59], and Abe *et al.* [60], non-linear eddy-viscosity models have not been based on the specific dissipation rate, ω, but instead are based on the dissipation rate, ε. The use of ε as the turbulence scale has been known to result in the lack of sensitivity to adverse pressure gradients by linear $k-\varepsilon$ models [7, 61–65]. The standard $k-\varepsilon$ model is calibrated using an equilibrium boundary layer. In such condition, the turbulent length scales are proportional with the distance from the wall. This assumption is not applicable in non-equilibrium situations which may result in an overprediction of the turbulent length scales [66]. This results in overpredictions of the turbulent kinetic energy in stagnation regions [58, 67]. This overprediction of the turbulence length scales also manifests as an overprediction of the turbulent shear stress, which consequently results in an inaccurate prediction of flow features such as separation [61]. This shortcoming has been observed in a set of separated test cases in [68], also in particular for flow over a backward-facing step [69], and flow over a simplified three-dimensional bluff body, also known as Ahmed's body [70]. The $k-\omega$ model, which uses specific turbulence dissipation rate, ω, on the other hand has been found to return more accurate representation of the near-wall behaviour, especially for predictions of flows under adverse pressure gradient conditions [60, 71, 72]. As a result, the $k-\omega$ model has been shown to return more accurate predictions for both attached boundary layers and separated flows, for example in a flow over a backward-facing step case [71]. Another example is how it is able to correctly predict separation in an asymmetric diffuser configuration, in contrast to the $k-\varepsilon$ model [73] which is not [15].

From a numerical point of view, the attraction of $k-\omega$ models over $k-\varepsilon$ models is also due to the

difficulty in prescribing a wall boundary condition for ε, which does not have a natural boundary condition since it does not go to zero at the wall. The choice of using ω instead is initially unexpected since it has the asymptotic behaviour of $\omega_{\text{wall}} \to \infty$ as $y \to 0$. However, the use of the asymptotic equation deduced by Wilcox *et al.* [74–76] has been shown to work well near the wall and is more preferable practically since it can be applied as a straightforward Dirichlet condition. Abe *et al.* [60] apply their quadratic eddy-viscosity formulation to both $k-\varepsilon$ [77] and $k-\omega$ [78] models and show that the non-linear $k-\omega$ variant shows a more accurate prediction of separation and reattachment in a flow over a periodic hill. Additionally, Larsson [58] modifies the non-linear $k-\varepsilon$ model of Shih *et al.* [79] to use in a $k-\omega$ framework to allow the model equations to be solved down to solid walls. Although not compared directly with the original non-linear $k-\varepsilon$ version, the resulting non-linear $k-\omega$ model shows improved predictions in stagnation regions compared to the linear $k-\omega$ model. The cubic $k-\omega$ model of Song *et al.* [59] also outperforms the linear $k-\omega$ on predicting the asymmetric velocity profiles in a curved channel flow by [47] and in a rotating channel flow by [80]. The curved channel prediction is resulted from a more accurate prediction of turbulent kinetic energy on the inner wall, which is much lower than that at the outer wall, compared to the $k-\omega$ model. The predicted skin friction coefficients across the inner and outer walls are also closer to the experimental values. However, applying the model to the fully-developed channel flow by Kim *et al.* [81], it is shown to underpredict the anisotropy level of the Reynolds stresses in the near-wall region. It is also observed that in a heat transfer prediction over a blunt plate case by [82, 83], the model is found to underpredict the Nusselt number near the walls. Song *et al.* [59] highlight that a near-wall modification is needed. The quadratic models of Abe *et al.* [60] include a modification for strong anisotropy in the near-wall region. The model uses additional strain and rotation terms for the wall modification which depend on wall-direction indicators. While it shows the correct asymptotic near-wall behaviour of the Reynolds stresses, the near-wall formulation includes more tensorial terms and uses wall distance in its formulation. In addition, the anisotropy expansion coefficients in their formulation are derived using an approach used by explicit algebraic Reynolds stress models, e.g. [44, 84, 85], resulting in a formulation that is somewhat different to the non-linear eddy-viscosity models that have been reviewed here.

From this review, it is evident that the linear Boussinesq approximation has often been found insufficient for the accurate predictions of flows that involve anisotropic and complex features. It also shows that the ultimate goal of improving the representation of turbulence (and its inherent anisotropy) using linear eddy-viscosity models is unattainable. In contrast, the full potential of extending the classic Boussinesq approximation by using a more general, non-linear formulation for the Reynolds stress tensor has not yet been exhausted. For example, in the literature there is a surprising shortage of non-linear eddy-viscosity models that use ω as the turbulence scale, despite evidence to the superior performance of ω-based models compared to ε-based models, in particular for complex flows involving adverse pressure gradients. Therefore, in this work ω is chosen as the turbulence scale. Furthermore, to the author's knowledge there is only one ω-based non-linear model [60] available in the literature that includes an explicit correction for near-wall anisotropy. However, the correction used by Abe *et al.* [60] uses the wall-normal distance in its formulation. The dependence on a wall distance is generally not

desirable in turbulence modelling since it is a non-local variable and presents limitations when applied to complex geometries. Therefore, in this work a novel approach to incorporate near-wall turbulence anisotropy is proposed which relies only on local variables to ensure its robustness for applications in complex configurations.

2.1 Aim and objectives

The aim of this work is to develop a new non-linear turbulence model that incorporates a novel method for representing near-wall turbulence anisotropy that will result in improved predictions of quantities of practical interest (e.g. pressure and friction losses) when applied to canonical or complex internal flows.

The following objectives are defined:

- To develop a non-linear eddy-viscosity model based on the standard $k - \omega$ turbulence model using an expanded tensor polynomial formulation for the Reynolds stress tensor
- To develop a novel formulation for near-wall turbulence anisotropy based on local flow variables only
- To evaluate and assess the performance of the new model using a range of canonical and complex configurations

Chapter 3

Turbulence modelling

3.1 Introduction

Bradshaw in the sixth Reynolds-Prandtl Lecture in 1972 described that the only short and satisfactory way to describe turbulence is that it is 'the general solution of the Navier-Stokes equation'. While the Navier-Stokes equations describe the deterministic nature of fluid motion, the non-linearity of the equations causes fluctuations that seem random in nature. These effects are due to the sensitivity of turbulent flows to perturbations, which can be caused by properties such as initial conditions, boundary conditions, or material properties. These seemingly random fluctuations cause the chaotic behaviour of turbulence which results in turbulent flows behaving in a way that is not intuitive and hence is difficult to predict. The fluctuations associated with turbulence consist of a broad range of length and time scales. They occur naturally in different directions, causing turbulence to be three-dimensional by nature. It is formed by 'patches' of rotating fluid called 'eddies' and therefore contains strong rotational motion, also known as vorticity. This generates a mixing behaviour which reduces the kinetic energy contained by the flow, resulting in turbulence being dissipative by nature.

Turbulence can be understood as an energy transfer process which involves three stages: production, cascade, and dissipation. Production is where energy is transferred from the mean flow to turbulence. Eddies grow to reach their largest size, generally in a scale comparable to the main geometry. There is a cascade of energy in which energy is transferred from the largest eddies to the smaller ones. As the length scales get smaller, the local Reynolds number falls. At a critically small size, at which the local Reynolds number is 1, the effects of viscosity are sufficiently strong to damp out the remaining turbulent energy. The turbulent energy then dissipates into heat. It is helpful to explain this energy transfer using an energy spectrum plot, obtained by Kolmogorov [86]. This is presented in Figure 3.1 in a log-log scale. $E(\kappa)$ represents the energy contained by eddies of size ℓ, plotted against ℓ in its wave number form, $\kappa = 2\pi/\ell$. Three important length scales are shown in this figure, which help describe the three stages of turbulence. The integral length scale, ℓ_{integral}, is associated the main production

process. This is the stage at which the majority of the energy transfer from the mean flow to turbulence occurs and it contains around 80% of the turbulent kinetic energy. The Taylor length scale, ℓ_{Taylor}, is associated with the stage at which isotropic motions occur. This is due to how as energy is transferred down the cascade, directional information is lost. The Kolomogorov length scale, $\ell_{\text{Kolmogorov}}$, which is the smallest length scale, is associated with viscous dissipation.

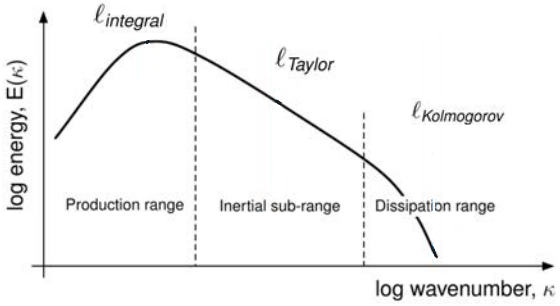

Figure 3.1: Turbulence energy spectrum [86]

Numerical approaches to modelling turbulence can be classified with reference to the energy spectrum in Figure 3.1. The first is Direct Numerical Simulation (DNS) in which all scales of motion are solved and no modelling is required. A less expensive approach is called Large Eddy Simulation (LES) which solves up to the Taylor length scale, and models the smaller scales. LES employs spatial filtering to the governing equations which separates the scales of motion that are solved and ones that are modelled. As described above, length scales that are smaller than ℓ_{Taylor} correspond to scales that are isotropic, which are therefore easier to model correctly. Length scales that are larger than ℓ_{Taylor} are directly solved. There exists another, most widely used approach: Reynolds-Averaged Navier-Stokes (RANS). Using RANS, only the mean flow is solved directly and the turbulent scales are modelled. This is the cheapest approach and has been shown to give reasonable predictions for practical engineering applications. The description and derivation of RANS formulation will be discussed in Section 3.4.

3.2 Wall-bounded turbulence

Many practical turbulent flows are wall-bounded, i.e. bounded by a solid surface or solid surfaces. The 'no-slip' condition of viscous fluids means the velocity of a fluid particle at the wall is zero. Consequently, a thin layer of fluid is generated in which a velocity gradient exists in the wall-normal direction from a velocity of zero at the wall to the freestream velocity. This layer is known as a boundary layer. Boundary layers exhibit common features unique to wall-bounded turbulent flows such as pipe flows, channel flows, and aerodynamic flows. In order to model these flows closely, a good understanding and prediction of the boundary layers are of great importance since the boundary layer behaviour heavily affects the overall development of the flow.

Works as early as von Kármán [87] and Prandtl [88, 89] allow a closer investigation into the different

regions within a turbulent boundary layer. This is illustrated in Figure 3.2, which shows the changing regions with varying wall-normal distance, y, normalised either using the wall-shear velocity, u_τ, resulting in $y^+ = yu_\tau/\nu$, or using the boundary layer thickness, δ, resulting in y/δ. Wall-shear velocity, u_τ, is defined as $u_\tau = (\tau_w/\rho)^{1/2}$ where τ_w and ρ are the wall shear stress and fluid density, respectively. ν is the kinematic viscosity. The boundary layer thickness, δ, is defined as the wall-normal distance at which the streamwise velocity reaches a certain percentage of the freestream value (usually defined as 99% U_∞).

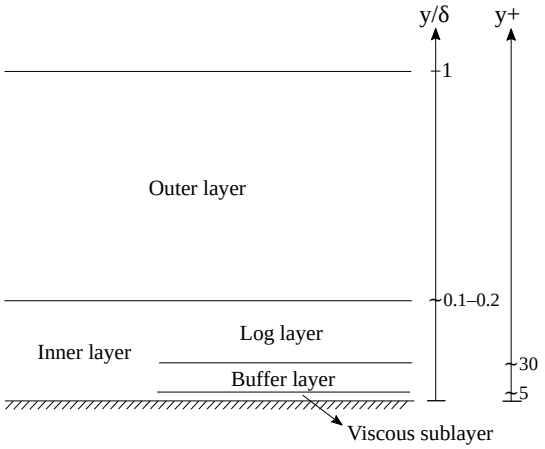

Figure 3.2: Boundary layer nomenclature [90]

In a turbulent boundary layer, mean kinetic energy from the freestream is converted into turbulent fluctuations and then dissipated into internal energy by viscous action. Fluid dynamicists have sought to understand the mechanisms of turbulence development in a boundary layer, i.e. how turbulence is generated at the expense of the mean motion and how it is dissipated. Comprehensive reviews are published in [91–94]. Most research into turbulent boundary layers agrees that a turbulent boundary layer is dominated by two regions: the inner layer and the outer layer. The distinction is usually made based on the influence of viscosity to the production of turbulence in the region. In the inner region, the effects of viscosity heavily influence the turbulent structures and therefore the length scale associated with it is the viscous or Kolmogorov scaling: u_τ/ν, resulting in the definition of the dimensionless y^+. In the outer region, the viscous effects to the turbulence production are minimum and therefore the length scale associated with it is related to the geometry, e.g. δ in a boundary layer flow or h in a channel flow where h is the half channel width, resulting in the dimensionless scale of y/δ or y/h.

The inner layer includes the viscous sublayer, the buffer layer, and the overlap or log layer (or at least a part of it). This inner region is found to exist within the distance of about $y < 0.1 - 0.2\delta$ or around $y^+ < 100 - 200$. The literature shows that this inner region, which is often referred to as the near-wall region, is the source for most of the turbulence production in a boundary layer [95, 96]. Research into the phenomenology of turbulence finds that this is associated with the organised or coherent motions

that exist here [97–102] (also termed coherent structures or turbulence structures). The development mechanisms of these turbulent structures consist of instantaneous events. In the context of Reynolds-Averaging, these structures and events are observed only on the average, i.e. only the resultant or byproduct, that is, the Reynolds stresses, are modelled. The details of each sublayer within this inner region are as follows.

Nearest to the wall, low-speed streamwise vortices, also known as low-speed streaks, cover most of the wall [97, 99, 101, 102]. This is the first sublayer, termed viscous sublayer, which is located within about $y^+ < 5$. In this sublayer, viscous effects dominate and the mean velocity is found to follow:

$$U^+ = y^+ \tag{3.1}$$

where $U^+ = U/u_\tau$.

Above the viscous sublayer, a layer of fluid is involved in a process known as bursting, where the low-speed fluid closer to the wall 'ejects' outwards from the wall, and the high-speed fluid further from the wall 'sweeps' towards the wall [100, 103–105]. This occurs within about $5 < y^+ < 30$ and the region is known as the buffer layer (refer to Figure 3.2). This bursting process results in the formation of a shear layer between the sweeps and the ejections, and causes this region to be populated with alternating streaks of low- and high- speed fluids. These streaky structures, which can be identified as quasi-streamwise vortices [91, 102], give rise to considerable Reynolds shear stress and are major contributors to the production of turbulent kinetic energy. The anisotropy of a turbulent boundary layer is also closely linked to these coherent structures, for example, due to the direction or alignment of the vortices [106, 107]. The mean strain rate as well as pressure gradients align these energy-containing eddies, resulting in their anisotropic behaviour. Therefore, as well as the production of turbulent kinetic energy, it is expected that the anisotropy of the boundary layer also reaches its maximum here.

Above the buffer layer, the transport of the turbulent stresses is negligible, resulting in a local energy equilibrium between the production and dissipation of the turbulence stresses. This is located within the layer that overlaps the inner and outer layers, and is therefore defined as the overlap layer. It contains a mix of quasi-streamwise vortices found in the region closer to the wall as well as the arch-like vortices that are found in the outer region, explained later. This overlap layer is found to be within the distance of between around $y^+ > 30$ and $y/\delta < 0.1 - 0.2$. Here, the mean velocity follows the 'law of the wall' or 'log law', defined as:

$$U^+ = \frac{1}{K} ln(y^+) + C \tag{3.2}$$

where K and C are absolute constants found experimentally to be about 0.41 and 5, respectively. As

the velocity profile in this overlap region is logarithmic, it is also commonly referred to as the log layer.

These different sublayers within the inner region of a boundary layer can be described using the non-dimensionalised velocity profile of a fully-turbulent channel flow near the wall, presented in Figure 3.3.

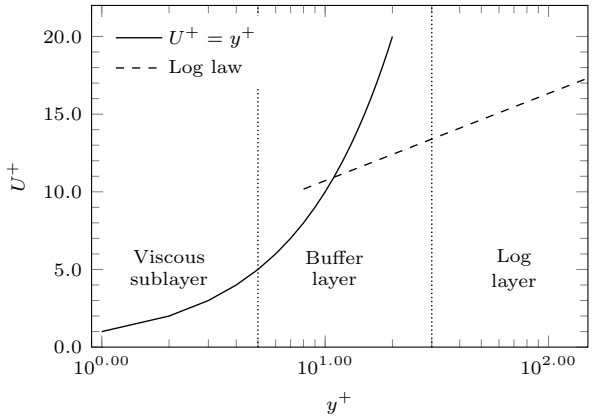

Figure 3.3: Profiles of the near-wall asymptote, $U^+ = y^+$, and the law of the wall, within the inner layer of a boundary layer [87]

Further away from the wall, from the end of the inner layer to the end of the boundary layer, the outer region exists. This is contained around $0.2\delta \leq y \leq \delta$. In this region, the fluid flow is now far enough from the wall that the effect of viscosity is less significant. The outer layer is therefore populated with eddies of larger length scales. The vortices here are in the spanwise direction, as opposed to the streamwise nature of the vortices in the inner region [108–110]. They have been identified as loop-shaped or arch-like vortical structures, which can also resemble a horse-shoe or hairpin shape [111–113]. An idealised illustration of the vortical structures populating the different regions of a turbulent boundary layer is published in [114]. This is shown in Figure 3.4. Almost two decades later, DNS results of a turbulent boundary layer by [115] also show these vortical structures in the turbulent region along a zero pressure gradient flat plate. This is shown in Figure 3.5.

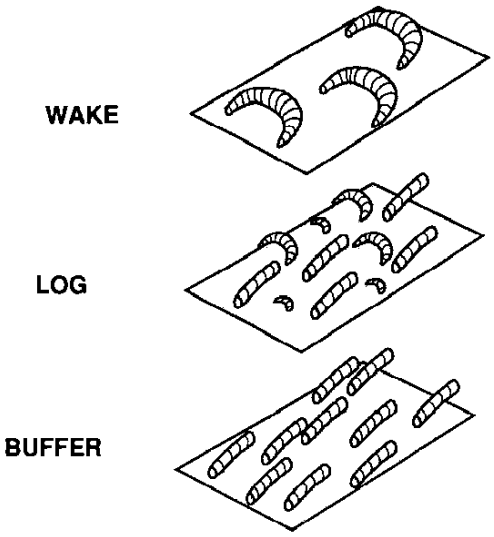

Figure 3.4: Idealised schematic of vortical-structures populations in different regions of the turbulent boundary layer (from [114])

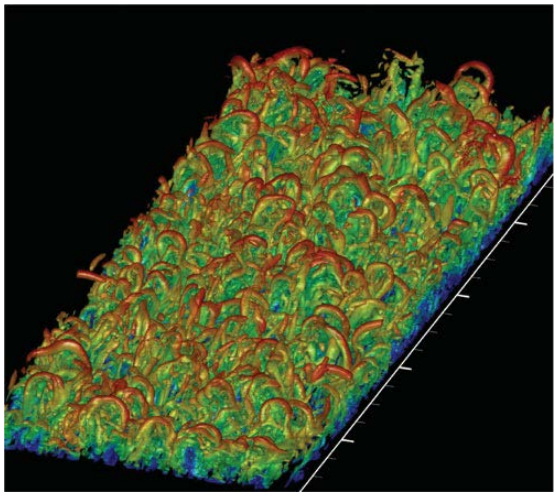

Figure 3.5: Iso-surfaces of the Q-criterion in a fully-developed region of a zero gradient flat plate at $Re_\theta = 900$ (from [115])

A number of theories into the mechanism of turbulence production identify the streamwise vortices in the near-wall region as the trailing 'legs' of these hairpin-like vortices [91,116–118]. The mean velocity in the outer region deviates slightly from the log law, particularly in non-equilibrium boundary layers with pressure gradient, and it follows instead the 'law of the wake', defined as:

$$U^+ = \frac{1}{K} ln(y^+) + C + \frac{2\Pi}{\kappa} f\left(\frac{y}{\delta}\right) \tag{3.3}$$

where Π is the wake parameter, typically 0 for pipe or channel flow and 0.45 for a zero pressure gradient flat plate, and K is the same as in equation (3.2). f is an S-shaped function of the dimensionless paramenter y/δ. Some popular forms are $f(\frac{y}{\delta}) = sin^2 \frac{\pi}{2} \frac{y}{\delta}$ and $f(\frac{y}{\delta}) = 3(\frac{y}{\delta})^2 - 2(\frac{y}{\delta})^3$.

3.3 The Navier-Stokes equations

The Navier-Stokes equations are a set of coupled, non-linear partial differential equations that have been known for over a century to be the governing laws of Newtonian-fluid flows. Newtonian refers to a fluid in which the viscous stresses arising from the flow are linearly proportional, through viscosity, to the rate of change of its deformation, also referred to as the local strain rate. The Navier-Stokes consist of an equation for the conservation of mass and three equations for the conservation of momentum. They will be presented in this section in the context of unsteady, incompressible, isothermal, three-dimensional flow in Cartesian coordinates using index notation. Unsteady refers to the characteristic where flow properties change with time. Incompressible refers to the constant density property of the fluid while isothermal refers to constant temperature. The derivation procedure of the Navier-Stokes

equations is presented in Appendix A.1, which results in the formulations as follows.

The conservation of mass equation, also known as the continuity equation, states that the mass of a fluid going into a certain control volume and leaving the control volume cannot change. This is represented using:

$$\frac{\partial u_i}{\partial x_i} = 0 \tag{3.4}$$

The conservation of momentum equations describe the balance of fluid forces acting on the control volume. The forces that are sufficiently significant to be considered in this framework are surface forces, which exist due to pressure and viscous effects. This is expressed as:

$$\frac{\partial u_j}{\partial t} + u_i \frac{\partial u_j}{\partial x_i} = -\frac{1}{\rho}\frac{\partial P}{\partial x_j} + \frac{\partial}{\partial x_i}\left(\nu \frac{\partial u_j}{\partial x_i}\right)\Bigg(\tag{3.5}$$

Due to the non-linear and coupled nature of the partial differential equations, the analytical solution to the Navier-Stokes equations is only available to simple flows such as the well-known Poiseuille or Couette flows. For practical and industrial flows, methods of approximations have to be employed to solve the equations numerically. To achieve this, averaging techniques can be employed. The averaging method that is regularly used in the context of turbulence modelling is time-averaging, an approach first introduced by Reynolds in 1894 [119] and hence referred to as Reynolds-Averaging. This is discussed in the next section.

3.4 Reynolds-Averaged Navier-Stokes (RANS)

The Reynolds-Averaging method starts by decomposing flow variables into their mean (average) and fluctuating parts. Using this definition, flow variables at any moment are defined as functions of space and time but on average, they do not vary with time. Using Reynolds-Averaging, the Reynolds-Averaged Navier-Stokes (RANS) equations are derived. The full derivation is presented in Appendix A.2. A summary is presented here.

For example, using Reynolds-Averaging the instantaneous velocity is decomposed as:

$$u_i(x_i, t) = U_i(x_i) + u_i'(x_i, t) \tag{3.6}$$

where u_i is the instantaneous quantity, U_i is the average quantity, and u_i' is the fluctuation from average. This can be illustrated using Figure 3.6.

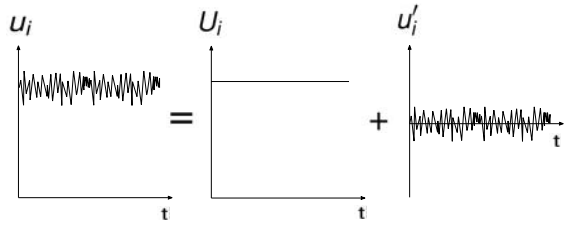

Figure 3.6: RANS decomposition

Applying this decomposition method to the momentum equation in equation (3.5) to split the flow quantities, both velocity and pressure, into their mean and fluctuating parts results in:

$$\frac{\partial}{\partial t}(U_j + u_j') + (U_i + u_i')\frac{\partial}{\partial x_i}(U_j + u_j') = -\frac{1}{\rho}\frac{\partial}{\partial x_j}(P + p') + \frac{\partial}{\partial x_i}\left[\nu\left(\frac{\partial}{\partial x_i}(U_j + u_j')\right)\right] \tag{3.7}$$

This equation is then averaged, taking into account that the average of a mean component is the mean component itself, the average of a fluctuating component is zero (since the flow is assumed to not vary with time on average). Applying these rules yields the following Reynolds-Averaged momentum equation:

$$\frac{\partial U_j}{\partial t} + U_i\frac{\partial U_j}{\partial x_i} = -\frac{1}{\rho}\frac{\partial P}{\partial x_i} + \frac{\partial}{\partial x_i}\left(\nu\left(\frac{\partial U_j}{\partial x_i} - \overline{u_i'u_j'}\right)\right) \tag{3.8}$$

It can be observed that the averaging procedure has led to the appearance of an extra momentum flux term, $\overline{u_i'u_j'}$, which is called the Reynolds stress tensor. In a three-dimensional framework, this tensor consists of 9 Reynolds stress components:

$$\overline{u_i'u_j'} = \begin{bmatrix} \overline{u'u'} & \overline{u'v'} & \overline{u'w'} \\ \overline{v'u'} & \overline{v'v'} & \overline{v'w'} \\ \overline{w'u'} & \overline{w'v'} & \overline{w'w'} \end{bmatrix} \tag{3.9}$$

All the flow fluctuations are therefore now regarded as part of turbulence, represented through $\overline{u_i'u_j'}$. Since $\overline{u'v'} = \overline{v'u'}$, $\overline{u'w'} = \overline{w'u'}$, and $\overline{v'w'} = \overline{w'v'}$, this translates to six new terms in the RANS system of equation. This introduces a fundamental closure problem in computing turbulent flows using RANS, i.e. there are more unknown variables than equations. To close this system of equations, the Reynolds stress tensor needs to be modelled. The efforts to modelling turbulent flows in the context of RANS are therefore focused on establishing a modelling approach for this Reynolds stress tensor. The most popular method is by using what is known as eddy-viscosity turbulence models. This is discussed in the next section.

3.4.1 Eddy-viscosity models

Eddy-viscosity models represent the most widely-used modelling approach in computing turbulent flows due to their performance at relatively low computational costs. In eddy-viscosity models, instead of directly modelling the Reynolds stress tensor, an approximation is made to relate the Reynolds stresses to the mean strain rate. This is called the Boussinesq hypothesis [120]. The details of this approximation will be explained first in this section. Subsequently, one of the most basic eddy-viscosity models, a two-equation model, in which two transport equations for the turbulent scales are employed, will be explored. While there are simpler turbulence models, a two-equation model is the most basic 'complete' model, i.e. it does not require algebraic or *a priori* definition of the scales or the turbulence structure.

3.4.1.1 The Boussinesq approximation

In the Navier-Stokes equations, the stresses due to viscous effects, which is the last term in equation (3.5), are expressed using Newton's law of viscosity, which linearly relates these stresses to the mean strain rate, S_{ij}, using the fluid viscosity, ν. Boussinesq in 1877 [120] proposed an approximation analogous to this relation: to relate the Reynolds stresses that arise from the turbulent fluctuations with the mean strain rate. To achieve this, a new positive scalar coefficient, ν_T (called eddy viscosity or turbulent viscosity), is introduced. This results in the following formulation for the Reynolds stress tensor:

$$\overline{u_i u_j} = -2\nu_T S_{ij} + \frac{2}{3}k\delta_{ij} \tag{3.10}$$

where k is the turbulent kinetic energy, δ_{ij} is Kronecker delta, and S_{ij} is the mean strain rate tensor, defined as:

$$S_{ij} = \frac{1}{2}\left(\frac{\partial U_i}{\partial x_j} + \frac{\partial U_j}{\partial x_i}\right)\Bigg(\tag{3.11}$$

Equation (3.10) describes the Boussinesq approximation, also referred to as the Boussinesq hypothesis or the eddy-viscosity hypothesis. The last term, $\frac{2}{3}k\delta_{ij}$, is the isotropic part of the stress. Isotropic refers to the property of a variable exhibiting the same value in all directions. This is therefore the part of the Reynolds stress tensor that are constant in x, y, and z, i.e. $\overline{u'u'} = \overline{v'v'} = \overline{w'w'}$. It is important to note that in contrast to viscosity, ν, which is a physical property of the fluid, the eddy viscosity, ν_T, is instead a modelled property of the flow. Applying the eddy-viscosity approximation to the Reynolds-Averaged momentum equation in equation (3.8) yields the following equation:

$$\frac{\partial U_j}{\partial t} + U_i \frac{\partial U_j}{\partial x_i} = -\frac{1}{\rho}\frac{\partial P}{\partial x_i} + \frac{\partial}{\partial x_i}\left[(\nu + \nu_T)\frac{\partial U_j}{\partial x_i}\right] \tag{3.12}$$

It can be observed that in eddy-viscosity models, the modelling approach is simplified from the need to model the full Reynolds stress tensor to modelling this eddy viscosity. The eddy viscosity can be obtained by modelling the turbulent scales. One approach to achieve this is by using a two-equation turbulence model, which solve for the turbulent length scale and time scale (or velocity scale). This is explored in the next section.

3.4.1.2 Two-equation models

Two-equation models attempt to represent the turbulent scales using two variables. For the first variable, a transport equation for turbulent kinetic energy, k, is used. k is defined to be half of the trace of the Reynolds stress tensor:

$$k = \frac{1}{2}\overline{u_j' u_j'} \tag{3.13}$$

The full transport equation for k can be derived from the transport equation for the Reynolds stress tensor, obtained from the Reynolds-Averaged momentum equation. The derivation process is presented in Appendix A.3 and this results in:

$$\overbrace{\underbrace{\frac{\partial k}{\partial t} + U_i\frac{\partial k}{\partial x_i}}_{\frac{Dk}{Dt}}}^{\text{Convection}} = \overbrace{\underbrace{-\overline{u_i' u_j'}\frac{\partial U_j}{\partial x_i}}_{P_k}}^{\text{Production}} - \overbrace{\underbrace{\nu\overline{\frac{\partial u_j'}{\partial x_i}\frac{\partial u_j'}{\partial x_i}}}_{\varepsilon}}^{\text{Dissipation}} + \overbrace{\frac{\partial}{\partial x_i}\left[\underbrace{-\overline{u_i' k}}_{\text{Turbulent transport}} \underbrace{-\overline{\frac{p'}{\rho}\delta_{ij}u_j'}}_{\text{Pressure diffusion}} + \underbrace{\nu\frac{\partial k}{\partial x_i}}_{\text{Molecular diffusion}}\right]}^{\text{Diffusion}} \tag{3.14}$$

Production of turbulent kinetic energy, P_k, is the rate at which energy is transferred from the mean flow to turbulence. It can be computed directly from the Reynolds stress tensor and the mean strain rate using the classical stress-strain approach:

$$P_k = -\overline{u_i' u_j'}\frac{\partial U_i}{\partial x_j} \tag{3.15}$$

The dissipation rate, ε, is by definition the rate at which turbulence dissipates into heat. It can be modelled using a second transport equation. The molecular diffusion term can be computed assuming the viscosity of the fluid is known. This leaves two terms that need to be modelled: the turbulent

transport term and the pressure diffusion term. Due to the lack of a straightforward analogy or experimental data for the pressure diffusion term, the two terms are generally grouped together. DNS data of a turbulent channel flow also indicates that the pressure diffusion term is very small compared to the turbulent transport term except very close to the wall, where the combination of the two terms are very small compared to the dissipation and viscous terms [121]. Therefore, this approximation is satisfactory. The turbulent transport term is modelled using a simple gradient diffusion model using the concept of eddy viscosity:

$$-\overline{u_i' k} \approx \sigma_k \nu_T \frac{\partial k}{\partial x_i} \tag{3.16}$$

where σ_k is a closure coefficient. Substituting equation (3.16) into equation (3.14) results in the following transport equation for k:

$$\frac{\partial k}{\partial t} + U_i \frac{\partial k}{\partial x_i} = -\overline{u_i' u_j'} \frac{\partial U_j}{\partial x_i} - \nu \overline{\frac{\partial u_j'}{\partial x_i} \frac{\partial u_j'}{\partial x_i}} + \frac{\partial}{\partial x_i} \left[(\nu + \sigma_k \nu_T) \frac{\partial k}{\partial x_i} \right] \tag{3.17}$$

or in a simplified form:

$$\frac{Dk}{Dt} = P_k - \varepsilon + \frac{\partial}{\partial x_i} \left[(\nu + \sigma_k \nu_T) \frac{\partial k}{\partial x_i} \right] \tag{3.18}$$

A number of approaches have been proposed for the second turbulence scale. The most popular choice is by using a transport equation for the dissipation rate, ε, as suggested earliest in [122–124] and popularised by Jones and Launder [125] and Launder and Sharma [73]. While it is possible to develop an exact transport for ε by manipulating the Reynolds-Averaged momentum equation, it will lead to a transport equation that contains complex terms that will require further modelling. Therefore, the transport equation for ε is formed to be analogous to the k equation. This is based on the attempt to explain the processes of ε using the four terms found in the k equation: convection, production, dissipation, and diffusion. Therefore, the widely-used transport equation for ε is as follows:

$$\frac{D\varepsilon}{Dt} = C_{\varepsilon,1} \frac{\varepsilon}{k} P_k - C_{\varepsilon,2} \frac{\varepsilon^2}{k} + \frac{\partial}{\partial x_i} \left[(\nu + \sigma_\varepsilon \nu_T) \frac{\partial \varepsilon}{\partial x_i} \right] \tag{3.19}$$

where σ_ε, $C_{\varepsilon,1}$, and $C_{\varepsilon,2}$ are closure coefficients.

Using these two turbulent variables, k and ε, the eddy viscosity can now be calculated. The standard $k - \varepsilon$ formulation prescribes the eddy viscosity using:

$$\nu_T = C_\mu \frac{k^2}{\varepsilon} \tag{3.20}$$

where C_μ is a constant of proportionality, also known as the eddy-viscosity constant.

The $k-\varepsilon$ model has been popular in its use in commercial CFD codes for over the past few decades due to its robustness and well-documented performance in a large variety of different flow situations. However, the model suffers from a number of well-known weaknesses. The most important one is its lack of sensitivity to adverse pressure gradients, as discussed earlier in the literature review in Chapter 2. In addition, the $k-\varepsilon$ model is numerically stiff when the model is applied up to the wall. It is difficult to prescribe a boundary condition for ε since it does not have a natural boundary condition, considering it does not go to zero at the solid wall.

A number of alternative scales have been proposed to overcome the deficiencies of the $k-\varepsilon$ models. One of the most successful in both improving prediction accuracy and numerical robustness is by using the specific turbulence dissipation rate, ω, or also referred to as the turbulence frequency, as proposed originally by Kolmogorov [126] and later most popularly by Wilcox *et al.* [71, 74–76, 127, 128]. The specific turbulence dissipation rate is by definition the rate of dissipation per turbulent kinetic energy, hence on dimensional grounds can be defined as:

$$\omega \sim \frac{\varepsilon}{k} \tag{3.21}$$

Applying this to the k and ε transport equations in equation (3.18) and equation (3.19), respectively, the following $k-\omega$ transport equations are derived:

$$\frac{Dk}{Dt} = P_k - \omega k + \frac{\partial}{\partial x_i}\left[(\nu + \sigma_k \nu_T)\frac{\partial k}{\partial x_i}\right]\Bigg(\tag{3.22}$$

$$\frac{D\omega}{Dt} = C_{\omega,1}\frac{\omega}{k}P_k - C_{\omega,2}\omega^2 + \frac{\partial}{\partial x_i}\left[(\nu + \sigma_\omega \nu_T)\frac{\partial \omega}{\partial x_i}\right]\Bigg(\tag{3.23}$$

where σ_k, σ_ω, $C_{\omega,1}$, and $C_{\omega,2}$ are closure coefficients. The eddy viscosity is now formulated as:

$$\nu_T = C_\mu \frac{k}{\omega} \tag{3.24}$$

The asymptotic behaviour of ω approaching a wall is that $\omega_{\text{wall}} \to \infty$. As an alternative for numerical reasons, an asymptotic relation has been proposed by [74–76]. ω is found to satisfy the following

equation near the wall:

$$\omega_{\text{wall}} \rightarrow \frac{6\nu}{C_{\omega,2}y^2} \qquad \text{as} \qquad y \rightarrow 0 \tag{3.25}$$

This has been shown to work well in providing a sufficiently large value of ω near the wall.

3.4.2 Reynolds stress models

The deficiencies exhibited by eddy-viscosity models, as discussed earlier in the literature review in Chapter 2, lead to the need to improve turbulence model predictions in a more general fashion. Approaches beyond the eddy-viscosity approximation are therefore considered. One approach is to solve the closure problem by approximating for the Reynolds stress tensor directly. This is known as Reynolds Stress Modelling (RSM). In RSM, transport equations for the Reynolds stress tensor are used. The exact transport equations for the Reynolds stress tensor, $\overline{u_i'u_j'}$, can be derived from the Reynolds-Averaged momentum equation. The derivation process is presented in Appendix A.3 and it yields:

$$\frac{D\overline{u_i'u_j'}}{Dt} = \overbrace{-\overline{u_i'u_k'}\frac{\partial U_j}{\partial x_k} - \overline{u_j'u_k'}\frac{\partial U_i}{\partial x_k}}^{\text{Production, } P_{ij}} \overbrace{-2\nu\overline{\frac{\partial u_i'}{\partial x_k}\frac{\partial u_j'}{\partial x_k}}}^{\text{Dissipation},\varepsilon_{ij}} \overbrace{+\overline{\frac{p'}{\rho}\left(\frac{\partial u_i'}{\partial x_j} + \frac{\partial u_j'}{\partial x_i}\right)}}^{\text{Pressure-strain},\Phi_{ij}} \underbrace{+\frac{\partial}{\partial x_k}\left[\underbrace{\overline{u_i'u_j'u_k'}}_{\text{Turbulent}} + \underbrace{\nu\frac{\partial\overline{u_i'u_j'}}{\partial x_k}}_{\text{Viscous}} - \underbrace{\overline{\frac{p'}{\rho}(\delta_{kj}u_i' + \delta_{ki}u_j')}}_{\text{Pressure}}\right]}_{\text{Diffusion},\mathcal{D}_{ij}} \tag{3.26}$$

The main disadvantage of RSM is in the introduction of six additional highly-coupled, non-linear partial differential equations, which makes this modelling approach computationally difficult and costly [33]. However, the difficulty in solving for this transport equation for all the Reynolds stress tensor components lies not only in the computational costs, but also in the assumptions and approximations that are required to solve it [34]. The dissipation term, ε_{ij}, for example, requires a separate transport equation. One example is the transport equation proposed by Hanjalic and Launder [29]:

$$\frac{D\varepsilon}{Dt} = C_{\varepsilon,1}\frac{\varepsilon}{k}P_k - C_{\varepsilon,2}\frac{\varepsilon^2}{k} + \frac{\partial}{\partial x_i}\left(C_\varepsilon\frac{k}{\varepsilon}\overline{u_i'u_j'}\frac{\partial\varepsilon}{\partial x_i}\right) \tag{3.27}$$

This equation can be observed to be similar to the ε transport equation in equation (3.19). Using this to model the ε_{ij} term means that assumptions of isotropy must be made. The turbulent transport term, which is $-\overline{u_i'u_j'u_k'}$, is usually modelled as a diffusion, which allows the use of a generalised gradient diffusion model by Daly and Harlow [129] which takes the form:

$$-\overline{u_i' u_j' u_k'} = C_s \frac{k}{\varepsilon} \overline{u_k' u_l'} \frac{\partial \overline{u_i' u_j'}}{\partial x_l} \tag{3.28}$$

The only terms in equation (3.26) that do not need additional modelling are the production and viscous terms. The pressure diffusion term is usually believed to be small and its modelling is less significant than the other terms [29]. The need for these modelling assumptions in RSM leads to complexity in its formulation and implementation and possibly offsets the physical gain of using this approach. This leads to the development of another group of turbulence models that do not belong precisely in eddy-viscosity models or Reynolds stress models. This is explored in the next section.

3.4.3 Non-linear eddy-viscosity models

Non-linear eddy-viscosity models aim to retain the simplicity of eddy-viscosity models while improving the model predictions. This is achieved by providing the means for modelling the anisotropy of the Reynolds stresses. A general, non-linear formulation is derived. As defined earlier, the isotropic part of the Reynolds stress tensor can be defined as $\frac{2}{3}k\delta_{ij}$. The Reynolds stress anisotropy is therefore defined simply as the departure of the Reynolds stress tensor from its isotropic components. It is commonly referred to in its dimensionless form using:

$$a_{ij} = \frac{\overline{u_i' u_j'}}{k} - \frac{2}{3}\delta_{ij} \tag{3.29}$$

A general relation for a_{ij} is proposed [2,3]. It is generally assumed that the Reynolds stress anisotropy is a function of the mean flow and the turbulent scales. The mean flow can be described using the mean strain and rotation rate tensors, S_{ij} and Ω_{ij}, respectively, while turbulent scales are described using a combination of turbulent variables, e.g. $k-\varepsilon$ or $k-\omega$. Based on this, the Reynolds stress anisotropy can be expressed in the following symbolic formulation which shows that it is a function of the aforementioned variables:

$$a_{ij} = \mathcal{F}(k, \omega, S_{ij}, \Omega_{ij}) \tag{3.30}$$

S_{ij} and Ω_{ij} are defined as:

$$S_{ij} = \frac{1}{2}\left(\frac{\partial U_i}{\partial x_j} + \frac{\partial U_j}{\partial x_i}\right), \qquad \Omega_{ij} = \frac{1}{2}\left(\frac{\partial U_i}{\partial x_j} - \frac{\partial U_j}{\partial x_i}\right) \tag{3.31}$$

A mathematical approach is proposed by Lumley [2] and Pope [3] for constructing a general relation for the a_{ij} tensor based on the two tensors S_{ij} and Ω_{ij}. The Reynolds anisotropy tensor, a_{ij}, is a

symmetric, traceless tensor of second order. Traceless means that the scalar invariant function of the tensor is zero. Second order means it has 3 directions associated with it, and in a given Cartesian coordinate system it has 3^2 components. A general representation for a symmetric, traceless second-order tensor (in this case a_{ij}) that depends on two other second-order tensors (in this case S_{ij} and Ω_{ij}) can be determined by using the theory of matrix polynomials [35,36] and the Cayley-Hamilton theorem [37–39]. Using the matrix polynomials theory, a_{ij} can be considered as a tensor polynomial formed from tensors S_{ij} and Ω_{ij}. Using the Cayley-Hamilton theorem, the number of terms in that polynomial can be limited by considering the tensors as matrices and relating matrices of higher extension to matrices of lower extension.

Since a second-order tensor such as a_{ij}, S_{ij}, and Ω_{ij} has 3 directions and 9 components, they can be considered as 3 x 3 matrices. It is shown that a matrix formed from two 3 x 3 matrices can be expressed as a polynomial of total degree ≤ 5 and of extension ≤ 3 [35,36]. Applying this to formulate an expression for a_{ij} from S_{ij} and Ω_{ij}, all the products that can be formed which are of total degree ≤ 5 and of extension ≤ 3 are listed as follows:

$$
\begin{array}{ll}
\text{Total degree 0} & \boldsymbol{I} \\
\text{Total degree 1} & \boldsymbol{S}, \boldsymbol{\Omega} \\
\text{Total degree 2} & \boldsymbol{S^2}, \boldsymbol{\Omega^2}, \boldsymbol{\Omega S}, \boldsymbol{S\Omega} \\
\text{Total degree 3} & \boldsymbol{S\Omega^2}, \boldsymbol{\Omega^2 S}, \boldsymbol{S^2\Omega}, \boldsymbol{\Omega S^2} \\
\text{Total degree 4} & \boldsymbol{S^2\Omega^2}, \boldsymbol{\Omega^2 S^2}, \boldsymbol{S\Omega S^2}, \boldsymbol{S^2\Omega S}, \boldsymbol{\Omega S\Omega^2}, \boldsymbol{\Omega^2 S\Omega} \\
\text{Total degree 5} & \boldsymbol{S\Omega^2 S^2}, \boldsymbol{S^2\Omega^2 S}, \boldsymbol{\Omega S^2\Omega^2}, \boldsymbol{\Omega^2 S^2\Omega}
\end{array}
\tag{3.32}
$$

For convenience, matrix notation (which is the bold font) is used here to avoid the need for repeating the tensor indices, i.e. $\boldsymbol{a} = a_{ij}$, $\boldsymbol{S} = S_{ij}$, and $\boldsymbol{\Omega} = \Omega_{ij}$. The reader is referred to [35,36] for more details on the derivation process. The first term which is of total degree 0 is the identity matrix, $\boldsymbol{I} = \delta_{ij}$. Because $\boldsymbol{a}$ is symmetric and has zero trace, all the symmetric, traceless independent tensor functions, $\boldsymbol{T}$, that can be formed from the terms listed in equation (3.32) are determined.

For the degree 1 terms, $\boldsymbol{S}$ is symmetric while $\boldsymbol{\Omega}$ is antisymmetric, thus forming the first independent function of the tensor polynomial:

$$
\boldsymbol{T}^{(1)} = \boldsymbol{S} \tag{3.33}
$$

For the degree 2 terms, the traceless forms of tensors $\boldsymbol{S^2}$ and $\boldsymbol{\Omega^2}$ can be obtained by getting the deviatoric components of those tensors. The deviatoric component of any second rank tensor $\boldsymbol{T}$ is $\boldsymbol{T} - \frac{1}{3}\{\boldsymbol{T}\}\boldsymbol{I}$. The curly brackets notation represents the trace of a tensor. Applying this to $\boldsymbol{S^2}$ and

$\boldsymbol{\Omega^2}$, two functions of the polynomial can be formed:

$$\begin{aligned} \boldsymbol{T}^{(2)} &= \boldsymbol{S^2} - \frac{1}{3}\{\boldsymbol{S^2}\}\boldsymbol{I} \\ \boldsymbol{T}^{(4)} &= \boldsymbol{\Omega^2} - \frac{1}{3}\{\boldsymbol{\Omega^2}\}\boldsymbol{I} \end{aligned} \tag{3.34}$$

Commutative property of matrix multiplication cannot be applied to $\boldsymbol{\Omega S}$ and $\boldsymbol{S\Omega}$, i.e. $\boldsymbol{\Omega S} \neq \boldsymbol{S\Omega}$ because $\boldsymbol{\Omega}$ is not a symmetric matrix. However, the trace of $\boldsymbol{\Omega S}$ is equal to the trace of $\boldsymbol{S\Omega}$, i.e. $\{\boldsymbol{\Omega S}\} = \{\boldsymbol{S\Omega}\}$. Since tensor trace is a linear mapping, the trace $\{\boldsymbol{\Omega S} - \boldsymbol{S\Omega}\}$ is equal to $\{\boldsymbol{\Omega S}\} - \{\boldsymbol{S\Omega}\}$ which is zero. Therefore, a traceless tensor function can be formed as the next function of the polynomial:

$$\boldsymbol{T}^{(3)} = \boldsymbol{\Omega S} - \boldsymbol{S\Omega} \tag{3.35}$$

We can apply the same procedure to the rest of the terms to obtain the remaining tensor functions. This results in a total of 10 tensor functions, which can be summarised using tensor notation as follows:

$$\begin{aligned} T_{ij}^{(1)} &= S_{ij} \\ T_{ij}^{(2)} &= S_{ik}S_{kj} - II_S\delta_{ij}/3 \\ T_{ij}^{(3)} &= \Omega_{ik}S_{kj} - S_{ik}\Omega_{kj} \\ T_{ij}^{(4)} &= \Omega_{ij}\Omega_{kj} - II_\Omega\delta_{ij}/3 \\ T_{ij}^{(5)} &= S_{ik}S_{kl}\Omega_{lj} - \Omega_{ik}S_{kl}S_{lj} \\ T_{ij}^{(6)} &= \Omega_{ik}\Omega_{kl}S_{lj} + S_{ik}\Omega_{kl}\Omega_{lj} - 2IV\delta_{ij}/3 \\ T_{ij}^{(7)} &= S_{ik}S_{kl}\Omega_{lp}\Omega_{pj} + \Omega_{ik}\Omega_{kl}S_{lp}S_{pj} - 2V\delta_{ij}/3 \\ T_{ij}^{(8)} &= S_{ik}\Omega_{kl}S_{lp}S_{pj} - S_{ik}S_{kl}\Omega_{lp}S_{pj} \\ T_{ij}^{(9)} &= \Omega_{ik}S_{kl}\Omega_{lp}\Omega_{pj} - \Omega_{ik}\Omega_{kl}S_{lp}\Omega_{pj} \\ T_{ij}^{(10)} &= \Omega_{ik}S_{kl}S_{lp}\Omega_{pq}\Omega_{qj} - \Omega_{ik}\Omega_{kl}S_{lp}S_{pq}\Omega_{qj} \end{aligned} \tag{3.36}$$

The independent scalar invariants are described using the traces of the functions:

$$\begin{aligned} II_S &= \{S_{kl}S_{lk}\} \\ II_\Omega &= \{\Omega_{kl}\Omega_{lk}\} \\ III_S &= \{S_{kl}S_{lm}S_{mk}\} \\ IV &= \{S_{kl}\Omega_{lm}\Omega_{mk}\} \\ V &= \{S_{kl}S_{lm}\Omega_{mn}\Omega_{nk}\} \end{aligned} \tag{3.37}$$

The Reynolds stress anisotropy tensor, a_{ij}, is then formulated as a tensor polynomial using these tensor functions, defined using:

$$a_{ij} = \sum_{n=1}^{10} \beta_{(n-1)} T_{ij}^{(n)} \tag{3.38}$$

in which $T_{ij}^{(n)}$ are the ten independent tensor functions defined in equation (3.36) and β_n are the expansion coefficients. Applying this to the formulation for the Reynolds stress obtained from equation (3.29) yields:

$$\begin{aligned}\overline{u_i' u_j'} &= a_{ij}k + \frac{2}{3}k\delta_{ij} \\ &= \sum_{n=1}^{10} \beta_{(n-1)} T_{ij}^{(n)} k + \frac{2}{3}k\delta_{ij}\end{aligned} \tag{3.39}$$

Equation (3.39) represents the most general formulation for the Reynolds stress tensor within the framework of algebraic turbulence modelling, i.e. without an added transport equation. A linear eddy-viscosity model can be observed to be a formulation retaining only the first term in the expansion, $T_{ij}^{(1)}$, which is simply the strain rate S_{ij}. Its coefficient, β_0, is proportional to the eddy viscosity and can be defined as $-2\nu_T/k$. The extra non-linear anisotropy terms are therefore the remaining terms from equation (3.38), which are calculated using $T_{ij}^{(n)}$ for $n \geq 2$ in the polynomial expansion. The formulation of the Reynolds stress tensor in the context of non-linear eddy-viscosity models can thus be defined using a linear eddy-viscosity formulation with the added extra anisotropy tensor terms:

$$\begin{aligned}\overline{u_i' u_j'} &= a_{ij}k + \frac{2}{3}k\delta_{ij} \\ &= \sum_{n=1}^{10} \beta_{(n-1)} T_{ij}^{(n)} k + \frac{2}{3}k\delta_{ij} \\ &= \beta_0 T_{ij}^{(1)} k + \sum_{n=2}^{10} \beta_{(n-1)} T_{ij}^{(n)} k + \frac{2}{3}k\delta_{ij} \\ &= -2\frac{\nu_T}{k} S_{ij} k + \sum_{n=2}^{10} \beta_{(n-1)} T_{ij}^{(n)} k + \frac{2}{3}k\delta_{ij} \\ &= \underbrace{-2\nu_T S_{ij} + \frac{2}{3}k\delta_{ij}}_{\text{Linear eddy-viscosity formulation}} + \underbrace{\sum_{n=2}^{10} \beta_{(n-1)} T_{ij}^{(n)}}_{\text{Extra anisotropy tensor, } a_{ij,\text{extra}}} k\end{aligned} \tag{3.40}$$

This structure of the formulation can be used for the implementation of a non-linear model because it allows a relatively straightforward incorporation of the extra anisotropy tensor into an existing linear eddy-viscosity code. The coupling with an eddy-viscosity model, e.g. a two-equation linear eddy-viscosity model, is done through the turbulent kinetic energy production term, P_k, using equation (3.15).

Chapter 4

Methodology

This chapter focuses on the methodologies used in the computations performed in the current work. All the calculations presented in this work are performed using OpenFOAM (version 6), an open-source CFD package developed by the OpenFOAM foundation [130]. OpenFOAM is chosen due to its open-source philosophy which allows the user to explore the assumptions and formulations used within the built-in codes as well as implement new models, solvers, and other numerical methods with relative ease. OpenFOAM has been gaining popularity in academia and industry over recent years and its validity has been established [131, 132].

The Navier-Stokes equations, or their Reynolds-Averaged forms, consist of a set of non-linear coupled partial differential equations for momentum transport. These have been presented in Section 3.3 and Section 3.4, respectively. Depending on the turbulence model that is used, one or more additional transport equations must also be solved for the turbulent scales, e.g. k and ε or ω. Non-linear partial differential equations are difficult to solve and analytical solutions only exist on the simplest of cases, e.g. a Poiseuille flow or Couette flow. The feasible approach for approximating the flow field is therefore to solve the governing equations numerically. This is achieved by approximating the differential equations using linear algebraic equations, through discretisation, and finding the solution to that system of algebraic equations. In the efforts to make numerical approximations within CFD more accurate, an abundance of approaches for the discretisation process as well as for solving the discretised equations have been proposed over the past decades. A comprehensive review is presented by Ferziger [133]. The approaches used in this work is presented here.

OpenFOAM, like most commercial CFD packages, employs the finite volume method for discretising the governing partial differential equations. Therefore, the finite volume method is introduced first. Some numerical approaches that are used for performing the computations are also mentioned. This includes the interpolation schemes for approximating the values of the control volume cells and the pressure-velocity coupling methods. Finally, the methodology for implementing a turbulence model

(in particular, a non-linear eddy-viscosity model) in OpenFOAM is presented.

4.1 Finite volume method

The finite volume method (FVM) divides a computational domain into a finite number of small control volumes, on each of which conservation principles are applied. The grid therefore only defines the boundaries of each control volume and not the computational nodes. One of the main advantages of FVM is therefore how global conservation is satisfied by construction, since each control volume respects the conservation principles. A main feature from a practical perspective is how it allows the grid used for dividing of the computational domain to be both structured and unstructured since discretisation is applied on the edges of each control volume instead of on the grid nodes. This opens up a wealth of possibilities for use in computing complex flow geometries in engineering applications.

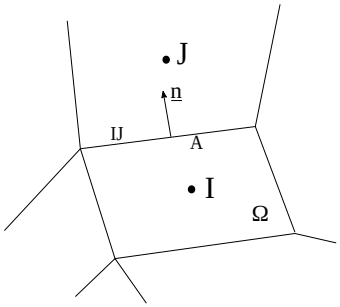

Figure 4.1: A typical control volume with notations used for FVM

To demonstrate the finite volume method, a general transport equation for some variable ϕ is considered:

$$\underbrace{\frac{\partial \rho\phi}{\partial t}}_{\text{Unsteady}} + \underbrace{\frac{\partial \rho u_j \phi}{\partial x_j}}_{\text{Convective}} = \underbrace{\frac{\partial}{\partial x_j}\left(\gamma \frac{\partial \phi}{\partial x_j}\right)}_{\text{Diffusive}} + \underbrace{S_\phi}_{\text{Source}} \tag{4.1}$$

where ρ is fluid density, u_j is instantaneous velocity, γ is the diffusion coefficient, and S_ϕ is a source term. Equation (4.1) is integrated over a control volume Ω. Refer to Figure 4.1 for a typical control volume and the notations. This integration results in:

$$\int_\Omega \frac{\partial \rho\phi}{\partial t} d\Omega + \int_\Omega \frac{\partial \rho u_j \phi}{\partial x_j} d\Omega = \int_\Omega \frac{\partial}{\partial x_j}\left(\gamma \frac{\partial \phi}{\partial x_j}\right) d\Omega + \int_\Omega S_\phi d\Omega \tag{4.2}$$

The convective and diffusive terms can be combined, resulting in:

$$\iint_{\Omega} \frac{\partial \rho\phi}{\partial t} d\Omega + \int_{\Omega} \frac{\partial}{\partial x_j} \left(\rho u_j \phi - \gamma \frac{\partial \phi}{\partial x_j} \right) d\Omega = \iint_{\Omega} S_\phi d\Omega \tag{4.3}$$

The Gauss divergence theorem can be used to convert the volume integrals of the convective and diffusive terms into surface integrals around the boundary edge, A, resulting in:

$$\iint_{\Omega} \frac{\partial \rho\phi}{\partial t} d\Omega + \int_{A} \left(\rho u_j \phi - \gamma \frac{\partial \phi}{\partial x_j} \right) n_k dA = \iint_{\Omega} S_\phi d\Omega \tag{4.4}$$

in which n_k is the vector normal to the surface A.

Simplifying this in the context of steady flows means the first (unsteady) term can be dropped. This results in the following equation which contains only the surface integral forms of the convective and diffusive terms, and the volume integral for the source term:

$$\int_{\partial\Omega} \left(\rho u_j \phi - \gamma \frac{\partial \phi}{\partial x_j} \right) n_k dA = \iint_{\Omega} S_\phi d\Omega \tag{4.5}$$

The left hand side terms simply represent the total net (convective and diffusive) flux of ϕ through the control volume. These integrals are therefore evaluated at the faces of the control volume. The simplest approximation to the integral is the midpoint rule: the integral is approximated as a product of the integrand at the face of the cell and the area of the face. This approximation can be shown to be second order in accuracy. The midpoint rule is applied for each face of the control volume and the surface integrals are approximated as the sum for all the faces, resulting in:

$$\int_{\partial\Omega} \left(\rho u_j \phi - \gamma \frac{\partial \phi}{\partial x_j} \right) n_k dA \approx \sum_k \left(\rho u_j \phi - \gamma \frac{\partial \phi}{\partial x_j} \right) n_k A_k \tag{4.6}$$

For example, this will be evaluated as a sum of the 4 faces in a rectangular 2-D control volume or 6 faces in a cuboid 3-D control volume. The subscript k represents an edge of the control volume. Referring to Figure 4.1, if we consider it as a 2-D grid, $A_k = A_{IJ}$ is the length of the edge between cell I and cell J and $n_k = n_{IJ}$ is the normal vector to this edge.

Similarly, the simplest second-order accurate approximation for the volume integral (the source term) is to replace the volume integral by the product of the mean value and the volume of the cell, *Vol*:

$$\iint_{\Omega} S_\phi d\Omega = (S_\phi)_P \, Vol \tag{4.7}$$

where the subscript P represents the cell centre node (say I in Figure 4.1).

In OpenFOAM, similarly to most CFD codes, the information of the global and turbulent quantities are stored at the cell-centres, i.e. the node at the centre of a control volume. Since convective and diffusive fluxes are evaluated at the control volume edges (commonly referred to as cell-faces), an interpolation method is needed to obtain the cell-face values. For example, referring to Figure 4.1, an interpolation is performed to obtain the cell-face value on edge IJ from the stored cell-centre values of the neighbouring cells which are I and J.

4.2 Interpolation schemes

There are two main interpolation schemes commonly used in CFD: the first-order upwind scheme and the second-order central-differencing scheme. A blended scheme between the two can be used. Some limiters can also be applied for stability.

4.2.1 Upwind scheme

The simplest scheme for approximating the cell-face values is the upwind scheme which, as the name suggests, directly takes the cell-centre values of the upwind neighbouring cell [134]. For example, we consider evaluating the value of ϕ_{IJ} which is the value of variable ϕ at some cell-face IJ that connects cells I and J (refer to Figure 4.1). The upwind scheme approximates ϕ_{IJ} from the values at cell-centres I and J depending on the flux direction using:

$$\phi_{IJ} = \begin{cases} \phi_J & \text{for} \quad u_{IJ} n_{IJ} > 0 \\ \phi_I & \text{for} \quad u_{IJ} n_{IJ} \leq 0 \end{cases} \tag{4.8}$$

The upwind scheme satisfies boundedness criteria by nature and therefore tends to give a stable solution. However, is it numerically diffusive, i.e. its leading truncation error resembles a diffusive flux. This can be magnified if the flow is oblique to the grid, leading to inaccurate solutions. In addition, it can be shown that the scheme is only first order in accuracy. This can be improved by using a very fine grid but a higher order scheme is usually preferred.

4.2.2 Central-differencing scheme

This scheme simply obtains the cell-face values using linear interpolation between the cell-centre values of the neighbouring cells. For example, we consider evaluating the value of ϕ_{IJ}:

$$\phi_{IJ} = \frac{1}{2} \left(\phi_I + \phi_J \right) \tag{4.9}$$

It can be shown that this scheme is second order accurate. However, it can produce oscillatory solutions, especially when the convective effects dominate compared to the diffusive terms [133].

The gradient term in the diffusive flux, $\partial\phi/\partial x_j$ on the right hand side of equation (4.6), is most commonly approximated using a linear interpolation in the same manner as the central-differencing scheme. For example, the gradient at cell-face IJ can be interpolated from values the neighbouring cells using:

$$\left(\frac{\partial\phi}{\partial x_j}\right)_{IJ} = \frac{\phi_J - \phi_I}{x_J - x_I} \tag{4.10}$$

This can also be shown to be second-order accurate. Higher-order interpolation schemes for obtaining the cell-face values exist. However, since the approximation for the gradient terms is almost always only second-order accurate (using equation (4.10)), the use of higher-order schemes for the other terms is rarely pursued because it does not offer improvement in the overall order of accuracy of the computation.

4.2.3 Blended scheme

As a compromise between stability and accuracy, another type of scheme exists which is a blend between the upwind scheme and the central-differencing scheme. This is useful for certain flow conditions where a converged solution to steady-state may not be possible with the use of higher-order discretisation schemes due to local flow fluctuations, but an accurate solution cannot be obtained with a first-order scheme. This is also referred to as a linear upwind scheme. It is first introduced in [135] and uses the following relation:

$$\phi = \lambda\phi_{\text{centred}} + (1-\lambda)\phi_{\text{upwind}} \tag{4.11}$$

The scheme can be observed to employ a weighting function to the interpolated values, ϕ_{centred} and ϕ_{upwind}, using an explicit correction. In OpenFOAM, the default figure is $\lambda = 0.25$. This scheme is used in the present work for evaluating all the divergence terms. This offers a blend between first and second order in accuracy.

4.2.4 Cell-based limiters

It is common practice in commercial CFD packages to apply limiters for calculating the cell-face values. It ensures that the cell-face values evaluated from the interpolation to the neighbouring cell-centre values are bounded by, hence do not exceed, the maximum or minimum values of the neighbouring cells. This is useful for improving solution stability by preventing spurious oscillations in areas where

rapid local changes in the flow field exist [136, 137]. An example is the limiter by [136] which simply limits the solution when it overshoots or undershoots. A variation of this limiter exists which applies the limit by bounding only the normal components of the gradient to the cell faces, instead of in all directions. This limiter is called a multidimensional limiter and as it avoids unnecessary bounding of the gradients, it is less diffusive than the standard limiter [137]. Cell-based limiters are applied in some of the computations presented in this work. This will be specified in the numerical setup section of the test cases.

4.3 Pressure-velocity coupling

Applying the approximation procedures in Section 4.1, replacing the variable ϕ with velocity, substituting fluid viscosity as the diffusive coefficient γ, and pressure gradients as the source term S_ϕ results in the following discretised momentum equation:

$$\sum_k \left(\rho u_i u_j - \mu \frac{\partial u_i}{\partial x_j} \right) n_k A_k = \left(\frac{\partial p}{\partial x_i} \right) Vol \tag{4.12}$$

This algebraic, discretised equation now needs to be solved. An iterative method is used. This involves starting from a guessed, initial 'solution', linearising the equations using that solution, improving the solution, and repeating the process until the result converges. Since the discretised momentum equations can only be solved for the velocities if the pressure field is known, and the remaining governing equation (the continuity equation) cannot be used directly to obtain pressure, a pressure-velocity coupling procedure is considered. The aim is to iteratively add corrections to the pressure field to get a resulting velocity field (from the momentum equations) that satisfies the continuity check. We consider the widely-used Semi-Implicit Method for Pressure Linked Equations (SIMPLE) method [138] and its consistent version, the SIMPLE-Consistent (SIMPLEC) method [139].

4.3.1 SIMPLE

SIMPLE uses an iterative procedure to solve a steady-state problem instead of fully resolving the pressure-velocity coupling. It works in a segregated manner which means it solves the equations for velocity and pressure separately. The algorithm is readily implemented within OpenFOAM as a steady-state incompressible flow solver `simpleFoam` and the procedure can be summarised in Figure 4.2.

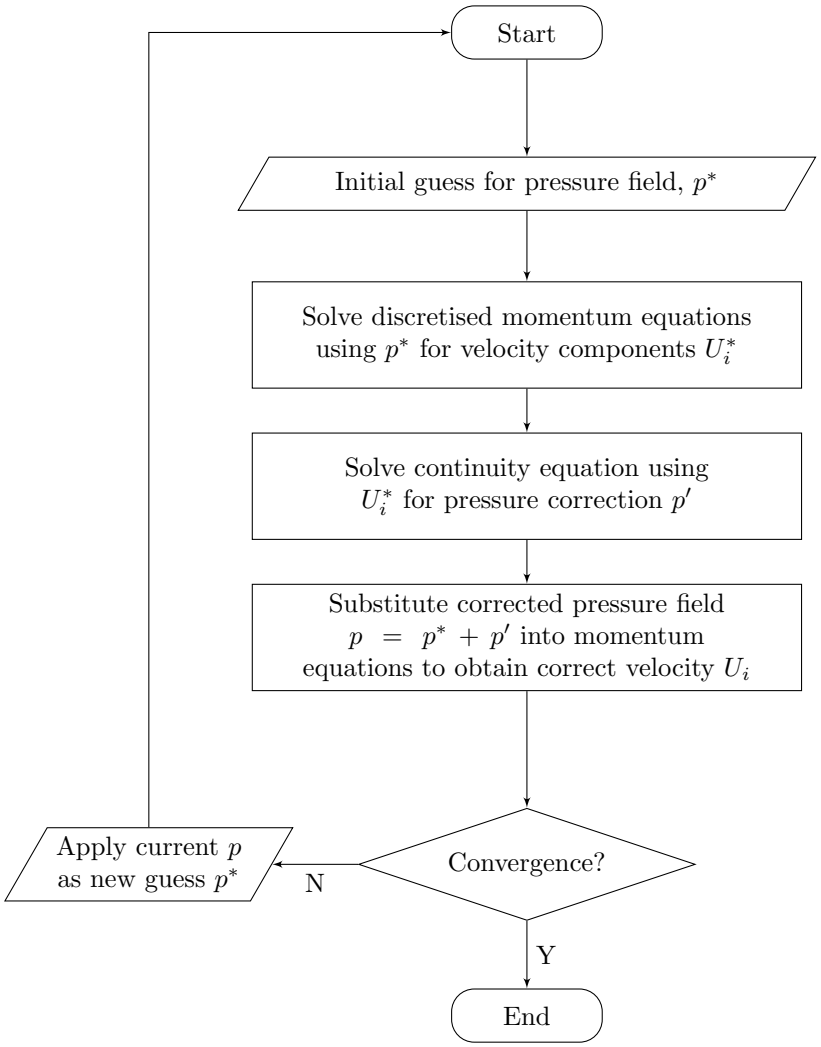

Figure 4.2: The SIMPLE algorithm

4.3.2 SIMPLEC

The major assumption in SIMPLE algorithm is the neglect of non-local velocity corrections, i.e. corrections that are obtained for each control volume are only applied for calculating the values in the respective control volume, and not the surrounding cells. Guessed or previously available values of the neighbouring cells are used for the interpolations. This can result in a slow convergence. Therefore, a number of modifications and variations of the SIMPLE scheme have been proposed over the years. A commonly used one, and one that is used in this work, is the SIMPLEC scheme. First proposed in [139], its procedure is similar to the SIMPLE algorithm except for the inclusion of the velocity corrections at the neighbouring cells.

4.3.3 Under-relaxation

During the iterative solving procedure, allowing the variables to change as much as the needed corrections could cause instabilities, especially at the start of the computation. Under-relaxation

technique is therefore often used for improving stability of the calculation by limiting the amount that a variable is allowed to change between iterations. An under-relaxation factor, α, is specified and used for calculating the value of a variable ϕ using the following formulation:

$$\phi^{\text{n}} = \phi^{\text{n-1}} + \alpha(\phi^{\text{calc}} - \phi^{\text{n-1}}) \tag{4.13}$$

where ϕ^{n} is the value of ϕ at iteration n, obtained by relaxing the value ϕ^{calc} which is calculated from the previous iteration, $n-1$, using α. It can be observed that α is a fraction, $0 < \alpha \leq 1$, which denotes the amount of change allowed for the next iterated value of ϕ, i.e. 0 refers to no change between iterations while 1 indicates no relaxation. A relaxation factor must be chosen which ensures stability but not too low such that it takes long computational time for convergence to be achieved. The value is specified by the user depending on the complexity of the flow.

4.4 Turbulence model implementation in OpenFOAM

The new non-linear eddy-viscosity turbulence model developed in the current work is implemented in OpenFOAM by the author. The new model is implemented within the `nonlinearEddyViscosity` base class in the RANS framework. It constructs the Reynolds stress tensor, `R`, by recalling the function to calculate it in the linear eddy-viscosity class, `eddyViscosity`, and adding the non-linear Reynolds stress components, `nonlinearStress`, calculated from the non-linear anisotropy tensor formulation in the turbulence model:

$$\begin{aligned} \underbrace{\overline{u_i' u_j'}}_{\texttt{R for nonlinearEddyViscosity}} &= \frac{2}{3}k\delta_{ij} + a_{ij}k \\ &= \underbrace{\frac{2}{3}k\delta_{ij} - 2\nu_T S_{ij}}_{\texttt{R from eddyViscosity}} + \underbrace{a_{ij,\text{extra}}k}_{\texttt{nonlinearStress}} \end{aligned} \tag{4.14}$$

This procedure motivates the separation of the linear and (extra) non-linear components of the Reynolds stress anisotropy in constructing the final formulation of the new model. The formulation of the extra anisotropy tensor developed in the current work, $a_{ij,\text{extra}}$, as described in its final form in Section 6.5 (presented later) is implemented in OpenFOAM using the code as follows. Note the highlighted line in which the `nonlinearStress` is defined. The full source code is described in Appendix E.

```
template<class BasicTurbulenceModel>
void nonlinearkOmega_fmu_fv_simplified<BasicTurbulenceModel>::
    correctNonlinearStress(const volTensorField& gradU)
{
```

```
        const volSymmTensorField S(symm(gradU));
        const volTensorField W(skew(gradU));

        const volScalarField fmuEff(fmu(S,W));

        this->nut_ = k_/(omega_ + this->omegaMin_);
        this->nut_.correctBoundaryConditions();
        fv::options::New(this->mesh_).correct(this->nut_);


        const volScalarField Cbeta1Eff ( min (
               min ( (Cbeta1_max_*fv1(Ret())*fv2(Ret())) , Cbeta1_max_ )
               + min ( (Cbeta1_mid_*fv1(Ret())*fv3(Ret())) , Cbeta1_mid_ )
               + min ( (Cbeta1_base_*(1-fv3(Ret()))) , Cbeta1_base_)
            , Cbeta1_max_ )
                        );

        const volScalarField Cbeta2Eff ( min (
               min ( (Cbeta2_max_*fv1(Ret())*fv2(Ret())) , Cbeta2_max_ )
               + min ( (Cbeta2_mid_*fv1(Ret())*fv3(Ret())) , Cbeta2_mid_ )
               + min ( (Cbeta2_base_*(1-fv3(Ret()))), Cbeta2_base_ )
             , Cbeta2_max_ )
                        );

        this->nonlinearStress_ =
        (
               fmuEff * scalingTerm()
               *(
                      Cbeta1Eff*dev(innerSqr(S))
                      + Cbeta2Eff*twoSymm(S&W)
                 )
        );

}
```

Chapter 5

Development of non-linear $k-\omega$ model

The literature has shown, as reviewed in Chapter 2, that a more accurate modelling of the Reynolds stress anisotropy can be achieved through non-linear eddy-viscosity modelling. Non-linear eddy-viscosity models use a formulation obtained from a generic, expanded expression for the Reynolds stress tensor, derived by Lumley [2] and Pope [3]. This approach is adopted in this work. The specific turbulence dissipation rate, ω, is used as the turbulence scale, in addition to the turbulent kinetic energy, k, since $k-\omega$ based models have been shown to perform better for modelling boundary layers and flows under adverse pressure gradients (compared to ε based models). A new non-linear turbulence model is proposed based on extending the classic linear $k-\omega$ model by Wilcox [71]. The development and formulation is explored in this chapter. A realisability condition is introduced to ensure physicality of the solutions, specifically to avoid negative turbulent kinetic energy. A simple scaling term is proposed to provide dimensional consistency for the non-linear terms. Finally, the model is calibrated using a plane channel flow and its performance is assessed.

5.1 Model formulation

5.1.1 $k-\omega$ equations and the anisotropy formulation coupling

The derivation process of the expanded non-linear anisotropy tensor relation that is used for the formulation of the Reynolds stress tensor has been established in Section 3.4.3 and therefore it will not be repeated here for succinctness. The transport equations for k and ω and their coupling with the anisotropy formulation is presented.

The transport equations for the turbulence scales used in the present model are described here. It is

based on the original $k-\omega$ model of Wilcox [71]. The model solves for the turbulent kinetic energy, k, and specific turbulence dissipation rate, ω, using the following transport equations:

$$\frac{Dk}{Dt} = P_k - \beta^* k\omega + \frac{\partial}{\partial x_j}\left[\left(\nu + \sigma_k \frac{k}{\omega}\right)\frac{\partial k}{\partial x_j}\right]\Bigg(\tag{5.1}$$

$$\frac{D\omega}{Dt} = C_{\omega,1} P_{k,\text{linear}} \frac{\omega}{k} - C_{\omega,2}\omega^2 + \frac{\partial}{\partial x_j}\left[\left(\nu + \sigma_\omega \frac{k}{\omega}\right)\frac{\partial \omega}{\partial x_j}\right]\Bigg(\tag{5.2}$$

The modelling approach pursued is one that requires minimal modification to the original $k-\omega$ model that is used. This is to avoid the need for a recalibration of a formulation that is commonly used, as well as to provide ease of implementation into existing CFD codes. The closure constants preserve the same values, i.e. $\beta^* = 0.09$, $C_{\omega,1} = 0.52$, $C_{\omega,2} = 0.072$, $\sigma_k = 0.5$, and $\sigma_\omega = 0.5$.

The production of turbulent kinetic energy, P_k, is modelled using the classical stress-strain approach:

$$P_k = -\overline{u_i' u_j'}\frac{\partial U_i}{\partial x_j} \tag{5.3}$$

in which the Reynolds stress tensor, $\overline{u_i' u_j'}$, is approximated using the classical Boussinesq approximation with the added non-linear, expanded terms. This is as defined in equation (3.40), through which the non-linear formulation is introduced, rewritten here:

$$\overline{u_i' u_j'} = -2\nu_T S_{ij} + \frac{2}{3}k\delta_{ij} + a_{ij,\text{extra}}k \tag{5.4}$$

The production term in the ω transport equation in equation (5.2) is formulated using $P_{k,\text{linear}}$, which is a production term calculated using the linear form of the Reynolds stress tensor, i.e. equation (5.4) without the last term. This is the preferred form in the present model for numerical stability. The non-linear form of the Reynolds stress enters through the production of the turbulent kinetic energy, P_k, using equation (5.3). Both forms have been tested for the production of ω, in combination with testing different numerical configurations, and they have been found to not affect the solution on the cases evaluated here.

A production limiter [140] is used for the production of turbulent kinetic energy, P_k, to prevent excessive production in regions where ω has low values. For example, in areas such as the freestream where it has been known that small changes in the mean strain rate can lead to large changes in the eddy viscosity due to this excessive production. To avoid this, a production limiter is used. It has also been found to be useful for eliminating unphysical buildup of eddy-viscosity in stagnation regions [69]. The

limiter is defined as:

$$P_k = \min(P_k, 20\beta^* k\omega) \tag{5.5}$$

The eddy viscosity is calculated using the classic formulation for $k-\omega$:

$$\nu_T = C_\mu \frac{k}{\omega} \tag{5.6}$$

in which C_μ is the eddy viscosity coefficient through which realisability is introduced. The formulation will be explained in the next section.

The extra anisotropy tensor, $a_{ij,\text{extra}}$, in equation (5.4) is a tensor polynomial as defined in equation (3.38), which contains ten independent tensor functions of the strain and rotation rates, S_{ij} and Ω_{ij}, respectively, without the first linear term. For clarity, this is rewritten here:

$$a_{ij,\text{extra}} = \sum_{n=2}^{10} \beta_{(n-1)} T_{ij}^{(n)} \tag{5.7}$$

$$\begin{aligned}
T_{ij}^{(1)} &= S_{ij} \\
T_{ij}^{(2)} &= S_{ik}S_{kj} - II_S\delta_{ij}/3 \\
T_{ij}^{(3)} &= \Omega_{ik}S_{kj} - S_{ik}\Omega_{kj} \\
T_{ij}^{(4)} &= \Omega_{ij}\Omega_{kj} - II_\Omega\delta_{ij}/3 \\
T_{ij}^{(5)} &= S_{ik}S_{kl}\Omega_{lj} - \Omega_{ik}S_{kl}S_{lj} \\
T_{ij}^{(6)} &= \Omega_{ik}\Omega_{kl}S_{lj} + S_{ik}\Omega_{kl}\Omega_{lj} - 2IV\delta_{ij}/3 \\
T_{ij}^{(7)} &= S_{ik}S_{kl}\Omega_{lp}\Omega_{pj} + \Omega_{ik}\Omega_{kl}S_{lp}S_{pj} - 2V\delta_{ij}/3 \\
T_{ij}^{(8)} &= S_{ik}\Omega_{kl}S_{lp}S_{pj} - S_{ik}S_{kl}\Omega_{lp}S_{pj} \\
T_{ij}^{(9)} &= \Omega_{ik}S_{kl}\Omega_{lp}\Omega_{pj} - \Omega_{ik}\Omega_{kl}S_{lp}\Omega_{pj} \\
T_{ij}^{(10)} &= \Omega_{ik}S_{kl}S_{lp}\Omega_{pq}\Omega_{qj} - \Omega_{ik}\Omega_{kl}S_{lp}S_{pq}\Omega_{qj}
\end{aligned} \tag{5.8}$$

A quadratic formulation is adopted here. The extra, non-linear anisotropy terms, $a_{ij,\text{extra}}$, reduces to the following formulation which retains up to $n = 4$ in the polynomial in equation (5.7), resulting in:

$$a_{ij,\text{extra}} = C_\mu \left[\beta_1 \left(S_{ik}S_{kj} - \frac{1}{3}II_S\delta_{ij}\right) + \beta_2 \left(S_{ik}\Omega_{kj} - \Omega_{ik}S_{kj}\right) + \beta_3 \left(\Omega_{ik}\Omega_{kj} - \frac{1}{3}II_\Omega\delta_{ij}\right)\right] \tag{5.9}$$

The invariants, II_S are II_Ω, are as presented in equation (3.37). To reiterate, they are described using the traces of the tensor functions, $II_S = \{S_{kl}S_{lk}\}$ and $II_\Omega = \{\Omega_{kl}\Omega_{lk}\}$. S_{ij} and Ω_{ij} are the mean strain and rotation rates, respectively. β_1, β_2, and β_3 are the anisotropy expansion terms, which are formulated using a scaling term, presented later in Section 5.1.3. C_μ is included here to incorporate

the realisability condition into the extra anisotropy formulation. The formulation is discussed in the next section.

5.1.2 Realisability

Since the extra anisotropy tensor, $a_{ij,\text{extra}}$, modelled using equation (5.9), takes into account the mean strain and vorticity rates at a quadratic level, it can cause the production of turbulent kinetic energy to decrease significantly (refer to equation (5.3)), especially at the start of a calculation. This can result in k becoming negative, hence non-physical. Therefore, a realisability condition is applied. Realisability is a concept introduced by Schumann [141] and Lumley [50]. It is defined as the requirement of non-negativity of turbulent normal stresses. It also represents a minimal requirement to prevent a turbulence model from producing unphysical results. Reynolds [142] and Shih *et al.* [143] suggest using non-constant C_μ as the model coefficient of their Reynolds stress algebraic models. This is in contrast to defining C_μ as the constant $C_\mu = \beta^* = 0.09$ as most turbulence models assume. This assumption is based on experimental and DNS data of wall-bounded flows and it is observed that this value is not applicable for other types of flows such as a homogeneous shear flow [144].

Therefore, to guarantee physically sound solutions, a new formulation for C_μ is proposed in [142, 143]. It uses realisability principles, from which constraints are derived using the ratios between the the mean strain and vorticity rates. A similar formulation is proposed by Kimura *et al.* [145] by using the maximum between the strain and rotation rates instead of the ratio. This is recalibrated and applied for the current model as:

$$C_\mu = min\left(1.00, \frac{1}{1 + 0.01M^2}\right)\left(\tag{5.10}$$

in which M is a parameter that takes the maximum between the strain and rotation rates in the form of their dimensionless invariants, $\widetilde{S}$ and $\widetilde{\Omega}$, respectively. These are defined as:

$$M = \max(\widetilde{S}, \widetilde{\Omega}) \qquad , \qquad \widetilde{S} = \frac{1}{\omega}\sqrt{2S_{ij}S_{ij}} \qquad , \qquad \widetilde{\Omega} = \frac{1}{\omega}\sqrt{2\Omega_{ij}\Omega_{ij}} \tag{5.11}$$

This realisability condition is applied to the formulation of the eddy viscosity, as calculated using equation (5.6). Since the anisotropy tensor does not include the eddy viscosity in its formulation, this is also applied directly in the quadratic formulation for $a_{ij,\text{extra}}$, as shown in equation (5.9).

5.1.3 Scaling term

The last part of the non-linear $k-\omega$ model development is to complete the formulation by defining the anisotropy expansion terms, β_1, β_2, and β_3 in equation (5.9) (or β_n for convenience). It is important to

note that these expansion terms are not constants. In addition to satisfying dimensional consistency, β_n must relate to the turbulent scales to ensure generality. The approach proposed here uses a scaling term proportional to $1/\omega^2$, which satisfies both requirements. Applying this to the proposed formulation for β_n results in the following equation:

$$\beta_n = \frac{C_{\beta,n}}{\max(\omega, \kappa S)^2} \tag{5.12}$$

The limiter in the denominator is introduced to ensure stability by avoiding excessive influence of the non-linear formulation in regions where the mean strain and vorticity rates are particularly high, for example, stagnation regions. S is the magnitude of the mean strain rate which ensures that the formulation scales to the local velocity field. This also avoids the need for an ad hoc cutoff at small value of ω (to avoid division by zero). The constant κ is calibrated iteratively such that stable solutions are obtained whilst ensuring that the anisotropy formulation remained active in the freestream and developed boundary layers. The calibrated value is $\kappa = 2.5$. Finally, $C_{\beta,n}$, which are $C_{\beta,1}$, $C_{\beta,2}$, $C_{\beta,3}$, corresponding to β_1, β_2, and β_3, respectively, are the expansion coefficients which require calibration.

5.1.4 Wall boundary conditions

At wall boundaries, no-slip condition applies which sets the velocity components and turbulent kinetic energy to zero. The specific dissipation rate, ω, is resolved using the classic solution for smooth walls, as derived by [74–76]:

$$\omega_{\text{wall}} \rightarrow \frac{6\nu}{C_{\omega,2} y^2} \qquad \text{as} \qquad y \rightarrow 0 \tag{5.13}$$

5.2 Initial calibration and assessment

In order to complete the model formulation, three coefficients need to be calibrated: $C_{\beta,1}$, $C_{\beta,2}$, and $C_{\beta,3}$, which originated from the formulation for the expansion terms β_n as defined in equation (5.12). The coefficient $C_{\beta,3}$ originates from the third term on the right-hand side of equation (5.9) (which contains the expansion term β_3). This term, however, has been found to cause unphysical behaviour in rotating isotropic flow [146] as well as cause a model to violate realisability [147]. Therefore, $C_{\beta,3}$ is taken as 0.

The initial step of the development is to calibrate $C_{\beta,1}$ and $C_{\beta,2}$ to be constants. This is carried out using an iterative procedure described here on a number of canonical cases, some of which are presented later for the validation of the final form of the model. To show the calibration process and present an initial assessment of the model, one case is presented here, which is a fully-developed plane channel flow. The case follows the DNS results of Lee and Moser [148], which is based on the DNS first done

by Kim *et al.* [81]. The case is a flow bounded by two static, infinitely long parallel plates separated by a distance h with the flow direction along the x-axis. The Reynolds number of the flow is 2850 based on the channel half-width and mean centreline velocity, or 180 based on the channel half-width and wall-shear velocity. The details of the computational setup is presented later in the validation section of the final form of the model (Section 6.6).

First, the linear $k-\omega$ model is applied for predicting this flow. It is immediately apparent that the isotropy assumption of the model results in the velocity fluctuations in x, y, and z directions to be identical as expected. These Reynolds stresses are shown in Figure 5.1 in their normalised form: $\overline{u_i'u_i'}^+ = \overline{u_i'u_i'}/u_\tau^2$ in which u_τ is the wall-shear velocity. As a consequence of this isotropic prediction, the rise in the streamwise velocity fluctuation is severely underpredicted, while the wall-normal and spanwise fluctuations are overpredicted.

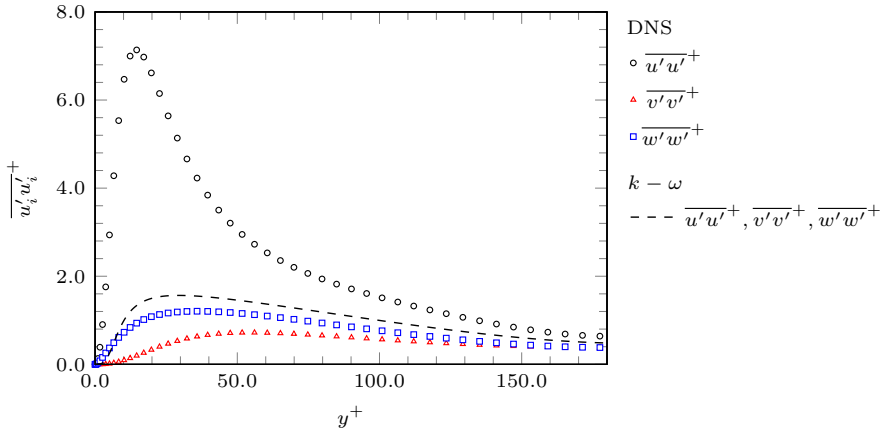

Figure 5.1: Reynolds stresses in a plane channel flow at $Re_\tau = 180$ predicted using the standard $k-\omega$ model. Markers correspond to DNS data [148].

Using numerical experimentation, the effects of changing the $C_{\beta,1}$ and $C_{\beta,2}$ values in the non-linear $k-\omega$ model to the prediction of Reynolds stresses for this flow configuration can be observed. Some examples are presented in Figure 5.2. Figure 5.2 (a) illustrates the effect of changing the $C_{\beta,1}$ constant on the prediction of the Reynolds stresses, while Figure 5.2 (b) shows the effect of changing the $C_{\beta,2}$ constant. It is observed that increasing the value of $C_{\beta,1}$ has the effect of increasing the streamwise fluctuations, $\overline{u'u'}$, as well as the wall-normal stress, $\overline{v'v'}$. The spanwise fluctuations, $\overline{w'w'}$, in contrast are seen to decrease with an increase in $C_{\beta,1}$. Meanwhile, the second coefficient, $C_{\beta,2}$, is seen to be responsible for the redistribution from the wall-normal to the streamwise component. Increasing the C_{β_2} value has the effect of increasing the predicted value of $\overline{u'u'}$ and decreasing the predicted value of $\overline{v'v'}$.

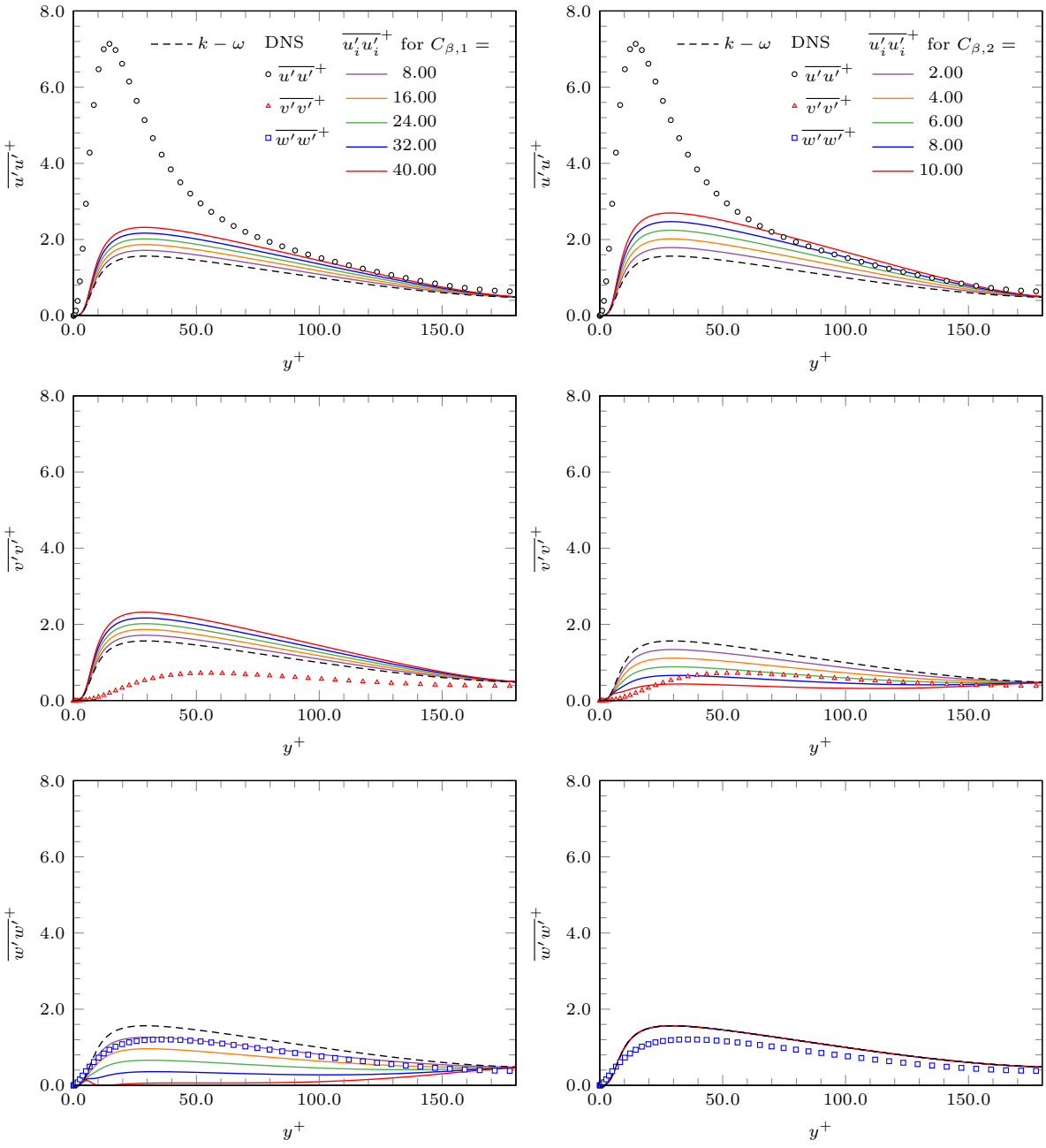

(a) $C_{\beta,1}$ test, $C_{\beta,2} = 0$ **(b)** $C_{\beta,2}$ test, $C_{\beta,1} = 0$

Figure 5.2: Profiles of velocity fluctuations in x, y, and z directions normalised using wall shear velocity in a plane channel flow at $Re_\tau = 180$ in response to change in $C_{\beta,1}$ and $C_{\beta,2}$ in the non-linear $k-\omega$ model. Markers correspond to DNS data [148].

Note that Figure 5.2 is shown as an example to illustrate how the Reynolds stress predictions change with the two coefficients and it does not show the complete range of values considered in the calibration process. An iterative process is used to calibrate the two coefficients as constants. The canonical configurations included for this calibration process are plane channel flows at three Reynolds numbers, a zero pressure gradient flow over a flat plate, and a curved channel flow. The details of the configurations are presented later in the validation section of the final form of the model (Section 6.6). The calibration process can be summarised in the flowchart in Figure 5.3 and is described as follows:

1. The process starts with setting minimum and maximum tested values (0 and 200, respectively) for the two coefficients.
2. At an increment of 10, a range of constants between those set minimum and maximum values are substituted as $C_{\beta,1}$ and $C_{\beta,2}$ into the non-linear $k-\omega$ formulation.
3. The model is used in the computations of the canonical configurations and the mean flow and turbulent quantities predictions are observed.
4. Two sets of values from the tested constants which result in a minimum error in the mean flow and turbulent quantities compared against the available DNS and experimental data are identified.
5. These two sets of values are subsequently set as the new minimum and maximum values for the tested constants in the next iteration, in which the increment in the range of tested values is reduced by multiplying it with 0.1.
6. The process is repeated until negligible change is seen with a reduction in the increment value, which is found to be 0.1.
7. The set of constants for $C_{\beta,1}$ and $C_{\beta,2}$ which results in minimum error in the cases considered is concluded to be the calibrated values.

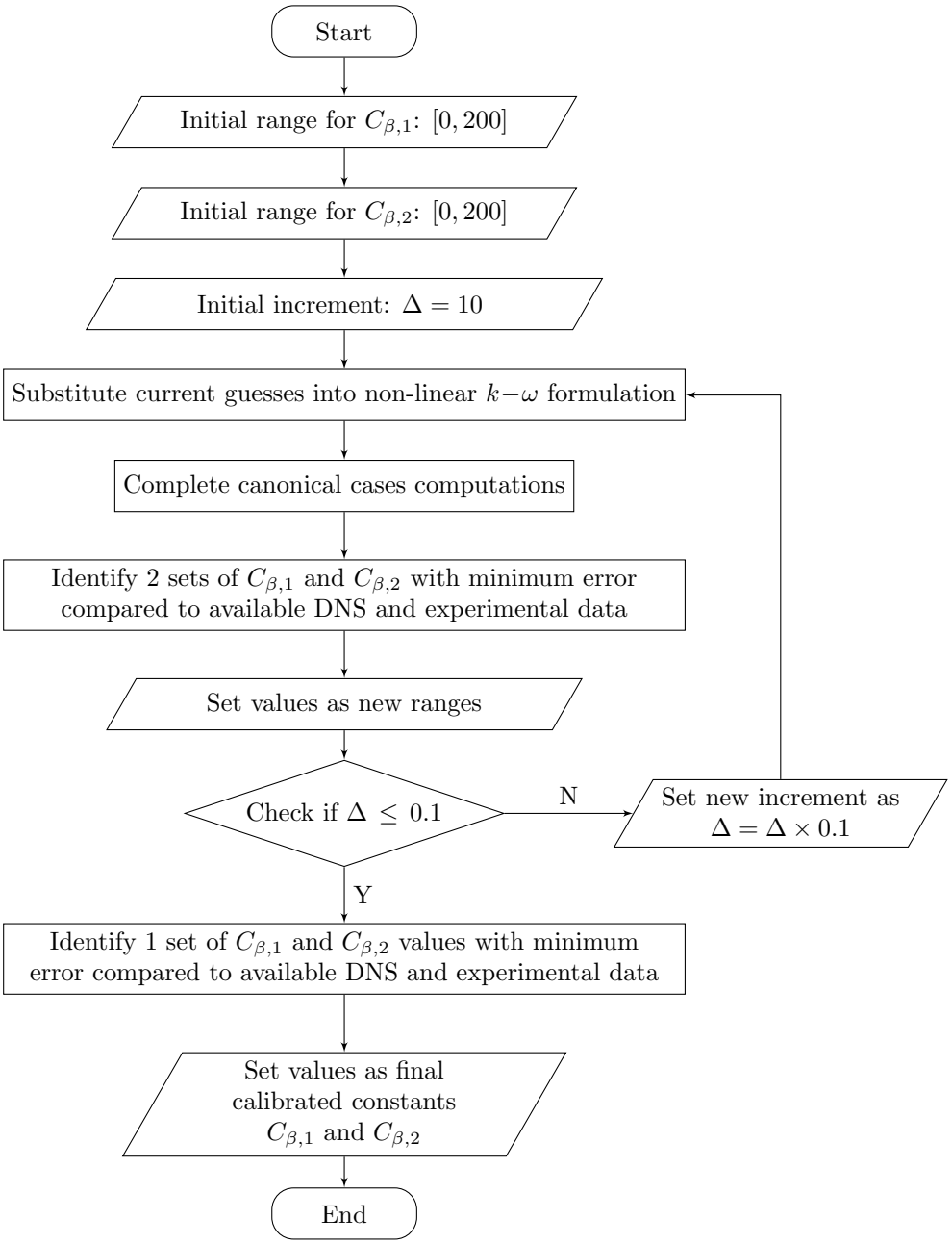

Figure 5.3: Flowchart of the iterative process for calibrating $C_{\beta,1}$ and $C_{\beta,2}$ as constants

The calibration results in the constants presented in Table 5.1 for the two expansion coefficients. The corresponding Reynolds stress prediction using these values for the plane channel flow case is presented in Figure 5.4. Improvements can be noted compared to the linear $k-\omega$ model, from which the three components are identical, marked by the dashed line. The spanwise velocity fluctuations, $\overline{w'w'}$, are predicted by the non-linear model at values closely matching the DNS data throughout. The model is shown to predict the rise in streamwise velocity fluctuations, $\overline{u'u'}$, and the suppressed wall-normal fluctuations, $\overline{v'v'}$, which correctly match the expected trend. Away from the wall, when $y^+ > 60$, the values for all three components closely agree with the DNS data. However, closer to the wall, within $y^+ < 60$, the anisotropy level can be seen to still be underpredicted.

Table 5.1: Summary of the baseline coefficients

$C_{\beta,1}$	$C_{\beta,2}$
10.2	8.0

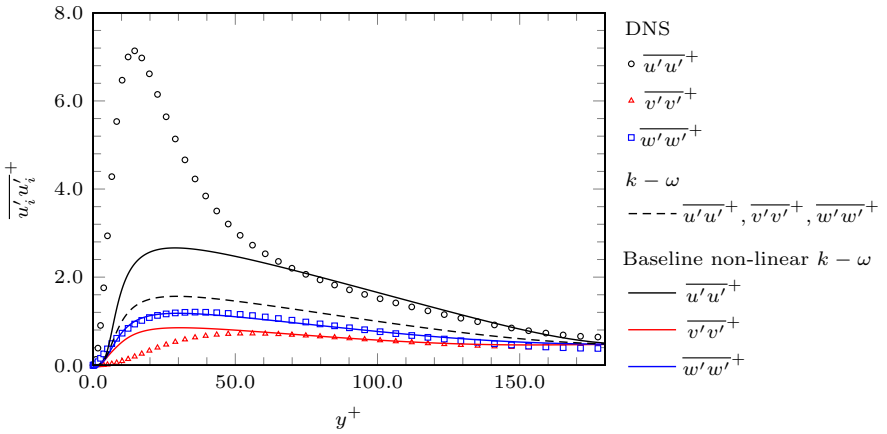

Figure 5.4: Reynolds stresses in a plane channel flow at $Re_\tau = 180$ predicted using the baseline non-linear $k-\omega$ model. Markers correspond to DNS data [148].

Consequently, a new approach is proposed. The aim is to incorporate the effects of near-wall anisotropy and improve the predictions of the model in the near-wall region. This modification is discussed in the next chapter. The results obtained using the calibrated constant values for $C_{\beta,n}$ in Table 5.1 is used as a 'baseline'. Even though this is a simple case, the anisotropic distribution of the Reynolds stress components has important effects when the model is used to model complex features near the wall [149, 150]. Durbin [150] observes based on the DNS data of Kim *et al.* [81] that the near-wall damping of eddy viscosity is caused by the suppression of the wall-normal velocity fluctuation, $\overline{v'v'}$, which when modelled accurately as a velocity scale can be used to avoid the overprediction of turbulent viscosity near the wall, hence promoting separation [151]. This redistribution is also especially important for modelling complex flow problems such as flows over curved surfaces. On such cases a transfer of energy exists that leaves the total kinetic energy unchanged but affects the distribution of the different fluctuating velocity components [152]. Therefore, an improvement on predicting the anisotropy of the Reynolds stress tensor near the wall is needed.

5.3 Summary

This chapter presents the formulation and the initial calibration and assessment of the new non-linear $k-\omega$ model. The model is proposed using a quadratic formulation for calculating the Reynolds stress anisotropy tensor. The transport equations used for modelling the turbulent scales, k and ω, have been described along with how they are coupled with the non-linear formulation of the Reynolds stresses. The model development includes the introduction of a realisability condition to ensure physicality of

the results. A scaling term formulation is proposed which relates the anisotropy expansion terms to the turbulence scales.

To complete the model, calibration of the anisotropy expansion coefficients is performed. The initial step, which has been presented in this chapter, is to calibrate them as constants. The performance of the resulting formulation on the plane channel flow case has been assessed. It can be observed that while offering improvement in the anisotropy prediction of the Reynolds stresses compared to the linear $k - \omega$ model, it underpredicts the anisotropy level near the wall. To improve the prediction of anisotropy near the wall, a new approach is proposed in the next chapter.

Chapter 6

Near-wall anisotropy modification

The development and calibration process of the 'baseline' non-linear $k-\omega$ model, for which the expansion coefficients in the non-linear Reynolds stress formulation are calibrated as constant values, has been presented in the previous chapter. The distribution of the Reynolds stresses predicted by this 'baseline' model for the plane channel flow case has been presented in Figure 5.4 and analysed. It is directly observable that the level of anisotropy closer to the wall, specifically in the region of $y^+ < 60$, is severely underpredicted. This highlights the need for a modification for the model to represent the high level of anisotropy in the near-wall region more closely. This is explored in this chapter. The development process is presented in Sections 6.1–6.4 and it can be summarised as follows:

1. Description of the rationale for a new concept of an anisotropy formulation that focuses on the inner region of a boundary layer — Section 6.1
2. Simplification of the Reynolds stress tensor distribution in a simple shear flow to directly relate the anisotropy expansion coefficients to the Reynolds stresses — Section 6.2
3. Using the simplified formulation of the Reynolds stresses and the available DNS data by [148] to obtain a benchmark distribution of the anisotropy expansion coefficients — Section 6.3
4. Definition of the new functions and the calibration process of new constants that arise — Section 6.4

Finally, a summary of the formulation of the new non-linear $k-\omega$ model with the new near-wall modification is presented Section 6.5. The model is subsequently validated on a number of canonical cases and its performance is assessed. This is presented in Section 6.6. The change in computational expense associated with the model is presented in Section 6.7 in comparison with the original $k-\omega$ model.

6.1 Rationale

Some details on the physics of wall-bounded turbulence has been presented in Section 3.2. To summarise, the inner layer, which is located within about $y/\delta < 0.1 - 0.2$ or $y^+ < 100 - 200$, has been identified in the literature as the region of the boundary layer in which the maximum turbulent kinetic energy is produced. This inner layer can be divided into 3 distinct regions: the viscous sublayer, the buffer layer, and the log layer.

The viscous sublayer, which is located within $y^+ < 5$, consists of low-speed streamwise vortices. The buffer layer, which is located within around $5 < y^+ < 30$, is associated with the bursting process, in which low-speed fluid and high-speed fluid ejects out of and sweeps towards the wall, respectively, which results in the generation of streaky turbulence structures here. In the context of RANS, these events are modelled as an average, that is, as the resultant Reynolds stresses. The bursting process therefore results in a significant production of Reynolds shear stress at the edge of the viscous sublayer into the buffer layer, accompanied by a major contribution to the production of turbulent kinetic energy. Moreover, the anisotropy of the boundary layer is also expected to reach its maximum here due to the direction of the vortices. This is evident in, among others, the DNS data by [148] as presented in Figure 5.4. It is notable that the underprediction of the streamwise fluctuations by the 'baseline' non-linear $k - \omega$ model, and consequently the underprediction of the level of anisotropy, is most apparent in this region, specifically around $3 < y^+ < 60$. This includes the edge of the viscous sublayer, the buffer layer, and the start of the log layer. Going further into the log layer, where a condition of local equilibrium exists, the level of anisotropy decreases as the flow approaches the outer region of the boundary layer. The 'baseline' non-linear $k - \omega$ formulation is shown to predict the anisotropic Reynolds stresses well in this log region.

A modification is consequently developed for incorporating these phenomena in the different regions of the boundary layer to improve the prediction of the model in the near-wall region. The term 'near-wall' here is used to refer to the inner region of the boundary layer: approximately $y/\delta < 0.1$ or $y^+ < 150$. The aim is to better represent the strongly turbulent boundary layer structures here through a more accurate prediction of the turbulent stresses, with a specific focus on improving the prediction of turbulence anisotropy. The new modification is introduced through the extra anisotropy tensor in the new non-linear $k - \omega$ model. For convenience, the formulation for the Reynolds stresses in the non-linear model is rewritten here:

$$\overline{u_i' u_j'} = -2\nu_T S_{ij} + \frac{2}{3} k \delta_{ij} + a_{ij,\text{extra}} k \tag{6.1}$$

where $a_{ij,\text{extra}}$ is the extra, non-linear anisotropy terms which are retained up to its quadratic terms and can be defined as:

$$a_{ij,\text{extra}} = C_\mu \left[\beta_1 \left(S_{ik}S_{kj} - \frac{1}{3}II_S\delta_{ij}\right)\right.\left(+ \beta_2 \left(S_{ik}\Omega_{kj} - \Omega_{ik}S_{kj}\right)\right]\left(\tag{6.2}$$

in which, the expansion terms β_n are formulated as:

$$\beta_n = \frac{C_{\beta,n}}{\max(\omega, \kappa S)^2} \tag{6.3}$$

The modification is developed to introduce a new formulation for the expansion coefficients $C_{\beta,n}$, replacing the constants to which they are calibrated in the previous chapter. To achieve this, three functional forms are proposed, corresponding to the three sublayers such that the high level of anisotropy at the edge of the viscous sublayer and within the buffer layer can be represented more accurately while the predictions in the log layer, which closely match the available DNS data in the plane channel flow, are retained. The functional forms are defined as f_{Viscous} (f_V), f_{Buffer} (f_B), and f_{Log} (f_L). This results in the following formulation for the expansion coefficients:

$$C_{\beta,n} = f_{V,n} + f_{B,n} + f_{L,n} \tag{6.4}$$

where $n = 1, 2$ to represent the two expansion terms in equation (6.2).

The definition of the three new functions are presented later in Section 6.4. Next, the simplification process for the distribution of Reynolds stresses in a simple shear flow is presented. It has been shown in Section 5.2 that the plane channel flow case provides the means to clearly demonstrate the effects of the non-linear formulation, specifically its corresponding expansion coefficients, on the predictions of Reynolds stresses and their anisotropy. Therefore, it is used in this chapter for the development of the new approach.

6.2 Simplification of plane channel flow case

Using an analytical simplification, the expression for the Reynolds tensor in for this flow configuration can be simplified into linear equations which directly relate the stresses to the anisotropy expansion coefficients, $C_{\beta,n}$, as their dependent variables. The case considered here is the same the one applied in the previous chapter, which is based on the DNS data of Lee *et al.* [148] at Reynolds number of 180 (based on half-width of the channel and the wall shear velocity). Fully-developed channel flow case is a simple flow bounded by two infinite parallel plates separated by a distance of h with the flow direction along the x-axis. The geometry is presented in Figure 6.1.

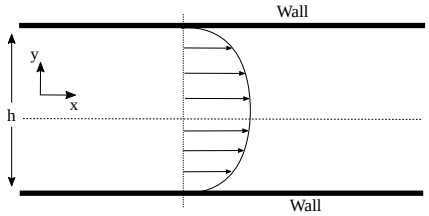

Figure 6.1: Geometry of the fully-developed channel flow test case

The flow can be described by the only non-zero mean-velocity component, the streamwise U_x, as a function of only the wall-normal coordinate, y. Therefore, there is only one non-zero velocity gradient: dU_x/dy. For conciseness, this will be referred to as $\lambda = dU_x/dy$. The mean strain and vorticity rate tensors are defined as:

$$S_{ij} = \frac{1}{2}\left(\frac{\partial U_i}{\partial x_j} + \frac{\partial U_j}{\partial x_i}\right) \qquad , \qquad \Omega_{ij} = \frac{1}{2}\left(\frac{\partial U_i}{\partial x_j} - \frac{\partial U_j}{\partial x_i}\right) \tag{6.5}$$

Therefore, for $i, j = 1, 2, 3$ (representing the three-dimensional Cartesian coordinates) and applying λ as the only non-zero velocity gradient, the following strain and rotation rate tensors for this case are obtained:

$$S_{ij} = \begin{bmatrix} 0 & \frac{1}{2}\lambda & 0 \\ \frac{1}{2}\lambda & 0 & 0 \\ 0 & 0 & 0 \end{bmatrix} \quad , \quad \Omega_{ij} = \begin{bmatrix} 0 & \frac{1}{2}\lambda & 0 \\ -\frac{1}{2}\lambda & 0 & 0 \\ 0 & 0 & 0 \end{bmatrix} \tag{6.6}$$

Reducing the deformation rates for this case to equation (6.6), an analytical simplification can be done for the Reynolds stress tensor, $\overline{u_i' u_j'}$, by substituting equation (6.6) into the $\overline{u_i' u_j'}$ formulation, rewritten here:

$$\overline{u_i' u_j'} = -2\nu_T S_{ij} + \frac{2}{3} k \delta_{ij} + a_{ij,\text{extra}} k \tag{6.7}$$

For the linear $k - \omega$ model, only the first two terms on the right hand side of equation (6.7) are applicable. A simplified expression for the first term in the Reynolds stress tensor, $\overline{u'u'}$, can be obtained by applying equation (6.6) into equation (6.7) for $i = 1$ and $j = 1$, resulting in:

$$\overline{u'u'} = \overline{u_1' u_1'} = -2\nu_T S_{11} + \frac{2}{3} k \delta_{11} = \frac{2}{3} k \tag{6.8}$$

It can be shown that applying the same procedure to calculate the remaining normal Reynolds stress components results in the following for the linear model:

$$\overline{u'u'} = \frac{2}{3}k \qquad , \qquad \overline{v'v'} = \frac{2}{3}k \qquad , \qquad \overline{w'w'} = \frac{2}{3}k \tag{6.9}$$

The complete derivation process is presented in Appendix B. The values of $\overline{u'u'}$, $\overline{v'v'}$, and $\overline{w'w'}$ are isotropic as expected.

For the new non-linear $k-\omega$ model, the quadratic extra anisotropy tensor formulation in equation (5.9), defined earlier in Section 5.1.1, is substituted into the last term in equation (6.7) and a similar procedure is applied. For the first term in the Reynolds stress tensor, $\overline{u'u'}$ ($i = 1$ and $j = 1$), the following is obtained:

$$\begin{aligned}\overline{u'u'} = \overline{u_1'u_1'} =& -2\nu_T S_{11} + \frac{2}{3}k\delta_{11} + C_\mu \left[\frac{C_{\beta,1}}{\max(\omega, \kappa S)^2}\left(S_{12}S_{21} - \frac{1}{3}\{\boldsymbol{S}^2\}\delta_{11}\right)\right. \\ &\left. + \frac{C_{\beta,2}}{\max(\omega, \kappa S)^2}\left(S_{12}\Omega_{21} - \Omega_{12}S_{21}\right)\right] \\ =& \frac{2}{3}k + C_\mu \frac{1}{\max(\omega, \kappa S)^2}\lambda^2\left(\frac{1}{12}C_{\beta,1} + \frac{1}{2}C_{\beta,2}\right)\end{aligned} \tag{6.10}$$

The complete derivation process is shown in Appendix B. Applying the same procedure to simplify for the remaining normal Reynolds stress components results in the following for the new quadratic $k-\omega$ model:

$$\begin{aligned}\overline{u'u'} &= \frac{2}{3}k + C_\mu \frac{1}{\max(\omega, \kappa S)^2}\lambda^2\left(\frac{1}{12}C_{\beta,1} + \frac{1}{2}C_{\beta,2}\right) \\ \overline{v'v'} &= \frac{2}{3}k + C_\mu \frac{1}{\max(\omega, \kappa S)^2}\lambda^2\left(\frac{1}{12}C_{\beta,1} - \frac{1}{2}C_{\beta,2}\right) \\ \overline{w'w'} &= \frac{2}{3}k + C_\mu \frac{1}{\max(\omega, \kappa S)^2}\lambda^2\left(-\frac{1}{6}C_{\beta,1}\right)\end{aligned} \tag{6.11}$$

The simplified expressions in equation (6.11) show how the Reynolds stress tensor and its inherent anisotropy are directly dependent on the expansion coefficients, $C_{\beta,1}$ and $C_{\beta,2}$. If the two coefficients are set to zero, the isotropic expression in equation (6.9) is returned. This analytical simplification allows a relatively straightforward approach for determining the 'ideal' or benchmark values for these two coefficients.

6.3 Obtaining benchmark $C_{\beta,n}$

Using the simplified equations for the Reynolds stresses in (6.11), which are direct functions of the two expansion coefficients, benchmark values for $C_{\beta,n}$ can be obtained. For this purpose, DNS data by Lee *et al.* [148] is used. The aim is to approximate a distribution of $C_{\beta,n}$ that would result in a Reynolds stress distribution that closely match the DNS data. Subsequently, this benchmark distribution is used to inform the development process of the new anisotropy formulation. The approach to obtain this 'ideal' or benchmark distribution for the anisotropy expansion coefficients is summarised in the flowchart in Figure 6.2 and is described as follows:

1. Information on the 'benchmark' distribution of the Reynolds stresses $\overline{u'u'}$, $\overline{v'v'}$, $\overline{w'w'}$ are obtained from available DNS data [148].
2. Plane channel flow computation is completed using the existing linear $k-\omega$ model.
3. Obtain predictions of k, ω, and velocity gradients from the $k-\omega$ computation.
4. Calculate the realisability coefficient, C_μ, (using equation (5.10)) as well as the magnitude of the mean strain rate, S, from the velocity gradient predictions.
5. Consider the system equation in (6.11) as a linear problem in which the variables $\overline{u'u'}$, $\overline{v'v'}$, $\overline{w'w'}$, k, ω, C_μ, λ, and S are known (from the available DNS data and a linear $k-\omega$ computation) and the variables $C_{\beta,1}$ and $C_{\beta,2}$ are unknown.
6. Substitute known variables into equation (6.11), which can be manipulated and expressed in a matrix form as:

$$\underbrace{\begin{bmatrix} \frac{1}{12} & \frac{1}{2} \\ \frac{1}{12} & -\frac{1}{2} \\ -\frac{1}{6} & 0 \end{bmatrix}}_{\boldsymbol{A}} \underbrace{\begin{bmatrix} C_{\beta,1} \\ C_{\beta,2} \end{bmatrix}}_{\boldsymbol{x}} = \underbrace{\frac{\max(\omega, \kappa S)^2}{C_\mu \lambda^2 k} \begin{bmatrix} \overline{u'u'} - \frac{2}{3}k \\ \overline{v'v'} - \frac{2}{3}k \\ \overline{w'w'} - \frac{2}{3}k \end{bmatrix}}_{\boldsymbol{B}} \tag{6.12}$$

7. Apply a numerical approach to the problem $\boldsymbol{A} \cdot \boldsymbol{x} = \boldsymbol{B}$ above to find an approximate solution for $\boldsymbol{x}$.

The use of the predictions of k, ω, and velocity gradients from a linear $k-\omega$ computation for this process (Steps 2 and 3 above) is allowed due to the simplicity of this flow configuration. The turbulent kinetic energy, k, is defined as the trace of the Reynolds stress tensor, i.e. $k = \frac{1}{2}\left(\overline{u'u'} + \overline{v'v'} + \overline{w'w'}\right)$. It can be shown that the trace of the Reynolds stress tensor as expressed in the anisotropic form of equation (6.11) is the same as the trace of the Reynolds stress tensor as expressed in the isotropic form of equation (6.9). Therefore, while the Reynolds stress components obtained using the non-linear $k-\omega$ model are anisotropic and not equal to the isotropic components obtained using the linear $k-\omega$ model, the turbulent kinetic energy predicted by the two models are identical in this case. Note that this is due to the simplicity of this flow configuration in which there is only one non-zero component of the velocity gradient and is not applicable to other flow cases.

The numerical method applied here (Step 7 above) is to obtain the best approximate solution for $\boldsymbol{x} = \begin{bmatrix} C_{\beta,1} \\ C_{\beta,2} \end{bmatrix}$ for which the minimum squared error $(\boldsymbol{A}\cdot\boldsymbol{x}-\boldsymbol{B})^2$ is returned, i.e. treating equation (6.12) as a least-squares problem. As the initial baseline calibration process for $C_{\beta,1}$ and $C_{\beta,2}$ in Chapter 5 shows that positive values for the expansion coefficients return the correct trend of Reynolds stresses, the problem can be further constrained as a Non-Negative Least-Squares (NNLS) problem, that is, to find $\boldsymbol{x}$ such that $\min(\boldsymbol{A}\cdot\boldsymbol{x}-\boldsymbol{B})^2$ is obtained where $\boldsymbol{x} \geq 0$. The numerical approach considered here is the Standard NNLS algorithm proposed by Lawson and Hanson [153] which is readily available as the `lsqnonneg` function in the open-source numerical computation package GNU Octave [154]. It is an active set method which starts with a set of possible basis vector and computes the associated dual vector. It then selects the basis vector corresponding to the maximum value in the dual vector to swap it out of the basis in exchange for another possible candidate. This continues until the dual vector is ≤ 0.

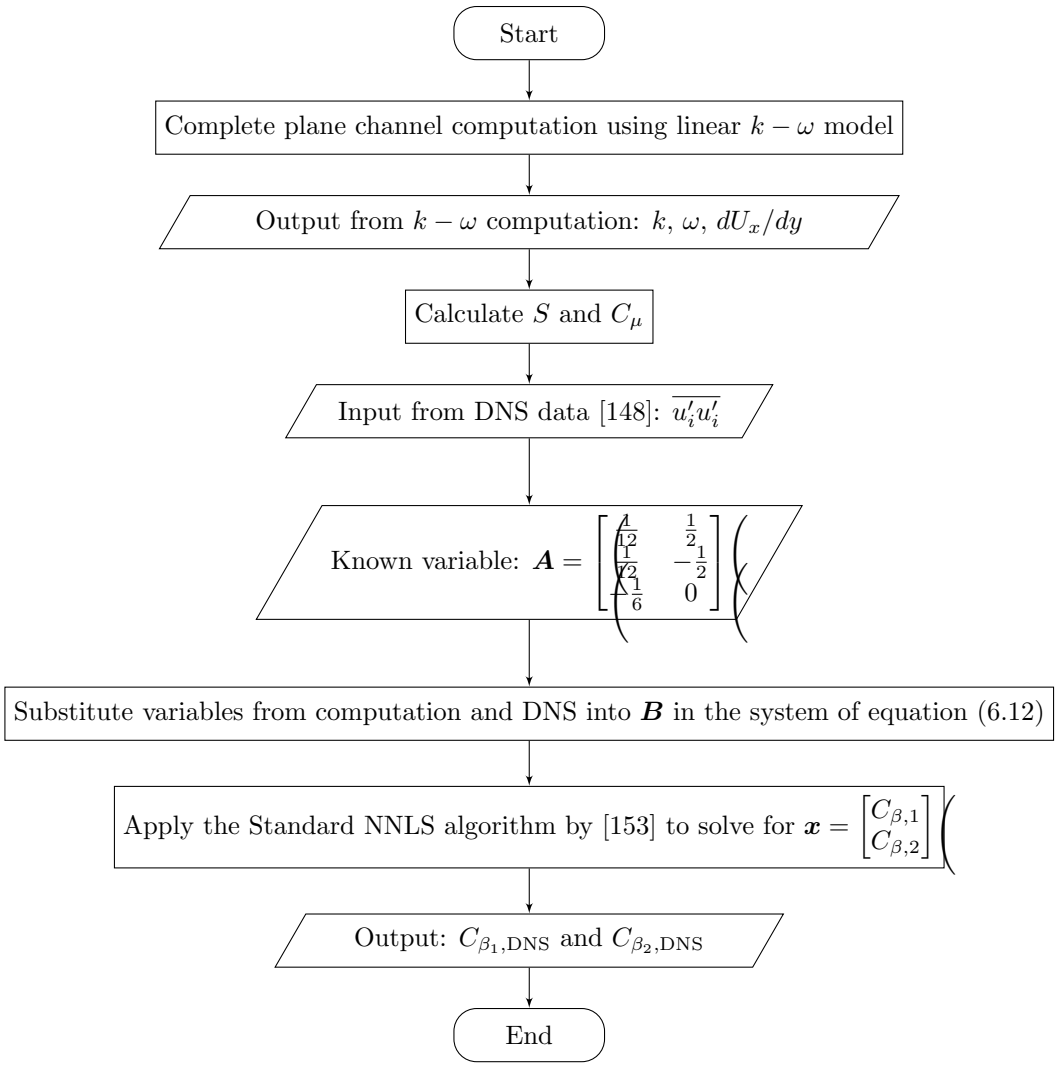

Figure 6.2: Flowchart of the process for obtaining benchmark $C_{\beta,1\ \mathrm{DNS}}$ and $C_{\beta,2\ \mathrm{DNS}}$ using DNS data

The aforementioned methodology for obtaining the benchmark expansion coefficients here can be summarised using the flowchart in Figure 6.2. Since the available DNS data for the Reynolds stresses is used as the benchmark, this results in a distribution of the expansion coefficients that minimise the least-squares error of the Reynolds stresses compared to DNS data. These values are therefore referred to as benchmark values $C_{\beta,1\ \mathrm{DNS}}$ and $C_{\beta,2\ \mathrm{DNS}}$. The distribution is presented in Figure 6.3.

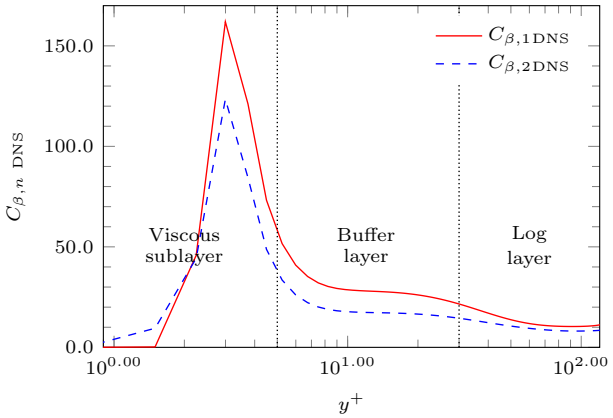

Figure 6.3: Profile of the benchmark expansion coefficient $C_{\beta,n\ \mathrm{DNS}}$ in reference to the regions of an inner layer

To avoid the expansion coefficients reaching asymptotically large values at the wall due to the turbulent kinetic energy, k, being a denominator in the right hand side of equation (6.12), a limiting factor of 1×10^{-12} is applied to k to avoid division by zero. This is also needed to avoid instability in the computation which may happen if the anisotropy expansion coefficient has an excessively large gradient in its distribution.

It is observed from Figure 6.3 that both coefficients exhibit the same trend, although the $C_{\beta,1\ \mathrm{DNS}}$ values are higher than $C_{\beta,2\ \mathrm{DNS}}$. The need to represent the enhanced anisotropy near the wall by having an increased anisotropy coefficient is exhibited clearly by the peak values around $y^+ = 4$, with increased values still exhibited within the buffer layer. Away from the wall, into the log region around $y^+ > 50$, both coefficients exhibit a return to almost constant values.

It is notable that the constant values to which the benchmark $C_{\beta,n\ \mathrm{DNS}}$ distribution flattens here are approximately the same to the 'baseline' calibrated constants established in the previous chapter (Table 5.1 in Section 5.2). It is worth reiterating that while only one case is presented in Chapter 5, the calibration process for the baseline constants involves a number of canonical flow configurations. As the 'ideal' benchmark values for the coefficients away from the wall (which are obtained only using one plane channel flow case) agree with the baseline calibrated constants (which are obtained using multiple configurations at various Reynolds numbers), an assumption of 'universality' can be applied. This justifies the use of this case in the development and calibration of the new near-wall formulation and avoids the need for a calibration on the other configurations. The validity of this assumption will

be verified when the final formulation of the model is applied on other canonical configurations later in Section 6.6.

6.4 New functions definition

The motivation to incorporate how the physical structures and processes in the near-wall region manifest in the turbulence anisotropy, as described in Section 6.1, combined with the observation from the benchmark distribution of anisotropy expansion coefficients obtained from the analysis of DNS data in Section 6.2 and Section 6.3 allow a set of requirements to be applied for the development of a new approach for modelling turbulence anisotropy. Figure 6.3 shows that the distribution of the benchmark expansion coefficients terms can be suggested to correspond to the different regions of a boundary layer. This validates the approach considered in this work to develop a new formulation for the expansion coefficients that contains functional forms representing the different regions of a boundary layer: f_{Viscous} (f_V), f_{Buffer} (f_B), and f_{Log} (f_L), as discussed in Section 6.1.

f_V is to be used to predict how velocity fluctuations vanish at the wall due to the no-slip condition and it is used together with f_B to predict the increased anisotropy level towards the edge of the viscous sublayer into the buffer layer due to the strong shearing that occurs between the low-speed and high-speed streaks in the turbulent structures here. f_L is to be used to predict the log layer, in which a lower level of turbulence anisotropy is expected compared to the regions closer to the wall, and returns the expansion coefficients to the baseline calibrated values.

Using the information of the benchmark $C_{\beta,n}$, the three functional forms are developed such that they meet 1) the quantitative level of the distribution and 2) the shape of the profile. To meet the first requirement, scaling constants are identified from the distribution of the benchmark coefficients. To meet the second requirement, damping functions are used. The approach is such that the damping functions are formulated to go from zero to one, and the scaling constants are used as a multiplication factor such that the correct level is reached. As the benchmark $C_{\beta,n\ \text{DNS}}$ distribution in Figure 6.3 shows that the two expansion coefficients exhibit the same trend with increasing y^+, only one set of damping functions needs to be formulated, with two sets of scaling constants identified for the two expansion coefficients. For the scaling factors, three distinct points can be noted from each of the distribution. This is highlighted in Figure 6.4.

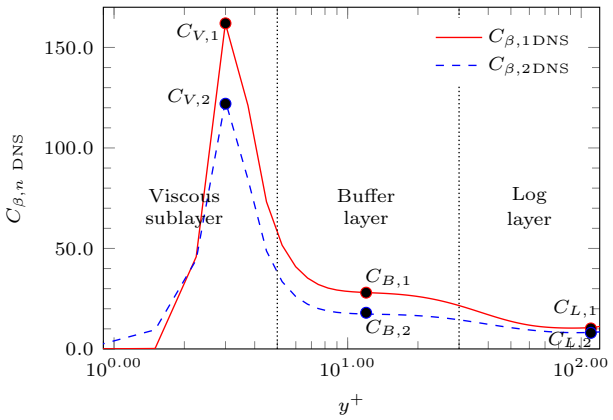

Figure 6.4: Profile of the benchmark expansion coefficient $C_{\beta,n\ \mathrm{DNS}}$. Markers correspond to the scaling constants $C_{V,n}$, $C_{B,n}$, $C_{L,n}$.

The first, located at $y^+ \approx 4$ which is approximately at the end of the viscous sublayer, denotes the peak anisotropy expansion coefficient which as mentioned above and in Section 6.1 can be associated with the need to model the increased level of anisotropy due to the turbulence producing events in the region at the edge of the viscous sublayer and into the buffer layer. The second, located at $y^+ \approx 10.5$ which is in the buffer layer, denotes the increased level needed to represent the presence of streaky turbulence structures here. The last, located at $y^+ \approx 100$ which is in the log layer, denotes the return to baseline level of anisotropy towards the outer region of the boundary layer. The values of these identified scaling factors are considered as model constants and they are summarised in Table 6.1.

Table 6.1: The first set of model constants for the near-wall anisotropy modification of the non-linear $k-\omega$ model

$C_{V,1}$	$C_{B,1}$	$C_{L,1}$	$C_{V,2}$	$C_{B,2}$	$C_{L,2}$
160.0	25.0	10.2	122.0	15.0	8.0

As mentioned above, for the second requirement, that is, to represent the correct distribution of anisotropy expansion coefficients with increasing wall distance, damping functions are used. To ensure that the near-wall formulation proposed here can be applied to complex geometries with confidence, only local variables are used in the damping functions. Existing turbulence models have used non-local variables such as wall distance or momentum thickness to enhance model predictions in the near-wall region. However, this has been known to introduce limitations when applied to complex geometries, for example in configurations where more than one solid surface closely affect the boundary layer development. Therefore, this is avoided here. Turbulence Reynolds number, $Re_T = k/\nu\omega$, is used instead. The use of Re_T in turbulence models has been shown to allow a distinction between near-wall and far-field areas due to the wall boundary conditions of the turbulent quantities, particularly, due to the asymptotic behaviour of ω to tend towards infinity (or a very large value) as the wall is

approached. Its use in the modification proposed here therefore offers simplicity as well as allows the near-wall modification to adjust to local conditions.

The damping functions are defined as S-shaped functions of Re_T that either monotonically increase from 0 to 1 or decrease from 1 to 0. The aim is to allow a smooth increase or decrease of the expansion coefficient to avoid instabilities. They are formulated as:

$$f_1 = 1 - exp \quad \frac{-Re_T^{C_1}}{C_2} \right) \quad , \quad f_2 = exp \quad \frac{-Re_T^{C_3}}{C_4} \right) \left(\quad , \quad f_3 = 1 - tanh \quad \frac{Re_T^{C_5}}{C_6} \right) \left(\tag{6.13}$$

The three damping functions are used together to form the functions $f_{V,n}$, $f_{B,n}$, $f_{L,n}$ that result in the correct distribution of expansion coefficients across the three sublayers with increasing wall distance. Specifically, they form the new functions using the equations as follows:

$$\begin{aligned} f_{V,n} &= C_{V,n}(f_1 f_2) \\ f_{B,n} &= C_{B,n}(f_1 f_3) \\ f_{L,n} &= C_{L,n}(1 - f_3) \end{aligned} \tag{6.14}$$

The new functions are applied to the non-linear formulation for the Reynolds stresses through equation (6.4) as discussed in Section 6.1. The three new functions in equation (6.14) can be observed to consist of two parts: the constants $C_{V,n}$, $C_{B,n}$, and $C_{L,n}$ which have been defined in Table 6.1 and the products of the damping functions, i.e. $(f_1 f_2)$, $(f_1 f_3)$, and $(1 - f_3)$.

The new constants $C_1, C_2, \ldots, C_6$ that arise in equation (6.13) are calibrated using the approach described below and can be summarised in the flowchart in Figure 6.5.

1. Complete plane channel computation using the linear $k - \omega$ model.
2. Obtain k and ω from the output of the $k - \omega$ computation.
3. Calculate Re_T from the k and ω predictions above.
4. Define $C_{\beta,n}$ as a function of $C_1, C_2, \ldots, C_6$ using equations (6.4), (6.13), and (6.14).
5. The information of $C_{\beta,n\ \mathrm{DNS}}$ is obtained from the analysis presented in Section 6.3.
6. Define a non-linear equation: $\mathcal{F} = C_{\beta,n} - C_{\beta,n\ \mathrm{DNS}}$.
7. Apply a numerical approach to get an approximate solution for $C_1, C_2, \ldots, C_6$ which satisfy:

$$\mathcal{F} = C_{\beta,n} - C_{\beta,n\ \mathrm{DNS}} = 0 \tag{6.15}$$

The calibration process can therefore be summarised as an approach to estimate the unknown constants $C_1, C_2, \ldots, C_6$ using a numerical algorithm with the aim of minimising the difference between the

expansion coefficients ($C_{\beta,n}$) that result from the new functions with the benchmark distribution ($C_{\beta,n\ \mathrm{DNS}}$). The algorithm used for solving the non-linear equation (6.15) is the trust-region dogleg method readily implemented in GNU Octave as the `fsolve` function. As discussed earlier, the approach to use the predictions of k and ω from a linear $k-\omega$ computation for the calibration is valid since the anisotropic distribution of the Reynolds stresses in this test case does not affect the total turbulent kinetic energy due to the nature of the flow configuration.

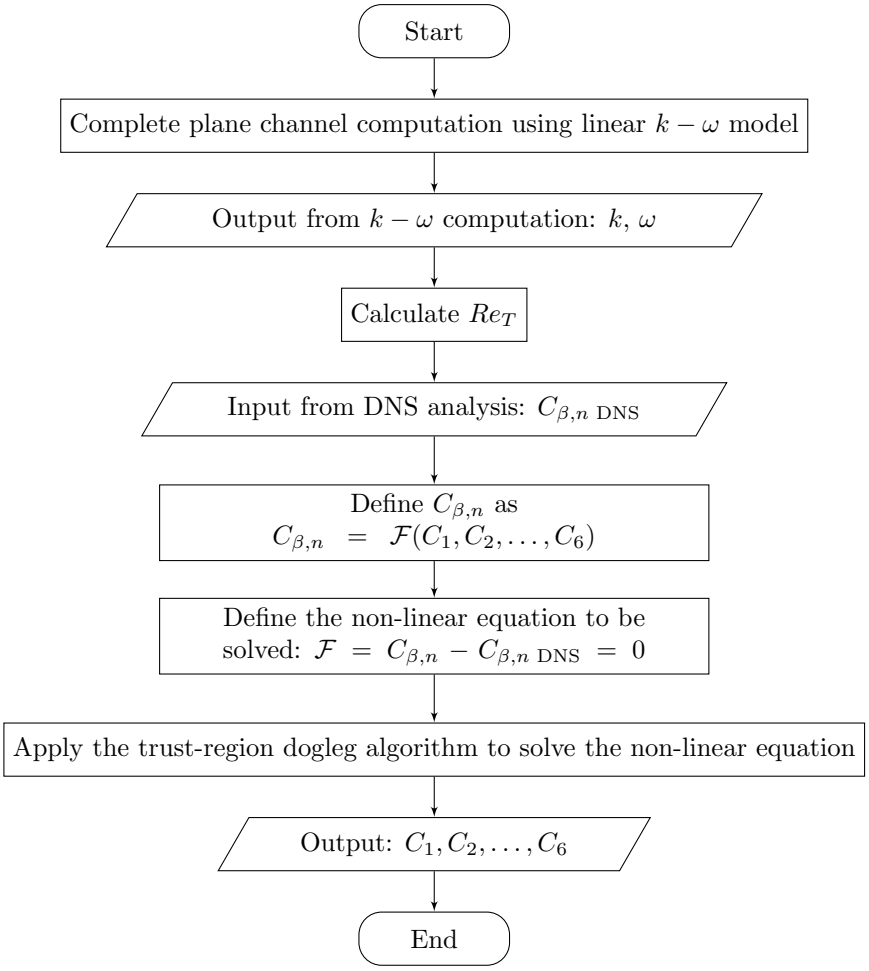

Figure 6.5: Flowchart of the calibration process of the near-wall modification constants

The resulting calibrated constants are summarised in Table 6.2. These values result in the profiles of the damping functions f_1, f_2, and f_3 (refer to equation (6.13)) as shown in Figure 6.6 (a). The profiles of the products of these damping functions (refer to equation (6.14)) are presented in Figure 6.6 (b).

Table 6.2: The second set of model constants for the near-wall anisotropy modification of the non-linear $k-\omega$ model

C_1	C_2	C_3	C_4	C_5	C_6
0.92	0.01	0.40	0.18	1.90	70.00

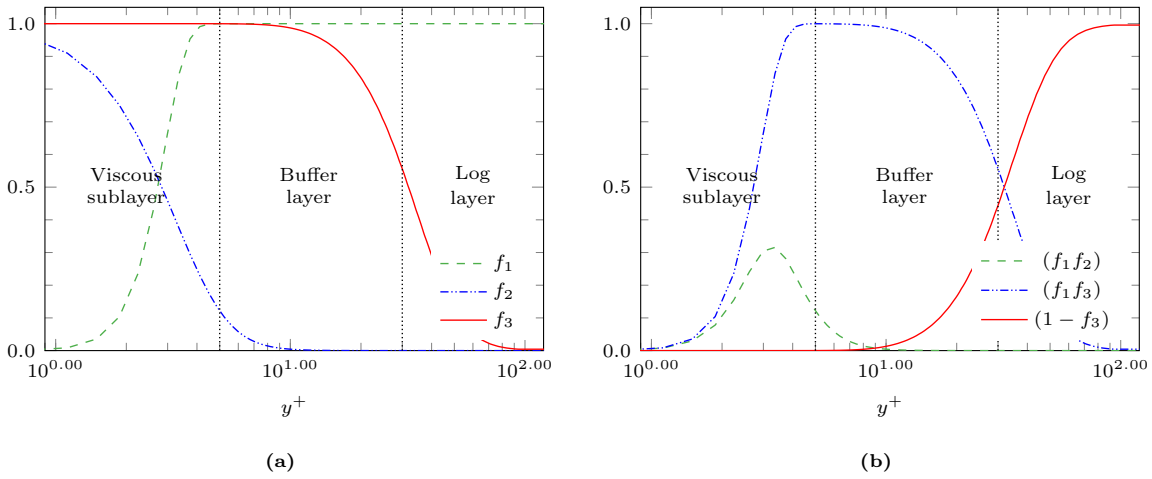

Figure 6.6: Profiles of damping functions and the products of the damping functions used in the near-wall anisotropy modification of the non-linear $k - \omega$ model

The new formulations and calibrated constants result in the distribution of the anisotropy expansion coefficients $C_{\beta,1}$ and $C_{\beta,2}$ predicted by the new model as presented in Figure 6.7. It can be observed that, as designed, these expansion coefficient distributions can be used to predict the marked increase in the anisotropy level at the edge of the viscous sublayer as well as through the buffer level, and the return to baseline level from the middle of the log region onwards. The applicability and performance of the new near-wall formulation will now be validated using a number of canonical configurations. First, for clarity, a summary of the final form of the new model is summarised below.

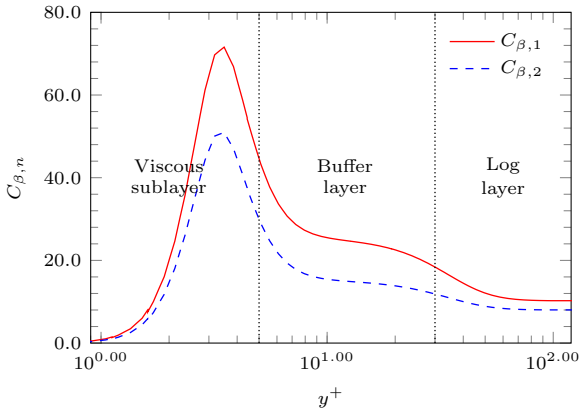

Figure 6.7: Profiles of the two anisotropy expansion coefficients $C_{\beta,1}$ and $C_{\beta,2}$ calculated using the new near-wall modification for the non-linear $k - \omega$ model

6.5 Summary of the new NL $k - \omega$ model formulation

The final form of the new non-linear $k - \omega$ model which includes the new near-wall formulation presented above is summarised in this section. This is referred to from hereon as the NL $k - \omega$ model.

The transport equations for k and ω are written as:

$$\frac{Dk}{Dt} = P_k - \beta^* k\omega + \frac{\partial}{\partial x_j}\left[\left(\nu + \sigma_k \frac{k}{\omega}\right)\frac{\partial k}{\partial x_j}\right] \tag{6.16}$$

$$\frac{D\omega}{Dt} = C_{\omega,1} P_{k,\text{linear}} \frac{\omega}{k} - C_{\omega,2}\omega^2 + \frac{\partial}{\partial x_j}\left[\left(\nu + \sigma_\omega \frac{k}{\omega}\right)\frac{\partial \omega}{\partial x_j}\right] \tag{6.17}$$

in which $\beta^* = 0.09$, $C_{\omega,1} = 0.52$, $C_{\omega,2} = 0.072$, $\sigma_k = 0.5$, and $\sigma_\omega = 0.5$.

The production of the turbulent kinetic energy, P_k, is limited using the following formulation:

$$P_k = \min(P_k, 20\beta^* k\omega) \tag{6.18}$$

in which the unlimited P_k is defined using the classical stress-strain approach:

$$P_k = -\overline{u_i' u_j'}\frac{\partial U_i}{\partial x_j} \tag{6.19}$$

The Reynolds stress tensor is defined as:

$$\overline{u_i' u_j'} = -2\nu_T S_{ij} + \frac{2}{3}k\delta_{ij} + a_{ij,\text{extra}}k \tag{6.20}$$

The production of ω uses the production calculated using the linear form of the Reynolds stress tensor, i.e.:

$$P_{k,\text{linear}} = -\left(-2\nu_T S_{ij} + \frac{2}{3}k\delta_{ij}\right)\frac{\partial U_i}{\partial x_j} \tag{6.21}$$

The eddy viscosity is calculated using:

$$\nu_T = C_\mu \frac{k}{\omega} \tag{6.22}$$

whereas the non-linear anisotropy formulation is defined as:

$$a_{ij,\text{extra}} = C_\mu\left[\beta_1\left(S_{ik}S_{kj} - \frac{1}{3}II_S\delta_{ij}\right) + \beta_2\left(S_{ik}\Omega_{kj} - \Omega_{ik}S_{kj}\right)\right] \tag{6.23}$$

The C_μ coefficient in the ν_T and $a_{ij,\text{extra}}$ formulations is introduced for applying the realisability

condition:

$$C_\mu = min\left(1.00, \frac{1}{1+0.01M^2}\right)\left(\tag{6.24}$$

in which

$$M = \max(\widetilde{S}, \widetilde{\Omega}) \quad , \quad \widetilde{S} = \frac{1}{\omega}\sqrt{2S_{ij}S_{ij}} \quad , \quad \widetilde{\Omega} = \frac{1}{\omega}\sqrt{2\Omega_{ij}\Omega_{ij}} \tag{6.25}$$

The anisotropy expansion terms, β_1 and β_2, are defined using:

$$\beta_n = \frac{C_{\beta,n}}{\max(\omega, \kappa S)^2} \tag{6.26}$$

where $\kappa = 2.5$ and S is the magnitude of the strain rate tensor.

The expansion coefficients, $C_{\beta,n}$, are calculated using the following formulation:

$$C_{\beta,n} = f_{V,n} + f_{B,n} + f_{L,n} \tag{6.27}$$

in which the functions are defined as:

$$\begin{aligned} f_{V,n} &= C_{V,n}(f_1 f_2) \\ f_{B,n} &= C_{B,n}(f_1 f_3) \\ f_{L,n} &= C_{L,n}(1 - f_3) \end{aligned} \tag{6.28}$$

where

$$f_1 = 1 - exp \quad \frac{-Re_T^{C_1}}{C_2}\right)\left(\quad , \quad f_2 = exp \quad \frac{-Re_T^{C_3}}{C_4}\right)\left(\quad , \quad f_3 = 1 - tanh \quad \frac{Re_T^{C_5}}{C_6}\right)\left(\tag{6.29}$$

in which turbulence Reynolds number, Re_T, is defined as:

$$Re_T = \frac{k}{\nu\omega} \tag{6.30}$$

and the closure coefficients are calibrated to be:

Table 6.3: Model constants in the NL $k-\omega$ model

$C_{V,1}$	$C_{B,1}$	$C_{L,1}$	$C_{V,2}$	$C_{B,2}$	$C_{L,2}$
160.0	25.0	10.2	122.0	15.0	8.0

C_1	C_2	C_3	C_4	C_5	C_6
0.92	0.01	0.40	0.18	1.90	70.00

6.6 Validation on canonical cases and assessment

In this section, the validity and performance of the NL $k-\omega$ model are established using three canonical cases. The configurations tested include a simple shear flow at various Reynolds numbers, a zero-pressure-gradient flat plate, and a U-bend curved channel flow. To assess the effectiveness of the non-linear Reynolds stress formulation as well as the near-wall modification, the predictions of the NL $k-\omega$ model are assessed in comparison with the predictions of the original linear $k-\omega$ model. To compare the performance of the NL $k-\omega$ model against other non-linear eddy-viscosity models, computation results obtained at Coventry University by the author, recently published in Fadhila *et al.* [155] are included. Two existing non-linear eddy-viscosity models are used which are readily available in OpenFOAM, namely the realisable quadratic high-Re $k-\varepsilon$ model of Shih *et al.* [31] and the cubic $k-\varepsilon$ low-Re model of Lien *et al.* [156]. The application of the new model on two more complex configurations, namely a planar diffuser with a downstream monolith and a swirling flow through a sudden expansion, are explored in the next two chapters of the thesis.

6.6.1 Numerical setup

The computation results presented throughout this work are obtained using the open-source CFD package OpenFOAM (version 6). A steady state incompressible flow solver `simpleFoam` (consistent) based on the SIMPLEC algorithm available in OpenFOAM is used to perform the calculations. A summary of the SIMPLEC algorithm has been presented in Section 4.3. The various terms in the model equations are discretised using the standard finite volume discretisation of Gaussian integration. The gradient terms are computed using linear interpolation. For the Laplacian terms, diffusion coefficients are discretised using linear interpolation. Finally, divergence terms are evaluated using a blended linear upwind scheme offering first/second order accuracy. This scheme is selected because it provides a suitable compromise between stability and accuracy. The calculations are considered to have converged if the normalised residuals dropped below 10^{-5}. For these computations, the gradient terms for the turbulence quantities (k and ω) are limited using a cell-based limiter. The details of these computational methodologies have been presented in Section 4.1 and Section 4.2.

6.6.2 Plane channel flow

The configuration is the same as the case used in the calibration of the model. The case is set up to match the DNS cases by Lee at al. [148] at three wall-shear velocity based Reynolds numbers, Re_τ: 180, 500, and 1000.

6.6.2.1 Computational domain and boundary conditions

The geometry is shown earlier in Figure 6.1. The height of the channel, h, is 2 m. At the inlet, the freestream velocity, U_∞, is calculated from the Reynolds number using the kinematic viscosity defined in the DNS. The turbulent kinetic energy is calculated based on the freestream turbulence intensity, Tu_∞, using:

$$k_\infty = \frac{3}{2}(Tu_\infty U_\infty)^2 \tag{6.31}$$

The specific dissipation rate, ω, is estimated from k using the half width of the channel as the length scale using the relation:

$$\omega_\infty = \frac{k_\infty^{1/2}}{\beta^{*1/4}(h/2)} \tag{6.32}$$

where $\beta^* = 0.09$. Summary of the inlet conditions is presented in Table 6.4. For the pressure, a zero-gradient boundary condition is prescribed at the inlet. The wall boundary conditions for k, ω, and U are set up as detailed in Section 5.1.4 while a zero-gradient condition is set for the pressure. At the outlet, a zero-gradient condition is prescribed for the velocity and turbulent quantities and a fixed zero gauge pressure outlet is used. To simulate the 'infinite' plate, a mapping between the inlet and outlet patches is set.

Table 6.4: Summary of inlet conditions for the plane channel flow cases

Re_τ [−]	Re [−]	ν [m/s^2]	U_∞ [m/s]	Tu_∞ [−]	k [m^2/s^2]	ω [s^{-1}]
182.09	2850	3.5×10^{-4}	1.00	5.09 %	0.00388	0.11369
543.50	10000	1.0×10^{-4}	1.00	4.30 %	0.00277	0.09614
1000.51	20000	5.0×10^{-5}	1.00	4.19 %	0.00263	0.09369

6.6.2.2 Mesh generation and details

A mesh independence study is conducted to ensure that the computational grid is sufficiently refined and well-distributed to allow the capturing of the flow features (while still trying to minimise the

computational effort). The mesh generation utility `blockMesh`, available on OpenFOAM, is used to construct the meshes. Four computational grids are used for the mesh convergence test, namely the coarse, medium, fine, and very fine grids. All the tested meshes are structured hexahedral grids created using a user-defined number of cells, cell size, and stretching level in three dimensions. The size and stretching of the grids are set such that a y^+ less than 1 is achieved. Since the domain is two-dimensional, one cell is specified in the z-direction for all the meshes to meet the requirements of OpenFOAM, with an `empty` condition set for the front and back planes to specify that no solution is required in the z-direction (this is true for all two-dimensional configurations presented in this work).

The first comparison is made on the axial velocity predictions using the different grids. As the setup is such that it is a simple flow bounded by two 'infinite' parallel plates, there is only one non-zero velocity gradient, dU_x/dy, and therefore the axial velocity profile can be sampled at any station along the plate. This is presented in Figure 6.8. Note that all the mesh independence test results presented in this work are obtained using the NL $k-\omega$ model. The turbulent quantities predictions are also observed, specifically the turbulent kinetic energy and turbulent shear stress profiles. These are shown in Figure 6.9. All the predicted quantities are presented in their normalised form, made dimensionless using the wall-shear velocity, and plotted against y^+.

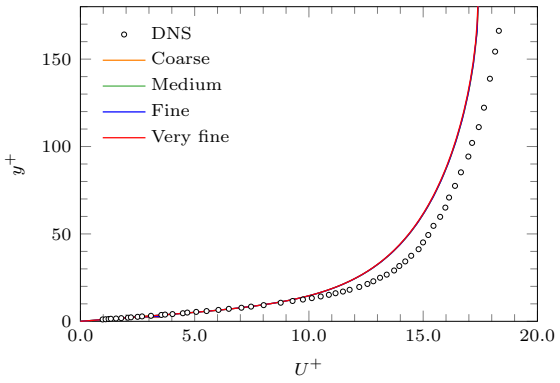

Figure 6.8: Mesh independence test for the plane channel flow configuration: axial velocity profile. Markers correspond to DNS data [148].

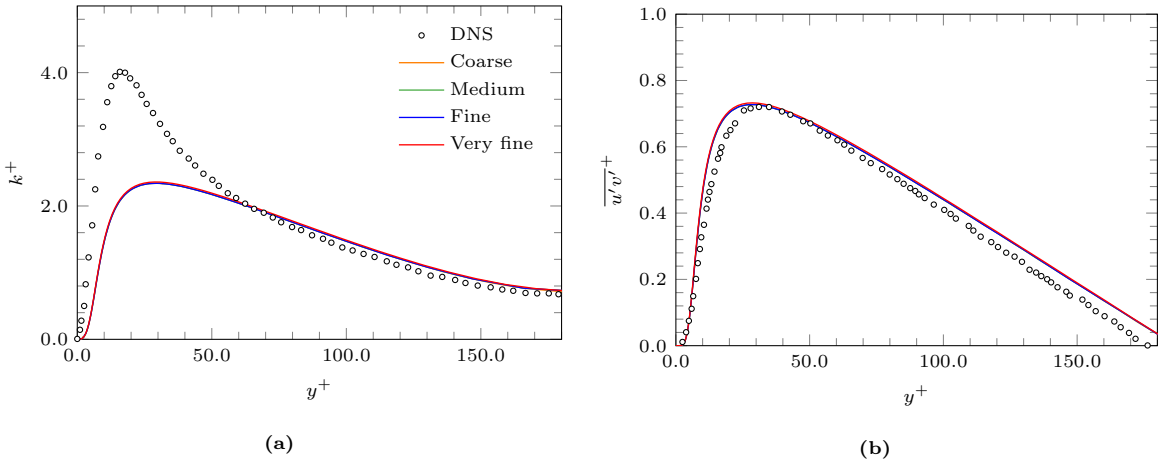

Figure 6.9: Mesh independence test for the plane channel flow configuration: (a) turbulent kinetic energy and (b) turbulent shear stress profiles. Markers correspond to DNS data [148].

It can be observed from Figure 6.8 and Figure 6.9 that the axial velocity, turbulent kinetic energy, and turbulent shear stress profiles predicted using the different grids are in close agreement. As this is non-dimensionalised, a quantification is done by calculating the percentage of difference of U_m, which is the mean axial velocity across the channel height. The comparison is presented in Table 6.5. The percentage of difference is benchmarked against the chosen grid, which is the coarse grid.

Table 6.5: Summary of grid independence test for the plane channel flow configuration

	Number of cells	U_m [m/s]	% Diff U_m
Coarse	42,000	1.6503	–
Medium	50,400	1.6644	0.38
Fine	67,200	1.6377	0.77
Very fine	86,400	1.6780	1.65

It can be observed that the change in the predicted U_m is less than 2% across all the tested meshes. The chosen grid, which is the coarse grid, has $300 \times 140 \times 1$ cells, giving a total of 42,000 cells. The computational grid is presented in Figure 6.10.

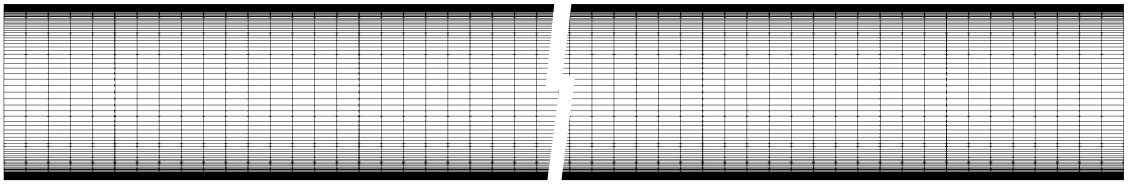

Figure 6.10: Computational grid for the plane channel flow configuration

To ensure that the mesh is of sufficient quality for the computations, the measures of its geometric properties are observed. A number of grid quality metrics can be used to characterise the shape of the control volumes, the uniformity of the control volumes across the grid, and the spatial distribution of the cells. Due to the simplicity of the domain and the flow, the computational grid for this case is constructed from orthogonal control volumes which results in a maximum cell non-orthogonality of 0 deg and maximum skewness of 0. Non-orthogonality refers to the measure of the angle between the line connecting two cell-centres and the normal of their common cell-face while skewness refers to the distance between the intersection of the line connecting two cell-centres with their common cell-face and the centre of that cell-face [130]. The maximum aspect ratio is 70. Aspect ratio refers to the ratio between the longest and the shortest length of a cell (or a face in the case of a two-dimensional grid). The corresponding maximum y^+ value is 0.33. Computation using the chosen grid is observed to result in a stable and converged solution.

6.6.2.3 Results and discussion

The Reynolds stress components predicted using the NL $k-\omega$ model for $Re_\tau = 180$ are presented in Figure 6.11, plotted against the normalised wall-normal distance. To highlight the effects of the near-wall formulation, they are plotted against the predictions from the 'baseline' non-linear $k-\omega$ model presented initially in the previous chapter.

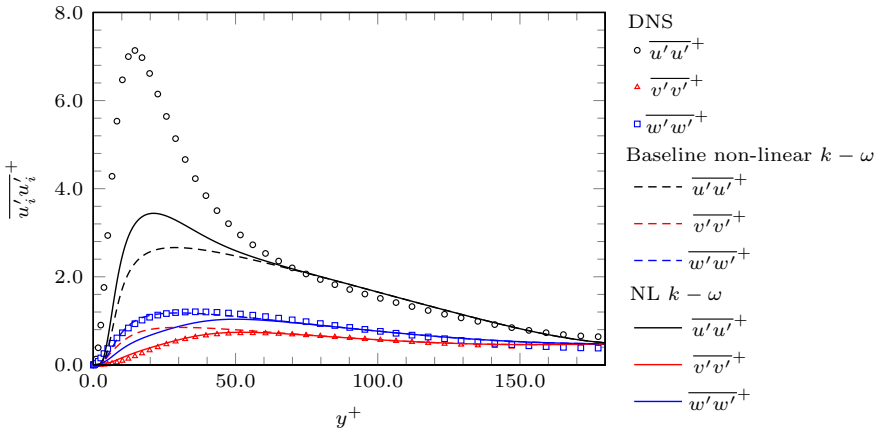

Figure 6.11: Reynolds stresses in a plane channel flow at $Re_\tau = 180$. Markers correspond to DNS data [148].

It can be observed that closer to the wall, around $y^+ < 60$, the prediction of wall-normal fluctuations, $\overline{v'v'}$, near the wall is significantly improved by the NL $k-\omega$ model compared to the baseline predictions, showing values that are matching closely to the DNS data. The predicted peak level of $\overline{u'u'}$ is also improved by approximately 30%. The improvement is quantified based on the change in the normalised percentage difference between a model prediction and the DNS data, e.g. for a variable ϕ: $\left(\frac{\phi_{\text{DNS}}-\phi_{\text{NL }k-\omega}}{\phi_{\text{DNS}}} \times 100\%\right) - \left(\frac{\phi_{\text{DNS}}-\phi_{\text{baseline}}}{\phi_{\text{DNS}}} \times 100\%\right)$. The same procedure is applied throughout this work for quantifying the improvement in predictions, using either DNS or experimental data. To

observe the anisotropy of the predicted Reynolds stresses more clearly, the Reynolds stress anisotropy, a_{ij}, can be calculated from these Reynolds stress components using its definition: $a_{ij} = \frac{\overline{u_i' u_j'}}{k} - \frac{2}{3}\delta_{ij}$. The profiles are presented in Figure 6.12 alongside the baseline predictions. The results are again compared with DNS data [148].

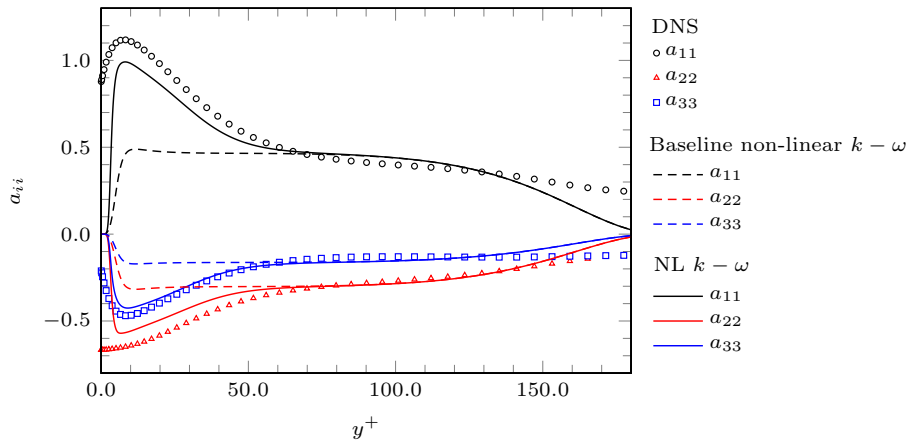

Figure 6.12: Reynolds stress anisotropy in a plane channel flow at $Re_\tau = 180$. Markers correspond to DNS data [148].

The improvements that result from the new near-wall modification can be observed clearly from the anisotropy profiles. In the region close to the wall, within $y^+ < 60$, the predictions of the peak values of the anisotropies by the NL $k-\omega$ model show marked improvements, approximately 50%, compared to the baseline predictions. This highlights the effectiveness of the new near-wall formulation in improving the predictions of near-wall anisotropy. The return to baseline predictions away from the wall is exhibited correctly by the NL $k-\omega$, and the anisotropies at $y^+ > 60$ match closely with the DNS data. This shows the combined effects from the proposed near-wall modifications and the quadratic $k-\omega$ formulation.

To ensure that the 'universality' assumption made when calibrating the near-wall modification is valid, the model is applied to the same configuration at different Reynolds numbers. The results are presented in Figure 6.13. The NL $k-\omega$ model consistently shows marked improvements on the predictions of turbulence anisotropy within the near-wall region, specifically in $y^+ < 60$. Of particular note is the marked increase in the anisotropies at the edge of the sublayer and within the buffer layer, around $5 < y^+ < 30$, which closely match the DNS data. This is consistent with the aim of the development of the near-wall modification which is to represent the strong shearing that occurs in this region due to the presence of the alternating turbulence streaks. Around 50% improvements are shown by the model on both cases for the predictions of the peak values of the anisotropies. The correct return to the baseline predictions away from the wall is also shown here.

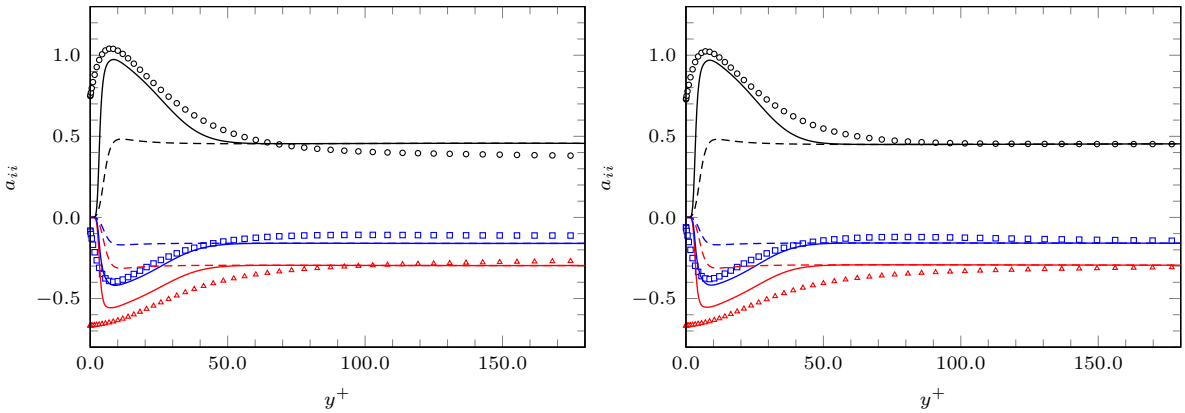

(a) $Re_\tau = 550$ **(b)** $Re_\tau = 1000$

Figure 6.13: Reynolds stress anisotropy in a plane channel flow at $Re_\tau = 550$ and $Re_\tau = 1000$. Markers correspond to DNS data [148]. Line notations are the same as Figure 6.12.

Profiles of the turbulence anisotropy predicted by the two other non-linear models included, namely the quadratic $k - \varepsilon$ model of Shih *et al.* [31] (referred to as Shih NL $k - \varepsilon$ in the figure legends for succinctness) and the cubic $k - \varepsilon$ model of Lien *et al.* [156] (referred to as Lien NL $k - \varepsilon$ in the figure legends) are shown in Figure 6.14 and Figure 6.15, respectively. The results for the three Reynolds numbers considered are included. It can be observed that the two non-linear models show the correct trend of turbulence anisotropy for the three components of Reynolds stresses. The increased level of the predicted turbulence anisotropies near the wall, specifically within $y^+ < 30$, can be noted. However, the level of anisotropy is severely underpredicted here as well as further away from the wall by the two models on all the Reynolds numbers considered.

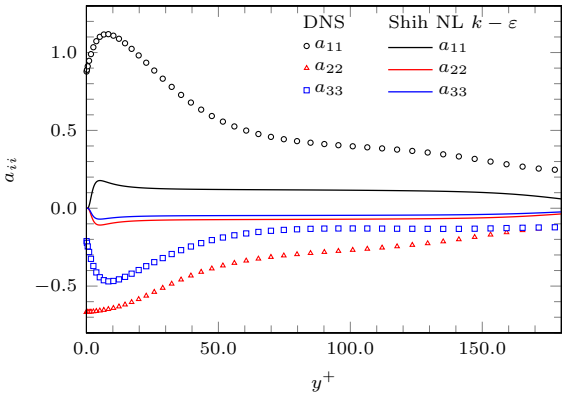

(a) $Re_\tau = 180$

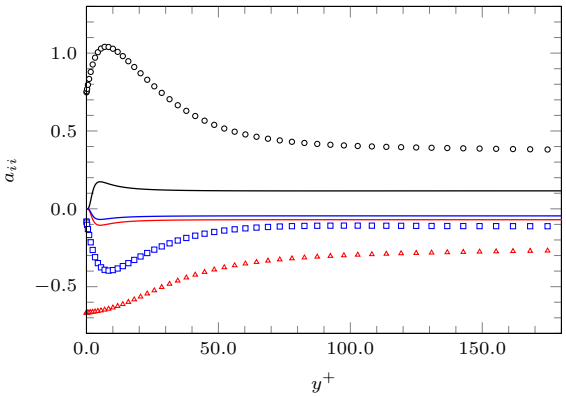

(b) $Re_\tau = 550$

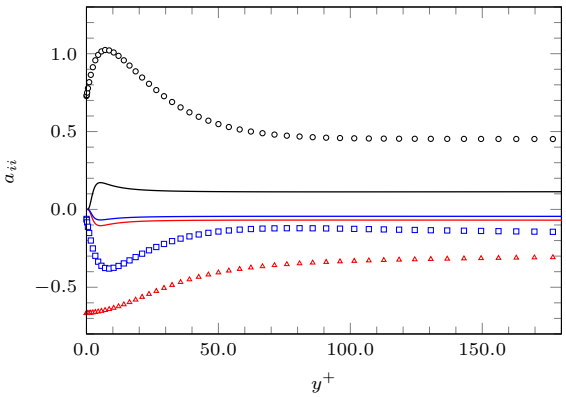

(c) $Re_\tau = 1000$

Figure 6.14: Reynolds stress anisotropy in a plane channel flow at various Reynolds numbers predicted using the Shih quadratic $k-\varepsilon$ model. Markers correspond to DNS data [148].

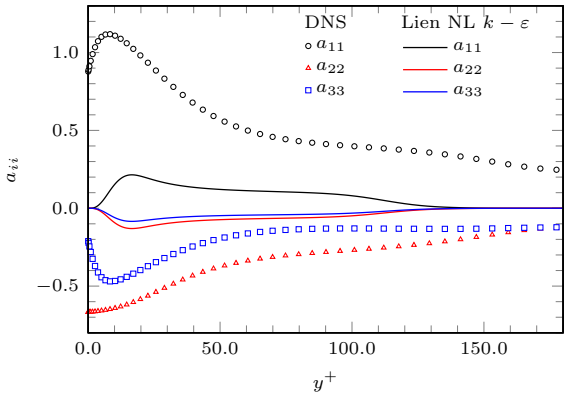

(a) $Re_\tau = 180$

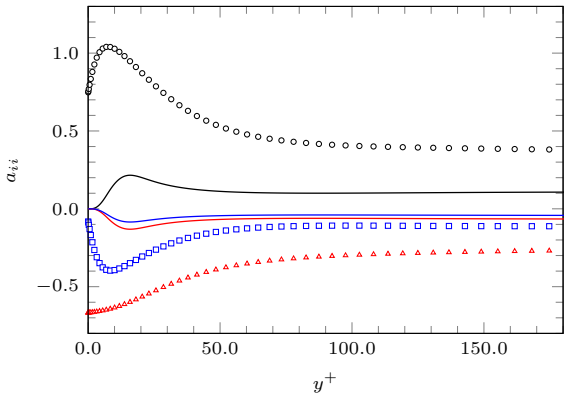

(b) $Re_\tau = 550$

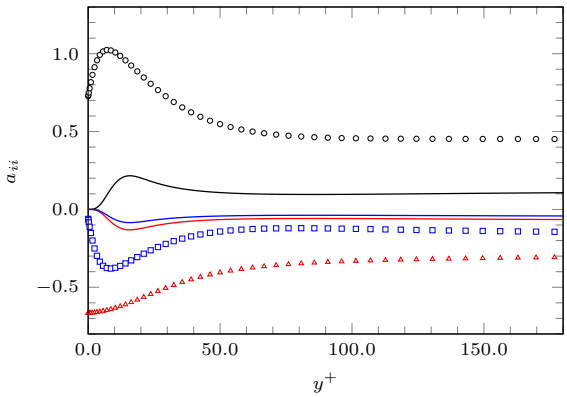

(c) $Re_\tau = 1000$

Figure 6.15: Reynolds stress anisotropy in a plane channel flow at various Reynolds numbers predicted using the Lien cubic $k-\varepsilon$ model. Markers correspond to DNS data [148].

6.6.3 Zero-pressure-gradient flat plate

This is a classical test case for evaluating the performance of a turbulence model in predicting boundary layer flow. It is also useful for testing the correct implementation of a model. The computation is set up to match the T3B case by ERCOFTAC [157] which is a zero-pressure-gradient flat plate at freestream turbulence intensity of $Tu_\infty = 6.0\%$.

6.6.3.1 Computational domain and boundary conditions

A schematic of the domain is shown in Figure 6.16. The length of the plate is 2.9 m. A 0.05-m extension of the domain is set upstream of the flat plate in the x-direction and the domain stretches 0.175 m in the y-direction.

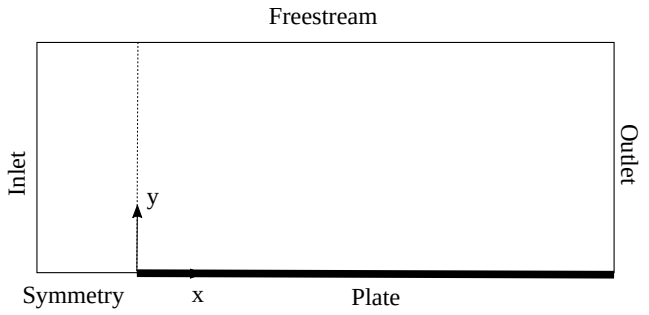

Figure 6.16: Computational domain of the T3 flat plate case

At the inlet, the freestream velocity is $U_\infty = 9.4$ m/s and the turbulent kinetic energy is calculated based on the turbulence intensity using equation (6.31). The specific dissipation rate, ω, is estimated using eddy viscosity ratio of $\nu_R = \nu_t/\nu = 100$ using:

$$\omega_\infty = \frac{k_\infty}{\nu_R \nu} \tag{6.33}$$

The bottom boundary upstream of the plate is given a symmetry condition. Freestream condition is used for the top boundary which prescribes a zero-gradient condition for the velocity and turbulent quantities and a fixed value of zero for the pressure. The boundary conditions at the walls and at the outlet are the same as the case configuration in Section 6.6.2.

6.6.3.2 Mesh generation and details

A mesh convergence study is conducted using four computational grids, namely the coarse, medium, fine, and very fine grids. The mesh generation utility `blockMesh`, available on OpenFOAM, is used. All the tested meshes are structured hexahedral grids created using a user-defined number of cells, cell size, and stretching level in three dimensions.

The first comparison is made on the velocity predictions using the different grids at two streamwise locations along the plate: $x = 1.495$ m and $x = 2.9$ m. This is presented in Figure 6.17. The first location represents the most downstream location at which experimental data is available while the second represents the location just before the outlet.

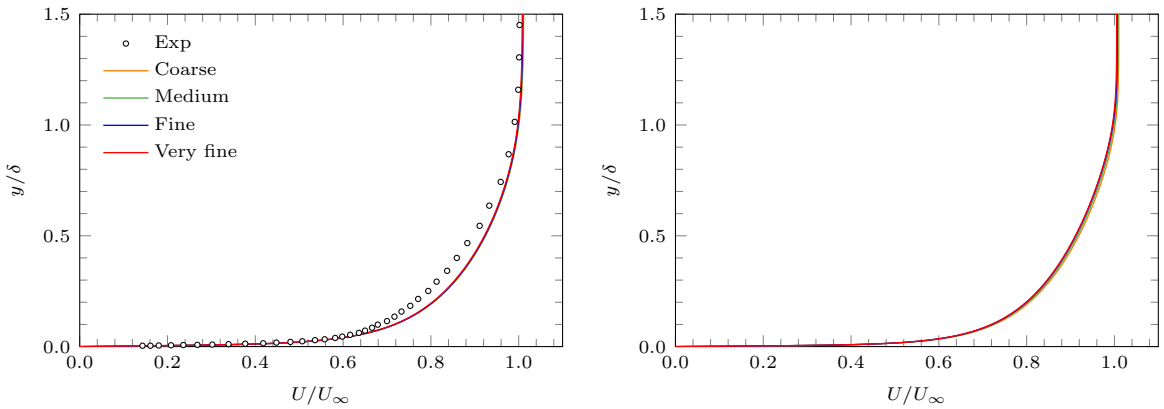

(a) $x = 1.495m$ **(b)** $x = 2.900m$

Figure 6.17: Mesh independence test for the T3B flat plate configuration: axial velocity profile across two stations. Markers correspond to experimental data [157].

It can be observed from Figure 6.17 that the axial velocity profiles at the two locations predicted using the different grids are in close agreement. As this is non-dimensionalised, a quantification is done by calculating the percentage of difference of U_m, which is the mean axial velocity across the location further downstream. This is presented in Table 6.6. The mesh independence result is also quantified using the average skin friction coefficient across the plate. This is also presented in Table 6.6. Notice the percentages of difference across the different grids are benchmarked against the chosen grid, which is the medium grid.

Table 6.6: Summary of grid independence test for the T3B flat plate configuration

	Number of cells	U_m [m/s]	% Diff U_m	$C_{f,\text{average}}$ $\times 10^{-2}[-]$	% Diff $C_{f,\text{average}}$
Coarse	56,000	5.405	0.04	1.289	0.69
Medium	88,000	5.407	–	1.298	–
Fine	138,000	5.420	0.24	1.304	0.46
Very fine	218,000	5.421	0.26	1.311	1.00

The chosen grid, which is the medium grid, has $635 \times 140 \times 1$ cells, giving a total of 88,900 cells. The computational grid is shown in Figure 6.18. Similar to the plane channel flow configuration, due to the simplicity of the domain, orthogonal control volumes are used to construct the grid which results in a maximum cell non-orthogonality of 0 deg and maximum skewness of 0. The maximum aspect ratio is 8500. While higher than desired, this is required in order to achieve y^+ less than unity and computation using the chosen grid still results in a stable and converged solution. The corresponding maximum y^+ value is 0.61.

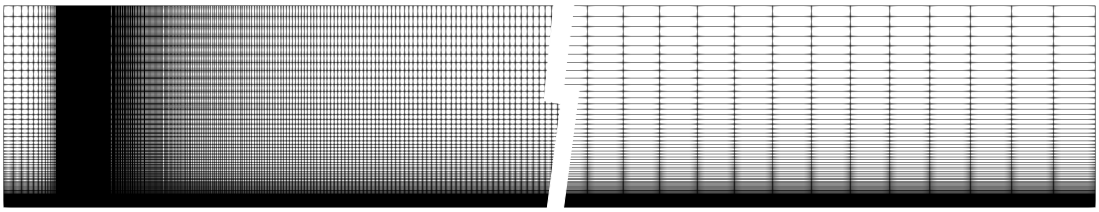

Figure 6.18: Computational grid for the T3B flat plate configuration

6.6.3.3 Results and discussion

Figure 6.19 presents the skin friction coefficient distribution along the plate predicted using all the turbulence models considered. The results from the NL $k-\omega$ and the linear $k-\omega$ models are identical, and they closely match the experimental values for $Re_x > 0.5 \times 10^6$, which correspond to the location at which the boundary layer is fully turbulent. This is as expected since the NL $k-\omega$ and $k-\omega$ models are fully-turbulent models. The Shih quadratic $k-\varepsilon$ and Lien cubic $k-\varepsilon$ models show lower skin friction coefficient predictions compared to the theoretical turbulent for $Re_x < 0.3 \times 10^6$, and closely match the turbulent line and the experimental values downstream. This behaviour has been observed previously on fully-turbulent $k-\varepsilon$ models [158, 159]. This result demonstrates that the formulation of the NL $k-\omega$ model retains the ability of the underlying $k-\omega$ model to correctly predict the skin friction of a turbulent boundary layer. It also provides confidence that the model has been implemented correctly.

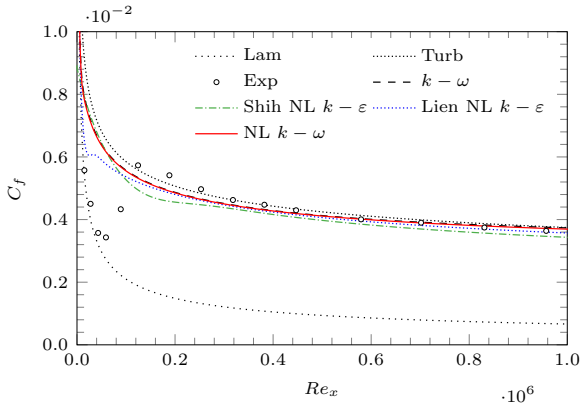

Figure 6.19: Streamwise skin friction distribution on the T3B case. Markers correspond to ERCOFTAC experimental data [157].

Profiles of the Reynolds stress components are shown in Figure 6.20, normalised with the freestream velocity. Reynolds stress predictions are observed at two stations on the plate at which the Reynolds numbers based on the streamwise distance are $Re_x = 183,000$ and $556,000$, which correspond to

locations at which the boundary layer is fully turbulent. Figure 6.20 shows that the NL $k-\omega$ model correctly predicts the experimental trend of the Reynolds stress profiles at both locations. At $Re_x = 183,000$, the NL $k-\omega$ model returns predictions closer to the experimental values for the streamwise and wall-normal Reynolds stress components compared to the linear $k-\omega$ model as expected. In particular, the peak value of $\overline{u'u'}$ is 46% closer to the experimental value and the $\overline{v'v'}$ peak is around 100% more accurate. These predictions correctly represent the increased streamwise fluctuations that occur during bypass transition, such as when a boundary layer flow is subjected to a freestream turbulence, which is the case in the configuration considered here. This agrees with experimental observations that indicate the presence of streamwise-oriented streaky structures in the viscous sublayer and the buffer layer after the transition point that are similar to the large-scale fluctuations observed in the pre-transitional region of a bypass transition [160, 161]. The profiles throughout are also predicted closer to the experimental data compared to the isotropic predictions that the standard $k-\omega$ presents. The underprediction returned by the NL $k-\omega$ model in the streamwise fluctuations very close to the wall can be attributed to the small amount of the aforementioned large-scale pre-transitional fluctuations (sometimes termed as 'laminar kinetic energy' by transitional models) which are known to be underpredicted by fully-turbulent models as expected. Further along the plate at $Re_x = 556,000$, away from the transition region, the NL $-\omega$ model predictions can be observed to be closer to the experimental values overall. Such an agreement is remarkable, especially considering the relative simplicity of the proposed near-wall modification.

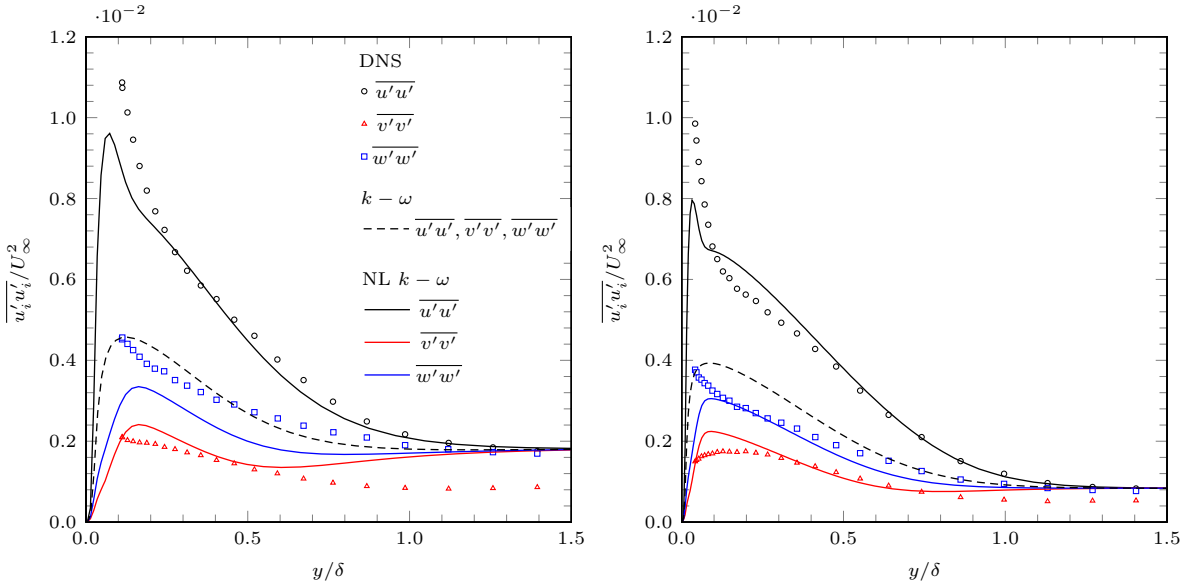

(a) $Re_x = 183,000$ **(b)** $Re_x = 556,000$

Figure 6.20: Velocity fluctuations at local Reynolds numbers $Re_x = 183,000$ and $Re_x = 556,000$ on the T3B case. Markers correspond to experimental data [157].

The two other non-linear models tested also correctly predict the experimental trend of the anisotropic Reynolds stress profiles at both locations. This is shown in Figure 6.21 and Figure 6.22. However, although the Shih quadratic $k-\varepsilon$ model correctly shows the rise in streamwise fluctuations and decrease

in the other two components of the Reynolds stresses at both locations, it can be observed to suffer from its high-Re formulation, and consequently the high y^+ grid that it requires. The Lien cubic $k-\varepsilon$ model returns an underprediction of the Reynolds stress anisotropy level, highlighted by the underprediction of the streamwise fluctuations and the close predictions for the other two components at both locations.

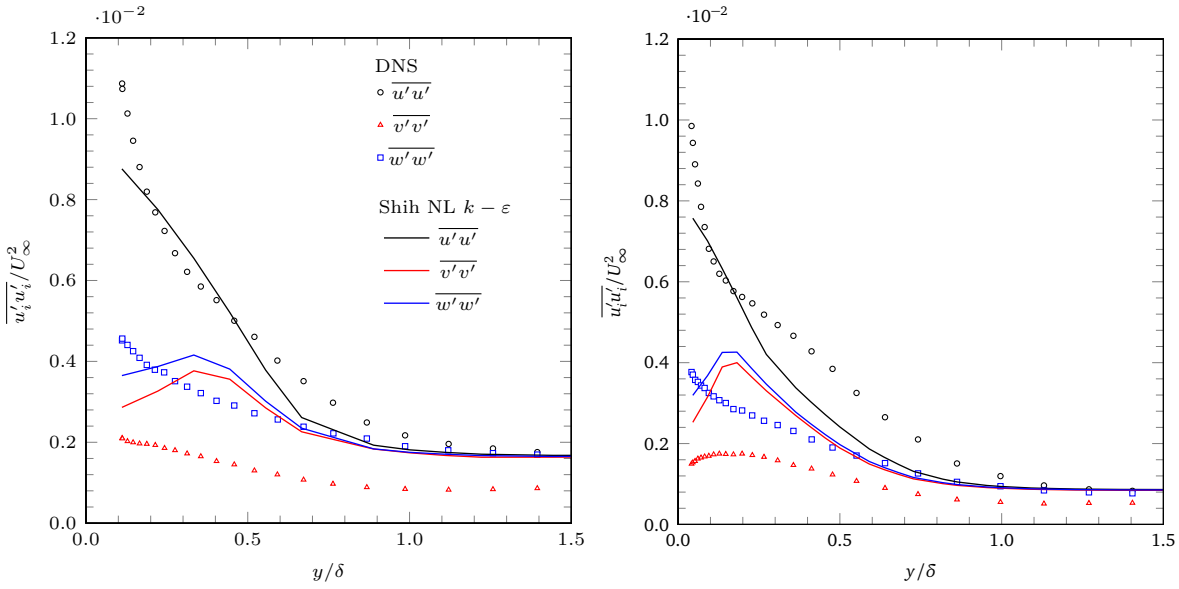

(a) $Re_x = 183,000$ **(b)** $Re_x = 556,000$

Figure 6.21: Velocity fluctuations at local Reynolds numbers $Re_x = 183,000$ and $Re_x = 556,000$ on the T3B case. Markers correspond to experimental data [157].

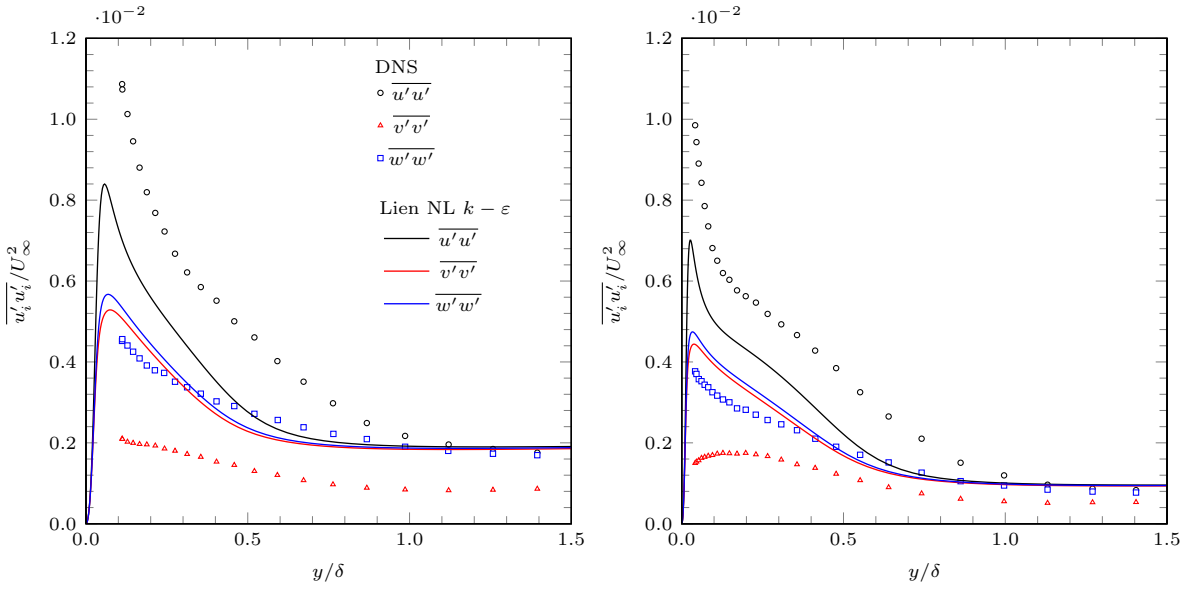

(a) $Re_x = 183,000$ **(b)** $Re_x = 556,000$

Figure 6.22: Velocity fluctuations at local Reynolds numbers $Re_x = 183,000$ and $Re_x = 556,000$ on the T3B case. Markers correspond to experimental data [157].

6.6.4 U-bend curved channel flow

The U-bend curved channel configuration is widely used for validating the performance of turbulence models against the effects of strong streamline curvature, as well as internal shear layers. The case considered here reproduces the experiment by Monson *et al.* [162].

6.6.4.1 Computational domain and boundary conditions

A schematic of the domain used for the computation is shown in Figure 6.23. A two-dimensional computational domain is used since the aspect ratio of the rectangular channel in the experiment is 10 and the experimental results show that the flow field is found to be reasonably two-dimensional throughout [162]. A precursor computation is carried out to match the boundary layer thickness recorded in the experiment, that is, $0.25h$ at the inlet. The inlet is located at $x/h = -4$ from the start of the bend and the outlet is placed at a distance of $6h$ from the end of the bend.

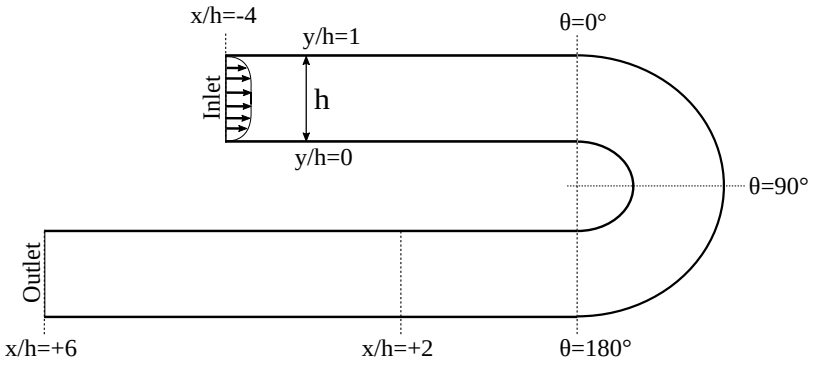

Figure 6.23: Computational domain of the curved channel flow case

At the inlet, the freestream velocity, U_∞ is calculated from the Reynolds number, which is 10^6, using the height of the channel, which is 38.1 mm. The turbulent kinetic energy at the inlet is calculated based on the turbulence intensity, reported in the experiment to be 1.16 %, using equation (6.31) while the specific dissipation rate, ω, is estimated using eddy viscosity ratio of $\nu_R = 38.7$ using equation (6.33). The boundary conditions at the walls and at the outlet are the same as the case configuration in Section 6.6.2.

6.6.4.2 Mesh generation and details

A mesh independence study is conducted using four computational grids, namely the coarse, medium, fine, and very fine grids. An open-source numerical package, Salome, is used to generate the grids. All the tested meshes are unstructured tetrahedral grids with prism layers allocated at the walls to ensure

capturing of boundary layers and y^+ of less than 1. The meshes are generated using user-defined cell size limitations and grading levels.

The result of the mesh independence study is presented here by comparing the velocity predictions using the different grids at two locations across the channel: $\theta = 180\,\text{deg}$ and $x/h = 2$. This is presented in Figure 6.24.

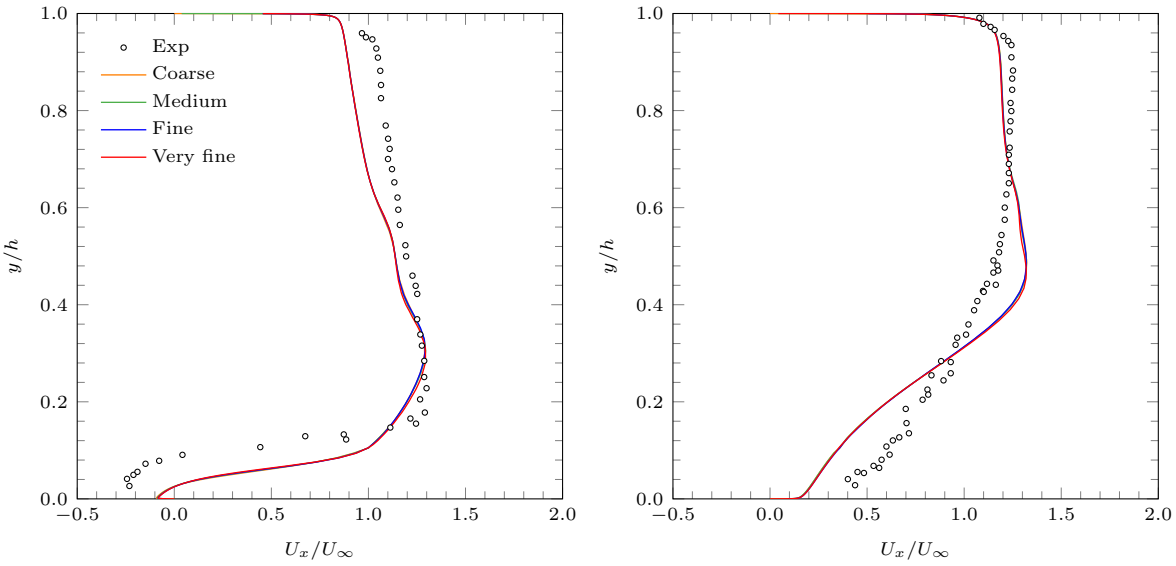

(a) $\theta = 180\,\text{deg}$ **(b)** $x/h = 2$

Figure 6.24: Mesh independence test for the curved channel configuration: longitudinal velocity profiles at two stations. Markers correspond to experimental data [162].

It can be observed from Figure 6.24 that the axial velocity profiles at the two locations predicted using the different grids are in close agreement. To quantify this, the percentage of difference of the mean axial velocity, U_m, across the station further downstream is calculated and presented in Table 6.7. The mesh independence test result is also quantified using the pressure drop across the domain, ΔP. This is also presented in Table 6.7. Notice the percentage of difference for the predicted quantities is benchmarked against the chosen grid, which is the coarse grid.

Table 6.7: Summary of grid independence test for the curved channel case

	Number of cells	U_m [m/s]	% Diff U_m	ΔP [Pa]	% Diff ΔP
Coarse	85,000	28.138	–	236.650	–
Medium	123,000	28.163	0.09	236.628	0.01
Fine	166,000	28.215	0.27	236.266	0.16
Very fine	308,000	28.215	0.27	236.300	0.15

The change of the mean axial velocity at the sampled station and the pressure drop across the different

grids is less than 1%. The chosen grid, which is the coarse grid, has 85,000 cells with a prism layer of 60 cells at the walls. The computational grid is shown in Figure 6.25. The maximum non-orthogonality of the grid is 24.6 deg with an average of 3.6 deg while the maximum skewness is 0.33. The maximum aspect ratio is 1400. While higher than desired, this is required in order to achieve y^+ less than unity and computation using the chosen grid still results in a stable and converged solution. The corresponding maximum y^+ value is 0.69.

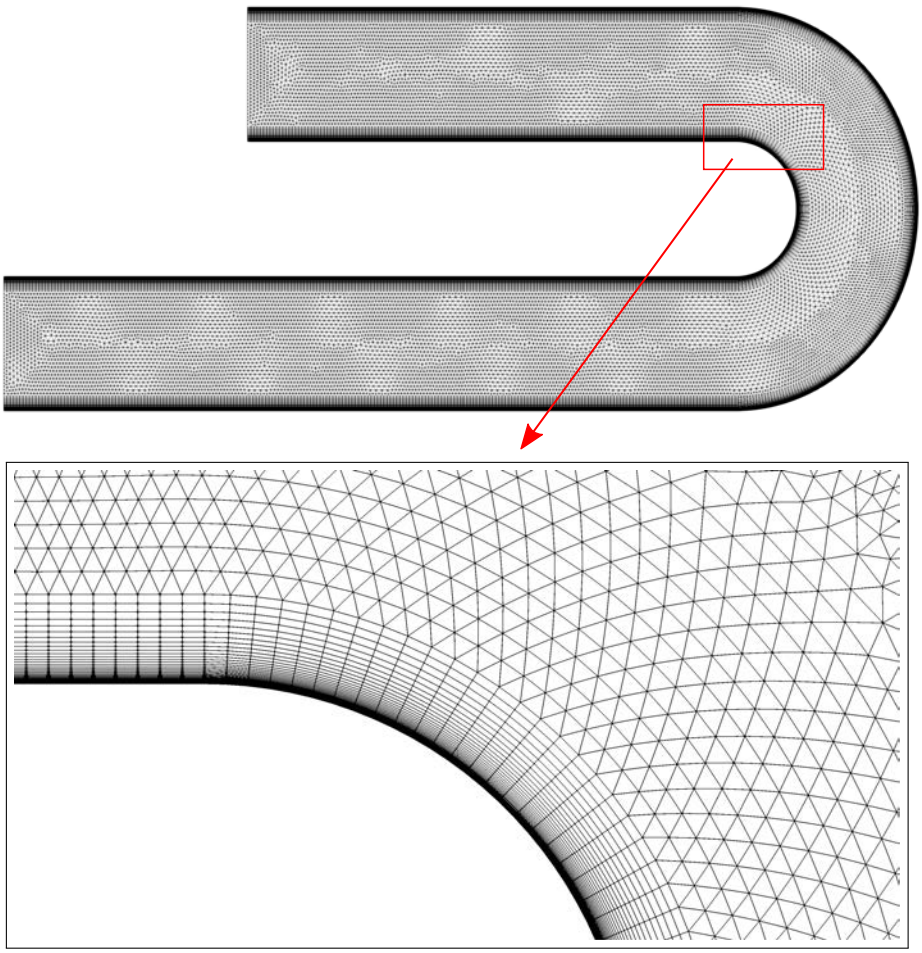

Figure 6.25: Computational grid for the curved channel flow configuration

6.6.4.3 Results and discussion

The general flow features can be examined from the velocity field prediction by the new model, shown in Figure 6.26. It can be observed that as the flow goes into the bend, the flow accelerates at the inner wall and decelerates at the outer wall. In the last half of the bend flow separation occurs at the inner wall due to a severe adverse pressure gradient.

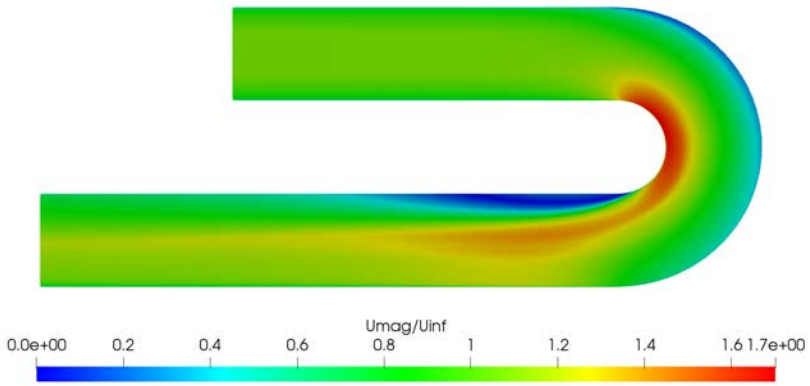

Figure 6.26: Velocity field prediction throughout the domain on the curved channel flow case predicted by the new model

Non-dimensional velocity profiles are presented in Figure 6.27. They are plotted against the wall-normal distance from the inner wall of the channel, y, normalised with h. The exit of the bend is located at $\theta = 180\,\text{deg}$ and $x/h = +2$ denotes a location $2h$ downstream of the bend. These locations are marked in Figure 6.23. In Figure 6.27 (a), which is the velocity profile at $\theta = 180\,\text{deg}$, the experimental results show the presence of reversed flow near the inner wall at the exit of the bend. The velocity profiles predicted by all the tested models show that separation at the inner wall is captured. However, the level of flow separation is generally underpredicted, with the NL $k-\omega$ model showing some improvement compared to the other models. Across the rest of the channel, the velocity profile is almost flat, except near the outer, concave wall where the boundary layer is thin. Downstream of the bend, at $x/h = +2$, the flow reattaches at the inner wall and accelerates at the outer wall, as shown in Figure 6.27 (b). The NL $k-\omega$ model predicts a slower recovery than the $k-\omega$ model at the inner wall, comparable to the other non-linear models. However, it predicts the acceleration at the outer wall more accurately.

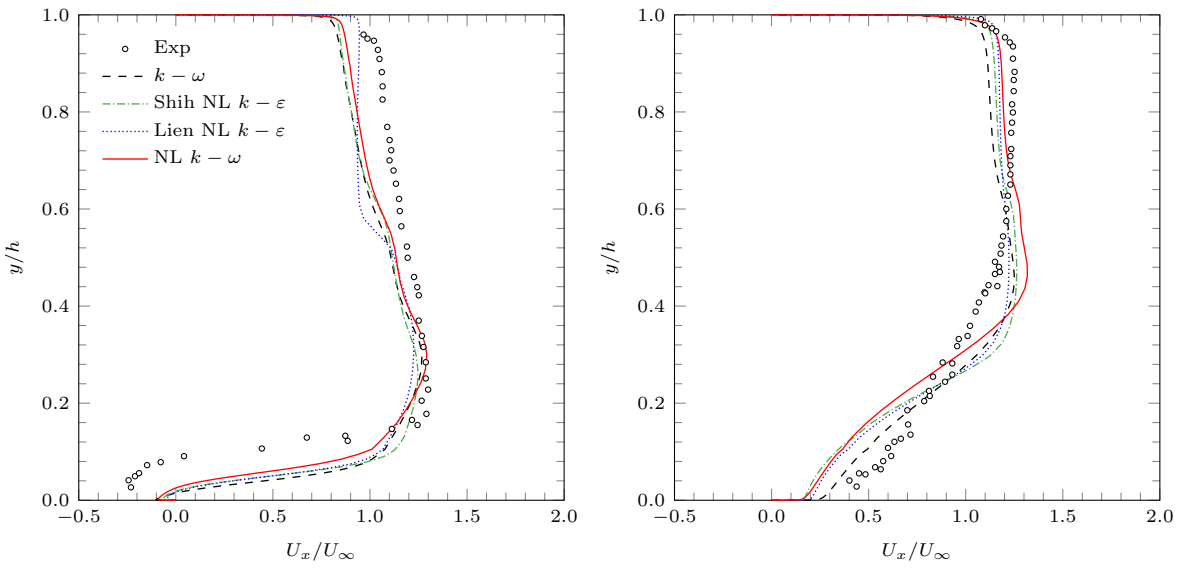

(a) $\theta = 180\,\text{deg}$ **(b)** $x/h = 2$

Figure 6.27: Longitudinal velocity profiles at two stations along the curved channel. Markers correspond to experimental data [162].

Figure 6.28 displays the turbulent kinetic energy profiles at the same location as the velocity profiles. The k profile at $\theta = 180\,\text{deg}$, plotted in Figure 6.28 (a), shows that at the exit of the bend all the tested models fail to capture the characteristic turbulent kinetic energy profiles for $0.2 < y/h < 0.9$, possibly as a result of underpredicting the onset of flow separation. Nonetheless, the peak in the value of k at the inner wall is captured by all models. Although significantly underpredicted, the NL $k-\omega$ model and the Lien cubic $k-\varepsilon$ model return closer predictions to the experimental data compared to the other models. Unfortunately, there is no experimental data for the turbulent shear stress at this location to explore how turbulence anisotropy is predicted. However, it is encouraging that further downstream at $x/h = +2$, the turbulent kinetic energy, which has now diffused outwards in the inner half of the channel, is predicted well by the NL $k-\omega$ model compared to the other models. Specifically, a 17% improvement is noted compared to the linear $k-\omega$ model. This is shown in Figure 6.28 (b). The NL $k-\omega$ model shows an important improvement in the prediction of the maxima here. This is echoed by a similar improvement of approximately 25% in the prediction of the peak value of the turbulent shear stress (Figure 6.29) compared to the linear $k-\omega$ model, which is also a 14% and 21% more accurate peak shear stress prediction compared to the Shih quadratic $k-\varepsilon$ and Lien cubic $k-\varepsilon$ models, respectively.

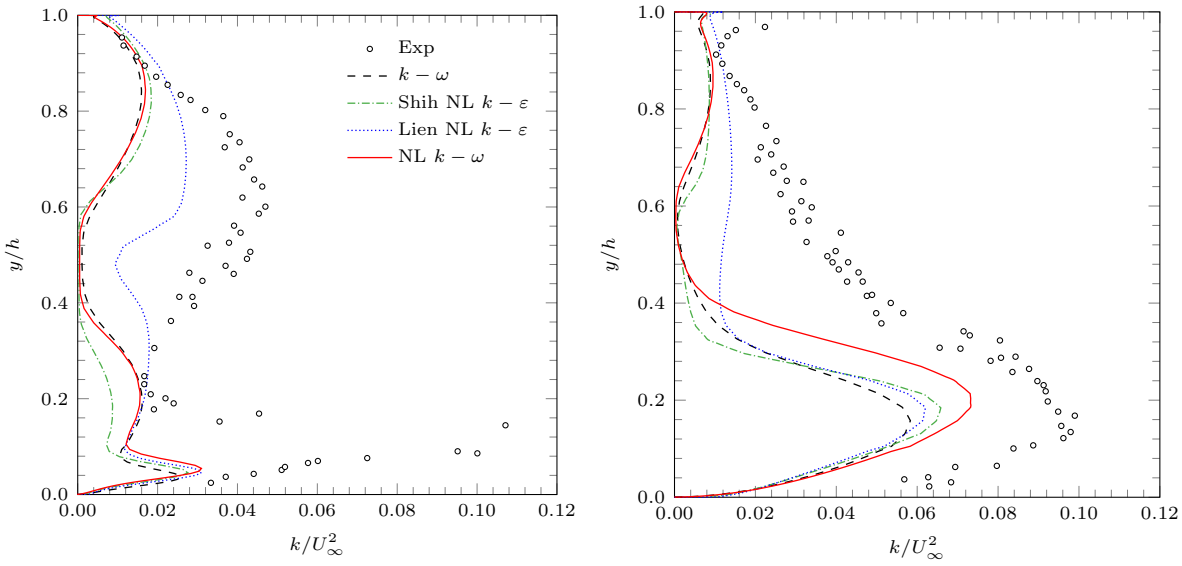

(a) $\theta = 180\,\text{deg}$ **(b)** $x/h = 2$

Figure 6.28: Turbulent kinetic energy profiles at two stations along the curved channel. Markers correspond to experimental data [162].

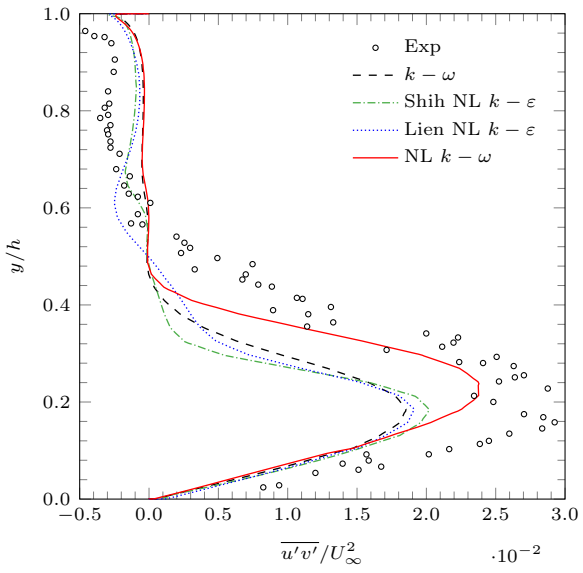

Figure 6.29: Turbulent shear stress at $x/h = 2$ along the curved channel. Markers correspond to experimental data [162].

The predictions for global quantities through the entire domain are illustrated through the pressure and skin friction coefficients at the outer and inner walls in Figures 6.30 and 6.31, respectively. They are plotted against the downstream distance, s, measured from the channel entrance on the centreline between the inner and outer walls and non-dimensionalised using h. The bend is located at $21.7 \leq s/h \leq 24.8$. These plots provide a means to assess of the performance of the NL $k-\omega$ model throughout the domain.

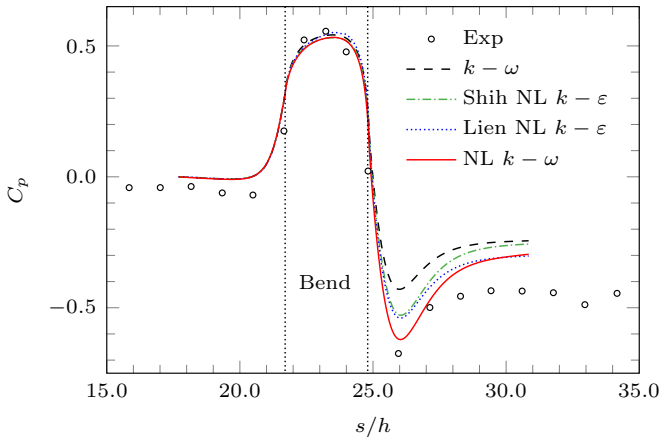

(a) Outer wall

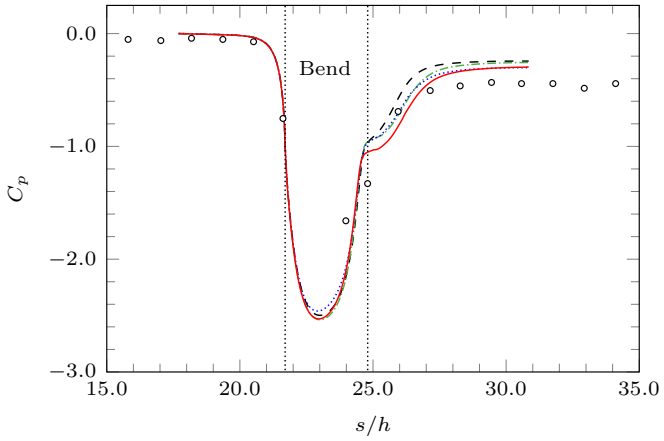

(b) Inner wall

Figure 6.30: Pressure coefficient distribution of curved channel flow on the outer and inner walls. Markers correspond to experimental data [162].

From a practical engineering point of view, an accurate prediction of skin friction is important since heat transfer is proportional to skin friction whilst the prediction of pressure is important for measuring losses in the domain, for example in this case due to curvature. In comparison to the experimental data, the NL $k-\omega$ model predicts the two quantities well upstream and through the bend. Downstream of the bend, at the location of minimum pressure on the outer wall where the flow accelerates (shown in Figure 6.30 (a) at $s/h \approx 26$), the NL $k-\omega$ model predicts the pressure minimum approximately 50% more accurately compared to the linear $k-\omega$ model and approximately 20% more accurately compared to the other tested non-linear models. This is accompanied by a prediction of the maximum skin friction coefficient at the outer wall (shown in Figure 6.31 (a) at the same location) within 1.5% of the experimental data, compared to the $k-\omega$ which underestimates it by 14%. The Shih quadratic $k-\varepsilon$ model also predicts this skin friction peak well, showing comparable prediction to the NL $k-\omega$ model, while the Lien cubic $k-\varepsilon$ model overpredicts it. It can be noted that the improvements shown by the NL $k-\omega$ model here are consistent with the more accurate predictions of the mean flow by the model on the outer wall, shown earlier in Figure 6.27. This highlights the strength of the NL $k-\omega$

model in predicting the destabilising effects of a concave curvature, which are known to result in a growth of longitudinal vortices and an increase in turbulent mixing [163]. Further downstream from the bend (approximately $s/h > 28$), the pressures on the inner and outer walls (shown in Figure 6.30) reach the same level at a lower value than the values upstream, signifying pressure losses in the flow due to the curvature. While the level of separation at the end of the bend is still underpredicted by the NL $k-\omega$ model, as shown earlier in Figure 6.27, the adverse pressure gradient across the curved channel is represented well. Specifically, the NL $k-\omega$ model provides a 15% improvement compared to the standard $k-\omega$ model in the prediction of the pressure drop between the measurements upstream and downstream of the bend. As mentioned earlier, this has important practical implications as it represents the energy losses in the domain. The Lien cubic $k-\varepsilon$ model predicts a similar level of pressure coefficient downstream of the bend with the NL $k-\omega$ model, although it overpredicts the skin friction coefficient here. The Shih quadratic $k-\varepsilon$ model returns comparable predictions to the standard $k-\omega$ model in terms of pressure coefficients here, underpredicting the pressure drop through the bend.

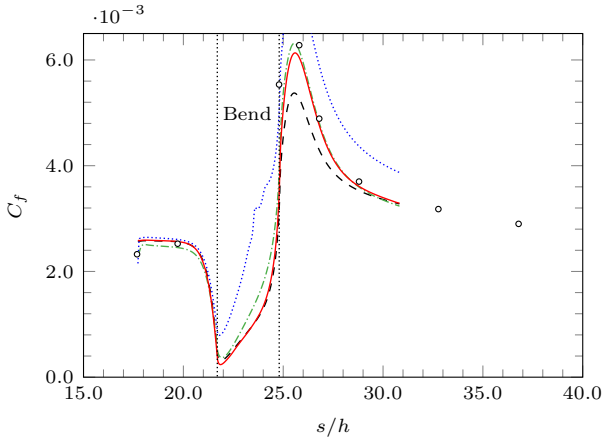

(a) Outer wall

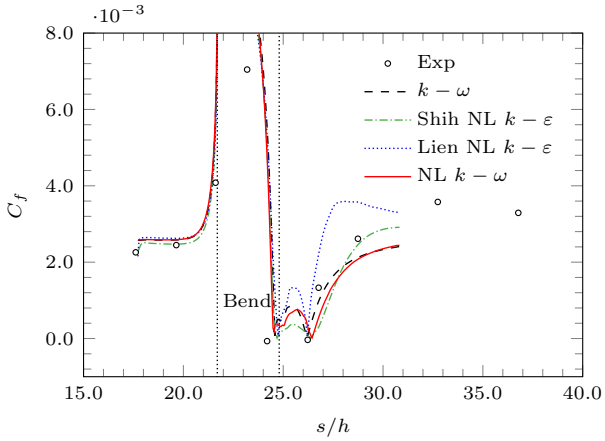

(b) Inner wall

Figure 6.31: Skin friction coefficient distribution of curved channel flow on the outer and inner walls. Markers correspond to experimental data [162].

6.7 Computational expense

All the computations completed in this work are performed using the High-Performance Computing (HPC) clusters at Coventry University. For the canonical cases presented in this chapter, HPC nodes consisting of Intel® Xeon® Nehalem L5530 CPUs with a base frequency of 2.40 GHz are used, in which each of the processor has an associated 4.0 Gb of RAM. Table 6.8 shows the number of CPU cores that are used for the computation of each test case presented in this chapter and the respective running times. A comparison is made on the running times of the computations using the $k-\omega$ model and the NL $k-\omega$ model to provide an information on the change in computational expense associated with the proposed modelling approach. Note that since the computations are completed in a computer cluster, the running time comparison presented here serves as a general estimation as computation time could change based on processor properties as well as node allocation.

Table 6.8: Comparison of computational expense for the canonical cases

Test case		CPU cores	Running time [s]		% Diff
			$k-\omega$	NL $k-\omega$	
Plane channel flow	$Re_\tau = 180$	4	617	557	-9.72
	$Re_\tau = 550$	4	818	545	-33.37
	$Re_\tau = 1000$	4	843	583	-30.84
T3B flat plate		4	7,677	6,397	-16.67
Curved channel		4	7,773	8,289	6.64

Table 6.8 shows that for the simpler configurations, namely the plane channel flow cases and the T3B flat plate case, the computations that use the NL $k-\omega$ model takes less time to converge compared to those with the $k-\omega$ model. For the curved channel flow case, there is a small increase (less than 10%) in the computation time associated with the NL $k-\omega$ model.

6.8 Summary

In this chapter, a novel approach for the enhanced treatment of turbulence anisotropy in near-wall regions is proposed, developed, and validated. The modification is formulated to capture how anisotropic turbulence effects are manifested in the boundary layer, specifically, within the inner region. Analytical simplification of the Reynolds stress distribution on a simple shear flow is used to obtain benchmark anisotropy expansion coefficient profiles that result in a Reynold stress distribution that approximately match the DNS data by [148]. Using this benchmark data, new functions are introduced in the new near-wall formulation using damping functions that represent the different regions in a boundary layer, specifically, the viscous sublayer, the buffer region, and the log layer. The functions are defined such that they only depend on local variables, specifically, the turbulence scales. The near-wall modification results in a number of coefficients that subsequently need calibrating. The resulting modification produces a distribution of the anisotropy expansion coefficients that reflects the raised level of anisotropy near the wall and returns the anisotropy coefficients to the baseline values away

from the wall.

The new model in its final form, referred to from hereon as the NL $k-\omega$ model, has been applied to a number of canonical cases to validate its implementation as well as analyse its performance. Comparison of the results is made against the predictions obtained using the standard $k-\omega$ model as well as the results in [155] which are obtained using the Shih quadratic $k-\varepsilon$ model [31] and the Lien cubic $k-\varepsilon$ model [156].

The following conclusions can be drawn from the analysis of the results:

- In a simple shear flow at various Reynolds numbers:
  - The NL $k-\omega$ model consistently shows improvements in the Reynolds anisotropy prediction compared to the linear $k-\omega$ model as well as the baseline predictions. It also predicts the turbulence anisotropy closer to the DNS data compared to the other two non-linear models included.
  - A marked improvement can be noted in the near-wall region in particular (approximately $y^+ < 40$), highlighting the strength of the NL $k-\omega$ model which is developed to represent the increased anisotropies within inner region of a boundary layer due to the presence of the 'streaky' turbulence structures here.
- In a flow over a zero-pressure-gradient flat plate:
  - The NL $k-\omega$ model correctly predicts a turbulent boundary layer, consistent with its formulation as a fully-turbulent model.
  - The modification is also shown to be effective for improving the predictions of turbulence anisotropy near the wall, particularly, in the increased level of the streamwise fluctuations which indicate the correct representation of streamwise-oriented streaky structures that are present in the inner region of a boundary layer downstream of a bypass transition. The two other non-linear models considered underpredict the level of turbulence anisotropy here.
- In a curved channel flow:
  - The NL $k-\omega$ model returns predictions of pressure and skin friction across the channel walls to be closer to the experimental data compared to the other models considered, highlighting the strength of the NL $k-\omega$ model in predicting the near-wall features such as the acceleration and separation along the curved wall.
  - Results show the advantage of the anisotropic NL $k-\omega$ model in representing the destabilising effects of the concave curvature in particular, which is known to be dependent on the behaviour of wall-normal fluctuations.

Chapter 7

Application: planar diffuser with a downstream monolith

7.1 Introduction

In this chapter, the new NL $k-\omega$ model is applied to a configuration that represents a simplified setup of an automotive exhaust catalytic converter. A catalytic converter is a ceramic monolith consisting of many small parallel channels, which is used to provide a large surface area for the conversion of the exhaust gases and particulates from an automotive engine into less harmful emissions. The design of automotive exhaust catalyst systems is of continuing importance, motivated by increasingly strict emissions regulations. In order for engineers to develop an efficient catalytic converter, a close understanding and prediction of flow distribution in the catalyst system is crucial. In the efforts to improve this, a number of experimental and computational studies of flow in a catalyst system have been conducted and reported in existing literatures [164–170] in which a simplified setup is used to represent the system. The setup consists of a planar diffuser followed downstream by a porous region and an outlet sleeve. This configuration is also adopted in this work. The geometry is presented in Figure 7.1. The dimensions are provided in the detailed computational domain section later in Section 7.3.2.

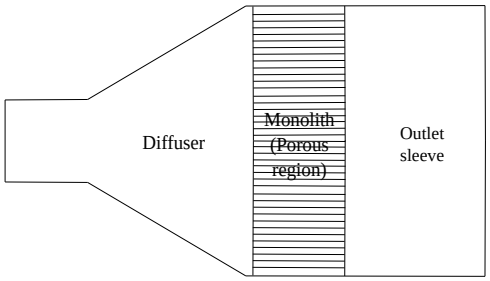

Figure 7.1: 2-D geometry of the planar diffuser configuration

The planar diffuser is used for connecting the exhaust pipe from the engine to the entrance of the monolith in order to maximise the surface area of the monolith while still meeting space constraints. From an application point of view, a number of aspects need to be considered closely in the flow predictions. It is crucial to predict how the flow is distributed as it enters the monolith since the conversion efficiency of a catalytic converter is strongly dependent on the flow distribution. As the use of a diffuser has been known to increase flow maldistribution in catalysts [164, 165], the flow field within the diffuser needs to be predicted accurately. In addition, it has been observed that the pressure losses associated with the inlet diffuser geometry contributes up to half of the total losses in a diffuser-monolith catalyst configuration [171]. Further pressure losses also occur within the monolith (e.g. due to contraction, friction, and expansion), which contribute to the overall back pressure of an exhaust system and could affect the engine efficiency. Therefore, the effects of the monolith itself to the flow field also need to be predicted closely.

In addition to these challenges, the inclusion of this configuration in the evaluation of the new model is motivated by the nature of the geometry which presents a number of flow processes suitable for evaluating a new turbulence model and for which the anisotropic formulation of the NL $k-\omega$ model can be expected to show advantages. Of particular note is how the high resistance of the monolith generates unique features in the flow behaviour in the diffuser compared to 'classic' diffuser test cases such as [52, 172] that are widely used in literatures for evaluating the performance of a turbulence model. In a traditional diffuser case, separation and reattachment typically occur on the diffuser wall, followed by the development of a boundary layer downstream. Since a monolith is fitted to the end of the diffuser, this natural development is not expected to be present here. Instead, these complex flow features are to be expected: separation, recirculation, and impingement [168, 169].

In order to improve separation prediction, a more accurate prediction of shear stress near the wall is needed, which can be obtained through a more accurate representation of the highly anisotropic turbulence near the wall. Therefore, the anisotropic formulation for Reynolds stresses in the NL $k-\omega$ model, combined with its enhanced treatment for near-wall turbulence anisotropy, are expected to result in the model showing advantages over the linear $k-\omega$ model here. In addition, beyond the separation point, the flow loses much of the direction-constraining influence of the boundary and all

components of the Reynolds stress tensor become dynamically significant. Furthermore, the presence of the monolith in the configuration introduces a high resistance to the flow, which effectively creates an impingement region. The limitation of linear eddy-viscosity models in predicting an impinging flow is known to be due to the prediction of isotropic Reynolds stresses, which results in an overprediction of turbulent kinetic energy in the stagnation region. Therefore, the NL $k-\omega$ model is expected to return improved predictions of the normal Reynolds stresses and thus improve the prediction of the mean flow through a better representation of the turbulent kinetic energy. Therefore, the application of the NL $k-\omega$ model in this flow configuration is expected to highlight its potential benefits.

The first part of this chapter discusses the approach for modelling the monolith. The method used in this work is the porous medium approach. The details of the modelling approach are presented. Next, the setup of the experimental work on a diffuser-catalyst configuration at Coventry University by Mat Yamin *et al.* [166, 167] and Porter *et al.* [168–170] on which this case is based is presented. This highlights the experimental method and instrumentation as well as how the measurements obtained in the experiments provide information for the inlet and boundary conditions setup of the computations. More importantly, the measurements by [166–170] also provide experimental data using which the model predictions are assessed. Next, the setup of the computations completed in this work is presented, which includes the computational domain and boundary conditions, as well as details of the different parameters considered and the mesh convergence study. The results and discussion are subsequently presented. As mentioned above, the effects resistance introduced by the monolith need to be modelled closely. Therefore, the first part of the results and discussion analyses different treatments within the porous medium modelling method. Once the methodology is established, the turbulence model predictions are presented and discussed. This includes an analysis on the mean flow predictions as well as the predictions of the turbulent quantities. Finally, the computational expense associated with the NL $k-\omega$ model is presented in comparison with the linear $k-\omega$ model.

7.2 Porous medium modelling

There are a number of methods for modelling the effects of a porous region (e.g. a monolith) on the flow features. A monolith contains many small parallel channels since its purpose is to provide a large surface area for chemical reactions. A modelling methodology is required to predict the change in pressure across the domain due to the compression and expansion of flow as it enters and exits the monolith channels, as well as the frictional losses due to the no-slip condition within the channels. A monolith can be modelled as individual channels; however, this corresponds to a very high computational cost since it requires the computational grid to describe the three-dimensional geometry of all the channels and provide enough number of cells within each channel to capture the boundary layer effects. Therefore, an alternative approach exists.

7.2.1 The approach

An alternative method is therefore to model the monolith as an equivalent continuum, or porous medium, as proposed by [173]. The flow in the porous zone is assumed to be unidirectional and its resistance characteristics are prescribed as a function of the local mean velocity. This approach has been applied widely in the literature [164,165,168]. Porter *et al.* [168] apply both individual channels and porous medium approaches in modelling the flow configuration presented in this chapter and find that results from the individual channels and porous medium approaches only differ downstream of the monolith, and are found to not arise differences in the diffuser upstream.

Using the porous medium approach, the resistance of the monolith can be characterised using experimental measurements and fitted using the Darcy-Forchheimer law [174]. It treats the porous zone as a sink term, S_m, in the momentum equation calculated using the following formulation for incompressible flow:

$$S_m = -\left(\nu D + \frac{1}{2}|u_{jj}|F\right)\left(u_i \right. \tag{7.1}$$

This equation represents the predicted momentum loss associated with a simple homogeneous porous medium. It is composed of two parts: a viscous loss term, which the first term on the right hand side, and an inertial loss term, which is the second term on the right hand side. They can be seen to generate pressure losses that are proportional to the velocity and velocity squared, respectively. D and F in equation (7.1), which are Darcy and Forchheimer coefficients, respectively, therefore represent these losses. The losses resulting from a porous region can therefore be characterised by deriving the values of D and F either theoretically or from experimental data. The porous medium modelling approach is readily implemented on OpenFOAM and an example of its use for computation is presented in Appendix C for reference.

7.2.2 Turbulence treatment

The approach to treat a porous zone as a sink term works as a loss in the momentum equations, as described above. The turbulence quantities, however, are still solved by default using the transport equations described by the turbulence model. This treatment assumes that the monolith has no direct effects on the turbulent kinetic energy production or dissipation rates. To illustrate, the planar diffuser configuration can be divided into three parts:

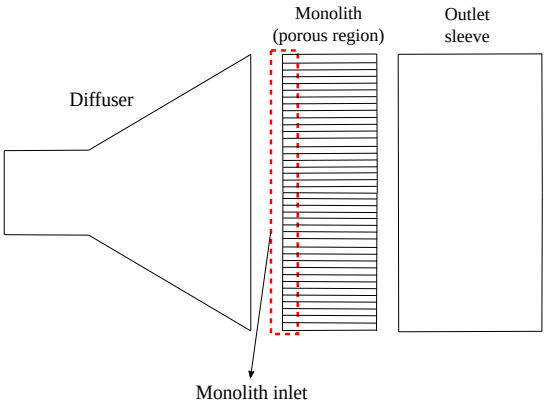

Figure 7.2: Planar diffuser configuration

The turbulent kinetic energy, k, at the monolith inlet patch on the diffuser-monolith interface is set as the same as k at the outlet patch of the diffuser by the treatment mentioned above. This is referred to as a 'cyclic' boundary condition. This treatment is referred to in this work as the *cyclic* approach. The assumption that the level of turbulence upstream of the porous zone is preserved through the resistance may be reasonable if it has a large permeability and the geometric scale of each channel within the porous medium does not interact with the scale of the turbulent eddies. Otherwise, suppression of turbulence within the porous medium may be more appropriate.

In commercial CFD packages, the turbulence in the porous zone can be suppressed by setting the eddy viscosity, ν_T, to zero at the monolith inlet. In this work, ν_T is calculated from the modelled turbulence scales, k and ω. Therefore, the suppression of turbulence within the porous medium can be achieved by setting the turbulent kinetic energy, k, at the monolith inlet to zero. This assumption is reasonable when the characteristic length of the channels is small enough such that the flow stays laminar within each channel. This treatment for damping or suppressing k is referred to in this work as the *damping* approach.

In order to establish the suitable treatment for the porous medium modelling, the two approaches for treating turbulent kinetic energy at the interface of a porous medium, namely the *cyclic* and *damping* methods, are used and evaluated first in this chapter. The findings are reported and discussed as the first part of the results section. The approach that returns the closest predictions to experimental data is applied for the comparison of the turbulence model predictions, as well as for the cases in the next chapter.

7.3 Case description

7.3.1 Experimental details

The configuration considered here is based on a series of experimental cases completed at Coventry University by Mat Yamin *et al.* [166, 167] and Porter *et al.* [168–170]. The schematic of the experimental assembly is shown in Figure 7.3. Of particular interest are the diffuser, monolith, and the outlet sleeve, represented by number (12), (13), and (14), respectively. The dimensions of the test section are shown later in Figure 7.4. Room temperature air flow is used throughout the experiments since it has been observed that normalised pressure losses in a catalyst system are not affected by changing the fluid between cold air, hot air, and engine exhaust gases and therefore evaluation of the flow distribution can be adequately ascertained using inexpensive cold air [171].

No chemical reactions are included in the experiments as the focus of the work is on characterising the flow distribution in the assembly. Two monolith lengths are tested: 27 mm and 100 mm. The monolith channels force the flow to be unidirectional in the x-direction. Each channel has a hydraulic diameter of 1.12 mm and the nominal cell density of the monolith is 62 cells/cm^2. Pressure losses measured in the experiments are used to characterise the monolith using the Darcy-Forchheimer law shown in equation (7.1), which results in the monolith having resistance properties of $D = 3.96 \times 10^7/\text{m}^2$ and $F = 23.38/\text{m}$ for the 27-mm length and $D = 1.40 \times 10^7/\text{m}^2$ and $F = 33.45/\text{m}$ for the 100-mm length. Four different mass flow rates are tested, which correspond to Reynolds number of 2.2, 3.0, 4.2, and 6.0 $\times 10^4$.

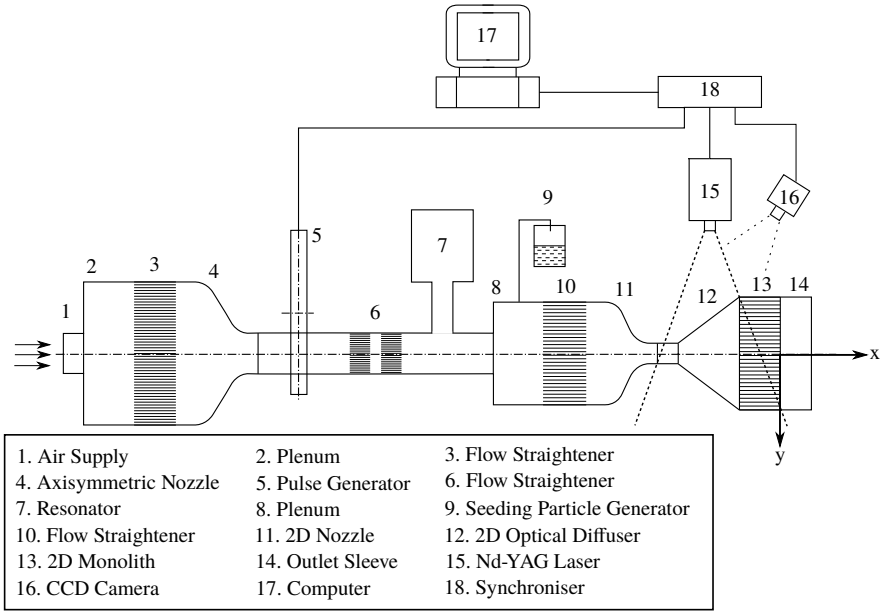

Figure 7.3: Diagram of experimental assembly for the planar diffuser case [168].

Measurements are taken in the nozzle (11), diffuser (12), and across the outlet sleeve (14). Two distinct approaches are used for these measurements. Particle image velocimetry (PIV) is applied for observing flow in the diffuser, while hot-wire anemometry (HWA) probe measurements are taken upstream of the diffuser, in the nozzle, and downstream of the monolith, at the outlet. The reader is referred to [166–169] for more details of the experimental data collection. It is not included here for succinctness.

Axial and transverse velocity profiles (U_x and U_y, respectively) in the diffuser are extracted from the PIV measurements at three cross-sections in the diffuser: 2.5 mm, 5.55 mm, and 10.13 mm upstream of the monolith. HWA measurements provide information on the velocity profiles at the outlet, located 40 mm downstream of the end of the monolith. At this location, the jets exiting the monolith channels are found to have mixed sufficiently to provide a smooth profile [165]. Therefore, this is considered as an appropriate location to sample the flow field downstream of the monolith. The available experimental data at these locations allow the comparison of the results from the computation in regards to the flow field within the diffuser as well as the effects of the porous medium at the outlet.

In addition to providing comparison for the flow predictions, the experimental results also justify the assumptions used in constructing the domain as well as the inlet and boundary conditions used in the computations. HWA measurements across the nozzle (marked by number (11) in Figure 7.3), which consequently serves as an inlet into the diffuser, i.e. an inlet for the computational domain, shows uniform axial velocity profiles across the nozzle in the y- and z- directions for a range of Reynolds numbers. This justifies a uniform inlet profile to be prescribed for the computations. It is also observed that limited variation across the z-plane of the outlet profiles is shown in the experiments, which allows the two-dimensionality of the computational domain. Both HWA results at the outlet and PIV results in the diffuser show acceptable symmetry on the x- axis (within 5%) which allows the computational domain to represent only half of the geometry and a symmetry boundary to be used across the x-axis instead.

7.3.2 Computational domain and boundary conditions

The computational domain consists of an inlet channel connected to a planar diffuser, which is fitted to a monolith (porous region) downstream, and followed by an outlet sleeve. The computational domain is shown in Figure 7.4. The height of the inlet channel is 12 mm and the height at the end of the expansion and the outlet is 39 mm, which corresponds to an overall expansion ratio of 3.25. The diffuser section has a length of 46 mm and a diverging angle of 30 deg. The two-dimensionality of the domain is justified by the experimental results, which confirm the theory that two-dimensional flow in a diffuser is observed when the aspect ratio at the inlet is greater than 4 to 5 [175]. Since the span of the diffuser is 96 mm, this condition is met. Two monolith lengths are explored: 27 mm and 100 mm. At the end of the monolith, a 40-mm outlet sleeve is fitted. The location of the sampling stations, which are (A) 10.13 mm, (B) 5.55 mm, and (C) 2.5 mm upstream of the monolith, and (D) 40 mm downstream of the monolith are marked by the red dashed lines in Figure 7.4.

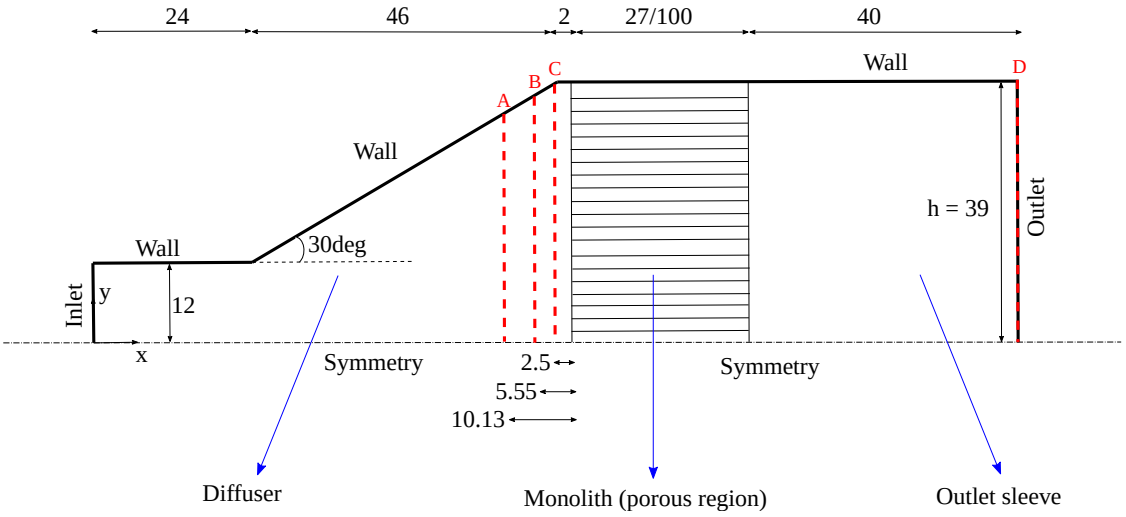

Figure 7.4: Computational domain of the planar diffuser case. Dimensions are in mm.

The computational domain represents half of the geometry of the configuration used in the experiment and a symmetry condition is set on the bottom boundary (along the x-axis). Prescribing a symmetry boundary condition allows the reduction of the computational costs by 50%. In addition, it can also avoid instability in the solutions which can occur if asymmetric flow fields are predicted during the computational iterations [133].

As previously mentioned, uniform axial velocity profiles are observed in the experiments upstream of the diffuser inlet which allows the inlet conditions in the computations to be set as uniform. The freestream velocity at the inlet, U_∞, is calculated from the Reynolds number of the cases tested using:

$$Re = \frac{U_\infty D_h}{\nu} \tag{7.2}$$

in which ν is the kinematic viscosity and D_h is the characteristic length which is the hydraulic diameter of the nozzle (marked by number (11) in Figure 7.3) that is located upstream of the inlet channel. The values are set as $\nu = 1.567 \times 10^{-5}$ m/s^2 and $D_h = 0.0384$ m to match the conditions in the experiment. For the turbulent quantities, the inlet conditions prescribed are as follows. The turbulent kinetic energy, k, is calculated using the freestream turbulence intensity, $Tu_\infty = 1\%$ while the dissipation frequency, ω, is calculated by setting the eddy viscosity ratio, ν_R to 10. The following relations are used:

$$k_\infty = \frac{3}{2}(Tu_\infty U_\infty)^2 \qquad , \qquad \omega_\infty = \frac{k_\infty}{\nu_R \nu} \tag{7.3}$$

A summary of the prescribed inlet conditions for the diffuser test cases is presented in Table 7.1. For the pressure, a zero-gradient boundary condition is prescribed at the inlet.

Table 7.1: Summary of inlet conditions for the planar diffuser cases

Re [−]	U_∞ [m/s]	k [m^2/s^2]	ω [s^{-1}]
2.2×10^4	8.98	0.01208	77.1316
3.0×10^4	12.24	0.0226	143.4265
4.2×10^4	17.14	0.0440	281.1160
6.0×10^4	24.48	0.0899	573.7061

At the outlet, a zero-gradient condition is prescribed for the velocity and turbulent quantities and a fixed zero gauge pressure outlet is used. At the walls, a no-slip condition is prescribed for the velocity and turbulent kinetic energy, and a zero-gradient condition is prescribed for the pressure. The specific dissipation rate, ω, is assigned using the classic solution for smooth walls:

$$\omega_{\text{wall}} = \frac{6\nu}{C_{\omega,2} y^2} \tag{7.4}$$

7.3.3 Summary of test cases

The parameters selected for the cases considered using this configuration are summarised in Table 7.2. This includes applying both monolith lengths that are tested in the experiments. Four different freestream Reynolds numbers are considered which match the experimental conditions. As the first objective of the chapter is to evaluate a suitable approach for the porous medium modelling, two treatments for modelling turbulence inside the porous medium are applied. The *damping* and *cyclic* approaches have been introduced and discussed in Section 7.2, and they refer to whether turbulent kinetic energy, k, is suppressed at the interface between the diffuser outlet and the monolith inlet.

The NL $k-\omega$ turbulence model is used for the computations and the results are discussed in comparison with the original $k-\omega$ model. The results of the NL $k-\omega$ model for the canonical cases are compared with two other non-linear models, namely the Shih quadratic $k-\varepsilon$ model and the Lien cubic $k-\varepsilon$ model, in addition to the standard $k-\omega$ model. However, on the more complex configurations, which are the planar diffuser cases discussed in this chapter and the swirling flow cases presented in the next chapter, the two tested non-linear $k-\varepsilon$ models are not able to achieve convergence in the computations. While this is not ideal, it demonstrates the robustness of the new NL $k-\omega$ model compared to other non-linear eddy-viscosity models. For benchmarking purposes, another comparison is instead made against the performance of one other linear turbulence model. The computation results obtained at Coventry University by Porter *et al.* [168, 169] are included. The turbulence model used is the $k-\varepsilon$ v^2-f model by Durbin *et al.* [151] which has been shown in the literature to have advantages in

predicting separated flows [176–181]. Note that the results for the $v^2 - f$ model from [168, 169] are only included for the purpose of comparing the predictions of the mean flow only, which is in Section 7.4.2. The analysis in regards to the porous medium approach (Section 7.4.1) and the analysis on the prediction of turbulent quantities (Section 7.4.3) are made in comparison with the standard $k - \omega$ model only.

Table 7.2: Summary of parameters for the planar diffuser cases

Porous length [mm]	Re [−]	Porous modelling method	Turbulence model
27	2.2×10^4	*damping*	$k - \omega$
100	3.0×10^4	*cyclic*	$v^2 - f$
	4.2×10^4		NL $k - \omega$
	6.0×10^4		

7.3.4 Meshing and convergence behaviour

A mesh independence study is conducted using six grids to ensure that the computational grid is sufficiently refined and well-distributed, to allow the capturing of the flow features (while still trying to minimise the computational effort). Two types of meshes are considered which correspond to two different shapes of the control volumes: a structured hexahedral grid and an unstructured tetrahedral grid. For the structured grid, the mesh generation utility, `blockMesh`, available in OpenFOAM is used. The grid is created using a user-defined number of cells, cell size, and cell stretching level in three dimensions. The `blockMesh` utility is used to produce three of the six grids used in the mesh independence test, namely the hexa - coarse, - medium, and - fine grids. The size and stretching of the grids are set such that a y^+ less than 1 is achieved. For the unstructured grid, an open-source numerical package, Salome, is used. The mesh is generated using user-defined cell size limitations and grading levels. A prism layer is allocated perpendicular to the walls to ensure capturing of boundary layer and a y^+ less than 1. Three tetrahedral meshes are generated using Salome, namely tetra - coarse, - medium, and - fine. Since the domain is two-dimensional, 1 cell is specified in the z-direction for all the meshes to meet the requirements of OpenFOAM.

The result of the mesh independence study is presented here by considering the 27-mm monolith case at the highest Reynolds number, $Re = 6.0 \times 10^4$, computed using the NL $k - \omega$ model with the *cyclic* porous medium modelling method. Predictions of axial velocity profiles are compared at the sampling station 40 mm downstream of the monolith (station (D) in Figure 7.4). The axial velocity, U_x, is non-dimensionalised using the mean velocity, U_m, across this location. It is plotted against the y-distance from the symmetry plane, non-dimensionalised using the maximum, expanded height of the diffuser, h in Figure 7.4.

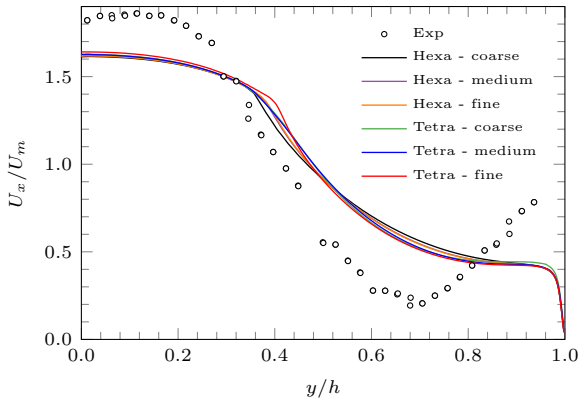

Figure 7.5: Mesh independence test: axial velocity profile 40 mm downstream of monolith at Re = 6.0 $\times 10^4$. Markers correspond to experimental data [168].

It can be observed from Figure 7.5 that the axial velocity profiles at the outlet predicted by the different grids are in close agreement. Since this is non-dimensionalised, the percentage of difference of U_m obtained from the tested grids is also calculated and presented in Table 7.3. The results can also be quantified using the non-uniformity index, ξ. The non-uniformity index characterises the level of flow maldistribution and is calculated using:

$$\xi = \frac{\frac{1}{n}\sum_{i=1}^{n}\left(|U_{x,i} - U_m|\right)}{U_m} \tag{7.5}$$

where $U_{x,i}$ is the local axial velocity and U_m is the mean velocity across this station. The non-uniformity index for the results of each grid is assessed using the velocity profile at the outlet. The results are also presented in Table 7.3. Notice the percentage of difference for U_m and ξ is benchmarked against the chosen grid, which is the hexa - medium mesh.

Table 7.3: Summary of grid independence test for the planar diffuser cases

	Number of cells	U_m [m/s]	% Diff U_m	ξ	% Diff ξ
Hexa - coarse	56,000	7.563	0.04	0.445	2.20
Hexa - medium	85,000	7.560	–	0.455	–
Hexa - fine	113,000	7.560	0.00	0.456	0.22
Tetra - coarse	39,000	7.548	0.16	0.462	1.54
Tetra - medium	87,000	7.557	0.04	0.463	1.76
Tetra - fine	146,000	7.548	0.16	0.476	5.50

The total number of cells is 85,000. The change of the value of U_m between this mesh and the finer hexahedral mesh is negligible and the change of the non-uniformity index across the outlet is less than 1%. With the exception of the tetra - fine mesh, the difference in U_m and ξ across all tested meshes are around 2% maximum. The high percentage of difference for the tetra - fine mesh may be attributed

to how excessive grid refinement could cause the computation to capture some unphysical features; therefore, this grid will not be used. The chosen mesh is illustrated in Figure 7.6. The corresponding maximum y^+ is 0.89.

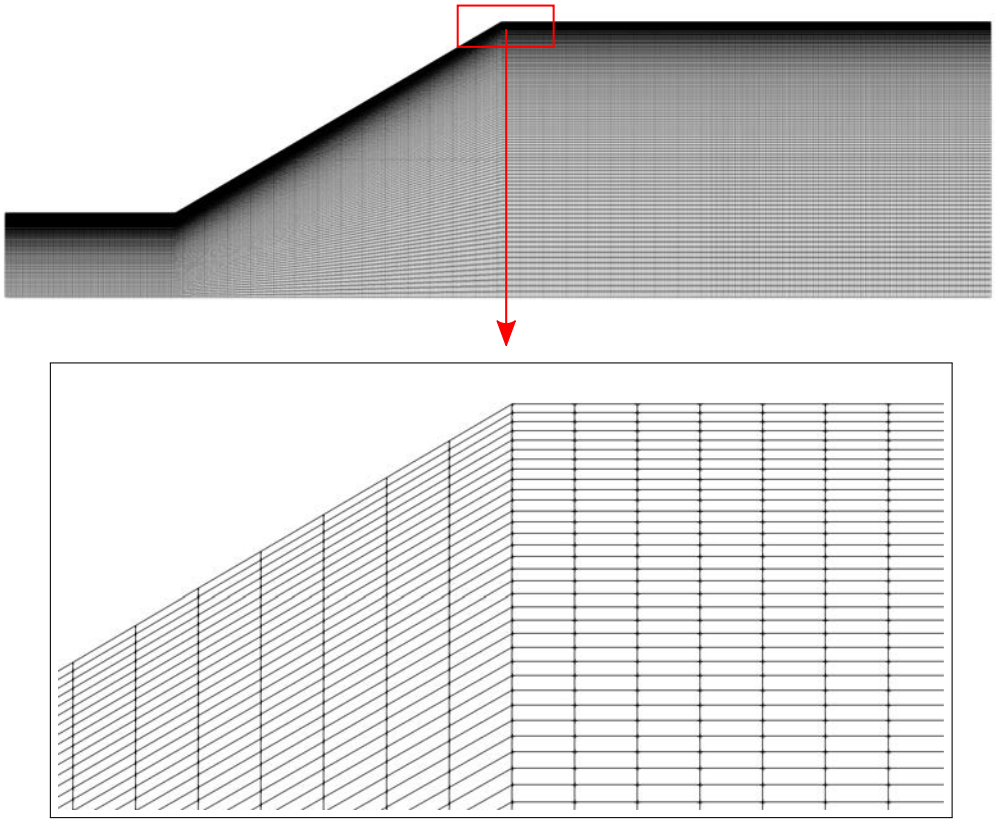

Figure 7.6: Computational grid for the planar diffuser configuration

In the canonical cases tested previously, convergence of the computations is assumed when the residuals for all variables dropped below 10^{-5}. However, this condition cannot be achieved in this case. The modelling of the porous medium as an extra sink term in the momentum equation results in higher residuals for the pressure and mean velocity. An example is presented in Figure 7.7 for both models. Convergence is therefore monitored based on flattening of the residuals and negligible change to the flow field. The residuals for turbulent quantities can be observed to be still less than 10^{-3}.

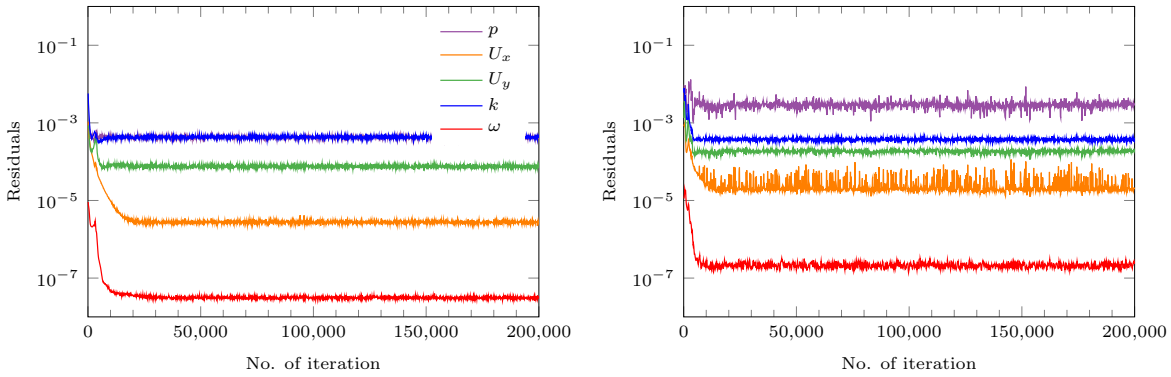

(a) $k-\omega$ **(b)** NL $k-\omega$

Figure 7.7: An example of the numerical residuals of the planar diffuser case

7.4 Results and discussion

The first part of this section discusses the approach used to model the monolith. Specifically, two turbulence treatment methods are applied for the porous region (the *damping* method which suppresses k at the monolith inlet and the *cyclic* method which preserves k) and the results are compared. After establishing a suitable approach, the performance of the turbulence models is subsequently discussed. The flow features in the domain and the velocity profiles in the diffuser are examined. The overall performance of the turbulence models is assessed using velocity profiles downstream of the monolith. This is followed by an analysis of the flow structures using pressure distribution. In addition to the mean flow predictions, the effects of adding the non-linear terms in the NL $k-\omega$ model are investigated further by looking at the predictions of turbulent kinetic energy and the Reynolds stress components.

It is observed, both in the experiments and in the computations, that the velocity profiles upstream of the monolith show limited variations between the 27-mm and 100-mm monolith cases. Since the monolith acts as a high resistance to the flow and longer flow resistance serves to redistribute the flow more uniformly, the maldistribution of velocity at the outlet is more pronounced in the 27-mm cases. Therefore, although all the parameters listed in Table 7.2 are considered, only the results for the 27-mm cases are discussed in detail since they provide a clear comparison for the predictions downstream of the monolith. It is also found that the trend of non-dimensional velocity profiles at all the sampled locations is comparable across all the Reynolds numbers tested. Therefore, only the results of one Reynolds number, $Re = 4.2 \times 10^4$, are analysed in detail here. The results for the remaining cases are presented in Appendix D and they served to show the generality of the turbulence model behaviour.

7.4.1 Evaluation of porous medium modelling

Two porous medium modelling approaches are applied, namely the *damping* and *cyclic* methods. While both methods model the porous medium as a sink term in the momentum equation, the *damping* approach limits the production of turbulent kinetic energy by setting k to be equal to zero at the

entrance of the monolith and the *cyclic* approach continues to solve the standard model equations for all turbulence quantities within the porous medium. The reader is referred to Section 7.2 for more details on the porous medium modelling methodology. To investigate the effects of the two approaches, flow predictions downstream of the monolith are observed.

Attention is paid to the axial velocity profile at 40 mm downstream of the monolith (location (D) in Figure 7.4). The results for both models are presented in Figure 7.8. It is immediately noticeable that preserving k by using the *cyclic* approach at the monolith inlet results in a flatter velocity profile at this location for both models when compared to the experimental values. The NL $k-\omega$ still returns a prediction of maldistribution, which is signified by the drop of velocity at approximately $y/h = 0.7$ and the first and secondary peaks near the symmetry plane and the wall, respectively. These features match the trend shown by the experimental data. The $k-\omega$ model completely misses all these features with the *cyclic* approach. The suppression of k using the *damping* approach is found to influence the flow distribution here and both models are able to reproduce the maldistribution of the flow. The models are able to capture the minimum and maxima found in the experimental velocity profiles. The difference can be observed throughout the channel for the $k-\omega$ model while for the NL $k-\omega$ model, it improves the prediction in approximately the top half, $y/h > 0.5$.

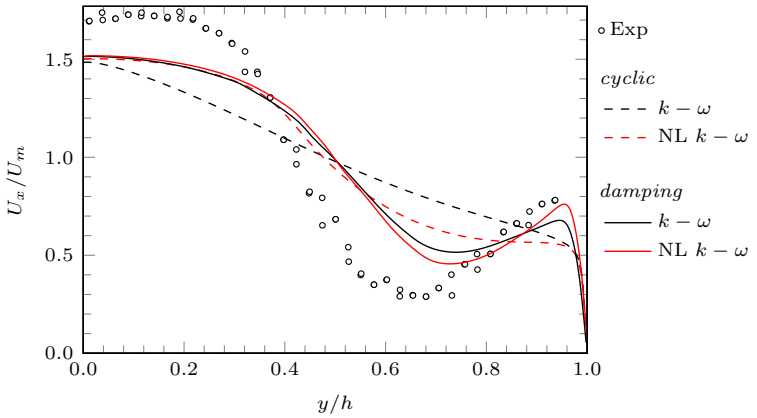

Figure 7.8: Axial velocity profile 40 mm downstream of monolith using two different porous medium modelling approaches. Markers correspond to experimental data [168].

To quantify the difference of the predictions, a non-uniformity index, ξ, is calculated. The results are presented in Table 7.4 and Table 7.5 for the $k-\omega$ and NL $k-\omega$, respectively. Equation (7.5) is used to calculate this index based on the velocity profiles at 40 mm downstream of the monolith. The non-uniformity index is calculated for all case configurations (refer to Table 7.2 for the case parameters). The percentages of difference shown in Table 7.4 and Table 7.5 are calculated against the experimental values. The results show that the *damping* method for k at the monolith inlet results in higher non-uniformity index for all the cases, with the exception of the 100-mm monolith length case at Re $= 2.2 \times 10^4$ by the NL $k-\omega$ where the non-uniformity index shows almost no change. Apart from that case, this translates to closer predictions to the experimental values by the *damping* method. A more

pronounced difference is exhibited by the $k-\omega$ model in general. For the case that is discussed in this chapter, which is the 27-mm monolith at $Re = 4.2 \times 10^4$, using the $k-\omega$ model with the *damping* approach results in a 20.5% more accurate non-uniformity index compared to the *cyclic*, while this figure is only 4.8% for the NL $k-\omega$.

Table 7.4: Non-uniformity index for planar diffuser cases using $k-\omega$ model

Monolith length [mm]	*Re*	Exp [168]	*cyclic*	% Diff	*damping*	%Diff
27	2.2×10^4	0.3468	0.1521	56.1	0.2328	32.9
	3.0×10^4	0.4622	0.1994	56.9	0.2926	36.7
	4.2×10^4	0.5239	0.2651	49.4	0.3723	28.9
	6.0×10^4	0.5830	0.3498	40.0	0.4757	18.4
100	2.2×10^4	0.1142	0.1139	0.3	0.1412	23.6
	3.0×10^4	0.1763	0.1389	21.2	0.1686	4.4
	4.2×10^4	0.2386	0.1677	29.7	0.2003	16.1
	6.0×10^4	0.3096	0.1991	35.7	0.2346	24.2

Table 7.5: Non-uniformity index for planar diffuser cases using NL $k-\omega$ model

Monolith length [mm]	*Re*	Exp [168]	*cyclic*	% Diff	*damping*	%Diff
27	2.2×10^4	0.3468	0.2331	32.8	0.2451	29.3
	3.0×10^4	0.4622	0.2894	37.4	0.3069	33.6
	4.2×10^4	0.5239	0.3630	30.7	0.3882	25.9
	6.0×10^4	0.5830	0.4546	22.0	0.4916	15.7
100	2.2×10^4	0.1142	0.1490	30.5	0.1480	29.6
	3.0×10^4	0.1763	0.1759	0.2	0.1762	0.1
	4.2×10^4	0.2386	0.2069	13.3	0.2078	12.9
	6.0×10^4	0.3096	0.2404	22.4	0.2425	21.6

To investigate how the two porous medium treatments result in these mean flow predictions downstream of the monolith, specifically how the *damping* approach results in a higher level of maldistribution and closer predictions to the experimental data, attention is paid to the predictions of turbulent kinetic energy. This is shown in Figure 7.9.

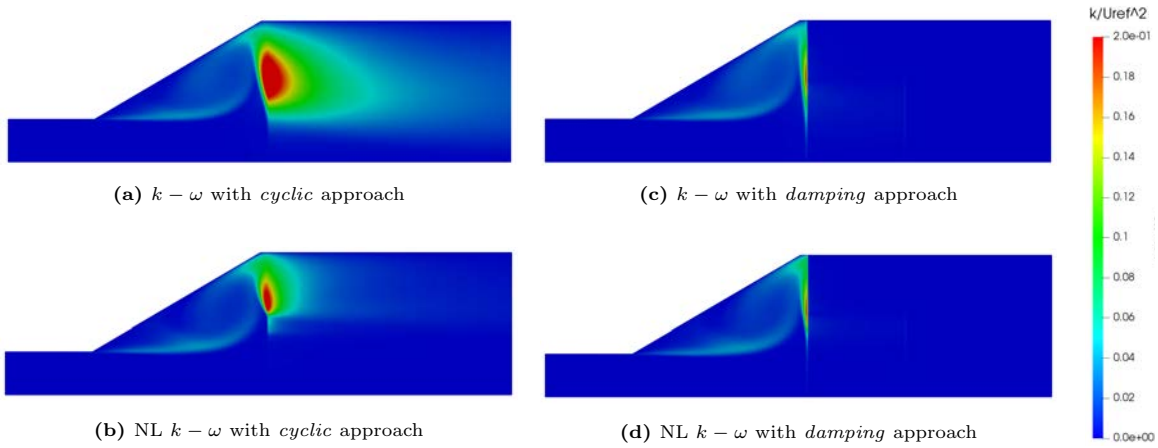

(a) $k-\omega$ with *cyclic* approach

(c) $k-\omega$ with *damping* approach

(b) NL $k-\omega$ with *cyclic* approach

(d) NL $k-\omega$ with *damping* approach

Figure 7.9: Turbulent kinetic energy field predicted using two different turbulence treatments for the modelling of the porous medium

The marked effects of the two approaches on the distribution of k throughout the domain can be observed in Figure 7.9. k is made dimensionless here using U_∞, as listed in Table 7.1. To ensure that the methods have the same effects across all turbulence models, the results predicted using both NL $k-\omega$ and $k-\omega$ models are presented. With the *cyclic* approach, which preserves k at the monolith inlet, the predicted k by the standard $k-\omega$ model (Figure 7.9 (a)) is considerably more extensive downstream of the diffuser than the prediction by the NL $k-\omega$ model using the same treatment (Figure 7.9 (b)). The $k-\omega$ model predicts comparatively higher values of k through the length of the monolith and extending into the outer sleeve. In contrast, the NL $k-\omega$ prediction is limited to approximately the first half portion of the resistance (monolith). The effect of suppressing turbulent kinetic energy at the porous medium inlet is directly observable on both models, seen as an absence (or very low levels) of k in the monolith in Figures 7.9 (c) and (d) and downstream.

The effect of this turbulence suppression on the prediction of k upstream of the porous region is also observed. This is shown in Figure 7.10. The profiles at three locations are observed, which correspond to the sampling stations 10.13 mm, 5.55 mm, and 2.5 mm upstream from the start of the porous region (locations (A), (B), and (C) in Figure 7.4, respectively). The turbulent kinetic energy is made dimensionless here using U_m, which is the mean velocity across the sampling station at each respective location. It can be observed that the *damping* treatment causes k in the diffuser to be lower at all locations. These observations are consistent on both models. As expected, the difference is more pronounced closer to the monolith at 2.5 mm upstream. Here, the $k-\omega$ model predicts a higher level of k compared to the NL $k-\omega$ when k is preserved (using the *cyclic* method) and when the *damping* method is used, the two models reach a similar level.

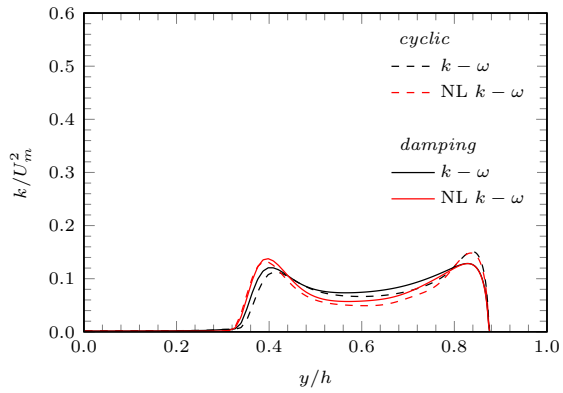

(a) 10.13 mm upstream

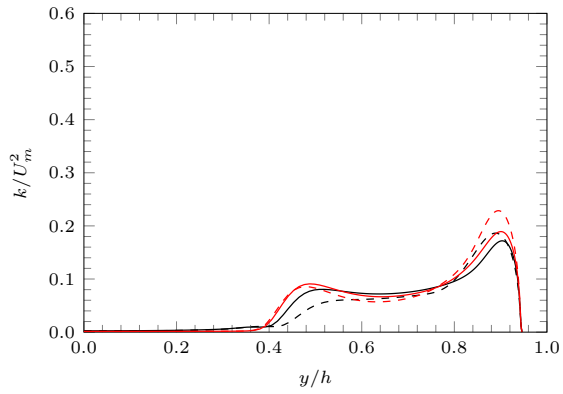

(b) 5.55 mm upstream

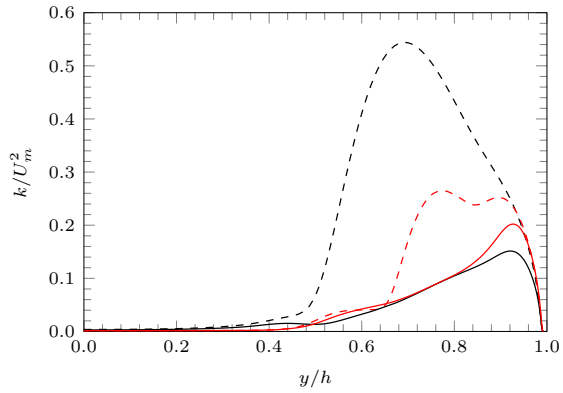

(c) 2.5 mm upstream

Figure 7.10: Turbulent kinetic energy at several stations upstream of monolith using two different porous medium modelling approaches.

Based on these observations, it can be concluded that the suppression of k at the monolith inlet using the *damping* approach returns a lower level of turbulent kinetic energy prediction both upstream and downstream of the porous region. This results in excessive prediction of turbulence level being avoided, which translates to a lower level of mean momentum loss to turbulence. This results in the maldistribution of flow downstream of the monolith being preserved, correctly returning the trend

shown by the experimental data.

Observation of the axial velocity prediction 40 mm downstream of the monolith (Figure 7.8) shows that this improvement is more pronounced in the top half of the channel, which is directly related to how the bulk of the turbulent kinetic energy is located in this region when the flow enters the monolith (as shown in Figures 7.9 and 7.10). This is as expected since this is the region where the effects of separation due to the expansion of the diffuser can be considered to be more significant. A closer look at the different flow features throughout the diffuser is presented in the next section.

The approach to damp turbulent kinetic energy at the inlet of the monolith is consistent with the assumption that the geometric scale of each channel in the monolith is very small such that it filters out the turbulent eddies with large length scales and causes the flow to stay laminar in the channels. This is analogous to the effect of using a 'honeycomb' in experiments to reduce turbulence intensity. The results of the evaluation presented in this section suggest that this assumption is justified, which results in the *damping* approach returning more accurate predictions of the flow field downstream of the monolith. Therefore, this is considered a more suitable approach for modelling the monolith and it is used as the porous modelling method for the rest of the results presented in this chapter.

7.4.2 Mean flow predictions

As an approach for modelling the monolith that results in more accurate flow predictions has been established, the performance of the turbulence models is now discussed. To discuss the flow features throughout the domain, the velocity field is presented in Figure 7.11. As the flow enters the diffuser from the inlet channel, it separates from the diffuser wall. This is a well-known feature in diffuser flows which is a result of the adverse pressure gradient created by the decelerating flow as it enters the expanded section. This separation results in a jet forming in the central region of the diffuser. This can be observed in the axial velocity profiles across three locations in the diffuser (presented in Figure 7.12 (left)) where the axial velocities are comparably high within $y/h < 0.4$. The NL $k-\omega$ shows some improvement in this prediction compared to the $k-\omega$ while the v^2-f model shows the closest predictions to experimental data here. Looking at the velocity field, the jet can be seen to subsequently spread as it crosses the diffuser, indicating a considerable prediction of entrainment. This is also shown by increased transverse velocities (presented in Figure 7.12 (right)) from 10.13 mm to 5.55 mm, with the highest being at 2.5 mm upstream of the monolith. The NL $k-\omega$ and $k-\omega$ models overpredict the transverse velocities at the two locations closer to the monolith, with comparable prediction returned by the v^2-f model at 2.5 mm. The NL $k-\omega$ model shows lower predictions at 10.13 mm and 5.55 mm, closer to the experimental values. The v^2-f model shows some advantages in these two locations. Since the porous medium acts as a resistance to the flow, there is an increase in pressure near the monolith 'wall'. Similar to an impinging jet, this results in the jet spreading radially. Some of the flow subsequently recirculates within the diffuser and a portion enter through the monolith at the top.

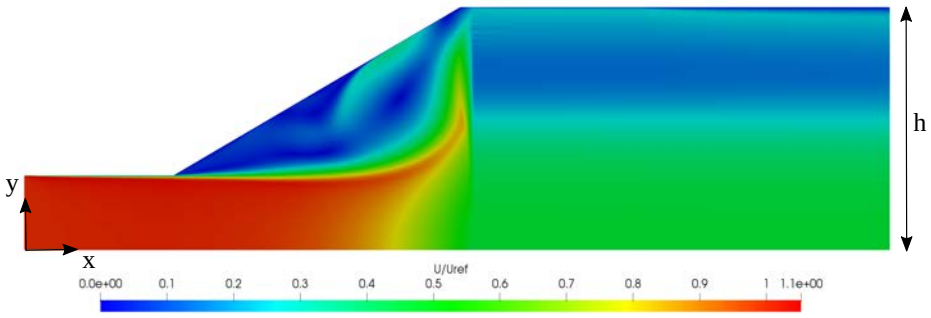

Figure 7.11: Typical velocity field of the planar diffuser configuration

As the flow enters the monolith, it is now predominantly moving in the x-direction due to the geometry of the monolith channels (refer to Section 7.3.1 for the experimental details and Section 7.2 for the modelling details). Within the monolith, in the top half region ($y/h \gtrsim 0.5$) the flow velocity is comparatively lower than the bottom half region where the main jet penetrates the monolith. This reduction in velocity is linked to the change of direction of the main jet as it spreads radially due to the pressure build up near the impingement region. The reduction is further influenced by an increase in turbulence levels near the entrance to the monolith which results in a loss of momentum. This leads to a maldistribution of the flow throughout the monolith. As the flow exits the monolith, a boundary layer also grows along the sleeve wall. When these effects are combined, they result in the development of a unique velocity profile at the outlet sleeve. Therefore, it can be argued that this velocity profile is a suitable feature to assess the ability of a new turbulence model to capture the key features that dominate the flow.

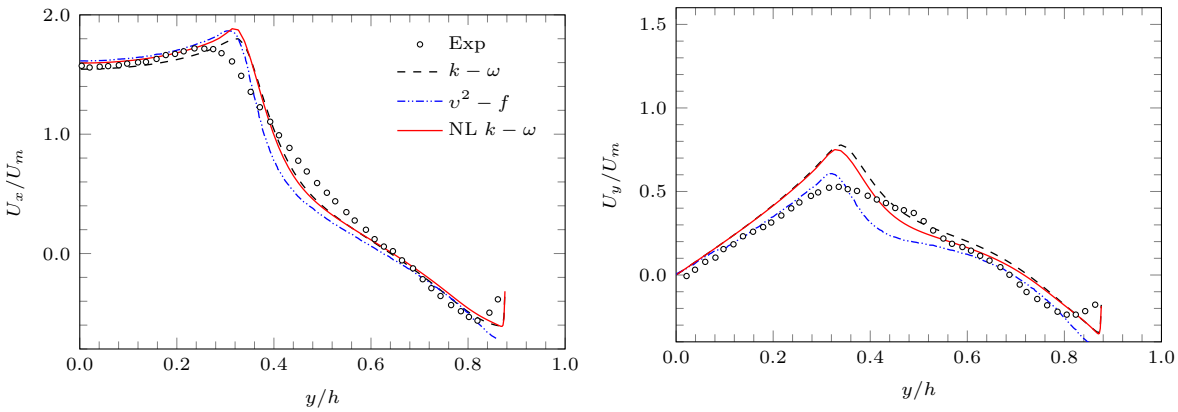

(a) 10.13 mm upstream

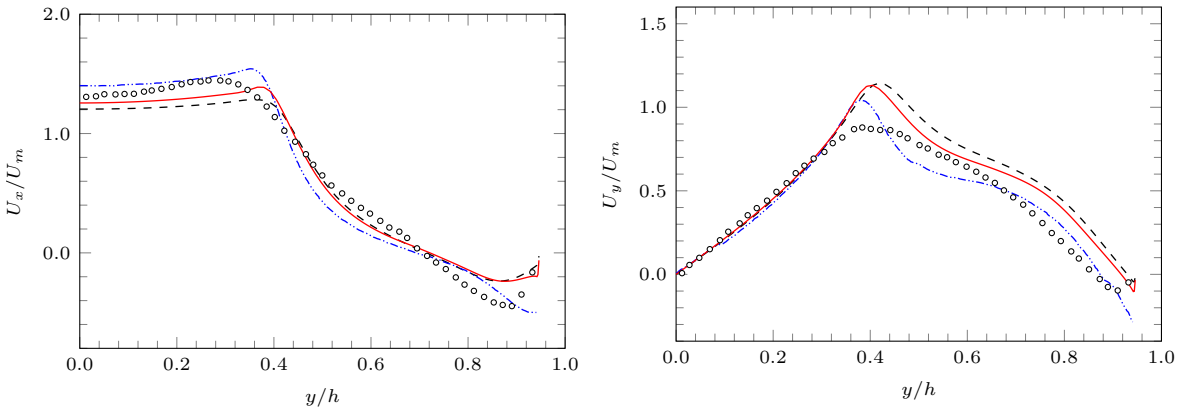

(b) 5.55 mm upstream

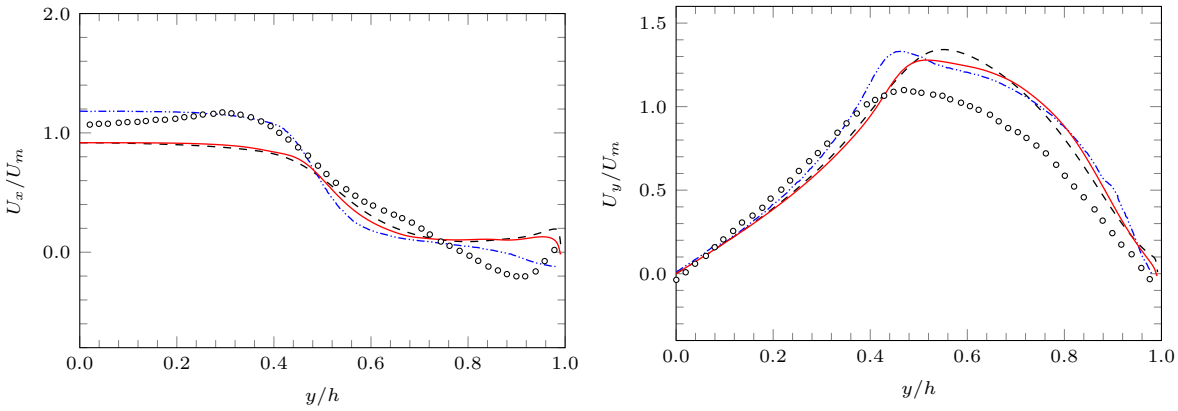

(c) 2.5 mm upstream

Figure 7.12: Axial (left) and transverse (right) velocity profiles at several stations upstream of monolith. Markers correspond to experimental data [168].

The velocity profiles in the outlet sleeve (40 mm downstream from the monolith) are shown in Figure 7.13. All the tested turbulence models show similar predictions in the peak velocity near the symmetry plane ($y/h = 0$). However, the NL $k-\omega$ model shows an improvement compared to the $k-\omega$ and the v^2-f models in the predicted maldistribution for $y/h > 0.5$. Particular improvements can be observed on the prediction of the axial velocity minimum (located around $y/h = 0.7$) compared to the

standard $k-\omega$ model and the secondary peak near the wall (located around $y/h = 0.95$) compared to both the $k-\omega$ model and the v^2-f model. Particularly, the NL $k-\omega$ predicts the velocity minimum 20.5% more accurately than the $k-\omega$ model and the secondary peak 10.6% more accurately than the two tested linear models which give similar predictions.

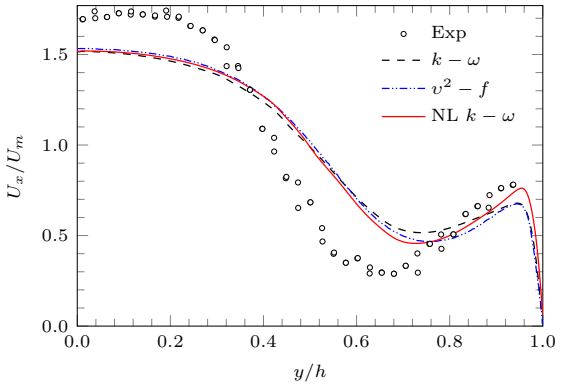

Figure 7.13: Axial velocity profile 40 mm downstream of monolith. Markers correspond to experimental data [168].

The flow maldistribution can be quantified using the non-uniformity index, ξ, using equation (7.5). For the results shown in Figure 7.13, the non-uniformity index calculated from the NL $k-\omega$ prediction is 0.3882, while the values calculated from the $k-\omega$ and v^2-f predictions are 0.3723 and 0.3768, respectively. The experimental value is 0.5239. This translate to the NL $k-\omega$ model showing around 2–3% more accurate prediction on this maldistribution index compared to the two tested linear models. The results of the computations performed in this work for the cases with the longer monolith length and the other Reynolds numbers are presented in Appendix D. Note that the computations are performed only using the NL $k-\omega$ and $k-\omega$ models. The non-uniformity indices calculated from these results are summarised in Table 7.6.

Table 7.6: Non-uniformity index for planar diffuser cases using $k-\omega$ model

Monolith length [mm]	Re	Exp [168]	$k-\omega$	% Diff	NL $k-\omega$	%Diff
27	2.2×10^4	0.3468	0.2328	32.9	0.2451	29.3
	3.0×10^4	0.4622	0.2926	36.7	0.3069	33.6
	4.2×10^4	0.5239	0.3723	28.9	0.3882	25.9
	6.0×10^4	0.5830	0.4757	18.4	0.4916	15.7
100	2.2×10^4	0.1142	0.1412	23.6	0.1480	29.6
	3.0×10^4	0.1763	0.1686	4.4	0.1762	0.1
	4.2×10^4	0.2386	0.2003	16.1	0.2078	12.9
	6.0×10^4	0.3096	0.2346	24.2	0.2425	21.6

The percentages of difference in Table 7.6 are calculated against the experimental values. It can be observed that the two models correctly reproduce the trend of non-uniformity index, increasing with Reynolds number and decreasing with monolith length. This is consistent with studies for axisymmetric

planar diffuser configurations [165,168,169]. The NL $k-\omega$ shows around 3–4% more accurate prediction on this maldistribution index on all cases with the exception of one (where the experimental data shows the lowest value of ξ and the models overpredict). The close predictions by the two models may be attributed to some of the deficiencies of using the porous medium modelling. For example, since the flow approaches the monolith obliquely (due to the aforementioned features in the diffuser), in reality there are additional losses associated with separation at the surface of the channels that result in a more pronounced maldistribution than the porous medium modelling predicts, as expected [165, 168, 169, 182].

Nevertheless, the NL $k-\omega$ returns more accurate flow maldistribution levels compared to the $k-\omega$ model. Particularly, this can be observed in the case that is discussed in details in this chapter which is the 27-mm monolith length at $Re = 4.2 \times 10^4$, in which the axial velocity is predicted more accurately near the wall. This is shown earlier in Figure 7.13. To analyse the predicted flow features that contribute to this prediction, pressure contour plots are used. These are presented in Figure 7.14. Since the predictions of axial velocity (Figure 7.13) near the wall, around $y/h > 0.9$, by the $k-\omega$ model and the $\upsilon^2 - f$ model closely match, the comparison on the pressure distribution predictions is discussed only for the NL $k-\omega$ and the $k-\omega$ models. In addition, this allows a closer analysis into the effects of the non-linear Reynolds stress formulation in particular.

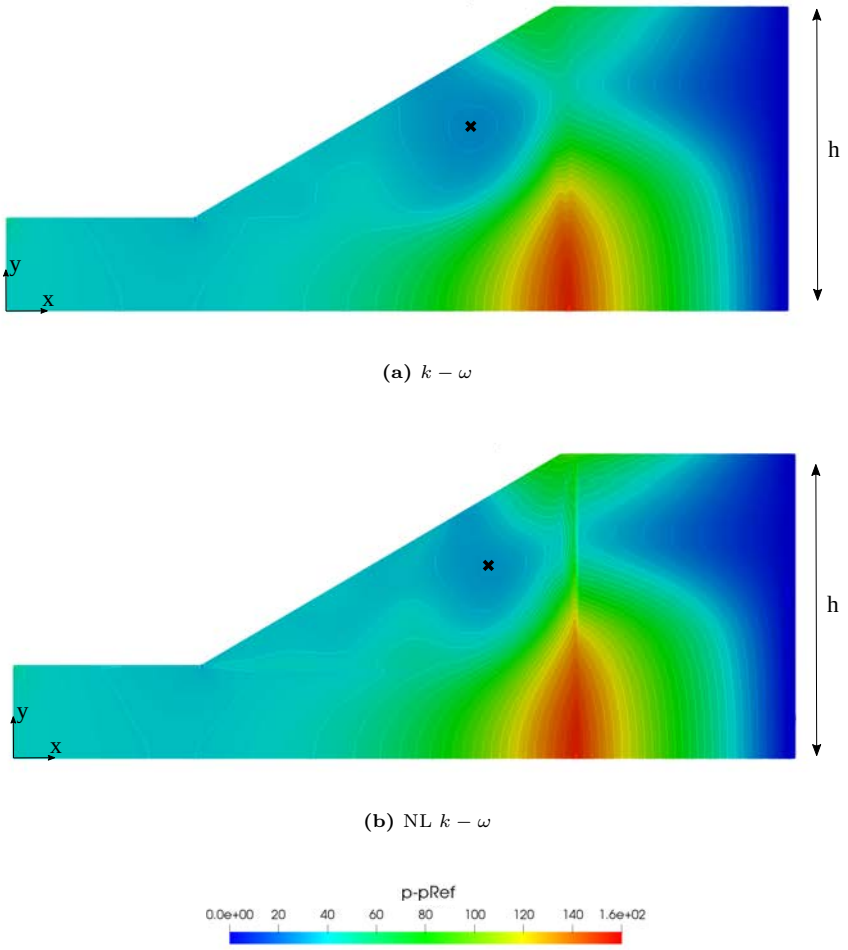

(a) $k-\omega$

(b) NL $k-\omega$

Figure 7.14: Pressure contour plots for the planar diffuser case. Markers correspond to the centres of low pressure areas in the diffuser.

For clarity, the domain has been 'clipped' at $x = 100$ mm. While other identification methods for flow structures have been used in literature, namely using vorticity rate, Ω, the Q-criterion [183], or the λ_2-criterion [184]; in this case, the absence of a coherent structure in the separated region in the diffuser means the predicted flow features cannot be visualised clearly using definitions that are heavily based on rotations. Therefore, pressure contours are used. From Figure 7.14, it can be observed that a distinct area of low pressure in the diffuser (marked by the crosses), is predicted by both models, which is indicative of a large 'vortex' or a recirculation region. This area is predicted to be smaller by the NL $k-\omega$ compared to the $k-\omega$. More notably, the location of the centre of this recirculation region is closer to the wall radially ($y/h = 0.69$ compared to the location predicted by the $k-\omega$ model which is $y/h = 0.61$). The axial location is also closer to the monolith entrance (11 mm upstream compared to the $k-\omega$ at 13.5 mm upstream). This means the radial spreading of the jet due to the monolith resistance occurs further downstream for the NL $k-\omega$ model. Additionally, as this transverse flow approaches the wall at the top, the increase in pressure associated with the stagnation can also be observed to be located higher, closer to the wall. This implies that more flow is pushed into the

monolith at the top compared to the $k-\omega$ which predicts more of the flow to recirculate instead. The higher axial velocity near the wall downstream of the monolith shown in the NL $k-\omega$ prediction (Figure 7.13) can be attributed to this behaviour. To analyse how the turbulence models predict these features, attention is now paid to the turbulent quantities.

7.4.3 Turbulent kinetic energy and Reynolds stresses distribution

Turbulent kinetic energy predictions across the three sampling locations within the diffuser are examined. Figure 7.15 shows that within the main jet ($y/h < 0.4$), the level of turbulent kinetic energy predicted by the $k-\omega$ model is higher compared to the NL $k-\omega$ model, especially as the flow gets closer to the monolith. This implies a lower momentum loss by the NL $k-\omega$ model around the jet region, leading to higher axial velocities here, as shown in Figure 7.12 (left). Closer to the porous region, at 2.5 mm upstream, the peak turbulent kinetic energy, which is located near the wall (around $y/h = 0.95$), is predicted at about one third higher by the NL $k-\omega$ model compared to the $k-\omega$ model. This is an interesting observation since a higher peak in axial velocity near the wall is returned by the NL $k-\omega$ model at the outlet, as shown earlier in Figure 7.13. Again, higher turbulent kinetic energy indicates a higher loss of momentum from the mean flow to turbulence, which should result in a lower mean velocity prediction. However, this is not the case here. Further investigation is therefore needed. A more thorough analysis is performed by looking at the Reynolds stresses distribution.

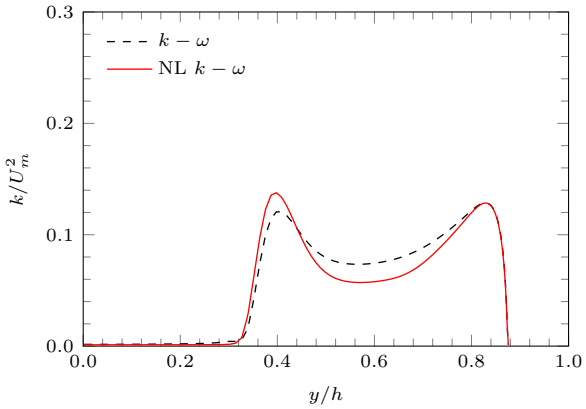

(a) 10.13 mm upstream

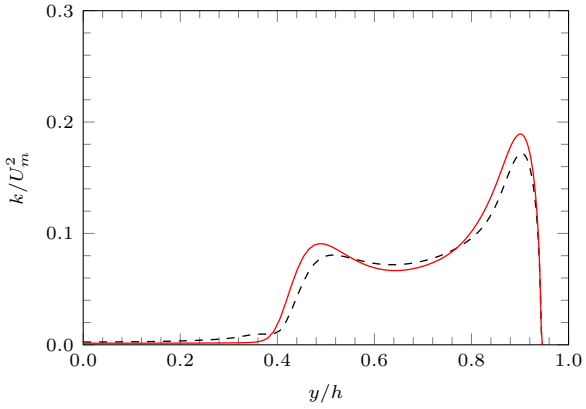

(b) 5.55 mm upstream

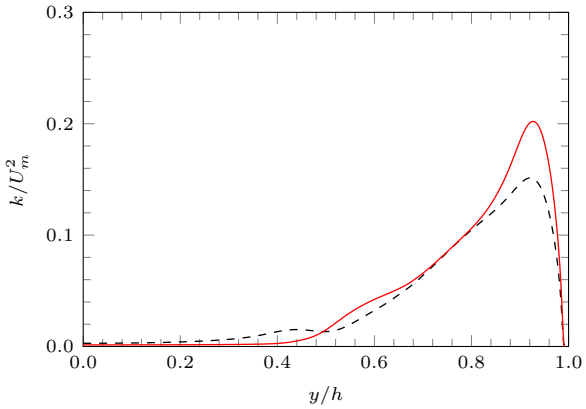

(c) 2.5 mm upstream

Figure 7.15: Turbulent kinetic energy at several stations upstream of monolith predicted using the NL $k-\omega$ model compared against $k-\omega$ predictions.

The prediction of velocity fluctuations in the x-direction, $\overline{u'u'}$, is examined first. The $k-\omega$ model shows a high level of $\overline{u'u'}$ at the entrance of the monolith with a spread down towards the symmetry plane, as shown in Figure 7.16 (a). The NL $k-\omega$ model shows a more limited extent of the $\overline{u'u'}$ distribution and returns a lower prediction overall, as shown in Figure 7.16 (b). Since Reynolds stresses indicate momentum loss, the $\overline{u'u'}$ component predicted by the $k-\omega$ model which extends almost all the way across the height of the diffuser can be suggested to result in the flatter axial velocity profile downstream

(as shown in Figure 7.13). This, however, does not explicitly explain the higher axial velocity peak shown by the NL $k-\omega$ model downstream.

As shown earlier, experimental data shows that transverse velocity increases as the flow spreads radially approaching the monolith. Observation of the flow structures (based on the pressure distribution in Figure 7.14) suggest that this spreading can contribute to the more accurate prediction of the secondary velocity peak near the wall downstream. Therefore, velocity fluctuations in the y-direction, $\overline{v'v'}$, are now examined (Figures 7.16 (c) and (d)). Higher wall-normal fluctuations are returned by the NL $k-\omega$ model closer to the monolith compared to the $k-\omega$, particularly in the region at the top near the wall (the region highlighted in Figure 7.16). It can be suggested that these fluctuations affect the location of the centre of the recirculation region examined earlier (which is located further outward radially by the NL $k-\omega$), which consequently contribute to how the flow is distributed just upstream of the monolith.

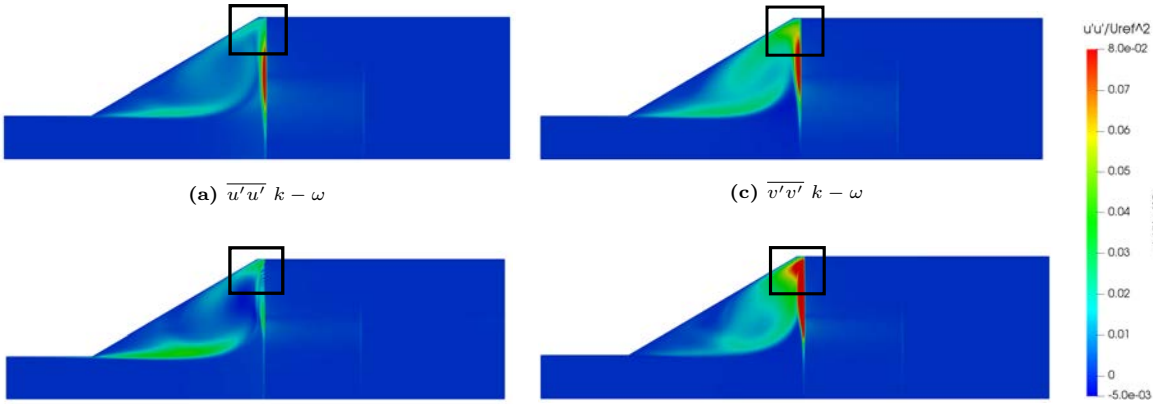

(a) $\overline{u'u'}$ $k-\omega$ **(c)** $\overline{v'v'}$ $k-\omega$

(b) $\overline{u'u'}$ NL $k-\omega$ **(d)** $\overline{v'v'}$ NL $k-\omega$

Figure 7.16: $\overline{u'u'}$ and $\overline{v'v'}$ components of the Reynolds stress tensor across the domain predicted using the NL $k-\omega$ and $k-\omega$ models.

This analysis shows the importance of anisotropy modelling in this case. The $k-\omega$ model can be seen to return similar pattern and level between the streamwise and wall-normal fluctuations while the NL $k-\omega$ limits the distribution of $\overline{u'u'}$ and returns a higher level of $\overline{v'v'}$. Although the level of turbulent kinetic energy predicted by the NL $k-\omega$ model close to the entrance of the monolith is higher than the level predicted by $k-\omega$, which intuitively could translate into a higher level of mixing and momentum loss, the distribution of the Reynolds stress components from the NL $k-\omega$ formulation could be considered to contribute to the more accurate results of the maldistribution of axial velocity downstream. We subsequently look into how the different terms in the NL $k-\omega$ formulation contribute to the Reynolds stresses distribution. Rewriting the equation for the non-linear formulation of the anisotropy tensor in the NL $k-\omega$ model (originally presented in equations (5.4) and (5.9)):

$$\overline{u_i' u_j'} = -2\nu_T S_{ij} + \frac{2}{3}k\delta_{ij} + \underbrace{C_\mu \beta_1 \left(S_{ik}S_{kj} - \frac{1}{3} II_S \delta_{ij} \right)}_{\boldsymbol{S}^2 \text{ term}} k + \underbrace{C_\mu \beta_2 \left(S_{ik}\Omega_{kj} - \Omega_{ik}S_{kj} \right)}_{\boldsymbol{S\Omega} \text{ term}} k \tag{7.6}$$

The first and second terms on the right hand side of the equation are the linear eddy-viscosity terms. The $\boldsymbol{S}^2$ and $\boldsymbol{S\Omega}$ terms are the non-linear terms which arise from the quadratic anisotropy formulation. The contribution of these non-linear terms to the Reynolds stresses in the diffuser is shown in Figure 7.17.

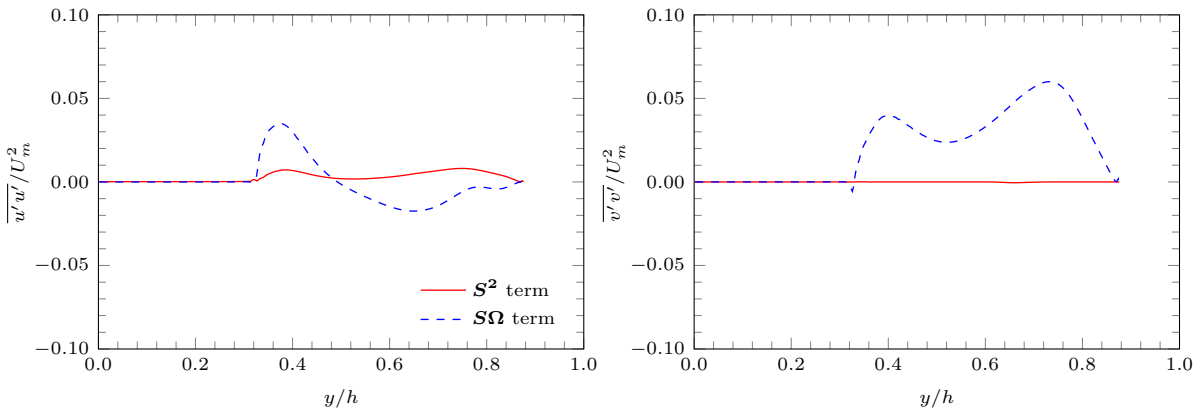

(a) 10.13 mm upstream

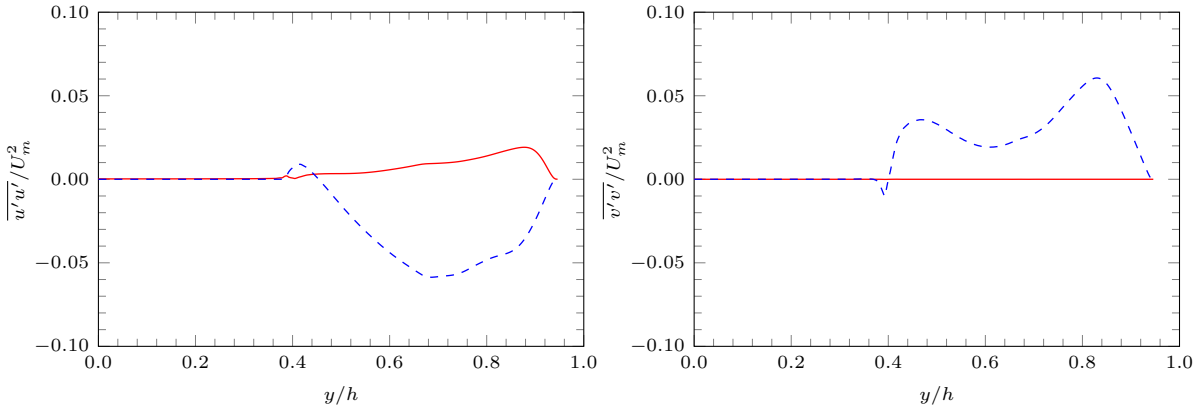

(b) 5.55 mm upstream

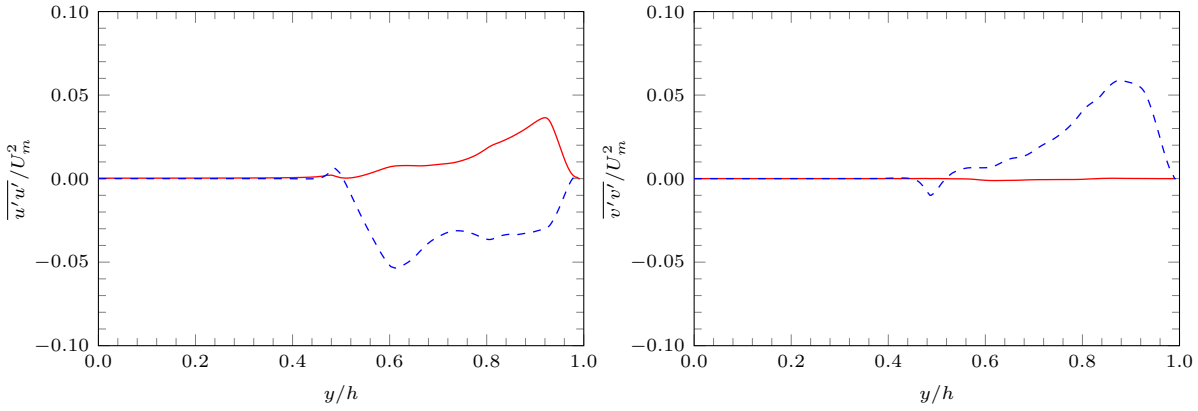

(c) 2.5 mm upstream

Figure 7.17: Non-linear terms contributions to Reynolds stresses at several stations upstream of monolith predicted using the NL $k-\omega$ model.

It is apparent that the $\boldsymbol{S\Omega}$ term is the dominating non-linear term. The lower prediction of $\overline{u'u'}$ component upstream of the monolith shown earlier in Figure 7.16 can be attributed to the negative $\boldsymbol{S\Omega}$ terms, shown in Figure 7.17 (left). Similarly, the positive $\boldsymbol{S\Omega}$ term contributes to the $\overline{v'v'}$ component (shown in Figure 7.17 (right)), while the $\boldsymbol{S}^2$ term returns negligible values here, indicating very low strain rate in this direction (as expected with the exception of very close to the monolith). This

highlights the importance of including the rotation rate tensor in the Reynolds stress formulation.

Figure 7.17 also shows that within $y/h < 0.4$, which corresponds to the location of the jet 'core', the Reynolds stress components from both non-linear terms are negligible. The same behaviour can be noted in the turbulent kinetic energy prediction in Figure 7.15. This can be attributed to the inherent problem of RANS modelling in general. The use of the stress-strain relation, which is the cornerstone of RANS, can result in an insufficient level of Reynolds stress predictions in areas of very low or no shearing, such as a jet core. In other areas where this is not the case, the NL $k-\omega$ can be concluded to show Reynolds stresses predictions that result in more accurate flow field predictions.

7.5 Computational expense

The computations for the planar diffuser cases presented in this chapter are completed using HPC nodes consisting of Intel® Xeon® Nehalem L5530 CPUs with a base frequency of 2.40 GHz, in which each of the processor has an associated 4.0 Gb of RAM. Table 7.7 and Table 7.8 show the number of CPU cores that are used for the computation of each case and the respective running times. This includes all the planar diffuser cases considered in this work, which includes a number of varying parameters as summarised in Table 7.2. Note that the comparison on the running times is only provided for the computations completed within this work, which include only the NL $k-\omega$ and the $k-\omega$ turbulence models and it serves to provide an information on the change in computational expense associated with the proposed modelling approach. Since the computations are completed in a computer cluster, the running time comparison presented here serves as a general estimation as computation time could change based on processor properties as well as node allocation.

Table 7.7: Comparison of computational expense for the planar diffuser cases using the *cyclic* approach for the porous medium

Monolith length [mm]	Re	CPU cores	Running time [s]		% Diff
			$k-\omega$	NL $k-\omega$	
27	2.2×10^4	16	35,006	7,698	-78.01
	3.0×10^4	16	22,305	10,884	-51.20
	4.2×10^4	16	27,902	10,704	-61.64
	6.0×10^4	16	18,786	10,602	-43.56
100	2.2×10^4	16	11,023	8,890	-19.35
	3.0×10^4	16	45,866	17,587	-61.66
	4.2×10^4	16	38,244	17,169	-55.11
	6.0×10^4	16	84,441	15,843	-81.24

Table 7.8: Comparison of computational expense for the planar diffuser cases using the *damping* approach for the porous medium

Monolith length [mm]	Re	CPU cores	Running time [s]		% Diff
			$k-\omega$	NL $k-\omega$	
27	2.2×10^4	16	9,013	11,514	27.75
	3.0×10^4	16	8,871	11,635	31.16
	4.2×10^4	16	8,950	11,123	24.28
	6.0×10^4	16	8,759	11,041	26.05
100	2.2×10^4	16	12,529	16,532	31.95
	3.0×10^4	16	12,394	17,126	38.18
	4.2×10^4	16	12,059	17,300	43.46
	6.0×10^4	16	12,116	17,363	43.31

It is interesting to see that there is a marked difference between the computation time associated with the two different approaches for modelling the porous medium. Using the *cyclic* approach (Table 7.7), the running times for the computations completed using the $k-\omega$ model are longer than the NL $k-\omega$ model. Specifically, the running times for the computations using the NL $k-\omega$ model are between 19–81% shorter. In contrast, for the cases that use the damping approach for the porous medium (Table 7.8), the computational times associated with the NL $k-\omega$ model are higher than the $k-\omega$ model. Specifically, the NL $k-\omega$ computations take around 24–43% longer to converged. However, it is worth noting that no numerical difficulties are encountered with the NL $k-\omega$ model compared to the $k-\omega$ model and as such there is no need for a change in the computational and numerical setup, e.g. a finer grid or an additional relaxation factor.

7.6 Summary

Computation results for flow in a diffuser with a downstream monolith have been presented and analysed in this chapter. The parameters considered include two monolith lengths and four Reynolds numbers. However, only one case is discussed in detail here, which is the 27-mm monolith at $Re = 4.2 \times 10^4$ case. The rest of the cases are presented in Appendix D. Two turbulence treatments are evaluated for the porous medium modelling. The predictions of the NL $k-\omega$ model are discussed in comparison with the predictions of the standard $k-\omega$ model. Results from [168, 169], in which the v^2-f model is used, have also been included for benchmarking purposes.

The following conclusions can be drawn from the results discussed:

- Suppression of turbulent kinetic energy at the entrance of the monolith is useful for avoiding excessive turbulence, and hence momentum loss, and preserving the velocity maldistribution that is shown in the experimental data.
- The NL $k-\omega$ model shows a more accurate prediction of velocity maldistribution downstream of the monolith compared to the $k-\omega$ model as well as compared to the results by [168, 169] obtained using the v^2-f model. Particular improvements are in 20.5% more accurate velocity

minimum compared to the $k-\omega$ model and 10.6% more accurate secondary peak near the wall compared to the $k-\omega$ and v^2-f models.

- Comparison of pressure distribution suggests that the more accurate prediction of the velocity peak near the wall downstream of the monolith by the NL $k-\omega$ is a consequence of the location of the predicted recirculation region in the diffuser by the model, which is closer to the wall and further downstream compared to the $k-\omega$ prediction.
- Results highlight an advantage of the NL $k-\omega$ model in predicting anisotropic Reynolds stress distribution which influence the location of the aforementioned recirculation region in the diffuser, contributing the more accurate prediction of the flow maldistribution downstream.
- The vorticity rate-containing term in the NL $k-\omega$ formulation is shown to be of particular importance in driving the anisotropic Reynolds stress predictions. This demonstrates the importance of its inclusion in the model for predicting flows that involve features such as recirculation.

Chapter 8

Application: swirling flow through a sudden expansion

8.1 Introduction

The final configuration to which the model is applied is a three-dimensional swirling flow configuration consisting of a swirl generator, an annular pipe, a sudden expansion diffuser, followed downstream by a monolith. The schematic is shown in Figure 8.1. This type of configuration can be used as a simplified setup of an automotive exhaust catalytic converter system with a swirling inlet. The diffuser and monolith represent part of the system that allow maximisation of surface area for the catalysis process to take place, in a similar way to the configuration considered in Chapter 7. However, in automotive applications, the major trend in the use of turbochargers in engines results in residual swirl from the turbines that subsequently enters the catalytic converter. These effects need to be considered in modelling the flow behaviour within the system. The swirl generator included in this configuration provides a swirling inlet and allows the study of the influence that residual swirling flow has on the catalyst system.

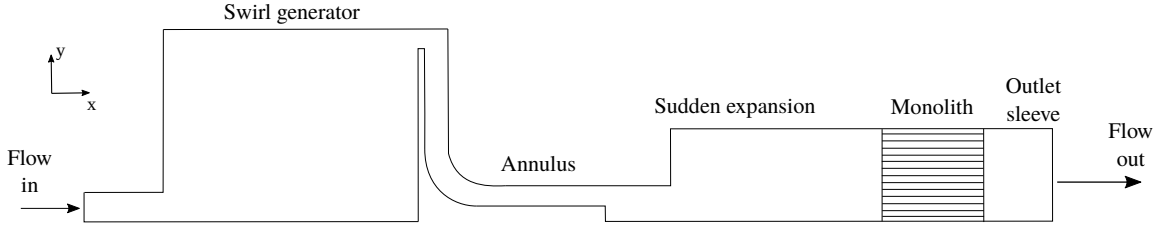

Figure 8.1: Side view geometry of the swirling flow configuration

While a diffuser-monolith configuration has been considered in Chapter 7, the diffuser considered in this case has a 90 deg diverging angle, i.e. a sudden expansion. More importantly, the inclusion of the swirl generator makes this configuration a suitable case for assessing the performance of a turbulence model on a three-dimensional application that involves rotational effects. In addition to the global flow features, there are three main aspects that are observed which correspond to the different parts of the configuration. The first is the velocity predictions within the annulus. This provides information on the swirling flow that exits the swirl generator and subsequently goes through the 90 deg bend before swirling around the annular cross-section. The second is the pressure distribution on the walls of the sudden expansion diffuser, which allows the analysis of the effects of the swirling flow on the separation and recirculation within the diffuser. Since the monolith is fitted at a distance of 162 mm into the sudden expansion, the flow features in the diffuser are able develop further than the configuration considered in Chapter 7 (where the monolith is fitted immediately at the end of the expansion). Finally, effects of the aforementioned flow features combined with the high resistance provided by the porous region are analysed by observing the flow field downstream of the monolith.

It is worth noting that the NL $k-\omega$ model is not explicitly sensitised or corrected for rotation (e.g. using frame indifference principles) since the focus of the model development is on improving predictions of near-wall anisotropy. However, it still of interest to analyse how the anisotropy of the model formulation, which takes into account the strain and rotation rates at a quadratic level, can be effective in improving the predictions of the swirling effects, particularly, how it affects flow features downstream.

8.2 Case description

8.2.1 Experimental details

The configuration considered here is based on the cases investigated experimentally at Coventry University by Rusli *et al.* [185, 186]. The schematic of the experimental assembly is shown in Figure 8.2. The parts marked as (1) and (2) represent the swirl generator. Air is supplied via the inlet, which then enters the plenum (1), before it is forced through a set of movable blocks that can be positioned to generate varying levels of swirl by adjusting the moveable plate (2). It then enters the nozzle (3) and an annular extension pipe (4). The annular extension is provided at the outlet of the swirl generator to facilitate the observation of the swirling flow from the generator. A sudden expansion diffuser (5) connects the swirl generator assembly to the monolith (6), followed by an outlet sleeve (7). Only one monolith length is tested which is 76 mm. Two mass flow rates are tested: 63 g/s and 100 g/s. The ceramic monolith used in the experiment has resistance properties of $D = 3.69 \times 10^7/\mathrm{m}^2$ and $F = 47.76/\mathrm{m}$.

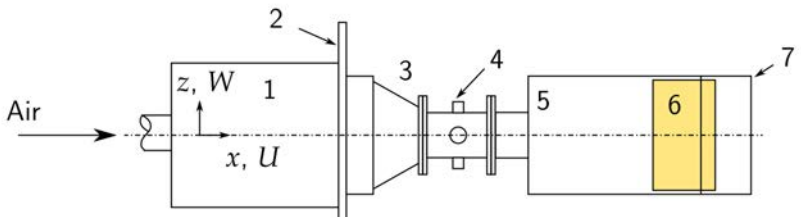

Figure 8.2: Diagram of experimental assembly for the swirling flow case [185].

Measurements of axial and tangential velocity components across the annulus (location (4) in Figure 8.2) are obtained using hot-wire anemometry (HWA) probes. Velocity profiles in the outlet sleeve (7) are measured using HWA as well, at a location 35 mm downstream of the end of the monolith. At this distance, the individual jets emerging from the monolith channels are found to have mixed sufficiently to provide a smooth profile [166, 187]. Pressure tappings are used along the diffuser wall (5) which allow the measurement of wall pressure distribution using water manometers. The reader is referred to [185, 186] for more details on the experimental data collection as it is not included here for succinctness.

The swirl generator is based on the moving-block principle [188]. It consists of a set of fixed and moving blocks which are positioned relative to each other to provide varying level of swirl. The swirl intensity is adjusted by changing the angle of the moveable plate, ζ, from 0 deg (no swirl) to its maximum relative angular displacement setting, ζ_m, which is 18 deg (maximum swirl). The number of vanes formed by these blocks, n, on this swirl generator is 8. These parameters are used to characterise the swirl generator and calculate the theoretical swirl level produced (presented later in Section 8.3.1).

8.2.2 Computational domain and boundary conditions

The swirling effect that is considered is reproduced in the experiments by using a swirl generator which produces a swirling inlet profile into the diffuser. In order to match the experiment, this is included in the modelling configuration. As mentioned above, the swirl generator consists of 8 identical blocks spread azimuthally. Therefore, a 45-deg wedge is used as the computational domain with periodic boundary conditions set on each side. An example of the domain is presented in Figure 8.3. The dimensions are shown in Figure 8.4. The sampling stations which are located at the (A) annulus, (B) sudden expansion walls, and (C) outlet sleeve downstream of the monolith are marked by the red dashed lines in Figure 8.4.

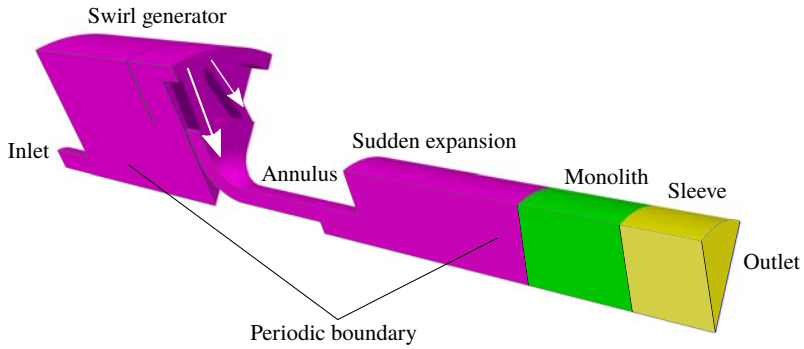

Figure 8.3: Computational domain for the swirling flow configuration

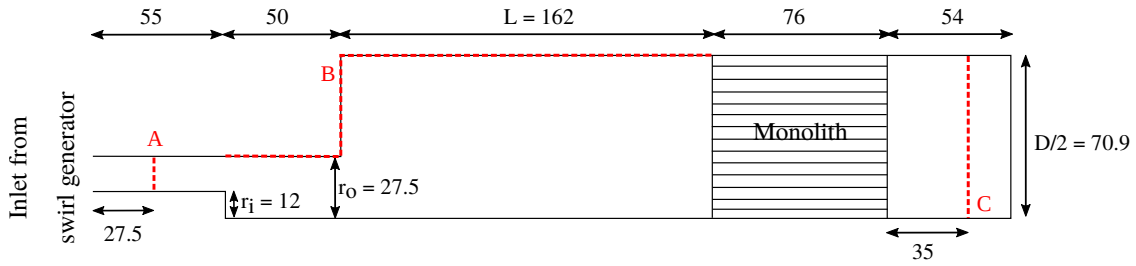

Figure 8.4: Side view of the computational domain for the swirling flow case. Dimensions are in mm.

A uniform velocity, $U_\infty = 45.34$ m/s (calculated from the mass flow rate of 63 g/s), is prescribed at the inlet. The kinematic viscosity is 1.5×10^{-5} m/s^2, which matches the condition of the experiments. For the turbulent quantities, k is calculated using freestream turbulence intensity, $Tu_\infty = 0.57\%$, and ω using eddy viscosity ratio, ν_R, of 1.3. using the relations shown in equation (7.3). For the walls and outlet, the same boundary conditions for the cases presented in Chapter 7 are used. The monolith is modelled using the porous medium approach with suppression of turbulent kinetic energy at the inlet of the monolith (the *damping* method) as this has been shown in Section 7.4.1 to result in a more accurate predictions of the maldistribution downstream of the porous region.

8.2.3 Summary of test cases

The parameters selected for the cases considered using this configuration are summarised in Table 8.1. To investigate the flow behaviours and model predictions at different swirl levels, three configurations are considered which correspond to three swirl generator angles: 0, 7, and 18 deg. The geometries are depicted in Figure 8.5. While the effects of Reynolds number on flow maldistribution in this type of configuration, i.e, a simplified catalytic converter geometry, is well-established [165, 189–191]; for the mass flow rates tested in the experiments, it is the swirl generator angles that predominantly shape the velocity profiles measured in the annulus [185]. Therefore, only one mass flow rate setting is considered.

The results obtained using the NL $k-\omega$ model are discussed in comparison with the original $k-\omega$ model. Similar to the planar diffuser cases presented in Chapter 7, the two tested non-linear $k-\varepsilon$ models that are used for comparison in the canonical cases in Chapter 6 are found to not be able to achieve convergence in the computations for the swirling flow configurations presented here. Therefore, for benchmarking purposes, another comparison is instead made against the performance of one other linear turbulence model. The computation results obtained at Coventry University by Rusli *et al.* [185] are included. The turbulence model used is the $k-\varepsilon\ v^2-f$ model by Durbin *et al.* [151]. Note that the results for the v^2-f model from [185] are included for the purpose of comparing the predictions of the mean flow and pressure coefficient distribution only. The analysis in regards to the turbulence structures are made in comparison with the standard $k-\omega$ model only.

Table 8.1: Summary of parameters for the swirling flow cases

$\dot{m}$ [g/s]	Swirl generator angles [deg]	Turbulence model
63	0	$k-\omega$
	7	v^2-f
	18	NL $k-\omega$

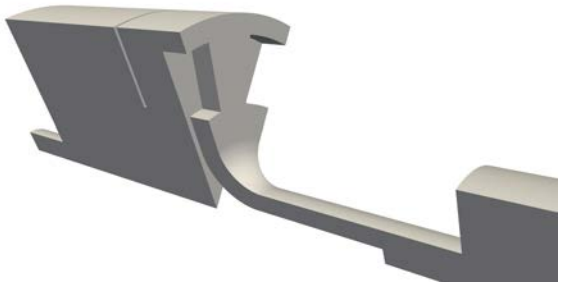

(a) Swirl generator angle = 0 deg

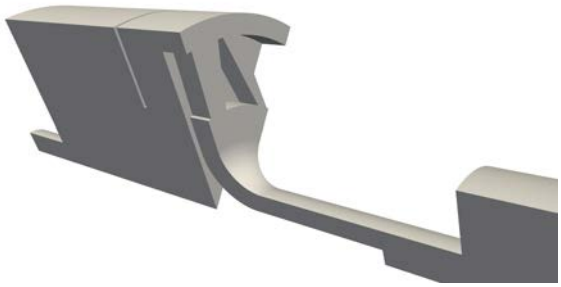

(b) Swirl generator angle = 7 deg

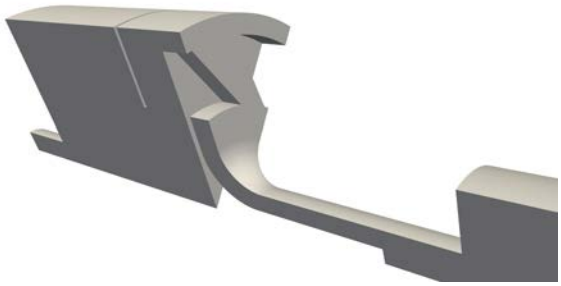

(c) Swirl generator angle = 18 deg

Figure 8.5: Geometry of the swirling flow rig configuration at several swirl generator angle settings

8.2.4 Meshing and convergence behaviour

A mesh independence study is conducted using four grids to ensure that the computational grid is sufficiently refined and well-distributed, which allows the capturing of the flow features (while still trying to minimise the computational effort). All the meshes considered are unstructured polyhedral grids. A prism layer is allocated perpendicular to the walls to ensure the capturing of the boundary layer and minimise the y^+ value. Four three-dimensional meshes are generated, namely very coarse, coarse, medium, and fine. The result of the independence study is presented here by considering the 7 deg swirl generator angle case, computed using the NL $k-\omega$ model. Predictions of axial and tangential velocity profiles in the annulus are compared, as well axial velocity profile at the sampling station 35 mm downstream of the monolith. They are presented in Figure 8.6 and Figure 8.7, respectively. The velocities non-dimensionalised using U_m, which is the mean velocity in the annulus as calculated from the mass flow rate. It is plotted against the radial distance, r, from centreline of the outlet sleeve

(bottom line on the domain), non-dimensionalised using the inner and outer radii of the annulus, r_o and r_i, respectively, and the diameter of the channel, D (refer to Figure 8.4).

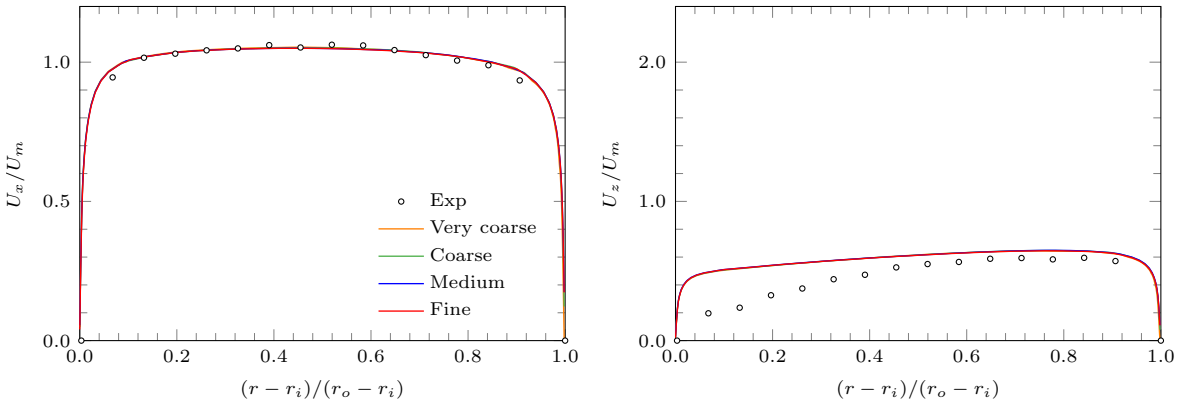

Figure 8.6: Mesh independence test: axial and tangential velocity profiles within the annulus for swirl generator angle = 7 deg. Markers correspond to experimental data [185].

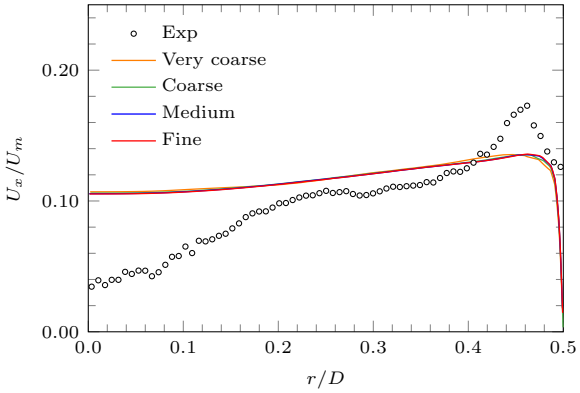

Figure 8.7: Mesh independence test: axial velocity profile 35 mm downstream of monolith for swirl generator angle = 7 deg. Markers correspond to experimental data [185].

It can be observed from Figure 8.6 and Figure 8.7 that the velocity profiles in the annulus and downstream of the monolith predicted by the different grids are in close agreement. Using the velocity profiles in Figure 8.6, the swirl number, S, is used to characterise the level of swirl predicted. It is calculated using equation (8.2), presented later in Section 8.3.1. The results are presented in Table 8.2. Notice the percentages of difference for S are benchmarked against the chosen grid, which is the medium mesh.

Table 8.2: Summary of grid independence test for the swirling flow cases

	Number of cells	S	% Diff S
Very coarse	1.2M	0.4464	0.6
Coarse	1.8M	0.4482	0.2
Medium	3.0M	0.4489	–
Fine	4.7M	0.4475	0.3

Based on the mesh independence test, the grid chosen for the computation is the medium grid. The total number of cells is 3.0 M. The grid used is illustrated in Figure 8.8. The mesh consists of polyhedral grid with a prism layer of 15 cells at the wall. The corresponding maximum y^+ is 3.62. The corresponding computational grids for the other swirl generator angle cases have between 2.7 to 3.0 M cells.

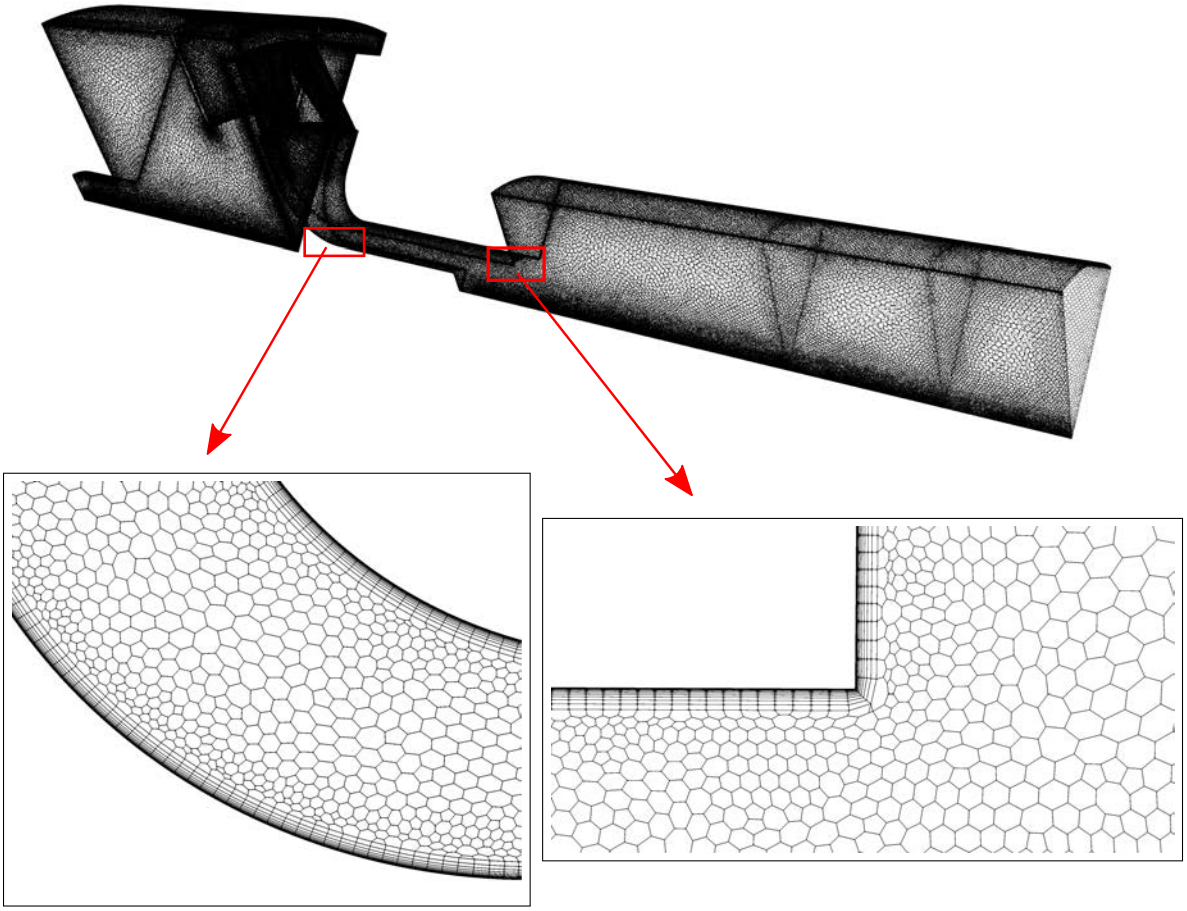

Figure 8.8: Computational grid of the swirling flow case

Similar to the planar diffuser cases in Chapter 7, the modelling of the porous medium as a sink term in the momentum equation results in higher residuals for the pressure and mean velocity compared to the canonical cases in Section 6.6. An example of the convergence behaviour is presented in Figure 8.9 for the highest swirl case. Convergence is monitored based the flattening of the residuals and negligible change to the flow field. It can be observed that all residuals drop to 10^{-3} and the residuals for turbulent quantities are less than 10^{-4}.

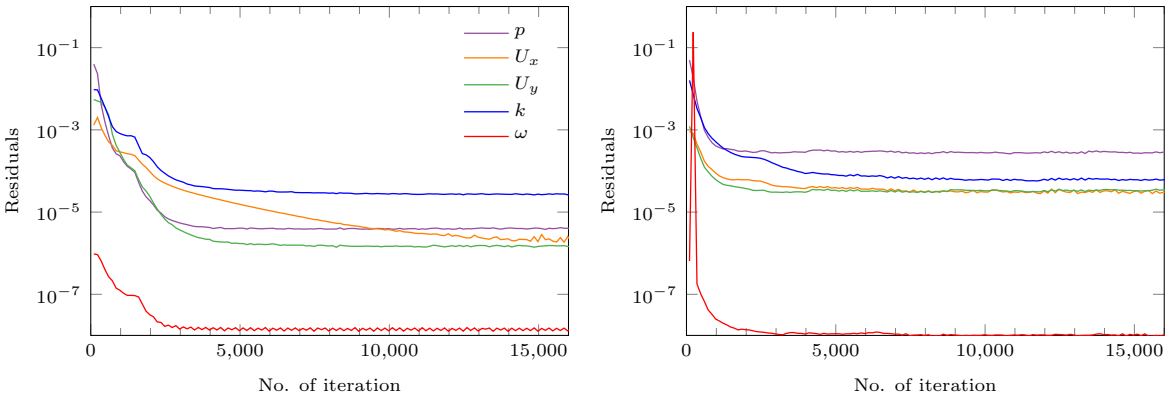

(a) $k-\omega$ **(b)** NL $k-\omega$

Figure 8.9: Numerical residuals for swirl generator angle = 18 deg of the swirling flow case

8.3 Results and discussion

To observe how the global features change with varying swirl levels, the velocity field predictions throughout the domain are presented first. The axial and tangential velocity profiles across the sampling station in the annular cross-section (location (A) in Figure 8.4) are presented as well since this characterises the swirling flow that the swirl generator produces and subsequently acts as an inlet to the diffuser. The effects of the swirling flow to the flow field in the sudden expansion are examined through the pressure distribution on the diffuser wall (location (B) in Figure 8.4). Pressure sampling is especially useful for analysing prediction of flow separation or reattachment. The flow structures within the diffuser are also investigated more closely. Finally, the velocity profiles downstream of the monolith (location (C) in Figure 8.4) are observed.

8.3.1 General flow features and swirling flow in annulus

The general flow behaviour in the domain can be observed through the velocity field prediction, presented in Figure 8.10 for all swirl generator angles. As the focus is on the effects of the swirling inlet, which is provided by the swirl generator, attention is paid to the flow field exiting the swirl generator and downstream. The velocities are presented in their normalised form, non-dimensionalised using the mean velocity in the annulus, U_m, which is calculated from the mass flow rate using:

$$\dot{m} = \rho\pi(r_o^2 - r_i^2)U_m \tag{8.1}$$

in which $\dot{m}$ = 63 g/s, ρ = 1.18 kg/m^3, r_o and r_i are as shown in Figure 8.4, which results in U_m = 27.76 m/s. The same characteristic velocity is used for the non-dimensionalisation of the velocity profiles presented in this chapter.

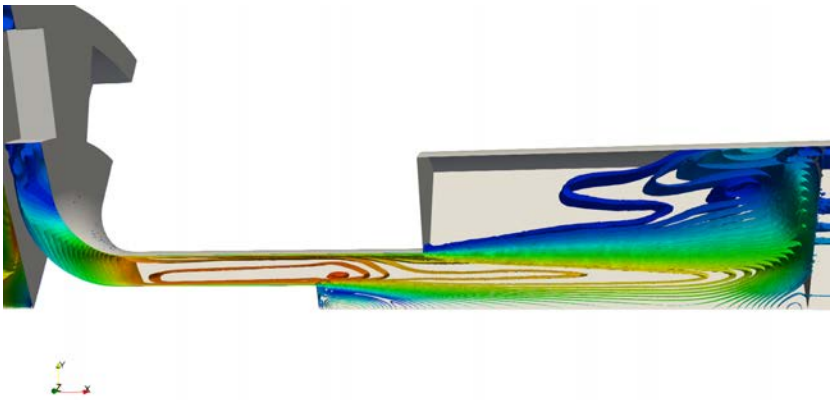

(a) Swirl generator angle = 0 deg

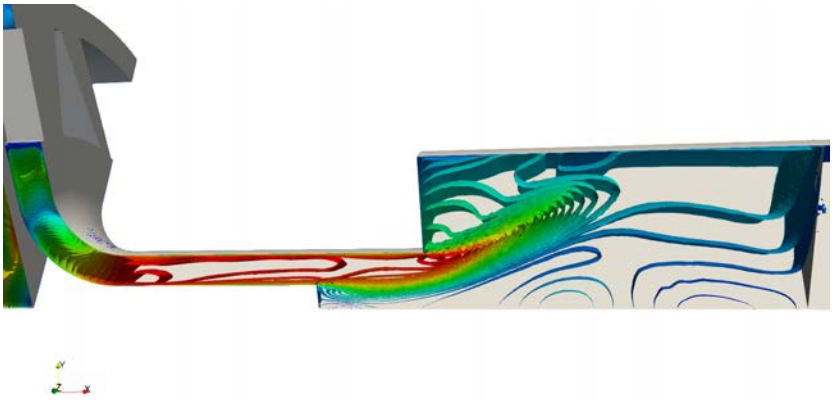

(b) Swirl generator angle = 7 deg

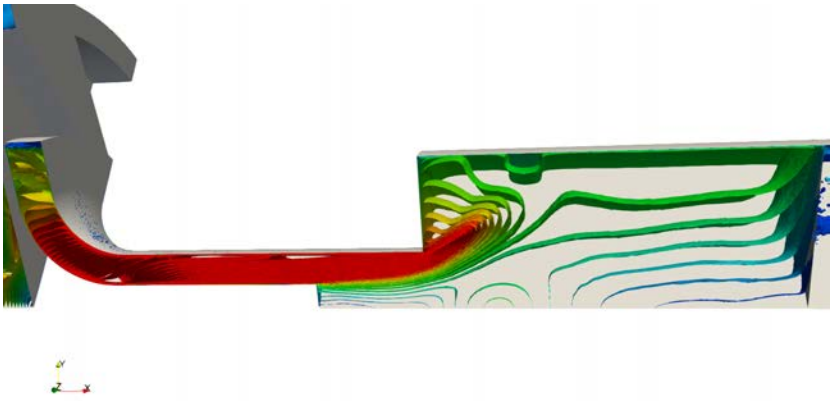

(c) Swirl generator angle = 18 deg

Figure 8.10: Velocity field across the domain at varying swirl generator angles predicted using the NL $k-\omega$ model

At swirl generator angle = 0 deg, i.e. no swirl, Figure 8.10 (a) shows that the flow in the annulus can be observed to be nearly uniform, with the exception of the boundary layers. This is also shown by the

velocity profiles, presented in Figure 8.11 (a). The thicker boundary layer at the outer wall (caused by the 90 deg bend at the swirl generator exit) is predicted more accurately by the NL $k-\omega$ model compared to the two other tested models. The standard $k-\omega$ model predicts a thicker of a boundary layer while the v^2-f is shown to predict a boundary layer at approximately the same thickness as at the inner wall, indicating underprediction of the effects of the curved wall at the swirl generator exit. Looking at the velocity field predicted using the NL $k-\omega$ model shown in Figure 8.10 (a), it can be observed that a separated shear layer exists behind the 'step' as the flow goes from the annular channel to the circular channel upstream of the diffuser. A non-swirling jet coming out of the circular channel is observed, which subsequently enters and traverses the sudden expansion diffuser. A large separation zone visibly forms behind the side wall of the diffuser. Part of the jet subsequently enters the monolith, while the rest spreads radially due to the flow resistance. It eventually hits the top wall and causes a recirculation as it impinges on the wall.

At swirl generator angle = 7 deg, the introduction of swirl is confirmed by the increase in tangential velocity in the annulus, presented in Figure 8.11 (b). This is overpredicted by all the models considered, with the NL $k-\omega$ showing improvement on predicting the asymmetry of the profile. This is accompanied by a more accurate prediction of the axial velocity compared to the other two models, particularly near the outer wall. At the inner wall, the v^2-f model predicts a lower axial velocity, indicating an overprediction of the effect of swirling here. Looking at the velocity field in Figure 8.10 (b), a massive change in the flow features can be observed compared to the no swirl level. Most notably, instead of crossing the diffuser axially as in the no swirl case, the jet flows more radially instead past the expansion point, directed towards the diffuser top wall, and eventually spreading into the region around the diffuser top wall.

At swirl generator angle = 18 deg, the swirl is now sufficiently strong to force the flow outwards, which results in a lower axial velocity near the inner wall, shown in Figure 8.11 (c). Figure 8.10 (c) shows that this causes most of the flow to go upwards upon entering the expansion, at a higher velocity to the 7 deg case, which results in an overall higher velocity in the top region of the diffuser. This is the opposite of the no swirl case, in which higher velocity is located near the centreline within the jet 'core'. Within the annulus, the increased tangential velocity is captured by all models (Figure 8.11 (c)) but its asymmetry is wrongly predicted. Near the inner wall, the v^2-f model shows an advantage over the NL $k-\omega$ and $k-\omega$ models in predicting the axial velocity. Nevertheless, the trend of the asymmetric axial velocity profile is predicted reasonably well by all the models.

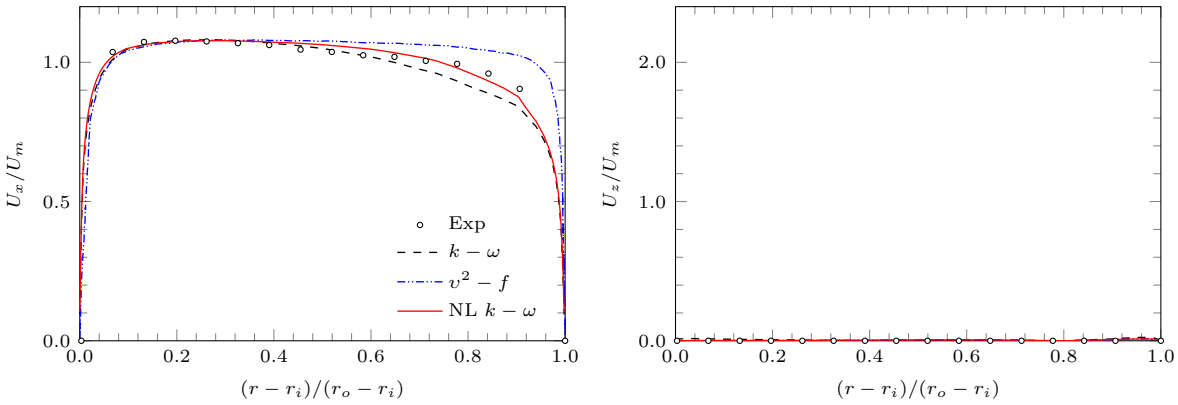

(a) Swirl generator angle = 0 deg

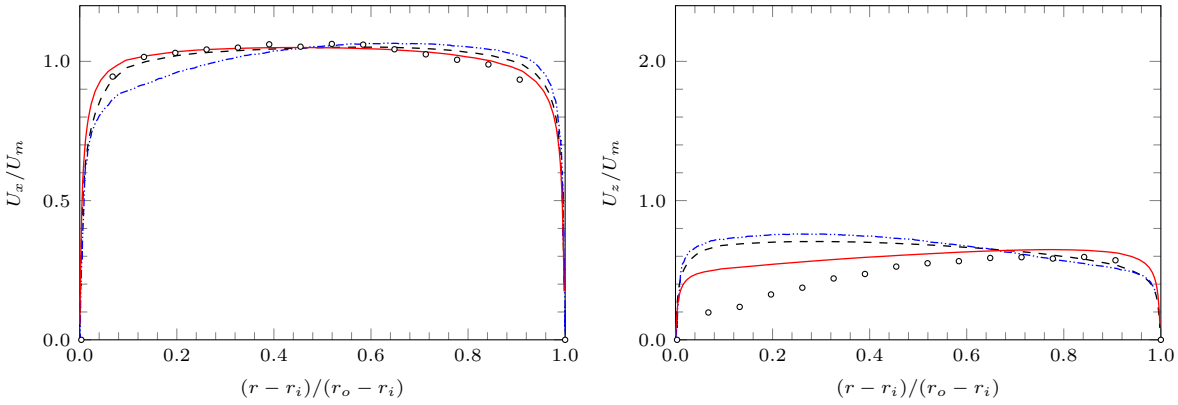

(b) Swirl generator angle = 7 deg

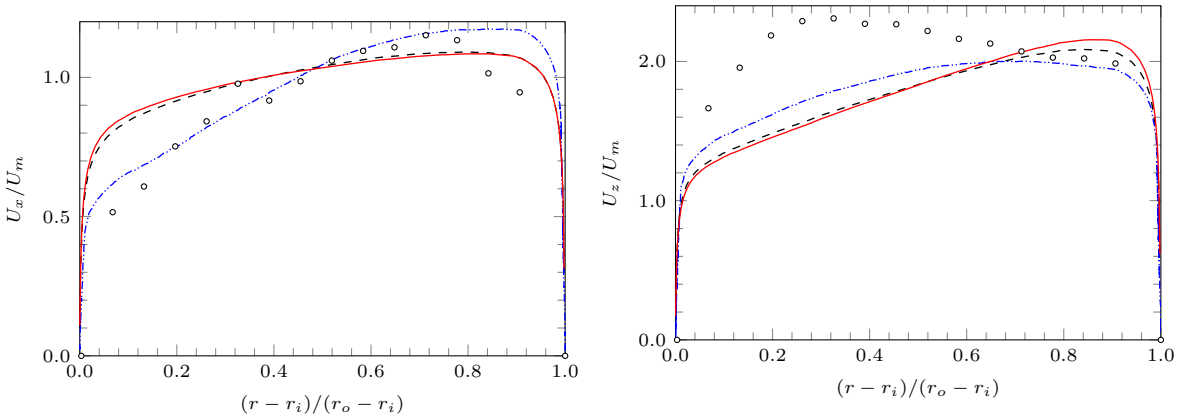

(c) Swirl generator angle = 18 deg

Figure 8.11: Axial and tangential velocity profiles within the annulus at several swirl numbers. Markers correspond to experimental data [185].

The swirl level produced by the swirl generator, as observed in the annular channel section, can be characterised using a non-dimensional swirl number, S. In its most general form, it is defined as the ratio of the axial flux of the tangential momentum to the axial flux of the axial momentum, as originally proposed by [192] and later simplified by [193]. This is calculated using:

$$S = \frac{G_z}{G_x r_o} \tag{8.2}$$

where G_x and G_z are the axial and tangential momentum fluxes, respectively, and r_o is the outer radius of the annulus. The fluxes are calculated from the integration of the axial and tangential velocities across the annular section (Figure 8.11) using:

$$G_x = \int_{r_i}^{r_o} \rho U_x U_x 2\pi r dr \qquad , \qquad G_z = \int_{r_i}^{r_o} \rho U_x U_z r 2\pi r dr \tag{8.3}$$

The S values from the two models at various swirl levels are compared against experimental and theoretical values. This is presented in Figure 8.12. The theoretical line is calculated based on the design of the swirl generator, following [188]. It is suggested in [188] that the swirl number can be directly related to the geometry of the swirl generator without knowledge of the fluid velocities using the swirl generator angle through the following formulation:

$$S = \frac{2\pi}{n\xi_m} tan\alpha \frac{cos^2\alpha \left(\frac{\xi}{\xi_m}\right)}{\left[1 - (1 - cos\alpha)\left(\frac{\xi}{\xi_m}\right)\right]^2} \tag{8.4}$$

in which the parameters n, ξ, and ξ_m are related to the geometry of the swirl generator used in the experiments, as defined in Section 8.2.1. The calculated theoretical, experimental, and predicted swirl numbers for the different swirl generator angles are presented in Figure 8.12.

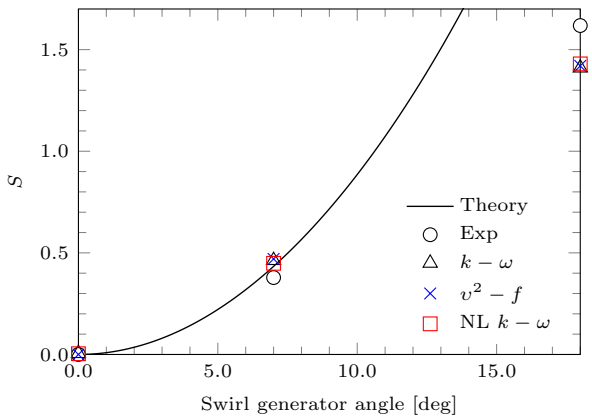

Figure 8.12: Swirl number calculated from velocities in the annulus. Experimental data is by [185].

The difference between the experimental data and the theoretical line can be attributed to either the assumption in the derivation of the theoretical swirl number, or the swirl decay between the exit of the swirl generator to the measurement point in the annulus in the experiments. Additionally, there are possibly some effects of uncertainty in the swirl number calculated from the experimental values, which is calculated from the velocities measured using HWA. The use of HWA means the velocity profile very close to the wall, within the boundary layer, cannot be captured. Hence, the fluxes calculated from

the integration of these values are not complete and may result in the difference with the theoretical values and the model predictions.

It can be observed that good agreement is attained by the models at no swirl as expected. An overprediction is shown at 7 deg, which corresponds to the overprediction of tangential velocity by both models (Figure 8.11 (b)). The NL $k-\omega$ shows some improvement, around 4%, in the swirl number here compared to the $k-\omega$ model and and around 6% compared to the v^2-f prediction. All models show underpredictions for the 18 deg case.

8.3.2 Flow in sudden expansion

The effects of swirl on the flow field within the sudden expansion diffuser are first examined through the pressure coefficients along the diffuser wall since experimental data is available here. The sampling location is along line (B) in the geometry presented in Figure 8.4. Pressure coefficient is an important flow aspect to predict since it represents the flow features in the domain. In this section, C_p is plotted against the axial distance from the expansion point, x, made non-dimensional using the length of the sudden expansion, L (refer to Figure 8.4). $x/L = 0$ therefore marks the horizontal axis where the expansion starts and $x/L = 1$ marks the start of the monolith. The results are further analysed by investigating the flow features that contribute to the pressure distribution predictions.

8.3.2.1 Swirl generator angle = 0 deg

The pressure coefficient across the diffuser walls is presented in Figure 8.13. In this no swirl case, an increase in pressure at the wall upstream of the expansion is shown in the experiment ($-0.2 < x/L \leq 0$), which is due to the opening of the flow path as the flow goes from the annular cross-section to the circular cross-section. As the flow goes past the expansion point, a large separation forms behind the diffuser side wall (as observed earlier in Figure 8.10 (a)). Therefore, all models predict the pressure coefficient to stay relatively constant here ($0 < x/L < 0.6$) until the flow gets closer to the monolith. Directly upstream of the monolith, around $x/L > 0.9$, there is a rapid increase of pressure due to the flow impinging into the resistance of the monolith. This trend is captured well by all models. The NL $k-\omega$ and the v^2-f predictions show a higher increase, closer to the experiment. However, the rapid increase is predicted by the v^2-f model further downstream than the experimental data, indicating that it underpredicts the impingement effects. The NL $k-\omega$ model shows a drop in pressure upstream of the impingement region at $0.75 < x/L < 0.85$. The v^2-f model also predicts this although at a larger extent, around $0.6 < x/L < 0.85$, while the $k-\omega$ returns nearly constant pressure until the rapid increase at the impingement region. Since this location is close to the porous region, it is expected that the radial spreading and a possible recirculation could contribute to the prediction of this pressure coefficient drop by the NL $k-\omega$ model. The experimental data shows decreased values at $0.6 < x/L < 0.86$ although not as rapidly. To investigate, the predicted flow structures are visualised by using iso-surface contours of the Q-criterion. Note that this is only available for the results obtained

using the NL $k-\omega$ and $k-\omega$ models.

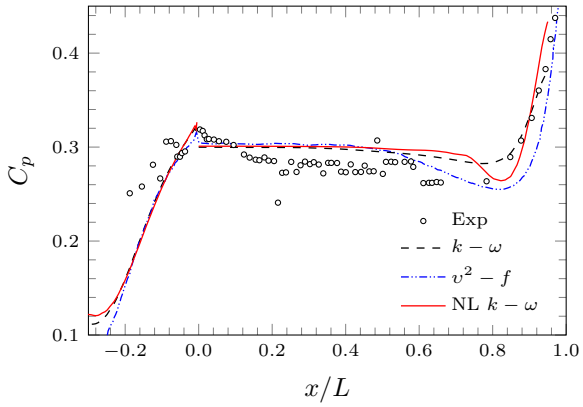

Figure 8.13: Pressure coefficient along the diffuser wall for swirl generator angle = 0 deg. Markers correspond to experimental data [185].

The Q-criterion denotes the second invariant of the velocity gradient and it can be used as a method to identify and visualise vortical structures in a flow field [183,194]. Figure 8.14 shows the iso-surfaces of the Q-criterion for the flow in the diffuser close to the monolith inlet. A line is added at $x/L \approx 0.85$ which corresponds approximately to the location of the drop in pressure coefficient shown by the NL $k-\omega$ model. It can be observed that both models predict a recirculation region upstream of the monolith as expected. This is the result of the flow spreading radially upon impinging on to the monolith and subsequently recirculating into the diffuser due to the presence of the top wall. The NL $k-\omega$ predictions show the recirculation region to be larger and more extended at the top. This means there is a relatively larger vortex with increased velocity close to the top wall of the diffuser which results in the drop of pressure coefficient in this area by the NL $k-\omega$ model, similar to the prediction of the v^2-f model as shown in Figure 8.13. It can be observed that this behaviour is similar to the predictions of the flow structures by the NL $k-\omega$ and $k-\omega$ models on the planar diffuser configuration discussed in Chapter 7 (Figure 7.14), in which the recirculation region predicted by the NL $k-\omega$ model is also located further outward radially. It can be noted that the case considered here is the no swirl case; therefore, this similarity is as expected.

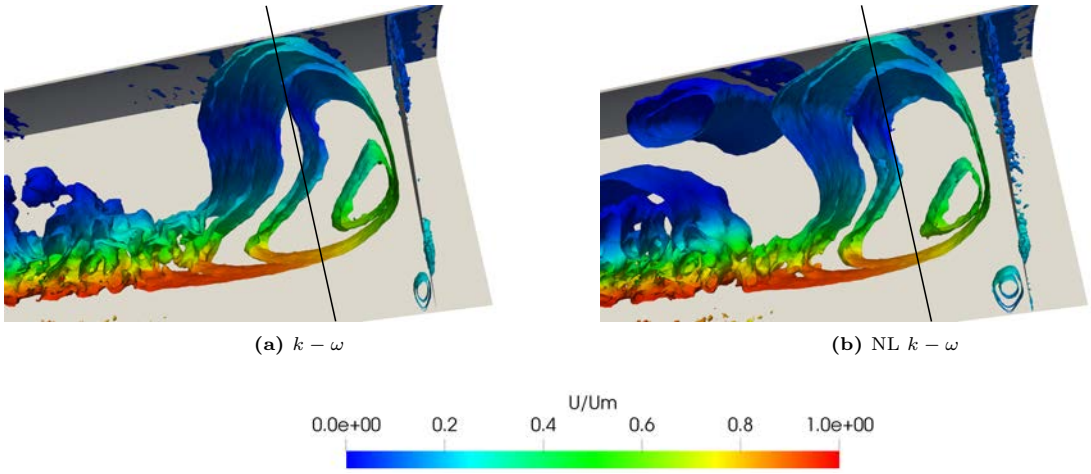

(a) $k-\omega$ **(b)** NL $k-\omega$

Figure 8.14: Iso-surfaces of the Q-criterion, limited at 1000, coloured using mean velocity at swirl generator angle=0 deg

8.3.2.2 Swirl generator angle = 7 deg

The pressure coefficient across the sudden expansion walls is presented in Figure 8.15. A decrease in pressure at the wall upstream of the expansion ($-0.2 < x/L < 0$) is shown in the experiment. This is the location where the flow transitions from an annular cross-section to a circular section. The NL $k-\omega$ model shows closer predictions to the experimental data on the pressure coefficient here compared to the $k-\omega$ model, showing 7 % improvement on the maximum pressure upstream of the expansion point, which results in a larger drop. The υ^2-f model markedly overpredicts the pressure coefficient here. The lower pressure coefficient predicted by the $k-\omega$ model can be attributed to the higher swirl level it predicts (Figure 8.12) since high radial pressure gradients are characteristics to swirling flows [195]. The flow structures predicted by the NL $k-\omega$ and the $k-\omega$ models in this area are analysed.

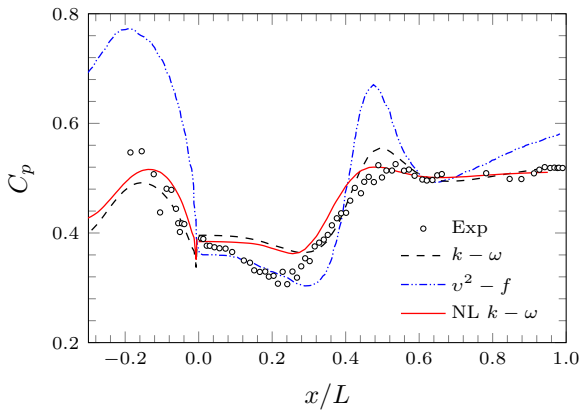

Figure 8.15: Pressure coefficient along the diffuser wall for swirl generator angle = 7 deg. Markers correspond to experimental data [185].

Although it is expected that this region contains high vorticity, the lack of a 'coherent' vortex structure

in the annulus makes the use of vorticity based visualisation difficult. Therefore, pressure contours are used. This is presented in Figure 8.16. A line located at $x/L = -0.16$, which approximately corresponds to the location of the peak pressure coefficients predicted by the models, is added for reference. The pressure contour predictions by the two models indicate that a higher level of swirl is returned by the $k-\omega$ model in the area between the annulus and the expansion, as shown by the closer contour lines in this region in the $k-\omega$ prediction which again indicates high radial pressure gradient here. This results in a lower pressure coefficient at the wall upstream of the expansion, which confirms the observation made above.

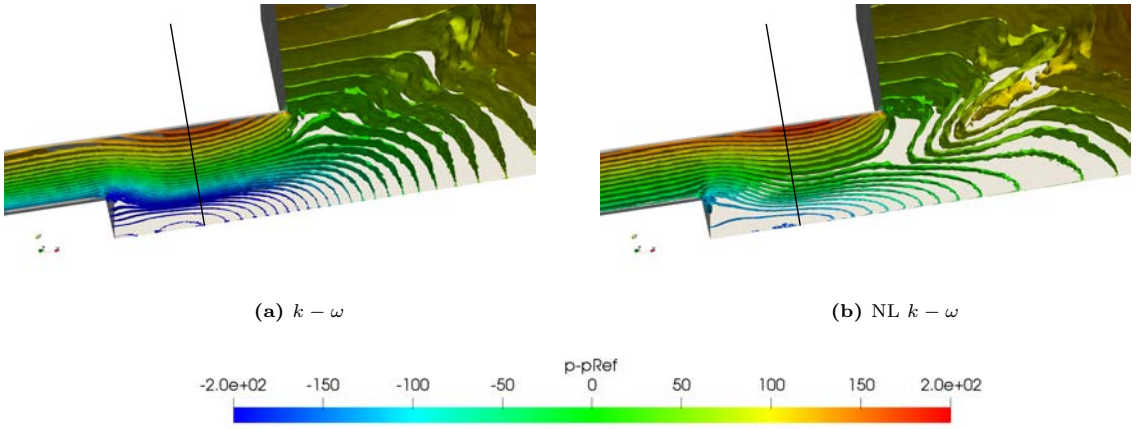

(a) $k-\omega$ **(b)** NL $k-\omega$

Figure 8.16: Pressure contours at swirl generator angle = 7 deg

Further downstream, as the flow enters the sudden expansion ($0 < x/L < 0.25$), Figure 8.15 shows that a further drop in pressure along the wall is observed in the experiment as well as in the predictions by the models. This can be attributed to the spreading of the jet at the top region of the diffuser, as shown in Figure 8.10 (b), which may cause a recirculation in the top left corner. The NL $k-\omega$ and $k-\omega$ models return comparable predictions here while the v^2-f shows a markedly larger pressure drop, closely matching the experimental data. Further downstream ($x/L > 0.25$), the pressure then recovers until the flow reattaches at the wall, which is marked by the pressure peak. The NL $k-\omega$ model predicts this pressure peak 11% closer to the experimental value compared to the $k-\omega$ and 28% more accurately compared to the v^2-f model. The lower pressure peak by the NL $k-\omega$ model suggests that it predicts the flow to be slower just before it reattaches, which indicates a higher loss of momentum due to turbulence. Therefore, the turbulent kinetic energy distribution in the diffuser is observed. The k contour plots are presented in Figure 8.17. A line located at the halfway point in the diffuser ($x/L = 0.5$) is added which corresponds approximately to the location of the pressure peak in the experiment and by the models. The NL $k-\omega$ model shows a higher level of turbulent kinetic energy in the upstream half of the diffuser compared to the $k-\omega$ model prediction, as well as a larger highly turbulent area, which indicates that the jet is more diffused as it directs towards the top wall. This results in the velocity being comparably lower as it reattaches at the wall, which results in the lower pressure coefficient predicted by the NL $k-\omega$ model at the impingement point, matching closely

to the experimental value. The more pronounced pressure variation along the wall shown by the $v^2 - f$ model therefore indicates that it predicts the jet flow entering the diffuser to be more 'preserved' and less diffused.

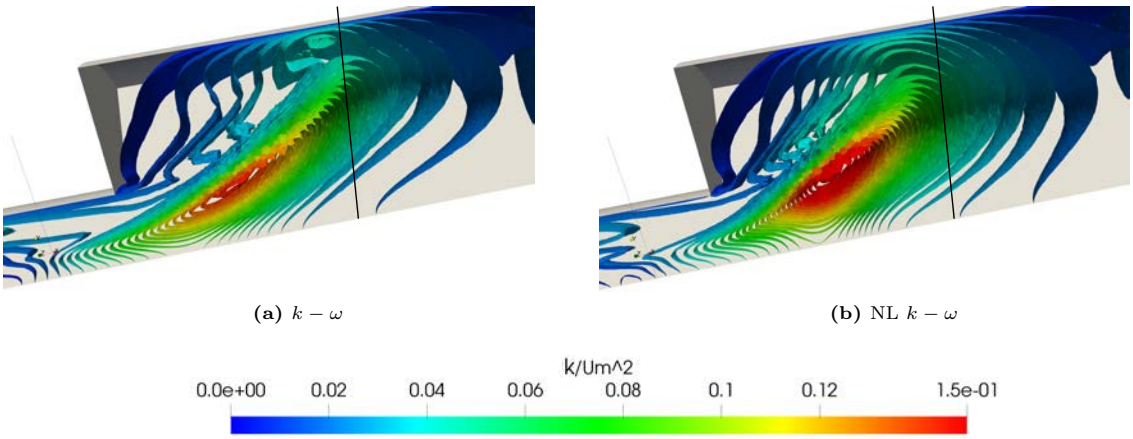

(a) $k - \omega$ **(b)** NL $k - \omega$

Figure 8.17: k contours at swirl generator angle = 7 deg

8.3.2.3 Swirl generator angle = 18 deg

In the 18 deg case, a similar trend is shown to the 7 deg case in the decrease of pressure coefficient upstream of the diffuser ($-0.2 < x/L < 0$) by the experimental data as well as the models predictions. This is presented in Figure 8.18. However, the drop is more pronounced here. The NL $k - \omega$ model returns a comparable prediction to the $v^2 - f$ model here, which is an 16% improvement on the maximum pressure coefficient compared to the $k-\omega$ model. This is interesting since similar predictions are made by the NL $k-\omega$ and the $k-\omega$ models in the velocity profiles upstream in the annulus. Within the diffuser, a flatter pressure coefficient profile is shown by the experimental data, which is indicative of the flow being attached along most of the diffuser wall. This is predicted more accurately by the NL $k - \omega$ model compared to the other two tested models. It has been observed in the velocity field (Figure 8.10 (c)) that this is due to the high level of swirling, which causes the jet to rapidly flow radially upon entering the sudden expansion, reattaching at the diffuser wall very close to the top left corner. This results in a smaller separation region behind the diffuser compared to the other cases. The reattachment is shown by the experimental data to be located around $x/L \approx 0.36$. The NL $k - \omega$ shows a slightly higher pressure here but the reattachment location is predicted well. Particularly, a 44% improvement is shown compared to the reattachment location predicted by the $k - \omega$, which also corresponds to a 22% more accurate reattachment location compared to the $v^2 - f$ prediction. The $k - \omega$ model, and more noticeably the $v^2 - f$ model, show more pronounced pressure variations within this region (around $0 < x/L < 0.4$). Looking at the pressure contour plots, presented in Figure 8.19, the NL $k - \omega$ model can be observed to show a smaller separated area in the top left region of the diffuser compared to the $k - \omega$, which results in a less pronounced, 'flatter' pressure coefficient here, indicating a more accurate prediction of separation and reattachment here and closely matching the

experimental data. As discussed above, the extent of this separated region is closely connected to the high level of swirling within the annulus which affects how the 'jet' enters the diffuser. Therefore, the improved prediction of the pressure distribution here by the NL $k-\omega$ also indicates a more accurate representation of the swirling flow in the annulus upstream of the diffuser. As the mean flow predictions at the sampling station in the annulus (Figure 8.11 (c)) show close predictions between the NL $k-\omega$ and $k-\omega$ models, the more accurate predictions of the flow downstream can be attributed to the rapid development of the flow caused by the high swirl level.

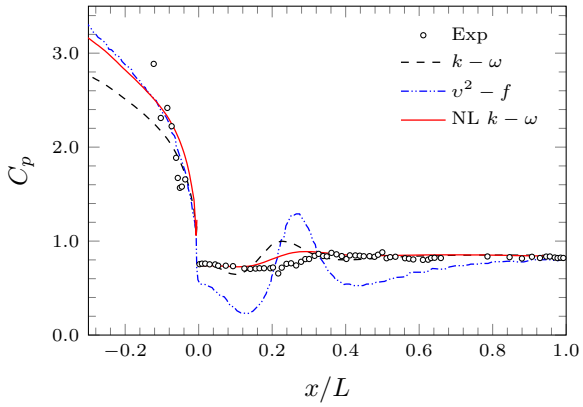

Figure 8.18: Pressure coefficient along the diffuser wall for swirl generator angle = 18 deg. Markers correspond to experimental data [185].

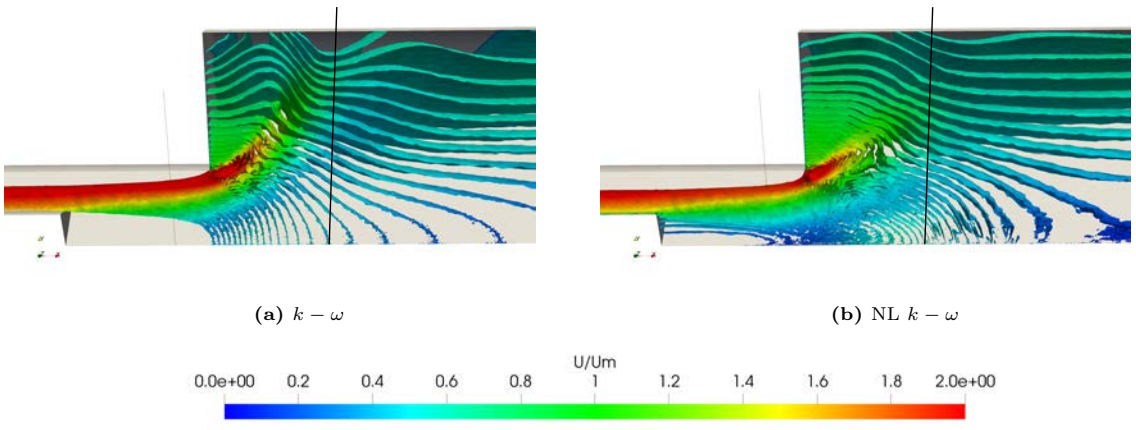

(a) $k-\omega$ **(b)** NL $k-\omega$

Figure 8.19: Pressure contours at swirl generator angle = 18 deg coloured using mean velocity

8.3.3 Flow downstream of monolith

Finally, the flow predictions downstream of the monolith are now assessed. This is presented in Figure 8.20 for the three swirl levels. Axial velocity, U_x, at 35 mm downstream of the end of the porous region is presented, non-dimensionalised using U_m, which as mentioned earlier is the mean velocity in the annulus as calculated from the mass flow rate. This is plotted against the radial distance from the centreline, r, non-dimensionalised using the diameter of the channel, D (refer to Figure 8.4).

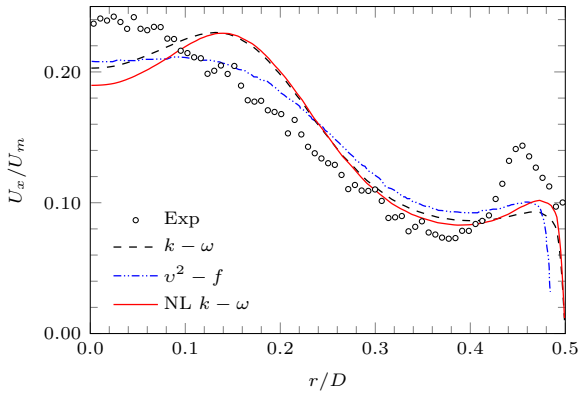

(a) Swirl generator angle = 0 deg

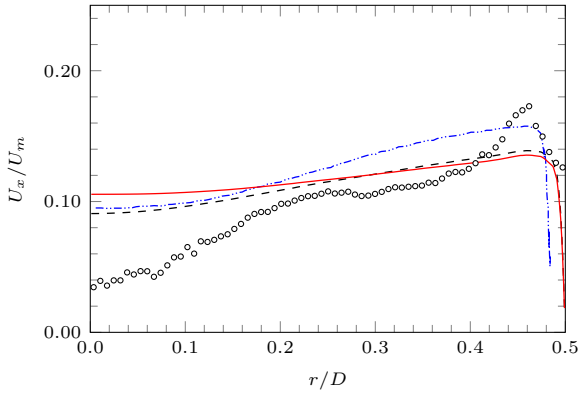

(b) Swirl generator angle = 7 deg

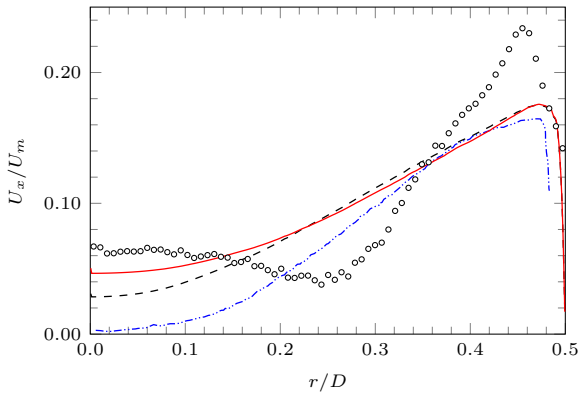

(c) Swirl generator angle = 18 deg

Figure 8.20: Axial velocity at 35 mm downstream of monolith for several swirl numbers. Markers correspond to experimental data [185].

In the 7 deg case, the velocity profile shows a minimum at the centreline, $r/D = 0$, and a maximum near the wall $r/D \approx 0.45$. This is the result of the swirling jet going into the sudden expansion diffuser which spreads upward towards the top region of the diffuser, as observed earlier in Figure 8.10 (b). It can be observed that the low axial velocity near the centreline is overpredicted by the three models, with the $k-\omega$ showing closer predictions to the experimental data. Additionally, the velocity peak is underpredicted by all the models considered, with the v^2-f model showing closer prediction to the experimental data. This is interesting since the NL $k-\omega$ model shows improvements in the

predictions of pressure coefficient on the sudden expansion wall for this case, which is indicative of the flow features within the diffuser being captured more accurately by the model. Therefore, the underprediction of the velocity maldistribution downstream of the monolith here could be attributed to the porous medium modelling method. As discussed earlier in Chapter 7, there are still some deficiencies in the porous medium modelling method, for example in the prediction of the effects of oblique entry into the monolith, as observed in [165, 168, 169, 182].

In the 18 deg case, it can be observed that the further increase in swirl, which causes the flow to be forced further outwards upon entering the diffuser, results in a higher peak velocity near the wall compared to the other cases as expected. This is underpredicted by all the tested models. This is again unexpected since the NL $k-\omega$ has shown improved predictions on the pressure coefficient in the sudden expansion and the standard $k-\omega$ and the v^2-f models show good agreement as well with the experimental data in the predictions of pressure coefficient closer to the monolith. The low axial velocity near the centreline which is contributed by the absence of a centreline jet (which is present in the no swirl case), is underpredicted by the three models, with the NL $k-\omega$ model showing some improvement.

8.4 Computational expense

The computations for the swirling flow cases presented in this chapter are completed using HPC nodes consisting of Intel® Xeon® Broadwell E5-2683 CPUs with a base frequency of 2.10 GHz, in which each of the processor has an associated 4.0 Gb of RAM. Table 8.3 shows the number of CPU cores that are used for the computation of each case and the respective running times. A comparison is made on the running times of the computations using the $k-\omega$ model and the NL $k-\omega$ model to provide an information on the change in computational expense associated with the proposed modelling approach. Note that since the computations are completed in a computer cluster, the running time comparison presented here serves as a general estimation as computation time could change based on processor properties as well as node allocation.

Table 8.3: Comparison of computational expense for the swirling flow cases

Swirl generator angle	CPU cores	Running time [s]		% Diff
		$k-\omega$	NL $k-\omega$	
0 deg	24	80,330	104,361	29.91
7 deg	24	87,040	113,108	29.95
18 deg	24	76,849	102,759	33.72

The increase in computational time associated with the NL $k-\omega$ model is around 30% for the swirling flow test cases. This is similar to the increase in computational time for the planar diffuser cases in which the *damping* approach for the porous medium is used. It is again worth noting that no numerical difficulties are encountered with the NL $k-\omega$ model compared to the $k-\omega$ model and as such there

is no need for a change in the computational and numerical setup, e.g. a finer grid or an additional relaxation factor.

8.5 Summary

Computation results of flow in a swirling sudden expansion configuration have been presented and analysed in this chapter. Three swirl generator angle settings are considered: 0, 7, and 18 deg. Predictions of the NL $k-\omega$ model are discussed in comparison with the predictions of the standard $k-\omega$ model. Additionally, results from [185], in which the v^2-f model is used, are also included.

The following conclusions can be drawn from the analysis of the results:

- In the annulus, the three tested models correctly capture the trend of the axial velocity profiles and the trend of increasing tangential velocities with increased swirl levels. However, the level of swirl is underpredicted by all the models considered.
- The disagreement in the swirl levels in the annulus, particularly at the highest swirl level, indicates a possible need for an explicit rotation correction for improved predictions on rotational flows in particular.
- The NL $k-\omega$ shows predictions of the pressure coefficient on the sudden expansion walls closer to the experimental data compared to the other tested models at the three swirl levels tested, which is indicative of a more accurate representation of the flow features such as the recirculation region upstream of the monolith in the 0 deg case, the diffused jet entering the diffuser in the 7 deg case, and the extent of the separation region behind the sudden expansion wall in the 18 deg case.
- An underprediction of the velocity maldistribution downstream of the monolith, even when good agreement in pressure coefficient to the experimental data on the sudden expansion wall is returned, indicates possible deficiencies in the porous medium modelling method.

Chapter 9

Conclusions

A new quadratic non-linear eddy-viscosity turbulence model with enhanced treatment for near-wall turbulence anisotropy (the NL $k-\omega$ model) has been developed and implemented in the present work and the performance of the model has been evaluated using a range of flow configurations. It employs the general, expanded tensor polynomial formulation for the Reynolds stress tensor derived by Pope [3]. The first step in this work was to extend the standard $k-\omega$ model using the non-linear anisotropy formulation. This initial formulation, which uses calibrated constant values for the anisotropy expansion coefficients, is shown to be efficient in improving the anisotropy prediction of the Reynolds stresses compared to the standard linear $k-\omega$ model except for in regions in the vicinity of the walls. Here, it was identified that a modification to account for near-wall anisotropy is needed. Consequently, a novel approach is proposed for this modification that relies only on local variables. It is formulated to capture how anisotropic turbulence effects are manifested in different regions of the boundary layer. This is achieved using damping functions that scale only with the turbulent Reynolds number. The new formulation shows to be effective in improving predictions of the Reynolds stress anisotropy near walls. Particular improvements are shown in the inner region of the boundary layer, $y^+ < 40$, which indicate a more accurate representation of the turbulent structures here, such as the low-speed streaks in the viscous sublayer and the strong shearing that is known to occur in the buffer layer. More accurate level of turbulence anisotropy in these regions is observed in a fully-developed channel flow at various Reynolds numbers and over the turbulent boundary layer on a flat plate.

The results also show improved predictions compared with the standard $k-\omega$ model in a curved channel configuration. Of particular note is the global quantities, in which the model returns an improvement of 50% in the prediction of the pressure minimum compared to the linear $k-\omega$ predictions, which is also approximately 20% closer to the experimental data compared to the predictions of two other non-linear models considered (Shih quadratic $k-\varepsilon$ and Lien cubic $k-\varepsilon$ models). The prediction of pressure drop across the curved channel by the NL $k-\omega$ model is also 15% closer to the experimental data compared to the linear $k-\omega$ model and the Shih quadratic $k-\varepsilon$ model predictions, and is comparable

to the prediction of the Lien cubic $k-\varepsilon$ model. These improvements highlight the advantages of the NL $k-\omega$ model in predicting the quantities that of particular significance near walls, such as skin friction and static pressure, as well as in predicting the adverse pressure gradient in the channel due to the curvature. The latter is important from a practical point of view since it represents the energy losses in the domain. In a more complex configuration, namely a planar diffuser with a downstream monolith, a 20% improvement is found compared to the $k-\omega$ model on the prediction of the velocity minimum downstream of the monolith and the prediction of the secondary peak near the wall is around 10% closer to the experimental data compared to prediction of two other models considered here: linear $k-\omega$ and v^2-f models. Although an improved prediction of the velocity maldistribution is desired overall to match the experimental data more closely, the results show that the anisotropy of the Reynolds stresses is successful in affecting the predictions of the general flow features such as the recirculation region in the diffuser that results in the aforementioned improvements. Meanwhile, the swirling flow configuration considered here provides the means of assessing the performance of the model when flow rotation is imposed. Although the model is not explicitly sensitised to rotation effects, the anisotropy formulation in the NL $k-\omega$ model, which takes into account the strain and rotation rates at a quadratic level, shows to have an effect on improving the pressure coefficient predictions on the sudden expansion walls, which is indicative of a more accurate representation of the flow features here, such as the recirculation region upstream of the monolith, the spreading of the swirling jet that enters the diffuser, and the separated region behind the sudden expansion wall. For example, a 7% improvement on the prediction of the pressure coefficient maximum upstream of the expansion point and an 11% improvement on the pressure coefficient at the reattachment point are returned by the NL $k-\omega$ predictions compared to the linear $k-\omega$ predictions (for the 7 deg case). Also, a 44% improvement on the prediction of the reattachment location in the diffuser (for the 18 deg case) is observed compared to the linear $k-\omega$ prediction, which is also 22% closer to the experimental data compared to the v^2-f prediction.

These results highlight the overall strength of the NL $k-\omega$ model in predicting the flow features that are present in internal flows such as separation, reattachment, recirculation, and impingement. Therefore, based on the cases considered, it is expected that the NL $k-\omega$ model would present advantages in applications involving these features, for example, for modelling flows in automotive exhaust catalytic converters, fuel systems, or turbochargers. Additionally, the near-wall modification is shown to be particularly effective in producing improvements for quantities that are of significance near walls, such as shear stresses, skin friction, and static pressure distribution. Therefore, configurations for which the predictions of these quantities are of interests, such as flows through heat exchangers, are also expected to be suitable for the application of the new model. The disagreement in the swirl level predictions by the model compared to the experimental data indicates a possible need for an explicit correction for improved predictions on rotational flows. This is not considered here since the focus of this work was on improving the predictions of anisotropy in near-wall regions. The maximum increase in computation time associated with the NL $k-\omega$ model compared to the linear $k-\omega$ model is around 40%. Nevertheless, the improvements mentioned above are encouraging and demonstrate the

robustness of the new model for applications in complex configurations.

9.1 Main contributions

The key contributions of the present work are summarised as follows:

- Development, implementation, calibration, and validation of a non-linear extension of the standard $k-\omega$ model based on a quadratic expansion for the formulation of the Reynolds stress tensor
- Proposal, development, implementation, calibration, and validation of a novel approach for formulating the anisotropy expansion terms that include an enhanced treatment of the near-wall anisotropy using only local variables.
- Evaluation of the effects of turbulence treatments at the porous region interface using the porous medium modelling method
- Evaluation and assessment of the robustness of the new near-wall anisotropic formulation to address complex flows (planar diffuser with downstream resistance) and geometries (swirling flow generator and sudden expansion configuration, also with a downstream resistance)

The following publications are also a result of this work:

- H Fadhila, H Medina, S Aleksandrova, and S Benjamin. A new non-linear RANS model with enhanced near-wall treatment of turbulence anisotropy. *Applied Mathematical Modelling*, 82:293–313, 2020.
- H Fadhila, H Medina, A Beechook, S Aleksandrova, and S Benjamin. Evaluation of transition-sensitive eddy-viscosity turbulence models for separated flow in OpenFOAM. In *AIP Conference Proceedings*, volume 1863, page 030034. AIP Publishing, 2017.
- H Medina, A Beechook, H Fadhila, S Aleksandrova, and S Benjamin. A novel laminar kinetic energy model for the prediction of pretransitional velocity fluctuations and boundary layer transition. *International Journal of Heat and Fluid Flow*, 69:150–163, 2018.
- H Fadhila, H Medina, S Aleksandrova, and S Benjamin. Evaluation of linear and non-linear eddy-viscosity turbulence models for prediction of swirl effects in automotive exhaust catalysts. Preprint under preparation for submission to Engineering Applications of Computational Fluid Mechanics, 2020.

9.2 Suggestions for future work

- Explicit sensitisation to rotation by considering frame indifference principles, for example by including a frame rotation rate [9, 84, 196–198]

- Exploration of the possibility of employing the new model in a hybrid RANS/LES modelling approach since its focus on predicting anisotropy in near-wall regions makes it a good candidate
- Implementation of the proposed approach and framework for the near-wall anisotropy modification to existing turbulence models

References

[1] J C Rotta. Statistische theorie nichthomogener turbulenz. *Zeitschrift für Physik*, 129(6):547–572, 1951.

[2] J L Lumley. Toward a turbulent constitutive relation. *Journal of Fluid Mechanics*, 41(02):413–434, 1970.

[3] S B Pope. A more general effective-viscosity hypothesis. *Journal of Fluid Mechanics*, 72(02):331–340, 1975.

[4] C G Speziale. On nonlinear $k - \ell$ and $k - \varepsilon$ models of turbulence. *Journal of Fluid Mechanics*, 178:459–475, 1987.

[5] D C Wilcox. *Turbulence modeling for CFD*. DCW industries La Canada, CA, 1 edition, 1993.

[6] J Luo and B Lakshminarayana. Prediction of strongly curved turbulent duct flows with Reynolds stress model. *AIAA Journal*, 35(1):91–98, 1997.

[7] C L Rumsey, T B Gatski, and J H Morrison. Turbulence model predictions of strongly curved flow in a U-duct. *AIAA Journal*, 38(8):1394–1402, 2000.

[8] T J Craft, B E Launder, and K Suga. Development and application of a cubic eddy-viscosity model of turbulence. *International Journal of Heat and Fluid Flow*, 17(2):108–115, 1996.

[9] W D York, D K Walters, and J H Leylek. A simple and robust linear eddy-viscosity formulation for curved and rotating flows. *International Journal of Numerical Methods for Heat & Fluid Flow*, 19(6):745–776, 2009.

[10] P Bradshaw. Effects of streamline curvature on turbulent flow. Technical report, DTIC Document, 1973.

[11] T von Kármán. Some aspects of the turbulence problem. *Proceeding of the 4th International Congress of Applied Mechanics*, pages 54–91, 1934.

[12] D C Wilcox and T L Chambers. Streamline curvature effects on turbulent boundary layers. *AIAA Journal*, 15(4):574–580, 1977.

[13] J P Bertoglio. Homogeneous turbulent field within a rotating frame. *AIAA Journal*, 20(9):1175–1181, 1982.

[14] C Heschl, K Inthavong, W Sanz, and J Tu. Evaluation and improvements of RANS turbulence models for linear diffuser flows. *Computers & Fluids*, 71:272–282, 2013.

[15] D D Apsley and M A Leschziner. Advanced turbulence modelling of separated flow in a diffuser. *Flow, Turbulence and Combustion*, 63(1-4):81–112, 2000.

[16] F G Schmitt. About Boussinesq's turbulent viscosity hypothesis: historical remarks and a direct evaluation of its validity. *Comptes Rendus Mecanique*, 335(9):617–627, 2007.

[17] F G Schmitt. Direct test of a nonlinear constitutive equation for simple turbulent shear flows using DNS data. *Communications in Nonlinear Science and Numerical Simulation*, 12(7):1251–1264, 2007.

[18] F G Schmitt, B K Hazarika, and C Hirsch. LDV measurements of the flow field in the nozzle region of a confined double annular burner. *Journal of Fluids Engineering*, 123(2):228–236, 2001.

[19] W Rodi, J H Ferziger, M Breuer, and M Pourquiée. Status of large eddy simulation: results of a workshop. *Journal of Fluids Engineering*, 119(2):248–262, 1997.

[20] R L Thompson, G Mompean, and L Thais. A methodology to quantify the nonlinearity of the Reynolds stress tensor. *Journal of Turbulence*, page N33, 2010.

[21] L Thais, A E Tejada-Martínez, T B Gatski, and G Mompean. Numerical simulations of turbulent viscoelastic drag reduction. In *Proceedings of the Second International Conference on Turbulence and Interaction, Sainte Luce, Martinique, France*, volume 31, 2009.

[22] S Gavrilakis. Numerical simulation of low-Reynolds-number turbulent flow through a straight square duct. *Journal of Fluid Mechanics*, 244:101–129, 1992.

[23] S Gavrilakis. Turbulent velocity structures derived from pod analyses. *Institut de Machines Hydrauliques et de Mécanique des Fluides, Ecole Polytechnique Fédérale de Lausanne*, 1993.

[24] B E Launder, C H Priddin, and B I Sharma. The calculation of turbulent boundary layers on spinning and curved surfaces. *Journal of Fluids Engineering*, 99(1):231–239, 03 1977.

[25] W Rodi. Influence of buoyancy and rotation on equations for the turbulent length scale. In *2nd Symposium on Turbulent Shear Flows*, pages 10–37, 1979.

[26] W Rodi and G Scheuerer. Calculation of curved shear layers with two-equation turbulence models. *The Physics of Fluids*, 26(6):1422–1436, 1983.

[27] B Lakshminarayana. Turbulence modeling for complex shear flows. *AIAA Journal*, 24(12):1900–1917, 1986.

[28] V C Patel and F Sotiropoulos. Longitudinal curvature effects in turbulent boundary layers. *Progress in Aerospace Sciences*, 33(1):1–70, 1997.

[29] K Hanjalić and B E Launder. A Reynolds stress model of turbulence and its application to thin shear flows. *Journal of Fluid Mechanics*, 52(04):609–638, 1972.

[30] B E Launder, G Reece, and W Rodi. Progress in the development of a Reynolds-stress turbulence closure. *Journal of Fluid Mechanics*, 68(3):537–566, 1975.

[31] T-H Shih, J Zhu, and J L Lumley. A realizable Reynolds stress algebraic equation model. Technical report, NASA, 1993.

[32] P A Durbin. A Reynolds stress model for near-wall turbulence. *Journal of Fluid Mechanics*, 249:465–498, 1993.

[33] B A Pettersson Reif, P A Durbin, and A Ooi. Modeling rotational effects in eddy-viscosity closures. *International journal of heat and fluid flow*, 20(6):563–573, 1999.

[34] S Li. *Predicting riblet performance with engineering turbulence models*. PhD thesis, University of Manchester, Institute of Science and Technology, 1992.

[35] A J M Spencer and R S Rivlin. The theory of matrix polynomials and its application to the mechanics of isotropic continua. *Archive for Rational Mechanics and Analysis*, 2(1):309–336, 1958.

[36] A J M Spencer and R S Rivlin. Further results in the theory of matrix polynomials. *Archive for Rational Mechanics and Analysis*, 4(1):214–230, 1959.

[37] W R Hamilton. *Lectures on quaternions*. University Press by MH, 1853.

[38] W R Hamilton. On the existence of a symbolic and biquadratic equation, which is satisfied by the symbol of linear operation in quaternions. In *Proceedings of the Royal Irish Academy*, volume 8, pages 190–191, 1864.

[39] W R Hamilton. On a new and general method of inverting a linear and quaternion function of a quaternion. In *Proceedings of the Royal Irish Academy*, volume 8, pages 182–183, 1864.

[40] S Nisizima and A Yoshizawa. Turbulent channel and Couette flows using an anisotropic $k - \varepsilon$ model. *AIAA Journal*, 25(3):414–420, 1987.

[41] R Rubinstein and J M Barton. Nonlinear Reynolds stress models and the renormalization group. *Physics of Fluids A: Fluid Dynamics (1989-1993)*, 2(8):1472–1476, 1990.

[42] H K Myong and N Kasagi. A new approach to the improvement of $k - \varepsilon$ turbulence model for wall-bounded shear flows. *JSME international journal. Ser. 2, Fluids engineering, heat transfer, power, combustion, thermophysical properties*, 33(1):63–72, 1990.

[43] J Kim, S J Kline, and J P Johnston. Investigation of a reattaching turbulent shear layer: flow over a backward-facing step. *Journal of Fluids Engineering*, 102(3):302–308, 1980.

[44] T B Gatski and C G Speziale. On explicit algebraic stress models for complex turbulent flows. *Journal of Fluid Mechanics*, 254:59–78, 1993.

[45] E Gutmark and I Wygnanski. The planar turbulent jet. *Journal of Fluid Mechanics*, 73(3):465–495, 1976.

[46] H Abrahamsson. *On turbulent wall jets*. PhD thesis, Chalmers University of Technology, 1997.

[47] L B Ellis and P N Joubert. Turbulent shear flow in a curved duct. *Journal of Fluid Mechanics*, 62(01):65–84, 1974.

[48] T J Craft, B E Launder, and K Suga. Prediction of turbulent transitional phenomena with a nonlinear eddy-viscosity model. *International Journal of Heat and Fluid Flow*, 18(1):15–28, 1997.

[49] K Suga and K Abe. Nonlinear eddy viscosity modelling for turbulence and heat transfer near wall and shear-free boundaries. *International journal of heat and fluid flow*, 21(1):37–48, 2000.

[50] J L Lumley. Computational modeling of turbulent flows. *Advances in applied mechanics*, 18(123):213, 1978.

[51] D D Apsley and M A Leschziner. A new low-Reynolds-number nonlinear two-equation turbulence model for complex flows. *International Journal of Heat and Fluid Flow*, 19(3):209–222, 1998.

[52] S Obi, K Aoki, and S Masuda. Experimental and computational study of turbulent separating flow in an asymmetric plane diffuser. In *Ninth Symposium on Turbulent Shear Flows*, pages 305–1, 1993.

[53] D D Apsley, W-L Chen, M Leschziner, and F-S Lien. Non-linear eddy-viscosity modelling of separated flows. *Journal of Hydraulic research*, 35(6):723–748, 1997.

[54] T B Gatski and T Jongen. Nonlinear eddy viscosity and algebraic stress models for solving complex turbulent flows. *Progress in Aerospace Sciences*, 36(8):655–682, 2000.

[55] T B Gatski and C L Rumsey. Linear and nonlinear eddy viscosity models. In B E Launder and N D Sandham, editors, *Closure strategies for turbulent and transitional flows*, chapter 1, pages 9–46. Cambridge University Press, 2002.

[56] M A Leschziner. Modelling turbulent separated flow in the context of aerodynamic applications. *Fluid dynamics research*, 38(2):174–210, 2006.

[57] A Hellsten and S Wallin. Explicit algebraic Reynolds stress and non-linear eddy-viscosity models. *International Journal of Computational Fluid Dynamics*, 23(4):349–361, 2009.

[58] J Larsson. Two-equation turbulence models for turbine blade heat transfer simulations. *ISABE paper*, pages 97–7163, 1997.

[59] B Song, R S Amano, and G R Liu. On computations of complex turbulent flow by using nonlinear $k-\omega$ model. *Numerical Heat Transfer: Part B: Fundamentals*, 39(5):421–434, 2001.

[60] K Abe, Y-J Jang, and M A Leschziner. An investigation of wall-anisotropy expressions and length-scale equations for non-linear eddy-viscosity models. *International Journal of Heat and Fluid Flow*, 24(2):181–198, 2003.

[61] W Rodi and G Scheuerer. Scrutinizing the $k-\varepsilon$ turbulence model under adverse pressure gradient conditions. *Journal of Fluids Engineering*, 108(2):174–179, 1986.

[62] P R Spalart and S Allmaras. A one-equation turbulence model for aerodynamic flows. In *30th Aerospace Sciences Meeting and Exhibit*, page 439, 1992.

[63] P G Huang, P Bradshaw, and T J Coakley. Assessment of closure coefficients for compressible-flow turbulence models. Technical Report NASA TM-103882, NASA, 1992.

[64] F R Menter. A comparison of some recent eddy-viscosity turbulence models. *Journal of Fluids Engineering*, 118(3):514–519, 1996.

[65] A Hellsten and S Laine. Explicit algebraic Reynolds-stress modelling in decelerating and separating flows. In *Fluids 2000 Conference and Exhibit*, page 2313, 2000.

[66] C R Yap. *Turbulent heat and momentum transfer in recirculating and impinging flows*. PhD thesis, University of Manchester, 1987.

[67] J Larsson, L-E Eriksson, and U Hall. External heat transfer predictions in supersonic turbines using the Reynolds averaged Navier-Stokes equations. In *Proceedings of the 12th ISABE Conference*, volume 2, pages 1102–1112, 1995.

[68] S J Kline, B J Cantwell, and G M Lilley. Comparison of computation and experiment. In *AFOSR-HTTM Stanford Conference on Complex Turbulent Flows, Stanford, California*, 1981.

[69] F R Menter. Improved two-equation $k-\omega$ turbulence models for aerodynamic flows. *NASA STI/Recon Technical Report N*, 93:22809, 1992.

[70] T Han. Computational analysis of three-dimensional turbulent flow around a bluff body in ground proximity. *AIAA journal*, 27(9):1213–1219, 1989.

[71] D C Wilcox. Reassessment of the scale-determining equation for advanced turbulence models. *AIAA Journal*, 26(11):1299–1310, 1988.

[72] F R Menter. Performance of popular turbulence model for attached and separated adverse pressure gradient flows. *AIAA Journal*, 30(8):2066–2072, 1992.

[73] B E Launder and B I Sharma. Application of an energy-dissipation model of turbulence to the calculation of flow near a spinning disc. *Letters in Heat and Mass Transfer*, 1(2):131–138, 1974.

[74] P G Saffman and D C Wilcox. Turbulence-model predictions for turbulent boundary layers. *AIAA Journal*, 12(4):541–546, 1974.

[75] D C Wilcox and R Traci. A complete model of turbulence. In *9th Fluid and PlasmaDynamics Conference*, page 351, 1976.

[76] D C Wilcox and M W Rubesin. Progress in turbulence modeling for complex flow fields including effects of compressibility. Technical Report NASA TP-1517, NASA, 1980.

[77] K Abe, T Kondoh, and Y Nagano. On Reynolds-stress expressions and near-wall scaling parameters for predicting wall and homogeneous turbulent shear flows. *International Journal of Heat and Fluid Flow*, 18(3):266–282, 1997.

[78] D C Wilcox. Simulation of transition with a two-equation turbulence model. *AIAA Journal*, 32(2):247–255, 1994.

[79] T-H Shih, J Zhu, and J L Lumley. A new Reynolds stress algebraic equation model. *Computer methods in applied mechanics and engineering*, 125(1):287–302, 1995.

[80] J P Johnston, R M Halleent, and D K Lezius. Effects of spanwise rotation on the structure of two-dimensional fully developed turbulent channel flow. *Journal of Fluid Mechanics*, 56(3):533–557, 1972.

[81] J Kim, P Moin, and R Moser. Turbulence statistics in fully developed channel flow at low Reynolds number. *Journal of Fluid Mechanics*, 177:133–166, 1987.

[82] N Djilali, I Gartshore, and M Salcudean. Calculation of convective heat transfer in recirculating turbulent flow using various near-wall turbulence models. *Numerical Heat Transfer*, 16(2):189–212, 1989.

[83] T Ota and N Kon. Heat transfer in the separated and reattached flow over blunt flat plates–effects of nose shape. *International Journal of Heat and Mass Transfer*, 22(2):197–206, 1979.

[84] S Wallin and A V Johansson. An explicit algebraic Reynolds stress model for incompressible and compressible turbulent flows. *Journal of Fluid Mechanics*, 403:89–132, 2000.

[85] D B Taulbee. An improved algebraic Reynolds stress model and corresponding nonlinear stress model. *Physics of Fluids A: Fluid Dynamics*, 4(11):2555–2561, 1992.

[86] A N Kolmogorov. The local structure of isotropic turbulence in an incompressible viscous fluid. In *Dokl. Akad. Nauk SSSR*, volume 30, pages 301–305, 1941.

[87] T von Kármán. Mechanische ähnlichkeit und turbulenz. In *Proceeding of the 3rd International Congress of Applied Mechanics*, page 85, 1930.

[88] L Prandtl. Motion of fluids with very little viscosity. Technical Report NASA TM-452, NASA, 1928.

[89] L Prandtl. Neuere ergebnisse der turbulenzforschung. *VDI-Ztschr*, 77(5):105, 1933.

[90] P Bradshaw. The understanding and prediction of turbulent flow. *The Aeronautical Journal*, 76(739):403–418, 1972.

[91] S K Robinson. Coherent motions in the turbulent boundary layer. *Annual Review of Fluid Mechanics*, 23:601–639, 1991.

[92] R L Panton. Overview of the self-sustaining mechanisms of wall turbulence. *Progress in Aerospace Sciences*, 37(4):341–383, 2001.

[93] A J Smits, B J McKeon, and I Marusic. High-Reynolds number wall turbulence. *Annual Review of Fluid Mechanics*, 43, 2011.

[94] J M Wallace. Highlights from 50 years of turbulent boundary layer research. *Journal of Turbulence*, 13(53):1–70, 2012.

[95] H T Kim, S J Kline, and W C Reynolds. The production of turbulence near a smooth wall in a turbulent boundary layer. *Journal of Fluid Mechanics*, 50(1):133–160, 1971.

[96] B J Cantwell. Organized motion in turbulent flow. *Annual Review of Fluid Mechanics*, 13(1):457–515, 1981.

[97] S J Kline and P W Runstadler. Some preliminary results of visual studies of the flow model of the wall layers of the turbulent boundary layer. *Trans. ASME Ser. E*, 2:166–170, 1959.

[98] F A Schraub, S J Kline, J Henry, P W Runstadler, and A Littell. Use of hydrogen bubbles for quantitative determination of time-dependent velocity fields in low-speed water flows. *Journal of Fluids Engineering*, 87(2):429–444, 1965.

[99] S J Kline, W C Reynolds, F A Schraub, and P W Runstadler. The structure of turbulent boundary layers. *Journal of Fluid Mechanics*, 30(4):741–773, 1967.

[100] E R Corino and R S Brodkey. A visual investigation of the wall region in turbulent flow. *Journal of Fluid Mechanics*, 37(1):1–30, 1969.

[101] F Waleffe and J Kim. How streamwise rolls and streaks self-sustain in a shear flow. In R L Panton, editor, *Self-Sustaining Mechanisms of Wall Turbulence*, pages 309–332. Computational Mechanics Publications, 1997.

[102] J Jeong, F Hussain, W Schoppa, and J Kim. Coherent structures near the wall in a turbulent channel flow. *Journal of Fluid Mechanics*, 332:185–214, 1997.

[103] J K Ferrell, F M Richardson, and K O Beatty. Dye displacement technique for velocity distribution measurements. *Industrial & Engineering Chemistry*, 47(1):29–33, 1955.

[104] F M Richardson and K O Beatty. Patterns in turbulent flow in the wall-adjacent region. *The Physics of Fluids*, 2(6):718–719, 1959.

[105] D G Bogard and W G Tiederman. Characteristics of ejections in turbulent channel flow. *Journal of Fluid Mechanics*, 179:1–19, 1987.

[106] S C Kassinos, W C Reynolds, and M M Rogers. One-point turbulence structure tensors. *Journal of Fluid Mechanics*, 428:213–248, 2001.

[107] K Liu and R H Pletcher. Anisotropy of a turbulent boundary layer. *Journal of Turbulence*, 9(18):1–18, 2008.

[108] M R Head and P Bandyopadhyay. New aspects of turbulent boundary-layer structure. *Journal of Fluid Mechanics*, 107:297–338, 1981.

[109] C R Smith. A synthesized model of the near-wall behavior in turbulent boundary layers. In J Zakin and Patterson G, editors, *Proceedings of the Eighth Symposium on Turbulence*, pages 299–325, 1984.

[110] R J Adrian, C D Meinhart, and C D Tomkins. Vortex organization in the outer region of the turbulent boundary layer. *Journal of Fluid Mechanics*, 422:1–54, 2000.

[111] A E Perry and M S Chong. On the mechanism of wall turbulence. *Journal of Fluid Mechanics*, 119:173–217, 1982.

[112] C R Smith, J D A Walker, A H Haidari, and U Sobrun. On the dynamics of near-wall turbulence. *Philosophical Transactions of the Royal Society of London. Series A: Physical and Engineering Sciences*, 336(1641):131–175, 1991.

[113] A H Haidari and C R Smith. The generation and regeneration of single hairpin vortices. *Journal of Fluid Mechanics*, 277:135–162, 1994.

[114] S K Robinson. *Kinematics of turbulent boundary layer structure*. PhD thesis, Stanford University, 1990.

[115] X Wu and P Moin. Direct numerical simulation of turbulence in a nominally zero-pressure-gradient flat-plate boundary layer. *Journal of Fluid Mechanics*, 630:5–41, 2009.

[116] T Theodorsen. Mechanisms of turbulence. In *Proceedings of the Second Midwestern Conference on Fluid Mechanics*, pages 1–18, 1952.

[117] A A Townsend. *The structure of turbulent shear flow*. Cambridge University Press, 1980.

[118] H M Blackburn, N N Mansour, and B J Cantwell. Topology of fine-scale motions in turbulent channel flow. *Journal of Fluid Mechanics*, 310:269–292, 1996.

[119] O Reynolds. On the dynamical theory of incompressible viscous fluids and the determination of the criterion. *Proceedings of the Royal Society of London*, 56(336-339):40–45, 1894.

[120] J Boussinesq. *Essai sur la théorie des eaux courantes*. Imprimerie nationale, 1877.

[121] N N Mansour, J Kim, and P Moin. Reynolds-stress and dissipation-rate budgets in a turbulent channel flow. *Journal of Fluid Mechanics*, 194:15–44, 1988.

[122] P Y Chou. On velocity correlations and the solutions of the equations of turbulent fluctuation. *Quarterly of Applied Mathematics*, 3(1):38–54, 1945.

[123] B I Davydov. On statistical dynamics of an incompressible turbulent fluid. In *Soviet Physics Doklady*, volume 6, page 10, 1961.

[124] F H Harlow and P I Nakayama. Transport of turbulence energy decay rate. Technical report, Los Alamos Scientific Lab., N. Mex., 1968.

[125] W P Jones and B E Launder. The prediction of laminarization with a two-equation model of turbulence. *International Journal of Heat and Mass Transfer*, 15(2):301–314, 1972.

[126] A N Kolmogorov. Equations of turbulent motion in an incompressible fluid. *Physics*, 6(1–2):56–58, 1942.

[127] D C Wilcox and I E Alber. A turbulence model for high speed flows. In *Proceedings of the 1972 Heat Transfer & Fluid Mechanics*, pages 231–252. Stanford University Press, 1972.

[128] D C Wilcox. *Turbulence modeling for CFD*. DCW industries La Canada, CA, 2 edition, 1998.

[129] B J Daly and F H Harlow. Transport equations in turbulence. *Physics of Fluids (1958-1988)*, 13(11):2634–2649, 1970.

[130] The OpenFOAM Foundation. *OpenFOAM v6 User Guide*.

[131] E Robertson, V Choudhury, S Bhushan, and D K Walters. Validation of OpenFOAM numerical methods and turbulence models for incompressible bluff body flows. *Computers & Fluids*, 123:122–145, 2015.

[132] N Ashton and V Skaperdas. Verification and validation of OpenFOAM for high-lift aircraft flows. *Journal of Aircraft*, pages 1–17, 2019.

[133] J H Ferziger and M Peric. *Computational methods for fluid dynamics*. Springer Science & Business Media, 2012.

[134] R Courant, E Isaacson, and M Rees. On the solution of nonlinear hyperbolic differential equations by finite differences. *Communications on Pure and Applied Mathematics*, 5(3):243–255, 1952.

[135] R F Warming and R M Beam. Upwind second-order difference schemes and applications in aerodynamic flows. *AIAA Journal*, 14(9):1241–1249, 1976.

[136] T Barth and D Jespersen. The design and application of upwind schemes on unstructured meshes. In *27th Aerospace Sciences Meeting*, 1989.

[137] S-E Kim, B Makarov, and Caraeni D. A multi-dimensional linear reconstruction scheme for arbitrary unstructured grids. In *16th AIAA Computational Fluid Dynamics Conference*, page 3990, 2003.

[138] S V Patankar and D B Spalding. A calculation procedure for the transient and steady-state behavior of shell-and-tube heat exchangers. Technical Report EF/TN/A/48, Imperial College, 1972.

[139] J P Van Doormaal and G D Raithby. Enhancements of the SIMPLE method for predicting incompressible fluid flows. *Numerical heat transfer*, 7(2):147–163, 1984.

[140] F Menter. Zonal two equation $k-\omega$ turbulence models for aerodynamic flows. In *23rd Fluid Dynamics, Plasmadynamics, and Lasers Conference*, page 2906, 1993.

[141] U Schumann. Realizability of Reynolds-stress turbulence models. *Physics of Fluids (1958-1988)*, 20(5):721–725, 1977.

[142] W C Reynolds. Fundamentals of turbulence for turbulence modeling and simulation. In *Modern Theoretical and Experimental Approaches to Turbulent Flow Structure and its Modelling*, 1987.

[143] T-H Shih, J Zhu, and J L Lumley. A realizable Reynolds stress algebraic equation model. Technical report, NASA, 1993.

[144] S Tavoularis and S Corrsin. Experiments in nearly homogenous turbulent shear flow with a uniform mean temperature gradient. part 1. *Journal of Fluid Mechanics*, 104:311–347, 1981.

[145] I Kimura and T Hosoda. A non-linear $k-\varepsilon$ model with realizability for prediction of flows around bluff bodies. *International Journal for Numerical Methods in Fluids*, 42(8):813–837, 2003.

[146] P A Durbin and B A Pettersson Reif. *Statistical theory and modeling for turbulent flows*. John Wiley & Sons, 2011.

[147] S B Pope. *Turbulent flows*. Cambridge University Press, 2000.

[148] M Lee and R D Moser. Direct numerical simulation of turbulent channel flow up to $Re_\tau \approx 5200$. *Journal of Fluid Mechanics*, 774:395–415, 2015.

[149] B E Launder. *Low-Reynolds number turbulence near walls*. University of Manchester Institute of Science and Technology (UMIST) Department of Mechanical Engineering, 1986.

[150] P A Durbin. Near-wall turbulence closure modeling without "damping functions". *Theoretical and Computational Fluid Dynamics*, 3(1):1–13, 1991.

[151] P A Durbin. Separated flow computations with the $k-\varepsilon-v^2$ model. *AIAA Journal*, 33(4):659–664, 1995.

[152] R N Meroney and P Bradshaw. Turbulent boundary-layer growth over a longitudinally curved surface. *AIAA Journal*, 13(11):1448–1453, 1975.

[153] C L Lawson and R J Hanson. *Solving least squares problems*. Prentice Hall, 1974.

[154] J W Eaton, D Bateman, S Hauberg, and R Wehbring. *GNU Octave version 5.1.0 manual: a high-level interactive language for numerical computations*, 2019.

[155] H Fadhila, H Medina, S Aleksandrova, and S Benjamin. A new non-linear RANS model with enhanced near-wall treatment of turbulence anisotropy. *Applied Mathematical Modelling*, 82:293–313, 2020.

[156] F-S Lien and P A Durbin. Non-linear $k-\varepsilon-v^2$ modelling with application to high-lift. In *Proceedings of the Summer Program*, pages 5–22. Stanford University Center for Turbulence Research, 1996.

[157] J Coupland. ERCOFTAC special interest group on laminar to turbulent transition and retransition. *T3A and T3B Test Cases*, 1990.

[158] R Abid. Evaluation of two-equation turbulence models for predicting transitional flows. *International Journal of Engineering Science*, 31(6):831–840, 1993.

[159] C L Rumsey, B A Pettersson Reif, and T B Gatski. Arbitrary steady-state solutions with the $k-\varepsilon$ model. *AIAA Journal*, 44(7):1586–1592, 2006.

[160] R J Volino and T W Simon. Boundary layer transition under high free-stream turbulence and strong acceleration conditions: part 2—turbulent transport results. *Journal of Heat Transfer*, 119(3):427–432, 1997.

[161] D K Walters and J H Leylek. A new model for boundary layer transition using a single-point RANS approach. *Journal of Turbomachinery*, 126(1):193–202, 2004.

[162] D Monson, H Seegmiller, and P McConnaughey. Comparison of experiment with calculations using curvature-corrected zero and two equation turbulence models for a two-dimensional U-duct. In *21st Fluid Dynamics, Plasma Dynamics and Lasers Conference*, page 1484, 1990.

[163] P H Hoffmann, K C Muck, and P Bradshaw. The effect of concave surface curvature on turbulent boundary layers. *Journal of Fluid mechanics*, 161:371–403, 1985.

[164] R J Clarkson, S F Benjamin, N S Girgis, and S Richardson. Theoretical and experimental investigation of the flow in catalytic converters. In *IMechE Seminar on the Validation of Computational Techniques in Vehicle Design*, 1994.

[165] S F Benjamin, R J Clarkson, N Haimad, and N S Girgis. An experimental and predictive study of the flow field in axisymmetric automotive exhaust catalyst systems. Technical report, SAE Technical Paper, 1996.

[166] A K Mat Yamin. *Pulsating flow studies in a planar wide-angled diffuser upstream of automotive catalyst monoliths*. PhD thesis, Coventry University, 2012.

[167] A K Mat Yamin, S F Benjamin, and C A Roberts. Pulsating flow in a planar diffuser upstream of automotive catalyst monoliths. *International Journal of Heat and Fluid Flow*, 40:43–53, 2013.

[168] S Porter, A K Mat Yamin, S Aleksandrova, S Benjamin, C A Roberts, and J Saul. An assessment of CFD applied to steady flow in a planar diffuser upstream of an automotive catalyst monolith. *SAE International Journal of Engines*, 7(4):1697–1704, 2014.

[169] S Porter. *An assessment of CFD applied to a catalytic converter system with planar diffuser*. PhD thesis, Coventry University, 2016.

[170] S Porter, J Saul, S Aleksandrova, H Medina, and S Benjamin. Hybrid flow modelling approach applied to automotive catalysts. *Applied Mathematical Modelling*, 40(19-20):8435–8445, 2016.

[171] D W Wendland, P L Sorrell, and J E Kreucher. Sources of monolith catalytic converter pressure loss. *SAE Transactions*, pages 1004–1016, 1991.

[172] C U Buice and J K Eaton. Experimental investigation of flow through an asymmetric plane diffuser. Technical report, Center for Turbulence Research, NASA Ames/Stanford University, 1997. Annual Research Briefs.

[173] R Aris. Models of the catalytic monolith. In D B Spalding, editor, *Physicochemical Hydrodynamics: V. G. Levich Festschrift*, pages 815–825. Oxford: Advance Publications Ltd, 1977.

[174] M Muskat. The flow of homogeneous fluids through porous media. *Soil Science*, 46(2):169, 1938.

[175] J A Schetz and A E Fuhs. *Fundamentals of fluid mechanics*. John Wiley & Sons, 1999.

[176] S Parneix, P A Durbin, and M Behnia. Computation of 3-D turbulent boundary layers using the V2F model. *Flow, Turbulence and Combustion*, 60(1):19–46, 1998.

[177] S Parneix, M Behnia, and P A Durbin. Predictions of turbulent heat transfer in an axisymmetric jet impinging on a heated pedestal. *Journal of Heat Transfer*, 121(1):43–49, 1999.

[178] A Sveningsson, B A Pettersson Reif, and L Davidson. Modelling the entrance region in a plane asymmetric diffuser by elliptic relaxation. In *4th International Symposium on Turbulence and Shear Flow Phenomena*, 2005.

[179] B A Pettersson Reif. A nonlinear eddy-viscosity model for near-wall turbulence. In *38th Aerospace Sciences Meeting and Exhibit*. American Institute of Aeronautics and Astronautics, 2000.

[180] G Iaccarino. Predictions of a turbulent separated flow using commercial cfd codes. *Journal of Fluids Engineering*, 123(4):819–828, 2001.

[181] D Cokljat, S-E Kim, G Iaccarino, and P Durbin. A comparative assessment of the v2f model for recirculating flows. In *41st Aerospace Sciences Meeting and Exhibit*, page 765, 2003.

[182] N Haimad. *A theoretical and experimental investigation of the flow performance of automotive catalytic converters*. PhD thesis, Coventry University, 1997.

[183] V Kolář. Vortex identification: New requirements and limitations. *International Journal of Heat and Fluid Flow*, 28(4):638–652, 2007.

[184] J Jeong and F Hussain. On the identification of a vortex. *Journal of Fluid Mechanics*, 285:69–94, 1995.

[185] I H Rusli, S Aleksandrova, H Medina, and S F Benjamin. The effect of swirl on the flow uniformity in automotive exhaust catalysts. Technical report, SAE Technical Paper, 2017.

[186] I H Rusli, S Aleksandrova, H Medina, and S F Benjamin. Using single-sensor hot-wire anemometry for velocity measurements in confined swirling flows. *Measurement*, 129:277–280, 2018.

[187] P Skusiewicz. Effect of swirl on the flow distribution across automotive emissions after-treatment devices. Master's thesis, Coventry University, 2012.

[188] W Leuckel. Swirl intensities, swirl types and energy losses of different swirl generating devices. Technical Report G02/a/16, IFRF, 1967.

[189] D W Wendland and W R Matthes. Visualization of automotive catalytic converter internal flows. *SAE Transactions*, pages 729–742, 1986.

[190] M-C Lai, J-Y Kim, C-Y Cheng, P Li, G Chui, and J D Pakko. Three-dimensional simulations of automotive catalytic converter internal flow. *SAE Transactions*, pages 241–250, 1991.

[191] R J Clarkson. *A theoretical and experimental study of automotive catalytic converters*. PhD thesis, Coventry University, 1995.

[192] N A Chigier and J M Beér. Velocity and static-pressure distributions in swirling air jets issuing from annular and divergent nozzles. *Journal of Basic Engineering*, 86(4):788–796, 1964.

[193] H J Sheen, W J Chen, S Y Jeng, and T L Huang. Correlation of swirl number for a radial-type swirl generator. *Experimental Thermal and Fluid Science*, 12(4):444–451, 1996.

[194] J C R Hunt, A A Wray, and P Moin. Eddies, streams, and convergence zones in turbulent flows. In *Proceedings of the Summer Program*. Stanford University Center for Turbulence Research, 1988.

[195] O Lucca-Negro and T O'Doherty. Vortex breakdown: a review. *Progress in Energy and Combustion Science*, 27(4):431–481, 2001.

[196] C L Rumsey, T B Gatski, W K Anderson, and E J Nielsen. Isolating curvature effects in computing wall-bounded turbulent flows. *International Journal of Heat and Fluid Flow*, 22(6):573–582, 2001.

[197] A Hellsten. Curvature corrections for algebraic Reynolds stress modeling A discussion. *AIAA journal*, 40(9):1909–1911, 2002.

[198] X Wang and S Thangam. Development and application of an anisotropic two-equation model for flows with swirl and curvature. *Journal of Applied Mechanics*, 73(3):397–404, 2006.

Appendix A

Derivation of turbulence equations

A.1 The Navier-Stokes equations

The derivation of the Navier-Stokes equations that follows is done using the the differential fluid elemental approach.

Starting with Newton's second law:

$$m \cdot \vec{a} = \sum \vec{F} \tag{A.1}$$

Using the definition of acceleration

$$\vec{a}(t) = \frac{D\overrightarrow{U(t)}}{Dt} \tag{A.2}$$

yields

$$m \cdot \frac{D\vec{U}}{Dt} = \sum \vec{F} \tag{A.3}$$

The total force can be expressed as the sum of body forces and surface forces:

$$m \cdot \frac{D\vec{U}}{Dt} = \sum \vec{F}_{body} + \sum \vec{F}_{surface} \tag{A.4}$$

Defining the velocity as $\vec{U} = (u, v, w)$ and the mass as $m = \rho\, dx\, dy\, dz$ and considering the x-component only yields

$$\rho\, dx\, dy\, dz \frac{Du}{Dt} = \sum \vec{F}_{x,body} + \sum \vec{F}_{x,surface} \tag{A.5}$$

The stress tensor due to surface forces is defined in (A.6). The components of this tensor are depicted in Figure A.1.

$$\sigma_{ij} = \begin{bmatrix} \sigma_{xx} & \sigma_{yx} & \sigma_{zx} \\ \sigma_{xy} & \sigma_{yy} & \sigma_{zy} \\ \sigma_{xz} & \sigma_{yz} & \sigma_{zz} \end{bmatrix} \tag{A.6}$$

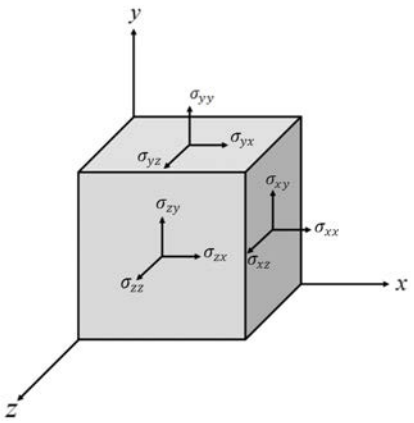

Figure A.1: Notation for stresses

The surface forces consist of pressure and viscous forces. The stress tensor due to viscous forces is defined as:

$$\tau_{ij} = \begin{bmatrix} \tau_{xx} & \tau_{yx} & \tau_{zx} \\ \tau_{xy} & \tau_{yy} & \tau_{zy} \\ \tau_{xz} & \tau_{yz} & \tau_{zz} \end{bmatrix} \tag{A.7}$$

Considering the x-component of the surface forces:

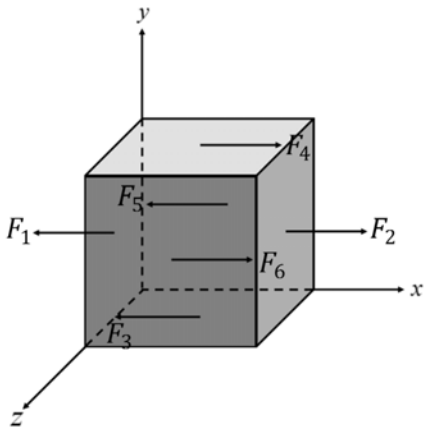

Figure A.2: Infinitesimally small fluid element showing the surface forces in the x direction only

The net force on the differential control surface is the result of gradients or differences of the surface

forces:

$$\begin{aligned} F_1 &= -\sigma_{xx}\, dy\, dz \\ F_2 &= \left(\sigma_{xx} + \frac{\partial \sigma_{xx}}{\partial x}\right)\left(dy\ dz \right. \\ F_3 &= -\sigma_{yx}\ dx\ dz \\ F_4 &= \left(\sigma_{yx} + \frac{\partial \sigma_{yx}}{\partial y}\right)\left(dx\ dz \right. \\ F_5 &= -\sigma_{zx}\ dx\ dy \\ F_6 &= \left(\sigma_{zx} + \frac{\partial \sigma_{zx}}{\partial z}\right)\left(dx\ dy \right. \end{aligned} \tag{A.8}$$

Taking the summation of the forces to get the total surface forces yields

$$\sum F_{x,surface} = F_1 + F_2 + F_3 + F_4 + F_5 + F_6 = \left(\frac{\partial \sigma_{xx}}{\partial x} + \frac{\partial \sigma_{yx}}{\partial y} + \frac{\partial \sigma_{zx}}{\partial z}\right)\ dx\ dy\ dz \tag{A.9}$$

Assuming that the only significant body force is due to gravity:

$$\sum F_{x,body} = m \cdot g_x = \rho\ dx\ dy\ dz\ g_x \tag{A.10}$$

Substituting the body and surface forces to equation (A.4):

$$\begin{aligned} \rho\ dx\ dy\ dz \frac{Du}{Dt} &= \rho\ dx\ dy\ dz\ g_x + \left(\frac{\partial \sigma_{xx}}{\partial x} + \frac{\partial \sigma_{yx}}{\partial y} + \frac{\partial \sigma_{zx}}{\partial z}\right)\left(dx\ dy\ dz \right. \\ \rho \frac{Du}{Dt} &= \rho g_x + \frac{\partial \sigma_{xx}}{\partial x} + \frac{\partial \sigma_{yx}}{\partial y} + \frac{\partial \sigma_{zx}}{\partial z} \end{aligned} \tag{A.11}$$

Expanding the total derivative for u:

$$\rho\left(\frac{\partial u}{\partial t} + u\frac{\partial u}{\partial x} + v\frac{\partial u}{\partial y} + w\frac{\partial u}{\partial z}\right)\left(= \rho g_x + \frac{\partial \sigma_{xx}}{\partial x} + \frac{\partial \sigma_{yx}}{\partial y} + \frac{\partial \sigma_{zx}}{\partial z}\right. \tag{A.12}$$

Splitting the stress tensor into the components due to pressure and viscous forces:

$$\sigma_{ij} = \left[\begin{matrix} -p + \tau_{xx} & \tau_{yx} & \tau_{zx} \\ \tau_{xy} & -p + \tau_{yy} & \tau_{zy} \\ \tau_{xz} & \tau_{yz} & -p + \tau_{zz} \end{matrix}\right]\left(\right. \tag{A.13}$$

Substituting the x-component in (A.13) into (A.12):

$$\rho\left(\frac{\partial u}{\partial t} + u\frac{\partial u}{\partial x} + v\frac{\partial u}{\partial y} + w\frac{\partial u}{\partial z}\right)\left(= \rho g_x - \frac{\partial p}{\partial x} + \frac{\partial \tau_{xx}}{\partial x} + \frac{\partial \tau_{yx}}{\partial y} + \frac{\partial \tau_{zx}}{\partial z}\right. \tag{A.14}$$

Using the Newton's law of viscosity, the viscous stresses can be related to elemental strain rates and dynamic and second viscosities. The strain rate tensor is defined as:

$$\varepsilon_{ij} = \begin{bmatrix} \varepsilon_{xx} & \varepsilon_{yx} & \varepsilon_{zx} \\ \varepsilon_{xy} & \varepsilon_{yy} & \varepsilon_{zy} \\ \varepsilon_{xz} & \varepsilon_{yz} & \varepsilon_{zz} \end{bmatrix} = \begin{bmatrix} \frac{\partial u}{\partial x} & \frac{1}{2}\left(\frac{\partial v}{\partial x} + \frac{\partial u}{\partial y}\right) & \frac{1}{2}\left(\frac{\partial w}{\partial x} + \frac{\partial u}{\partial z}\right) \\ \frac{1}{2}\left(\frac{\partial u}{\partial y} + \frac{\partial v}{\partial x}\right) & \frac{\partial v}{\partial y} & \frac{1}{2}\left(\frac{\partial w}{\partial y} + \frac{\partial v}{\partial z}\right) \\ \frac{1}{2}\left(\frac{\partial u}{\partial z} + \frac{\partial w}{\partial x}\right) & \frac{1}{2}\left(\frac{\partial v}{\partial z} + \frac{\partial w}{\partial y}\right) & \frac{\partial w}{\partial z} \end{bmatrix} \tag{A.15}$$

The viscous stresses in the x-direction are therefore:

$$\begin{aligned} \tau_{xx} &= 2\mu\frac{\partial u}{\partial x} + \lambda\nabla\cdot\vec{U} \\ \tau_{yx} &= \mu\left(\frac{\partial v}{\partial x} + \frac{\partial u}{\partial y}\right) \\ \tau_{zx} &= \mu\left(\frac{\partial w}{\partial x} + \frac{\partial u}{\partial z}\right) \end{aligned} \tag{A.16}$$

Substituting (A.16) into (A.14) gives:

$$\rho\left(\frac{\partial u}{\partial t} + u\frac{\partial u}{\partial x} + v\frac{\partial u}{\partial y} + w\frac{\partial u}{\partial z}\right) = \rho g_x - \frac{\partial p}{\partial x} + \frac{\partial}{\partial x}\left[2\mu\frac{\partial u}{\partial x} + \lambda\nabla\cdot\vec{U}\right] + \frac{\partial}{\partial y}\left[\mu\left(\frac{\partial v}{\partial x} + \frac{\partial u}{\partial y}\right)\right] \tag{A.17}$$

$$+ \frac{\partial}{\partial z}\left[\mu\left(\frac{\partial w}{\partial x} + \frac{\partial u}{\partial z}\right)\right] \tag{A.18}$$

For an incompressible flow, $\nabla\cdot\vec{U} = 0$, therefore (A.18) can be simplified to:

$$\rho\left(\frac{\partial u}{\partial t} + u\frac{\partial u}{\partial x} + v\frac{\partial u}{\partial y} + w\frac{\partial u}{\partial z}\right) = \rho g_x - \frac{\partial p}{\partial x} + 2\mu\frac{\partial}{\partial x}\left(\frac{\partial u}{\partial x}\right) + \mu\frac{\partial}{\partial y}\left(\frac{\partial v}{\partial x} + \frac{\partial u}{\partial y}\right) + \mu\frac{\partial}{\partial z}\left(\frac{\partial w}{\partial x} + \frac{\partial u}{\partial z}\right) \tag{A.19}$$

Rearranging this equation results in

$$\rho\left(\frac{\partial u}{\partial t} + u\frac{\partial u}{\partial x} + v\frac{\partial u}{\partial y} + w\frac{\partial u}{\partial z}\right) = \rho g_x - \frac{\partial p}{\partial x} + \mu\frac{\partial}{\partial x}\left(\frac{\partial u}{\partial x}\right) + \mu\frac{\partial}{\partial y}\left(\frac{\partial u}{\partial y}\right) + \mu\frac{\partial}{\partial z}\left(\frac{\partial u}{\partial z}\right) \tag{A.20}$$

$$+ \mu\frac{\partial}{\partial x}\left(\frac{\partial u}{\partial x} + \frac{\partial v}{\partial y} + \frac{\partial w}{\partial z}\right) \tag{A.21}$$

The $\left(\frac{\partial u}{\partial x} + \frac{\partial v}{\partial y} + \frac{\partial w}{\partial z}\right)$ term is zero due to continuity. Therefore:

$$\rho\left(\frac{\partial u}{\partial t} + u\frac{\partial u}{\partial x} + v\frac{\partial u}{\partial y} + w\frac{\partial u}{\partial z}\right) = \rho g_x - \frac{\partial p}{\partial x} + \mu\left(\frac{\partial^2 u}{\partial x^2} + \frac{\partial^2 u}{\partial y^2} + \frac{\partial^2 u}{\partial z^2}\right) \tag{A.22}$$

Following a similar procedure, the momentum equations for y and z components can be derived to be:

$$\rho\left(\frac{\partial v}{\partial t} + u\frac{\partial v}{\partial x} + v\frac{\partial v}{\partial y} + w\frac{\partial v}{\partial z}\right) = \rho g_y - \frac{\partial p}{\partial y} + \mu\left(\frac{\partial^2 v}{\partial x^2} + \frac{\partial^2 v}{\partial y^2} + \frac{\partial^2 v}{\partial z^2}\right) \tag{A.23}$$

$$\rho\left(\frac{\partial w}{\partial t}+u\frac{\partial w}{\partial x}+v\frac{\partial w}{\partial y}+w\frac{\partial w}{\partial z}\right)=\rho g_z-\frac{\partial p}{\partial z}+\mu\left(\frac{\partial^2 w}{\partial x^2}+\frac{\partial^2 w}{\partial y^2}+\frac{\partial^2 w}{\partial z^2}\right) \tag{A.24}$$

Or expressing it using the index notations in which $i, j = 1, 2, 3$ to represent three-dimensionality:

$$\rho\left(\frac{\partial u_j}{\partial t}+u_i\frac{\partial u_j}{\partial x_i}\right)=\rho g_j-\frac{\partial p}{\partial x_j}+\mu\left(\frac{\partial^2 u_j}{\partial x_i^2}\right) \tag{A.25}$$

A.2 Reynolds-averaged Navier-Stokes equations

To derive the time-averaged of the Navier-Stokes equations, the flow quantities can be split into a mean (average) part and a fluctuating part. This is described in (A.26) using index notations:

$$u_i = U_i + u_i' \tag{A.26}$$

where u_i is the instantaneous quantity, U_i is the average quantity, and u_i' is the deviation from average (fluctuation).

Defining the continuity equation in its instantaneous components:

$$\frac{\partial u}{\partial x}+\frac{\partial v}{\partial y}+\frac{\partial w}{\partial z}=0 \tag{A.27}$$

Expanding the instantaneous velocities to their the average and fluctuating components:

$$\frac{\partial(U+u')}{\partial x}+\frac{\partial(V+v')}{\partial y}+\frac{\partial(W+w')}{\partial z}=0 \tag{A.28}$$

Taking the time-average yields

$$\frac{\partial\overline{(U+u')}}{\partial x}+\frac{\partial\overline{(V+v')}}{\partial y}+\frac{\partial\overline{(W+w')}}{\partial z}=0 \tag{A.29}$$

By definition, the average of the mean component is the mean component itself and the average of the fluctuating component is zero. Therefore,

$$\frac{\partial U}{\partial x}+\frac{\partial V}{\partial y}+\frac{\partial W}{\partial z}=0 \tag{A.30}$$

or expressing it using index notations:

$$\frac{\partial U_i}{\partial x_i}=0 \tag{A.31}$$

Rewriting the x-component of the momentum equation, but considering only the pressure and viscous stresses:

$$\rho\left(\frac{\partial u}{\partial t}+\frac{\partial uu}{\partial x}+\frac{\partial uv}{\partial y}+\frac{\partial uw}{\partial z}\right)=-\frac{\partial p}{\partial x}+\mu\left(\frac{\partial^2 u}{\partial x^2}+\frac{\partial^2 u}{\partial y^2}+\frac{\partial^2 u}{\partial z^2}\right) \tag{A.32}$$

Splitting the flow quantities into their mean and fluctuating components and averaging:

$$\begin{aligned}\rho\quad &\frac{\partial\overline{(U+u')}}{\partial t}+\frac{\partial\overline{(U+u')(U+u')}}{\partial x}+\frac{\partial\overline{(U+u')(V+v')}}{\partial y}+\frac{\partial\overline{(U+u')(W+w')}}{\partial z}\\ &=-\frac{\partial\overline{(P+p')}}{\partial x}+\mu\quad\frac{\partial^2\overline{(U+u')}}{\partial x^2}+\frac{\partial^2\overline{(U+u')}}{\partial y^2}+\frac{\partial^2\overline{(U+u')}}{\partial z^2}\end{aligned} \tag{A.33}$$

Expanding the multiplications yields

$$\begin{aligned}\rho\quad &\frac{\partial\overline{(U+u')}}{\partial t}+\frac{\partial\overline{(UU+2Uu'+u'u')}}{\partial x}+\frac{\partial\overline{(UV+Uv'+u'V+u'v')}}{\partial y}+\frac{\partial\overline{(UW+Uw'+u'W+u'w')}}{\partial z}\\ &=-\frac{\partial\overline{(P+p')}}{\partial x}+\mu\quad\frac{\partial^2\overline{(U+u')}}{\partial x^2}+\frac{\partial^2\overline{(U+u')}}{\partial y^2}+\frac{\partial^2\overline{(U+u')}}{\partial z^2}\end{aligned} \tag{A.34}$$

By definition, the average of a mean component is itself and the average of a fluctuating component is zero. However, the average of a correlation of two fluctuating components is not zero. Applying these rules gives

$$\rho\left(\frac{\partial U}{\partial t}+\frac{\partial(UU+\overline{u'u'})}{\partial x}+\frac{\partial(UV+\overline{u'v'})}{\partial y}+\frac{\partial(UW+\overline{u'w'})}{\partial z}\right)=-\frac{\partial P}{\partial x}+\mu\left(\frac{\partial^2 U}{\partial x^2}+\frac{\partial^2 U}{\partial y^2}+\frac{\partial^2 U}{\partial z^2}\right) \tag{A.35}$$

Rearranging this equation to give

$$\frac{\partial U}{\partial t}+U\frac{\partial U}{\partial x}+V\frac{\partial U}{\partial y}+W\frac{\partial U}{\partial z}=-\frac{1}{\rho}\frac{\partial P}{\partial x}+\frac{\partial}{\partial x}\left(\nu\frac{\partial U}{\partial x}-\overline{u'u'}\right)+\frac{\partial}{\partial y}\left(\nu\frac{\partial U}{\partial y}-\overline{u'v'}\right)+\frac{\partial}{\partial z}\left(\nu\frac{\partial U}{\partial z}-\overline{u'w'}\right) \tag{A.36}$$

Following the same procedure for y and z momentum equations yields the following equations:

$$\frac{\partial V}{\partial t}+U\frac{\partial V}{\partial x}+V\frac{\partial V}{\partial y}+W\frac{\partial V}{\partial z}=-\frac{1}{\rho}\frac{\partial P}{\partial y}+\frac{\partial}{\partial x}\left(\nu\frac{\partial V}{\partial x}-\overline{v'u'}\right)+\frac{\partial}{\partial y}\left(\nu\frac{\partial V}{\partial y}-\overline{v'v'}\right)+\frac{\partial}{\partial z}\left(\nu\frac{\partial V}{\partial z}-\overline{v'w'}\right) \tag{A.37}$$

$$\frac{\partial W}{\partial t}+U\frac{\partial W}{\partial x}+V\frac{\partial W}{\partial y}+W\frac{\partial W}{\partial z}=-\frac{1}{\rho}\frac{\partial P}{\partial z}+\frac{\partial}{\partial x}\left(\nu\frac{\partial W}{\partial x}-\overline{w'u'}\right)+\frac{\partial}{\partial y}\left(\nu\frac{\partial W}{\partial y}-\overline{w'v'}\right)+\frac{\partial}{\partial z}\left(\nu\frac{\partial W}{\partial z}-\overline{w'w'}\right) \tag{A.38}$$

Or expressing it using the index notations:

$$\frac{\partial U_j}{\partial t} + U_i \frac{\partial U_j}{\partial x_i} = -\frac{1}{\rho}\frac{\partial P}{\partial x_j} + \frac{\partial}{\partial x_i}\left(\nu\left(\frac{\partial U_j}{\partial x_i} - \overline{u_i' u_j'}\right)\right) \tag{A.39}$$

in which $\overline{u_i' u_j'}$ is the Reynolds stress tensor:

$$\overline{u_i' u_j'} = \begin{bmatrix} \overline{u'u'} & \overline{u'v'} & \overline{u'w'} \\ \overline{v'u'} & \overline{v'v'} & \overline{v'w'} \\ \overline{w'u'} & \overline{w'v'} & \overline{w'w'} \end{bmatrix} \tag{A.40}$$

A.3 Reynolds stress and turbulent kinetic energy transport equations

Turbulent kinetic energy is defined to be the trace of the Reynolds stress tensor:

$$k = \frac{1}{2}(\overline{u'u'} + \overline{v'v'} + \overline{w'w'}) \tag{A.41}$$

or using the index notations:

$$k = \frac{1}{2}\overline{u_j' u_j'} \tag{A.42}$$

First, the momentum equation for the fluctuating velocity is derived by using the definition:

$$u_j' = u_j - U_j \tag{A.43}$$

The momentum equation for instantaneous velocity is

$$\frac{\partial u_j}{\partial t} + u_i \frac{\partial u_j}{\partial x_i} = -\frac{1}{\rho}\frac{\partial p}{\partial x_j} + \frac{\partial}{\partial x_i}\left(\nu\left(\frac{\partial u_j}{\partial x_i}\right)\right) \tag{A.44}$$

The momentum equation for average velocity is

$$\frac{\partial U_j}{\partial t} + U_i \frac{\partial U_j}{\partial x_i} = -\frac{1}{\rho}\frac{\partial P}{\partial x_j} + \frac{\partial}{\partial x_i}\left(\nu\left(\frac{\partial U_j}{\partial x_i} - \overline{u_i' u_j'}\right)\right) \tag{A.45}$$

Subtracting (A.45) from (A.44) to get the momentum equation for u_j':

$$\frac{\partial}{\partial t}(u_j - U_j) + \frac{\partial}{\partial x_i}(u_i u_j - U_i U_j) = -\frac{1}{\rho}\frac{\partial}{\partial x_j}(p - P) + \frac{\partial}{\partial x_i}\left[\nu\left(\frac{\partial}{\partial x_i}(u_j - U_j) + \overline{u_i' u_j'}\right)\right] \tag{A.46}$$

Expanding the instantaneous components into their average and fluctuating parts and rearranging gives:

$$\frac{\partial u_j'}{\partial t} + U_i \frac{\partial u_j'}{\partial x_i} + u_i' \frac{\partial U_j}{\partial x_i} + u_i' \frac{\partial u_j'}{\partial x_i} = -\frac{1}{\rho}\frac{\partial p'}{\partial x_j} + \frac{\partial}{\partial x_i}\left[\nu\left(\frac{\partial u_j'}{\partial x_i} + \overline{u_i' u_j'}\right]\right(\tag{A.47}$$

Replacing the index i with k, and multiplying by u_i' gives

$$u_i' \frac{\partial u_j'}{\partial t} + U_k u_i' \frac{\partial u_j'}{\partial x_k} + u_i' u_k' \frac{\partial U_j}{\partial x_k} + u_i' u_k' \frac{\partial u_j'}{\partial x_k} = -\frac{1}{\rho} u_i' \frac{\partial p'}{\partial x_j} + u_i' \frac{\partial}{\partial x_k}\left[\nu\left(\frac{\partial u_j'}{\partial x_k} + \overline{u_k' u_j'}\right]\right(\tag{A.48}$$

Adding equation (A.48) to itself with indices i and j swapped yields

$$\begin{aligned} u_i' \frac{\partial u_j'}{\partial t} + u_j' \frac{\partial u_i'}{\partial t} + U_k u_i' \frac{\partial u_j'}{\partial x_k} + U_k u_j' \frac{\partial u_i'}{\partial x_k} + u_i' u_k' \frac{\partial U_j}{\partial x_k} + u_j' u_k' \frac{\partial U_i}{\partial x_k} + u_i' u_k' \frac{\partial u_j'}{\partial x_k} + u_j' u_k' \frac{\partial u_i'}{\partial x_k} \\ = -\frac{1}{\rho} u_i' \frac{\partial p'}{\partial x_j} - \frac{1}{\rho} u_j' \frac{\partial p'}{\partial x_i} + u_i' \frac{\partial}{\partial x_k}\left[\nu\left(\frac{\partial u_j'}{\partial x_k} + \overline{u_k' u_j'}\right]\right(+ u_j' \frac{\partial}{\partial x_k}\left[\nu\left(\frac{\partial u_i'}{\partial x_k} + \overline{u_k' u_i'}\right]\right(\end{aligned} \tag{A.49}$$

Simplifying using the product rule of derivative gives

$$\begin{aligned} \frac{\partial u_i' u_j'}{\partial t} + U_k \frac{\partial u_i' u_j'}{\partial x_k} + u_i' u_k' \frac{\partial U_j}{\partial x_k} + u_j' u_k' \frac{\partial U_i}{\partial x_k} + \frac{\partial u_i' u_j' u_k'}{\partial x_k} \\ = -\frac{1}{\rho} u_i' \frac{\partial p'}{\partial x_j} - \frac{1}{\rho} u_j' \frac{\partial p'}{\partial x_i} + u_i' \frac{\partial}{\partial x_k}\left(\nu\left(\frac{\partial u_j'}{\partial x_k}\right)\right(+ u_j' \frac{\partial}{\partial x_k}\left(\nu\left(\frac{\partial u_i'}{\partial x_k}\right)\right(+ u_i' \frac{\partial \overline{u_k' u_j'}}{\partial x_k} + u_j' \frac{\partial \overline{u_k' u_i'}}{\partial x_k} \end{aligned} \tag{A.50}$$

The pressure terms (the first and second terms on the right hand side) can be split into:

$$\begin{aligned} -\frac{1}{\rho}\left[\nu\left(u_i' \frac{\partial p'}{\partial x_j} + u_j' \frac{\partial p'}{\partial x_i}\right]\right(&= -\frac{1}{\rho}\left[\left(\frac{\partial (p' u_i')}{\partial x_j} - p' \frac{\partial u_i'}{\partial x_j}\right) + \left(\frac{\partial (p' u_j')}{\partial x_i} - p' \frac{\partial u_j'}{\partial x_i}\right)\right] \\ &= \frac{p'}{\rho}\left(\frac{\partial u_i'}{\partial x_j} + \frac{\partial u_j'}{\partial x_i}\right) - \frac{1}{\rho}\frac{\partial (p' u_i')}{\partial x_j} - \frac{1}{\rho}\frac{\partial (p' u_j')}{\partial x_i} \\ &= \frac{p'}{\rho}\left(\frac{\partial u_i'}{\partial x_j} + \frac{\partial u_j'}{\partial x_i}\right) - \frac{1}{\rho}\frac{\partial}{\partial x_k}\left[p'(\delta_{kj} u_i' + \delta_{ki} u_j')\right] \end{aligned} \tag{A.51}$$

and the third and fourth terms on the right hand side can be rearranged into:

$$\nu\left[u_i' \frac{\partial^2 u_j'}{\partial x_k^2} + u_j' \frac{\partial^2 u_i'}{\partial x_k^2}\right] = \nu\left[\frac{\partial^2 (u_i' u_j')}{\partial x_k^2} - 2\frac{\partial u_i'}{\partial x_k}\frac{\partial u_j'}{\partial x_k}\right]\right(\tag{A.52}$$

Substituting equations (A.51) and (A.52) into (A.50) yields

$$\begin{aligned}
&\frac{\partial u_i' u_j'}{\partial t} + U_k \frac{\partial u_i' u_j'}{\partial x_k} + u_i' u_k' \frac{\partial U_j}{\partial x_k} + u_j' u_k' \frac{\partial U_i}{\partial x_k} + \frac{\partial u_i' u_j' u_k'}{\partial x_k} \\
&= \frac{p'}{\rho}\left(\frac{\partial u_i'}{\partial x_j} + \frac{\partial u_j'}{\partial x_i}\right) - \frac{1}{\rho}\frac{\partial}{\partial x_k}\left[p'(\delta_{kj}u_i' + \delta_{ki}u_j')\right] + \nu\left[\frac{\partial^2 (u_i' u_j')}{\partial x_k^2} - 2\frac{\partial u_i'}{\partial x_k}\frac{\partial u_j'}{\partial x_k}\right] + u_i'\frac{\partial \overline{u_k' u_j'}}{\partial x_k} + u_j'\frac{\partial \overline{u_k' u_i'}}{\partial x_k}
\end{aligned} \tag{A.53}$$

Rearranging and averaging results in the following transport equation for Reynolds stresses $\overline{u_i' u_j'}$:

$$\begin{aligned}
\frac{\partial \overline{u_i' u_j'}}{\partial t} + U_k \frac{\partial \overline{u_i' u_j'}}{\partial x_k} = &\overbrace{-\overline{u_i' u_k'}\frac{\partial U_j}{\partial x_k} - \overline{u_j' u_k'}\frac{\partial U_i}{\partial x_k}}^{\text{Production, } P_{ij}} \overbrace{- 2\nu\overline{\frac{\partial u_i'}{\partial x_k}\frac{\partial u_j'}{\partial x_k}}}^{\text{Dissipation, } \varepsilon_{ij}} \overbrace{+ \overline{\frac{p'}{\rho}\left(\frac{\partial u_i'}{\partial x_j} + \frac{\partial u_j'}{\partial x_i}\right)}}^{\text{Pressure-strain, } \Pi_{ij}} \\
&\underbrace{+ \frac{\partial}{\partial x_k}\left[\underbrace{\overline{u_i' u_j' u_k'}}_{\text{Turbulent}} + \underbrace{\nu\frac{\partial \overline{u_i' u_j'}}{\partial x_k}}_{\text{Viscous}} - \underbrace{\overline{\frac{p'}{\rho}(\delta_{kj}u_i' + \delta_{ki}u_j')}}_{\text{Pressure}}\right]}_{\text{Diffusion, } \mathcal{D}_{ij}}
\end{aligned} \tag{A.54}$$

Swapping the index i for j and the index k for i yields:

$$\begin{aligned}
\frac{\partial \overline{u_j' u_j'}}{\partial t} + U_i \frac{\partial \overline{u_j' u_j'}}{\partial x_i} = &-\overline{u_j' u_i'}\frac{\partial U_j}{\partial x_i} - \overline{u_j' u_i'}\frac{\partial U_j}{\partial x_i} - 2\nu\overline{\frac{\partial u_j'}{\partial x_i}\frac{\partial u_j'}{\partial x_i}} + \overline{\frac{p'}{\rho}\left(\frac{\partial u_j'}{\partial x_j} + \frac{\partial u_j'}{\partial x_i}\right)} \\
&+ \frac{\partial}{\partial x_i}\left[\overline{u_j' u_j' u_i'} + \nu\frac{\partial \overline{u_j' u_j'}}{\partial x_i} - \overline{\frac{p'}{\rho}(\delta_{ji}u_j' + \delta_{ji}u_j')}\right]
\end{aligned} \tag{A.55}$$

Using continuity $\partial u_j'/\partial x_j = 0$ and and the definition of k ($k = 0.5\overline{u_j' u_j'}$), equation (A.55) can be simplified to get the transport equation for turbulent kinetic energy:

$$\frac{\partial k}{\partial t} + U_i \frac{\partial k}{\partial x_i} = \underbrace{-\overline{u_i' u_j'}\frac{\partial U_j}{\partial x_i}}_{\text{Production, } P_k} \underbrace{- \nu\overline{\frac{\partial u_j'}{\partial x_i}\frac{\partial u_j'}{\partial x_i}}}_{\text{Dissipation, } \varepsilon} \underbrace{+ \frac{\partial}{\partial x_i}\left[-\overline{u_i'}k - \overline{\frac{p'}{\rho}u_i'} + \nu\frac{\partial k}{\partial x_i}\right]}_{\text{Diffusion, } \mathcal{D}_k} \tag{A.56}$$

Appendix B

Plane channel flow analysis

In this appendix, the simplification process to obtain the analytical solution for the Reynolds stresses in the case of a fully-developed channel flow is presented. The geometry is shown in Figure B.1.

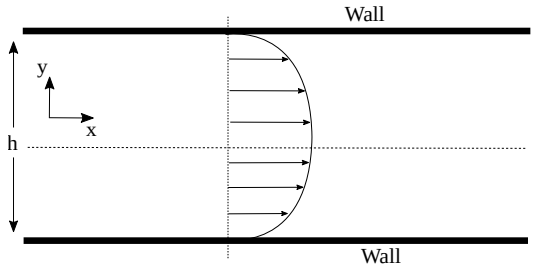

Figure B.1: Geometry of a fully-developed channel flow test case

Rewriting the Reynolds stress, $\overline{u_i' u_j'}$, formulation in relation to its anisotropy, a_{ij}:

$$\overline{u_i' u_j'} = \frac{2}{3} k \delta_{ij} + a_{ij} k \tag{B.1}$$

Using the tensor polynomial formulation for a_{ij} results in:

$$\overline{u_i' u_j'} = \frac{2}{3} k \delta_{ij} + \sum_{n=1}^{10} \beta_{(n-1)} T_{ij}^{(n)} \tag{B.2}$$

in which T_{ij} is the tensor polynomials containing 10 bases formed from the strain and rotation rate tensors:

$$
\begin{aligned}
T_{ij}^{(1)} &= S_{ij} \\
T_{ij}^{(2)} &= S_{ik}S_{kj} - II_S\delta_{ij}/3 \\
T_{ij}^{(3)} &= \Omega_{ik}S_{kj} - S_{ik}\Omega_{kj} \\
T_{ij}^{(4)} &= \Omega_{ij}\Omega_{kj} - II_\Omega\delta_{ij}/3 \\
T_{ij}^{(5)} &= S_{ik}S_{kl}\Omega_{lj} - \Omega_{ik}S_{kl}S_{lj} \\
T_{ij}^{(6)} &= S_{ik}\Omega_{kl}\Omega_{lj} + \Omega_{ik}\Omega_{kl}S_{lj} - 2IV\delta_{ij}/3 \\
T_{ij}^{(7)} &= S_{ik}S_{kl}\Omega_{lp}\Omega_{pj} + \Omega_{ik}\Omega_{kl}S_{lp}S_{pj} - 2V\delta_{ij}/3 \\
T_{ij}^{(8)} &= S_{ik}\Omega_{kl}S_{lp}S_{pj} - S_{ik}S_{kl}\Omega_{lp}S_{pj} \\
T_{ij}^{(9)} &= \Omega_{ik}S_{kl}\Omega_{lp}\Omega_{pj} - \Omega_{ik}\Omega_{kl}S_{lp}\Omega_{pj} \\
T_{ij}^{(10)} &= \Omega_{ik}S_{kl}S_{lp}\Omega_{pq}\Omega_{qj} - \Omega_{ik}\Omega_{kl}S_{lp}S_{pq}\Omega_{qj}
\end{aligned} \tag{B.3}
$$

The independent scalar invariants are described as:

$$
\begin{aligned}
II_S &= \{S_{kl}S_{lk}\} \\
II_\Omega &= \{\Omega_{kl}\Omega_{lk}\} \\
III_S &= \{S_{kl}S_{lm}S_{mk}\} \\
IV &= \{S_{kl}\Omega_{lm}\Omega_{mk}\} \\
V &= \{S_{kl}S_{lm}\Omega_{mn}\Omega_{nk}\}
\end{aligned} \tag{B.4}
$$

We know that the strain rate tensor is defined as:

$$
S_{ij} = \frac{1}{2}\left(\frac{\partial U_i}{\partial x_j} + \frac{\partial U_j}{\partial x_i}\right)\Bigg(\tag{B.5}
$$

The fully-developed channel flow can be described by the only non-zero mean-velocity component, the streamwise U, as a function of only the wall-normal coordinate, y. Therefore, there is only one non-zero velocity gradient: dU/dy. For conciseness this is referred to as λ.

For analysis in three-dimensions ($i, j = 1, 2, 3$) and applying $dU/dy = \lambda$ as the only non-zero component results in the following strain rate tensor:

$$S_{ij} = \begin{bmatrix} 0 & \frac{1}{2}\lambda & 0 \\ \frac{1}{2}\lambda & 0 & 0 \\ 0 & 0 & 0 \end{bmatrix} \tag{B.6}$$

The invariant of the first non-linear term (II_S) is therefore:

$$\{\boldsymbol{S}^2\} = \left\{ \begin{bmatrix} 0 & \frac{1}{2}\lambda & 0 \\ \frac{1}{2}\lambda & 0 & 0 \\ 0 & 0 & 0 \end{bmatrix}^2 \right\} = \left\{ \begin{bmatrix} \frac{1}{4}\lambda^2 & 0 & 0 \\ 0 & \frac{1}{4}\lambda^2 & 0 \\ 0 & 0 & 0 \end{bmatrix} \right\} = \frac{1}{4}\lambda^2 + \frac{1}{4}\lambda^2 = \frac{1}{2}\lambda^2 \tag{B.7}$$

The rotation rate tensor is defined as:

$$\Omega_{ij} = \frac{1}{2}\left(\frac{\partial U_i}{\partial x_j} - \frac{\partial U_j}{\partial x_i}\right) \tag{B.8}$$

For $i, j = 1, 2, 3$ and applying $dU/dy = \lambda$ as the only non-zero component results in:

$$\Omega_{ij} = \begin{bmatrix} 0 & \frac{1}{2}\lambda & 0 \\ -\frac{1}{2}\lambda & 0 & 0 \\ 0 & 0 & 0 \end{bmatrix} \tag{B.9}$$

Linear model

For linear model, the only term retained from equation (B.3) is the eddy-viscosity related term:

$$a_{ij} = \beta_0 S_{ij} \tag{B.10}$$

which from equation (B.1) means:

$$\frac{\overline{u_i' u_j'}}{k} - \frac{2}{3} = \beta_0 S_{ij} \tag{B.11}$$

Now we substitute the strain and rotation rate tensors previously defined in equations (B.6) and (B.9) into equation (B.11) to obtain the Reynolds stress components $\overline{u'u'}$, $\overline{v'v'}$, $\overline{w'w'}$, and $\overline{u'v'}$.

For $i = 1$ and $j = 1$ (to get $\overline{u'u'}$):

$$\frac{\overline{u'u'}}{k} - \frac{2}{3}\delta_{11} = \beta_0 S_{11} \tag{B.12}$$

$\delta_{11} = 1$ and $S_{11} = 0$ as defined in equation (B.6) so we obtain:

$$\frac{\overline{u'u'}}{k} = \frac{2}{3} \tag{B.13}$$

For $i = 2$ and $j = 2$ (to get $\overline{v'v'}$):

$$\frac{\overline{v'v'}}{k} - \frac{2}{3}\delta_{22} = \beta_0 S_{22} \tag{B.14}$$

$\delta_{22} = 1$ and $S_{22} = 0$ as defined in equation (B.6) so we obtain:

$$\frac{\overline{v'v'}}{k} = \frac{2}{3} \tag{B.15}$$

For $i = 3$ and $j = 3$ (to get $\overline{w'w'}$):

$$\frac{\overline{w'w'}}{k} - \frac{2}{3}\delta_{33} = \beta_0 S_{33} \tag{B.16}$$

$\delta_{33} = 1$ and $S_{33} = 0$ as defined in equation (B.6) so we obtain:

$$\frac{\overline{w'w'}}{k} = \frac{2}{3} \tag{B.17}$$

For $i = 1$ and $j = 2$ (to get $\overline{u'v'}$):

$$\frac{\overline{u'v'}}{k} - \frac{2}{3}\delta_{12} = \beta_0 S_{12} \tag{B.18}$$

$\delta_{12} = 0$ and $S_{12} = 1/2\lambda$ as defined in equation (B.6) so we obtain:

$$\overline{u'v'} = \frac{1}{2}\beta_0 \lambda k \tag{B.19}$$

To summarise, for linear model we have the following equations for the Reynolds stress tensor:

$$\frac{\overline{u'u'}}{k} = \frac{2}{3}, \qquad \frac{\overline{v'v'}}{k} = \frac{2}{3}, \qquad \frac{\overline{w'w'}}{k} = \frac{2}{3}, \qquad \frac{\overline{u'v'}}{k} = \frac{1}{2}\beta_0\lambda \tag{B.20}$$

The values of $\overline{u'u'}$, $\overline{v'v'}$, and $\overline{w'w'}$ are isotropic as expected.

Quadratic model

The anisotropy formulation used for the non-linear $k-\omega$ model proposed in this work, which retains the quadratic terms $T_{ij}^{(2)}$ and $T_{ij}^{(3)}$, in addition to the linear $T_{ij}^{(1)}$, is defined as:

$$a_{ij} \approx \beta_0 S_{ij} + \beta_1 \left(S_{ik}S_{kj} - \frac{1}{3}\{\boldsymbol{S}^2\}\delta_{ij} \right) + \beta_2 \left(S_{ik}\Omega_{kj} - \Omega_{ik}S_{kj} \right) \tag{B.21}$$

which when substituted into the definition of the anisotropy tensor in equation (B.1) results in:

$$\frac{\overline{u_i'u_j'}}{k} - \frac{2}{3}\delta_{ij} = \beta_0 S_{ij} + \beta_1 \left(S_{ik}S_{kj} - \frac{1}{3}\{\boldsymbol{S}^2\}\delta_{ij} \right) + \beta_2 \left(\Omega_{ik}S_{kj} - S_{ik}\Omega_{kj} \right) \tag{B.22}$$

Applying the same method as in the linear model:

For $i = 1$ and $j = 1$ (to get $\overline{u'u'}$):

$$\frac{\overline{u'u'}}{k} - \frac{2}{3}\delta_{11} = \beta_0 S_{11} + \beta_1 \left(S_{12}S_{21} - \frac{1}{3}\{\boldsymbol{S}^2\}\delta_{11} \right) + \beta_2 \left(\Omega_{12}S_{21} - S_{12}\Omega_{21} \right) \tag{B.23}$$

$\delta_{11} = 1$ and the strain and rotation rate terms are substituted from equations (B.6) and (B.9). Therefore we can obtain:

$$\begin{aligned} \frac{\overline{u'u'}}{k} - \frac{2}{3} &= \beta_0(0) + \beta_1 \left[\left(\frac{1}{2}\lambda\right)\left(\frac{1}{2}\lambda\right) - \frac{1}{3}\left(\frac{1}{2}\lambda^2\right)(1) \right] + \beta_2 \left[\left(\frac{1}{2}\lambda\right)\left(\frac{1}{2}\lambda\right) - \left(\frac{1}{2}\lambda\right)\left(\frac{1}{2}\lambda\right) \right] \\ &= \beta_1 \left[\frac{1}{4}\lambda^2 - \frac{1}{3}\left(\frac{1}{2}\lambda^2\right) \right] + \beta_2 \left[\frac{1}{4}\lambda^2 - \left(-\frac{1}{4}\lambda^2\right) \right] \\ &= \frac{1}{12}\beta_1\lambda^2 + \frac{1}{2}\beta_2\lambda^2 \end{aligned} \tag{B.24}$$

For $i = 2$ and $j = 2$ (to get $\overline{v'v'}$):

$$\frac{\overline{v'v'}}{k} - \frac{2}{3}\delta_{22} = \beta_0 S_{22} + \beta_1 \left(S_{21}S_{12} - \frac{1}{3}\{\boldsymbol{S}^2\}\delta_{22} \right) + \beta_2 \left(\Omega_{21}S_{12} - S_{21}\Omega_{12} \right) \tag{B.25}$$

$\delta_{22} = 1$ and the strain and rotation rate terms are substituted from equations (B.6) and (B.9). Therefore we obtain:

$$\begin{aligned}
\frac{\overline{v'v'}}{k} - \frac{2}{3} &= \beta_0(0) + \beta_1 \left[\left(\frac{1}{2}\lambda\right) \left(\frac{1}{2}\lambda\right) - \frac{1}{3}\left(\frac{1}{2}\lambda^2\right)(1) \right] + \beta_2 \left[\left(\frac{1}{2}\lambda\right) \left(\frac{1}{2}\lambda\right) - \left(\frac{1}{2}\lambda\right) \left(\frac{1}{2}\lambda\right) \right] \\
&= \beta_1 \left[\frac{1}{4}\lambda^2 - \frac{1}{3}\left(\frac{1}{2}\lambda^2\right) \right] + \beta_2 \left[\frac{1}{4}\lambda^2 - \frac{1}{4}\lambda^2 \right] \\
&= \frac{1}{12}\beta_1\lambda^2 - \frac{1}{2}\beta_2\lambda^2 \\
\frac{\overline{v'v'}}{k} &= \frac{1}{12}\beta_1\lambda^2 - \frac{1}{2}\beta_2\lambda^2 + \frac{2}{3}
\end{aligned} \tag{B.26}$$

For $i = 3$ and $j = 3$ (to get $\overline{w'w'}$):

$$\frac{\overline{w'w'}}{k} - \frac{2}{3}\delta_{33} = \beta_0 S_{33} + \beta_1 \left(S_{31}S_{13} - \frac{1}{3}\{\boldsymbol{S}^2\}\delta_{33} \right) + \beta_2 \left(\Omega_{31}S_{13} - S_{31}\Omega_{13} \right) \tag{B.27}$$

$\delta_{33} = 1$ and the strain and rotation rate terms are substituted from equations (B.6) and (B.9). Therefore we obtain:

$$\begin{aligned}
\frac{\overline{w'w'}}{k} - \frac{2}{3} &= \beta_0(0) + \beta_1 \left[0 - \frac{1}{3}\left(\frac{1}{2}\lambda^2\right)(1) \right] + \beta_2(0) \\
&= -\frac{1}{6}\beta_1\lambda^2 \\
\frac{\overline{w'w'}}{k} &= -\frac{1}{6}\beta_1\lambda^2 + \frac{2}{3}
\end{aligned} \tag{B.28}$$

For $i = 1$ and $j = 2$ (to get $\overline{u'v'}$):

$$\frac{\overline{u'v'}}{k} - \frac{2}{3}\delta_{12} = \beta_0 S_{12} + \beta_1 \left(S_{13}S_{32} - \frac{1}{3}\{\boldsymbol{S}^2\}\delta_{12} \right) + \beta_2 \left(\Omega_{13}S_{32} - S_{13}\Omega_{32} \right) \tag{B.29}$$

$\delta_{12} = 0$ and the strain and rotation rate terms are substituted from equations (B.6) and (B.9). Therefore we obtain:

$$\begin{aligned}
\frac{\overline{u'v'}}{k} &= \beta_0 \left(\frac{1}{2}\lambda\right) + \beta_1(0) + \beta_2(0) \\
&= \frac{1}{2}\beta_0\lambda
\end{aligned} \tag{B.30}$$

Summarised:

$$\begin{aligned}
\frac{\overline{u'u'}}{k} &= \frac{1}{12}\beta_1\lambda^2 + \frac{1}{2}\beta_2\lambda^2 + \frac{2}{3} \\
\frac{\overline{v'v'}}{k} &= \frac{1}{12}\beta_1\lambda^2 - \frac{1}{2}\beta_2\lambda^2 + \frac{2}{3} \\
\frac{\overline{w'w'}}{k} &= -\frac{1}{6}\beta_1\lambda^2 + \frac{2}{3} \\
\frac{\overline{u'v'}}{k} &= \frac{1}{2}\beta_0\lambda
\end{aligned}$$

Appendix C

Porous medium modelling in OpenFOAM

The approximation of the effects of porosity using the porous medium approach can be applied in OpenFOAM by specifying an `explicitPorositySource` in the `fvOptions` file. An example is presented below:

```
porosity1
{
    type explicitPorositySource;
    active true;

    explicitPorositySourceCoeffs
    {
        type DarcyForchheimer;
        selectionMode cellZone;
        cellZone porosity;

            DarcyForchheimerCoeffs
            {

                d d [0 -2 0 0 0 0 0] (39592901.65384 -1000 -1000);
                f      -1 0 0     0] (23.735 -1000 -1000);

                coordinateSystem
                {
                    type cartesian;
                    origin (0 0 0);
                    coordinateRotation
                    {
                        type axesRotation;
                        e1 (1 0 0);
                        e2 (0 0 1);
                    }
                }
            }
}
```

It can be observed that the resistance coefficients (highlighted) are defined as vectors, specifically for

the three Cartesian coordinates in this case. For a porous medium whose channels force the flow to be unidirectional in the x-direction, the coefficients for D and F as defined in equation (7.1) are applied for the x component. Very high values are set for the remaining components to specify that there is no flow in those directions. In OpenFOAM, negative values (which are invalid) can also be set to specify maximum resistance.

Appendix D

Additional results for planar diffuser case

D.1 Porous medium modelling methods comparison for $k-\omega$

D.1.1 Monolith length 27 mm

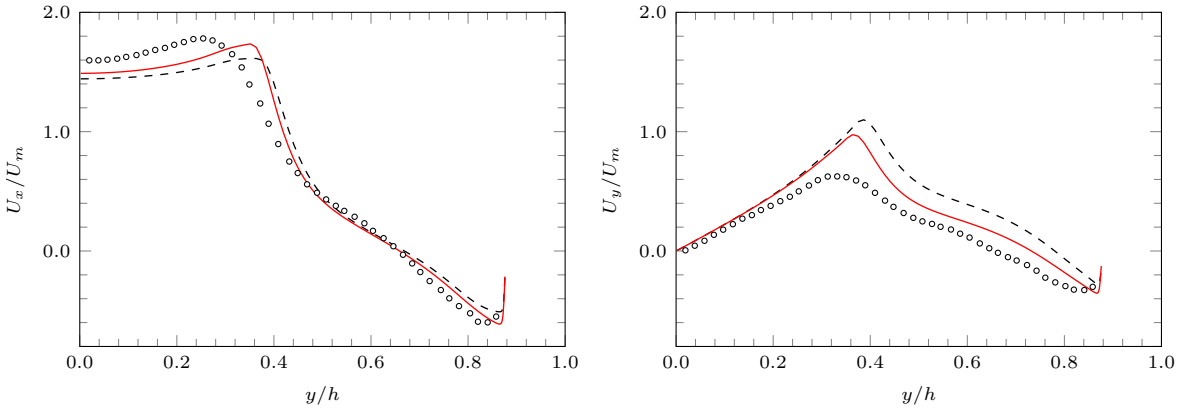

(a) 10.13 mm upstream

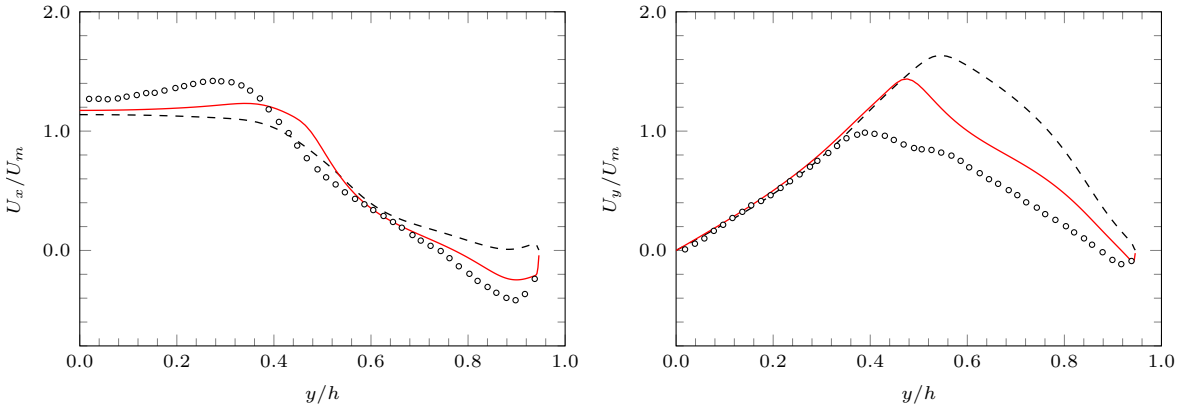

(b) 5.55 mm upstream

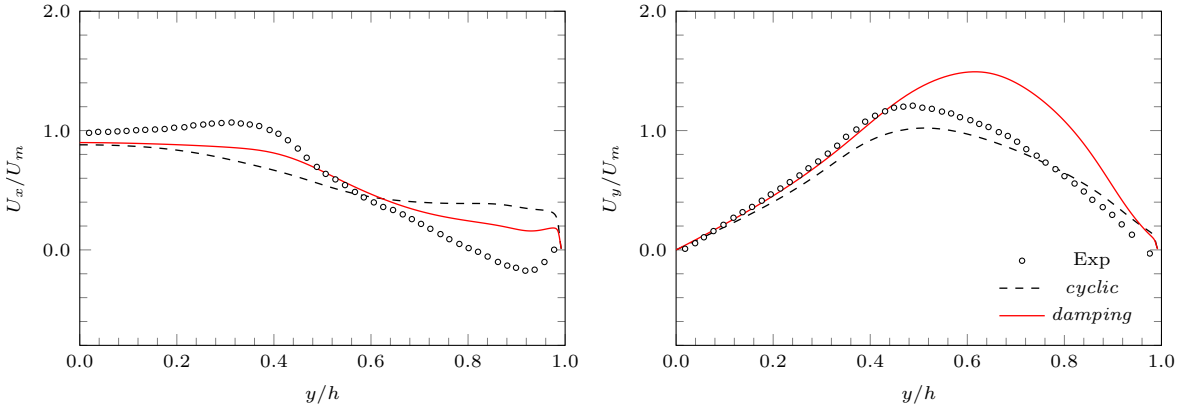

(c) 2.5 mm upstream

Figure D.1: Axial (left) and transverse (right) velocity profiles at several stations upstream of monolith at $Re = 2.2 \times 10^4$. Markers correspond to experimental data [168].

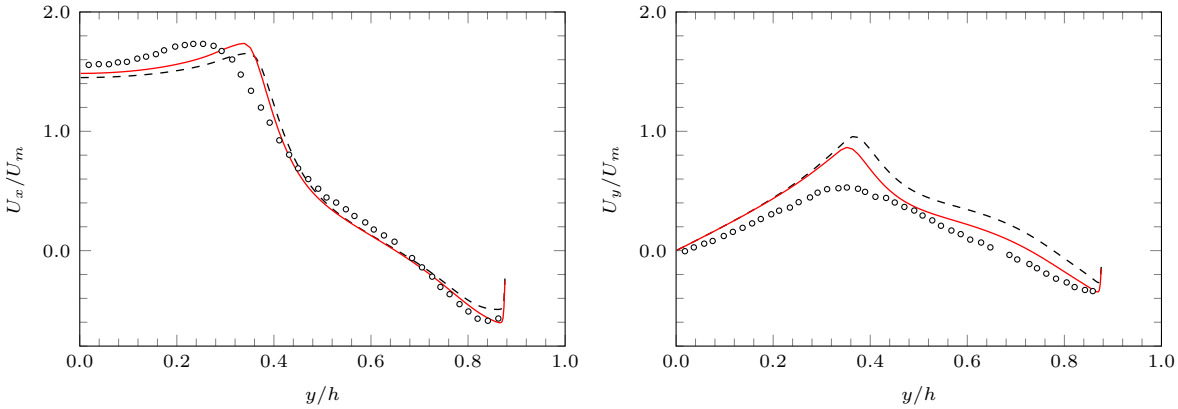

(a) 10.13 mm upstream

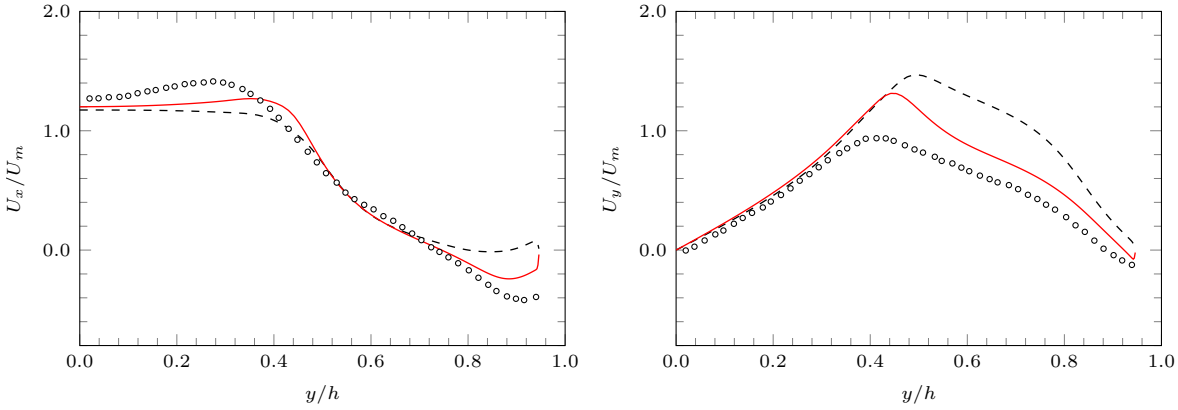

(b) 5.55 mm upstream

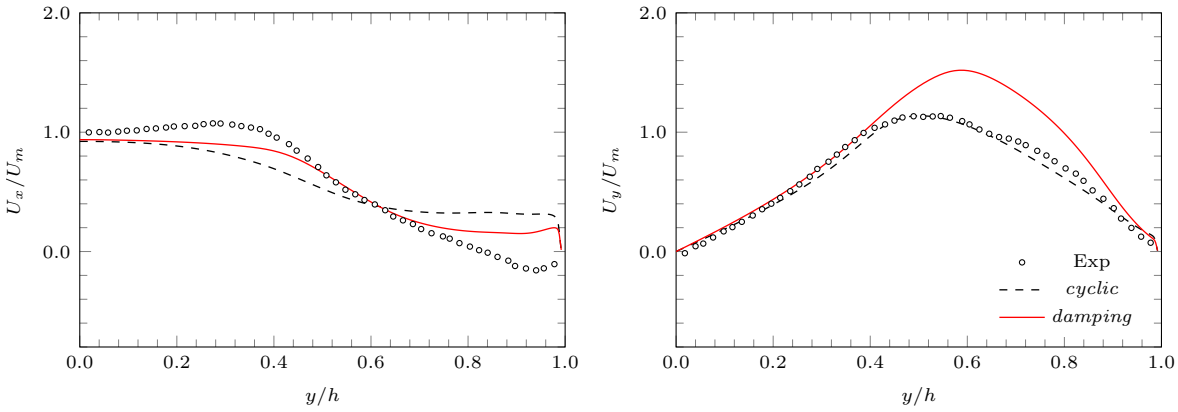

(c) 2.5 mm upstream

Figure D.2: Axial (left) and transverse (right) velocity profiles at several stations upstream of monolith at $Re = 3.0 \times 10^4$. Markers correspond to experimental data [168].

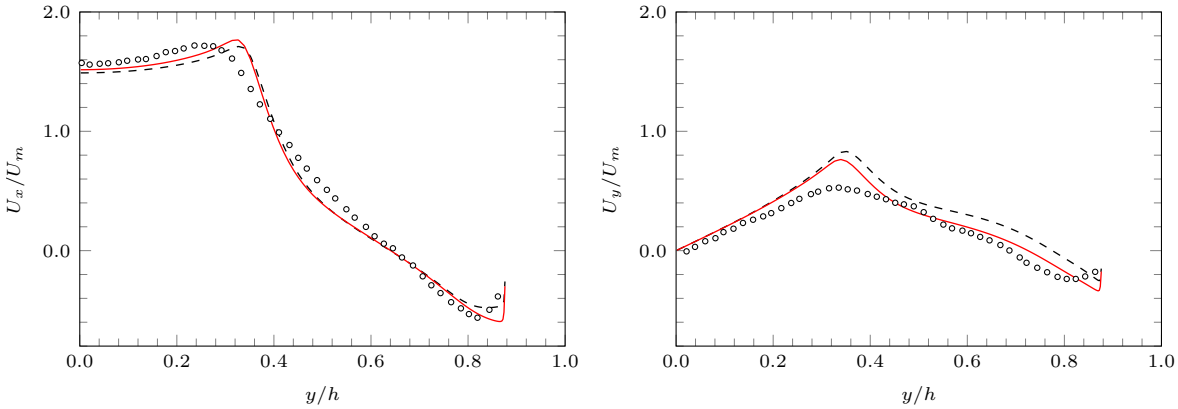

(a) 10.13 mm upstream

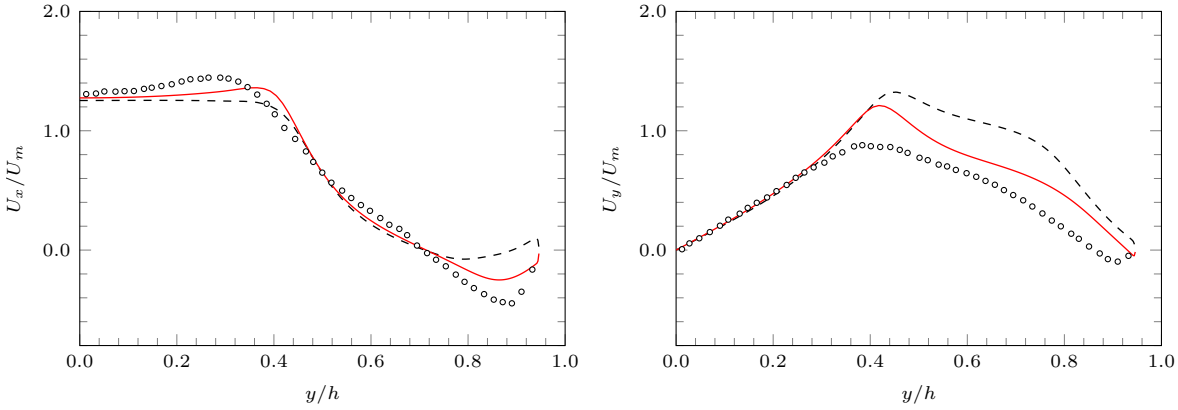

(b) 5.55 mm upstream

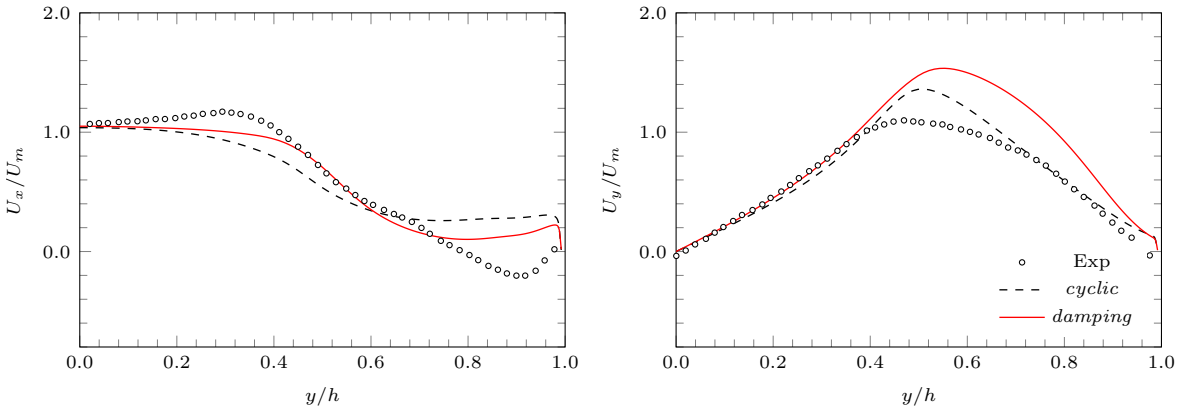

(c) 2.5 mm upstream

Figure D.3: Axial (left) and transverse (right) velocity profiles at several stations upstream of monolith at $Re = 4.2 \times 10^4$. Markers correspond to experimental data [168].

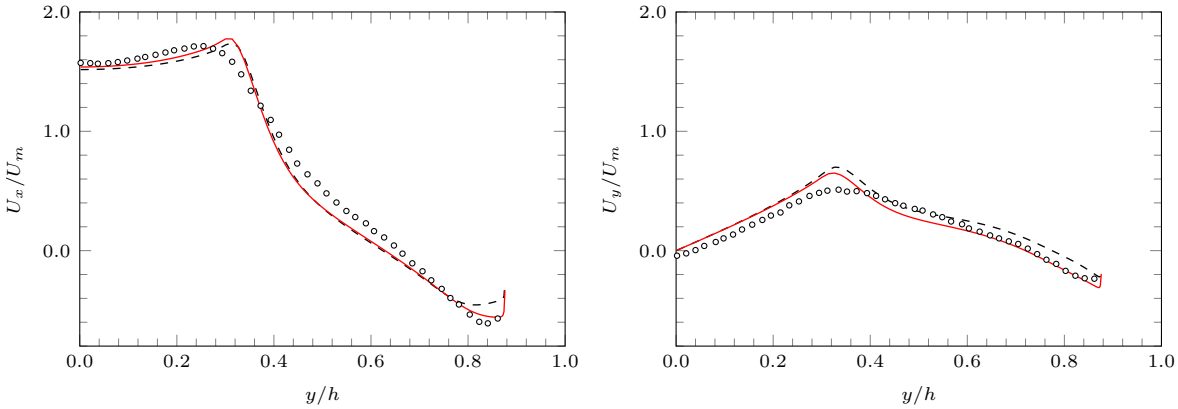

(a) 10.13 mm upstream

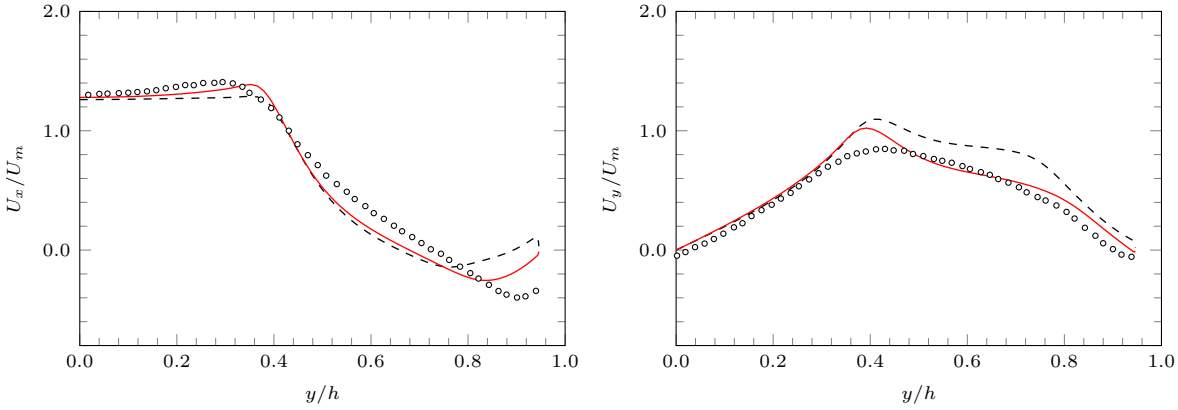

(b) 5.55 mm upstream

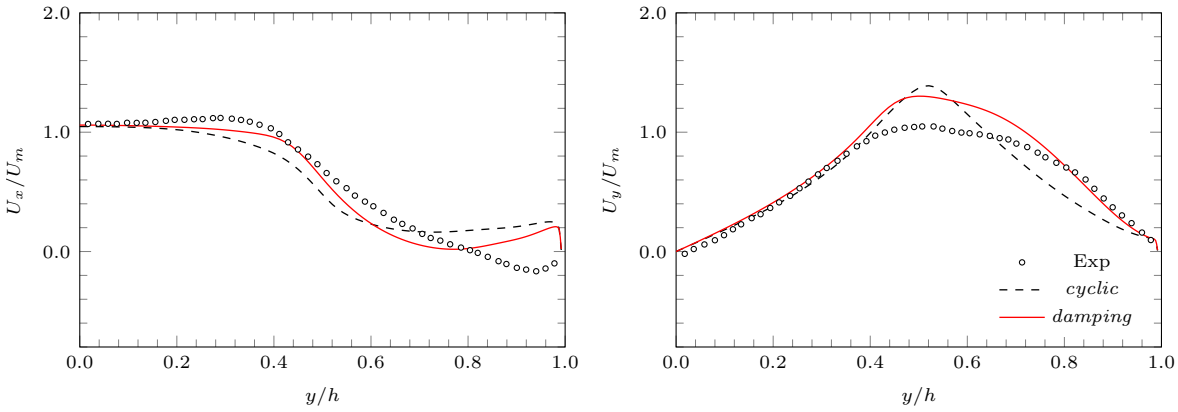

(c) 2.5 mm upstream

Figure D.4: Axial (left) and transverse (right) velocity profiles at several stations upstream of monolith at $Re = 6.0 \times 10^4$. Markers correspond to experimental data [168].

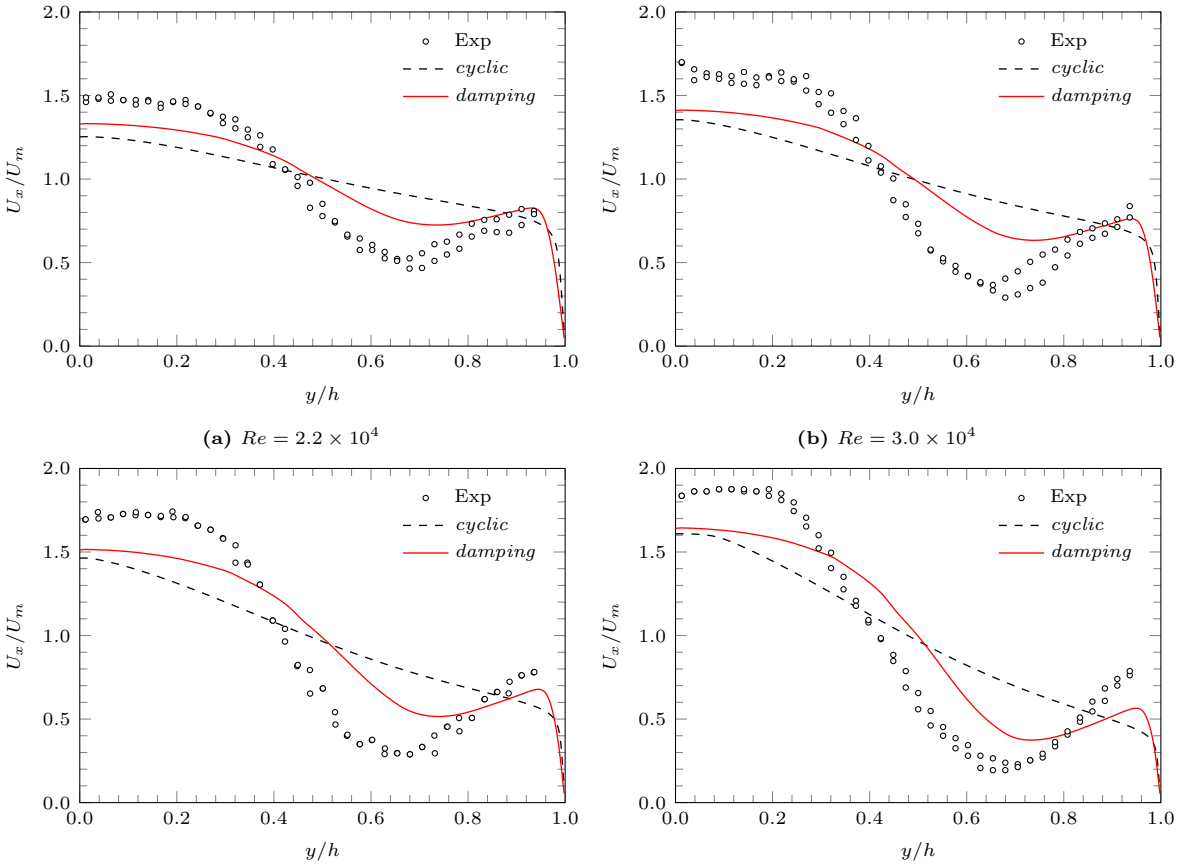

(a) $Re = 2.2 \times 10^4$ **(b)** $Re = 3.0 \times 10^4$

(c) $Re = 4.2 \times 10^4$ **(d)** $Re = 6.0 \times 10^4$

Figure D.5: Axial velocity profile 40 mm downstream of monolith. Markers correspond to experimental data [168].

D.1.2 Monolith length 100 mm

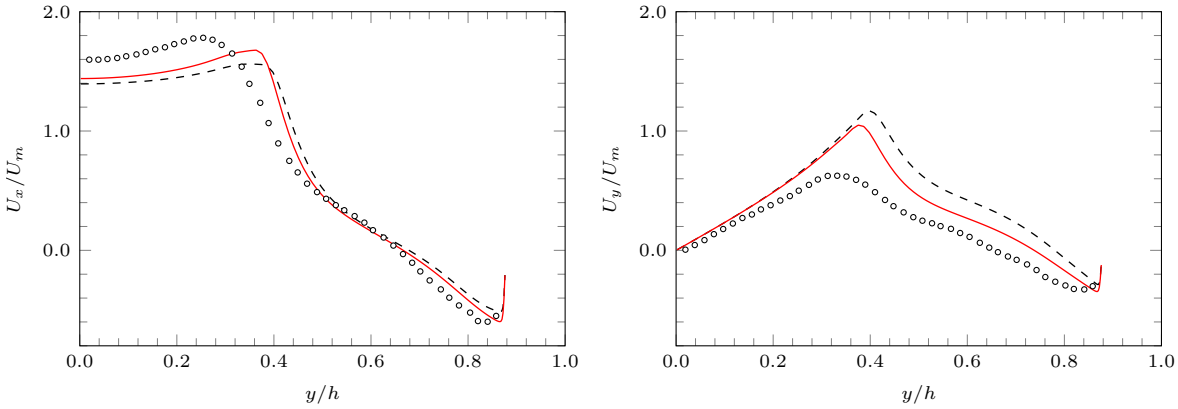

(a) 10.13 mm upstream

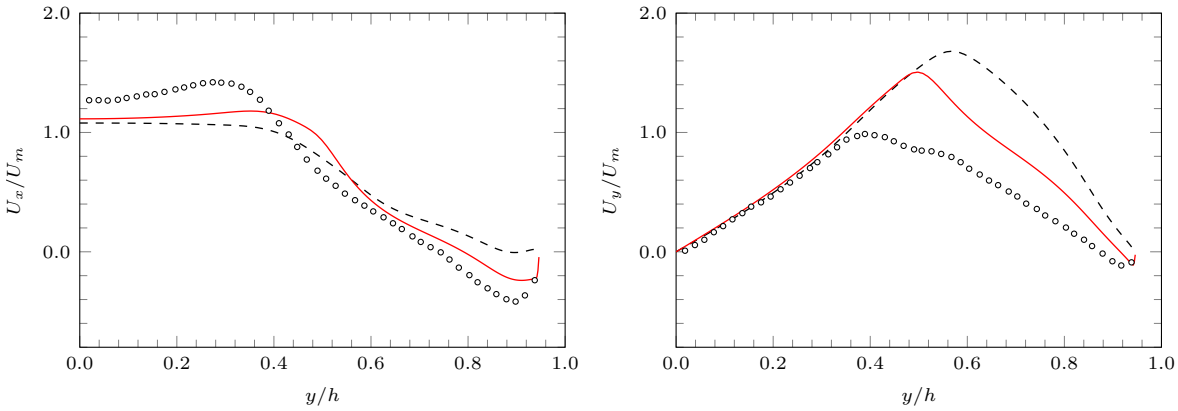

(b) 5.55 mm upstream

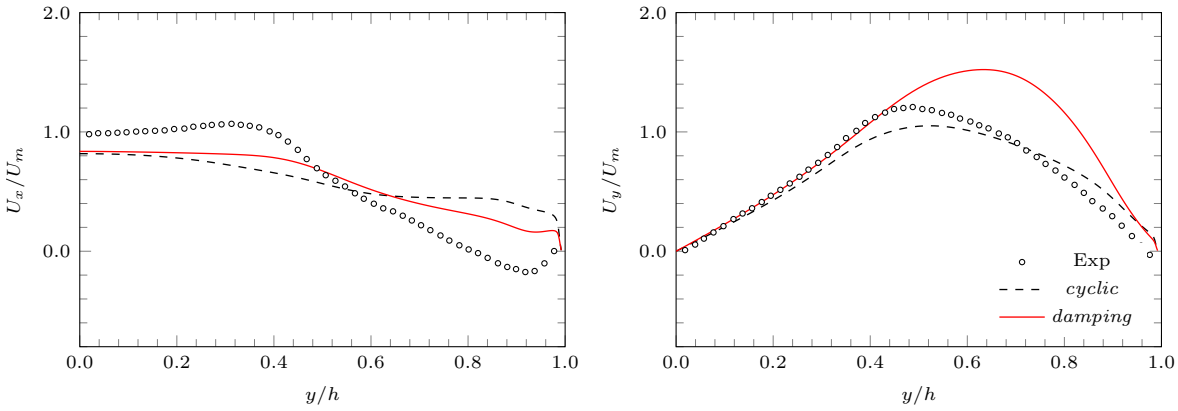

(c) 2.5 mm upstream

Figure D.6: Axial (left) and transverse (right) velocity profiles at several stations upstream of monolith at $Re = 2.2 \times 10^4$. Markers correspond to experimental data [168].

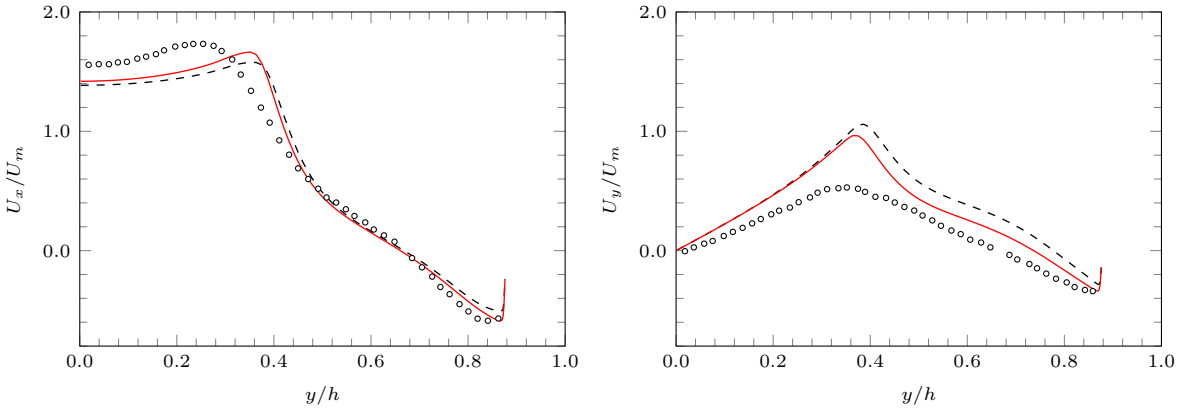

(a) 10.13 mm upstream

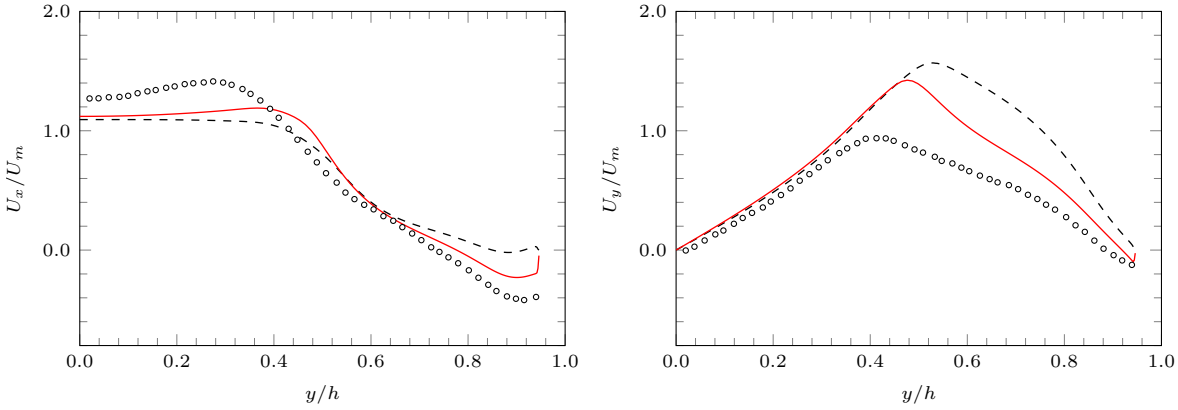

(b) 5.55 mm upstream

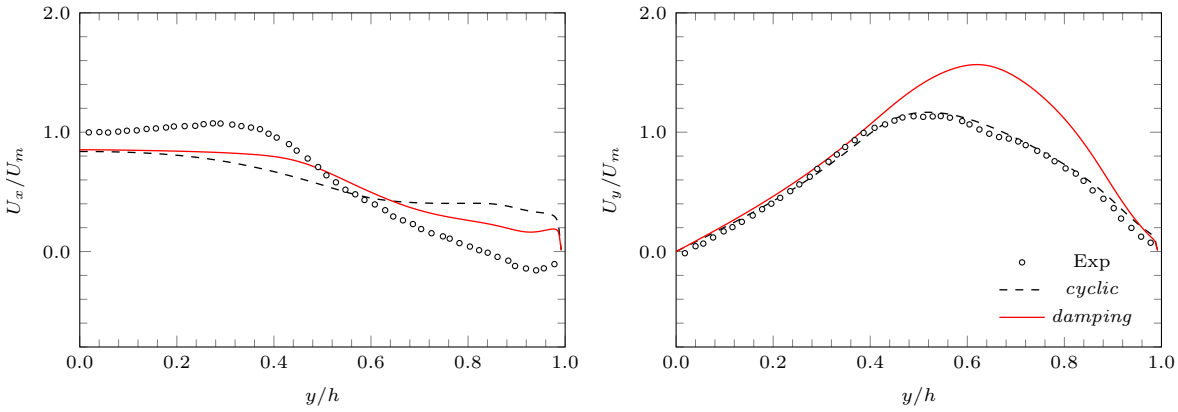

(c) 2.5 mm upstream

Figure D.7: Axial (left) and transverse (right) velocity profiles at several stations upstream of monolith at $Re = 3.0 \times 10^4$. Markers correspond to experimental data [168].

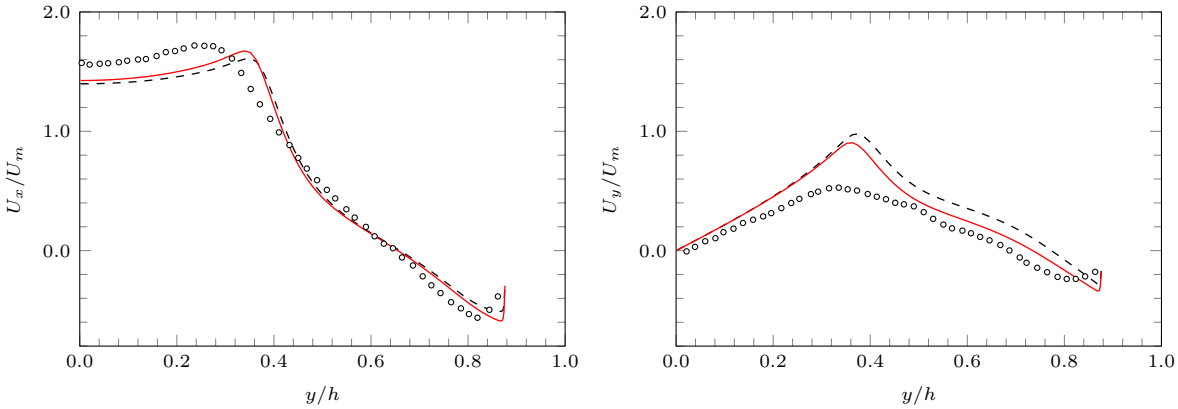

(a) 10.13 mm upstream

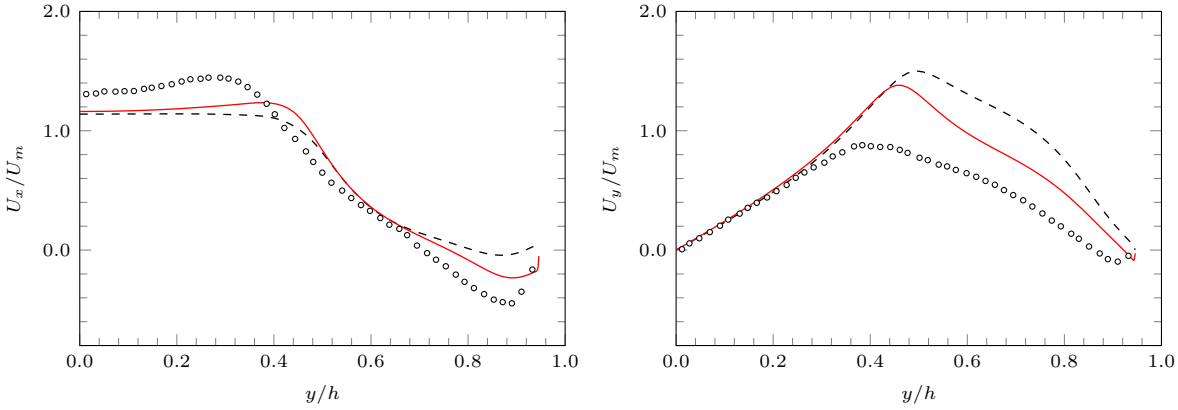

(b) 5.55 mm upstream

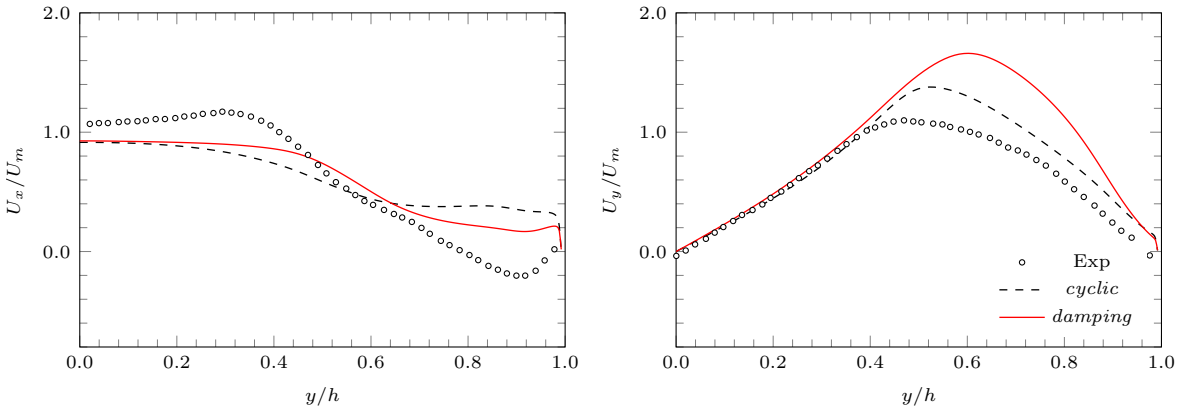

(c) 2.5 mm upstream

Figure D.8: Axial (left) and transverse (right) velocity profiles at several stations upstream of monolith at $Re = 4.2 \times 10^4$. Markers correspond to experimental data [168].

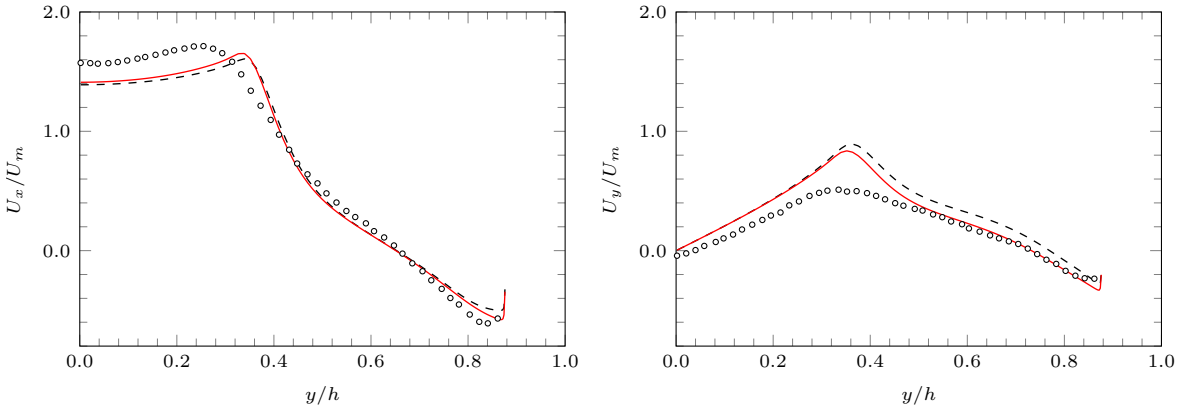

(a) 10.13 mm upstream

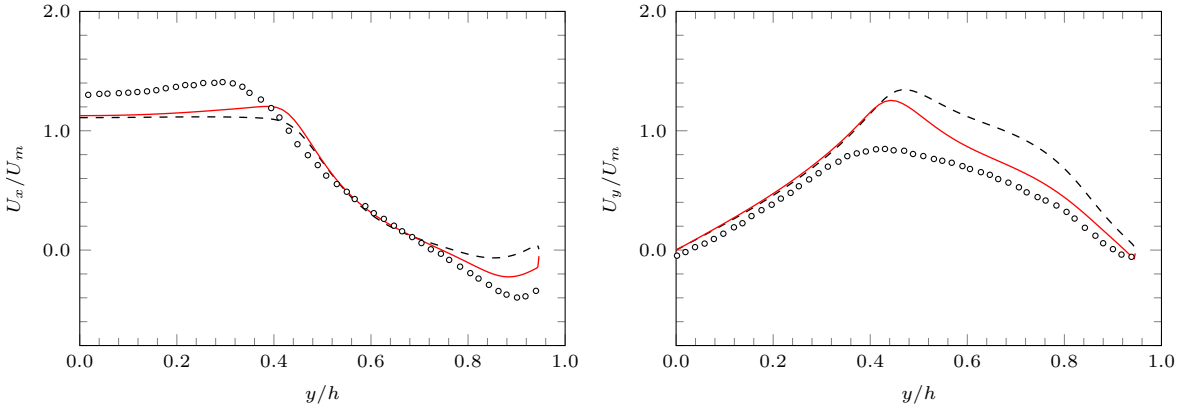

(b) 5.55 mm upstream

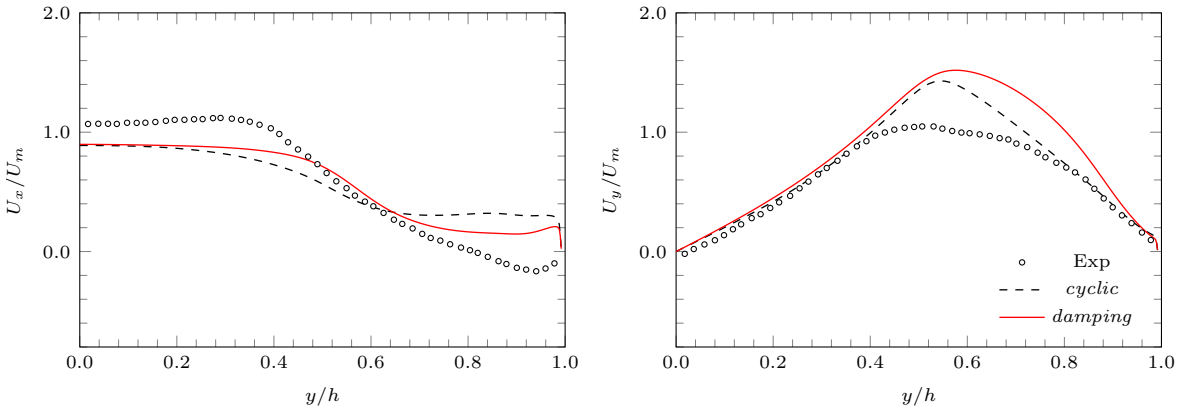

(c) 2.5 mm upstream

Figure D.9: Axial (left) and transverse (right) velocity profiles at several stations upstream of monolith at $Re = 6.0 \times 10^4$. Markers correspond to experimental data [168].

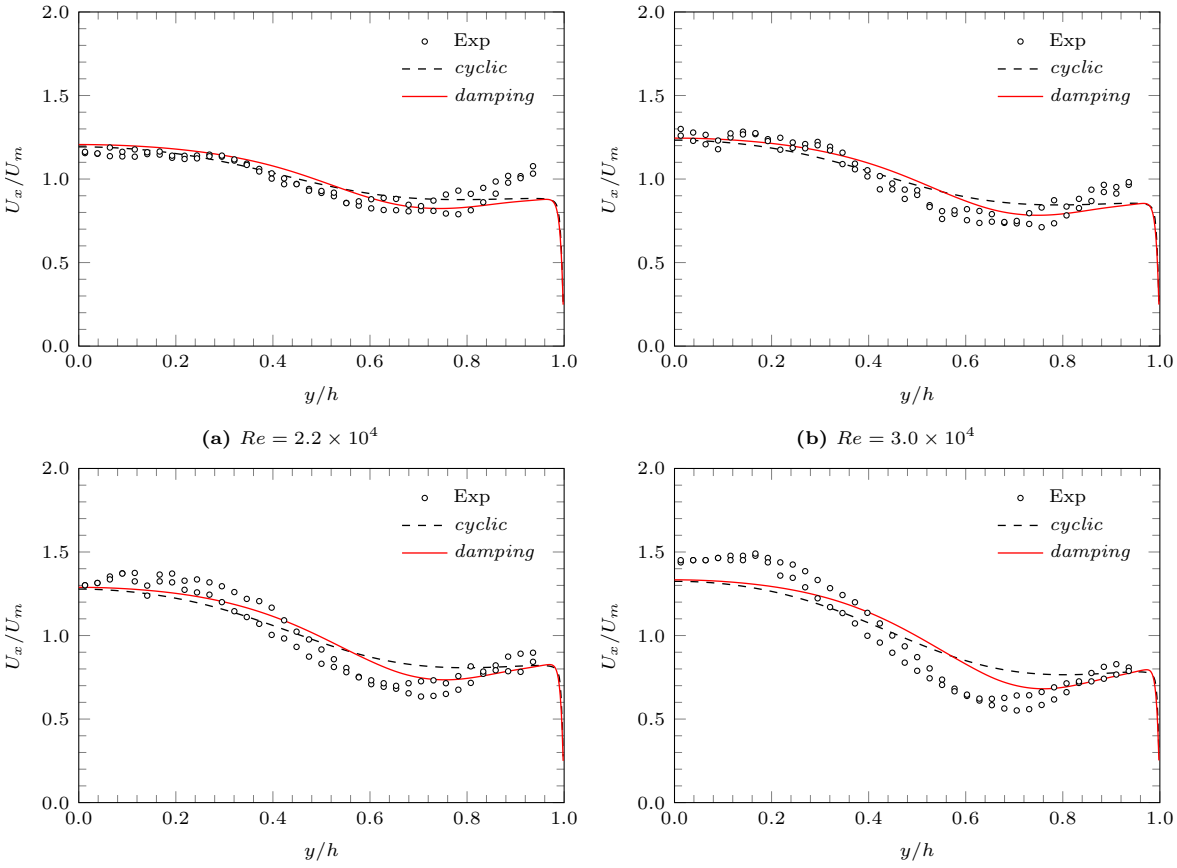

(a) $Re = 2.2 \times 10^4$ **(b)** $Re = 3.0 \times 10^4$

(c) $Re = 4.2 \times 10^4$ **(d)** $Re = 6.0 \times 10^4$

Figure D.10: Axial velocity profile 40 mm downstream of monolith. Markers correspond to experimental data [168].

D.2 Porous medium modelling methods comparison for NL $k-\omega$

D.2.1 Monolith length 27 mm

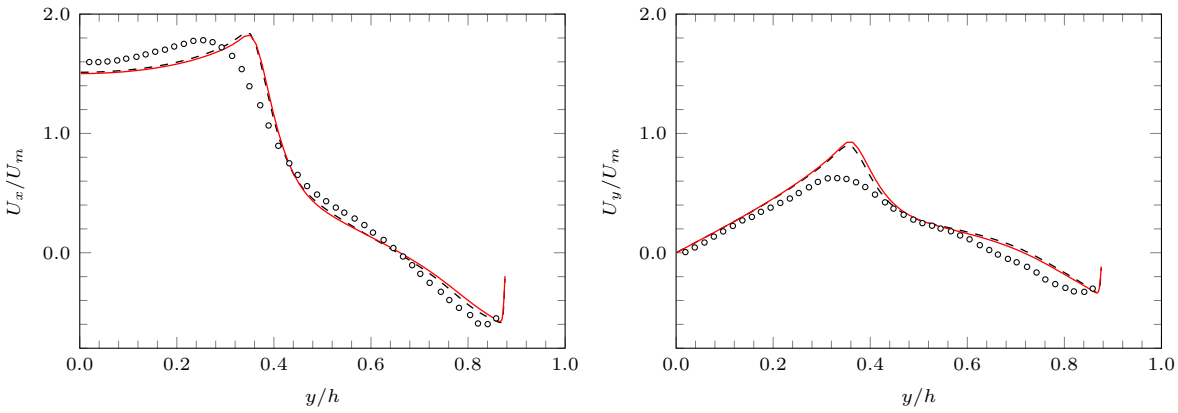

(a) 10.13 mm upstream

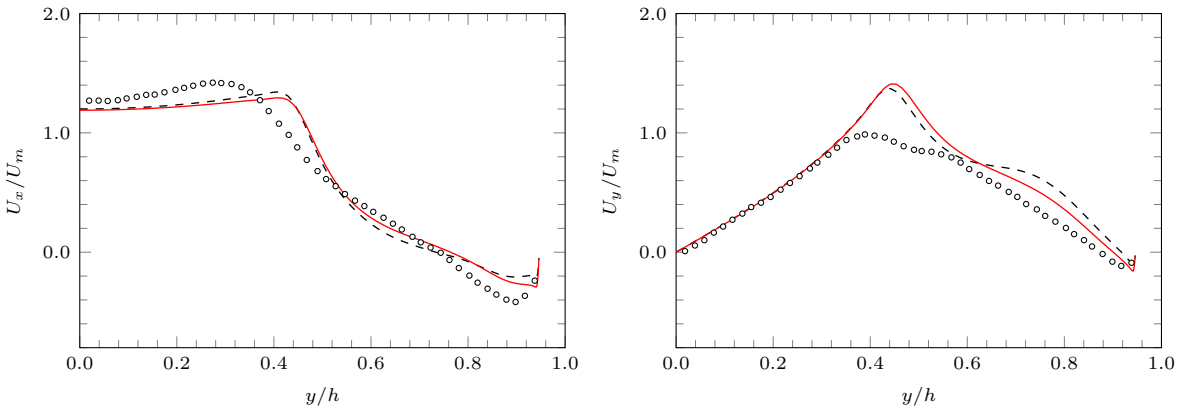

(b) 5.55 mm upstream

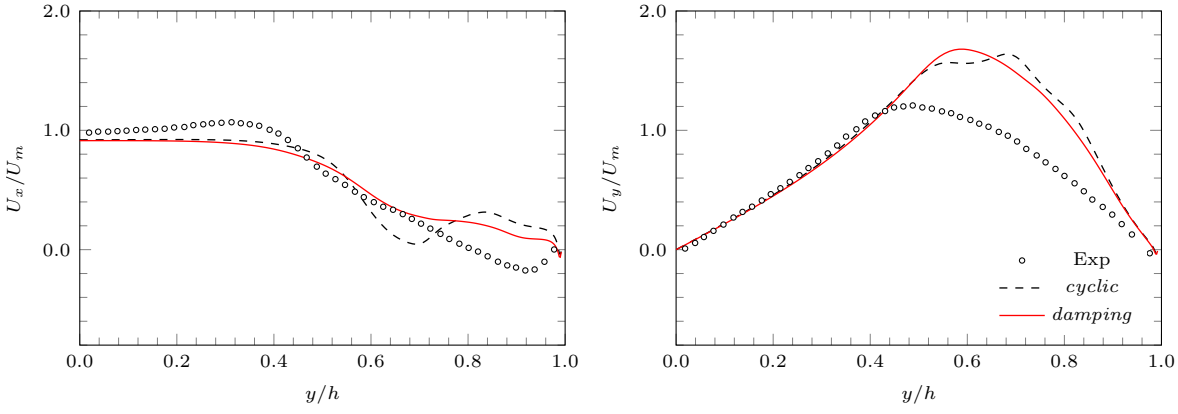

(c) 2.5 mm upstream

Figure D.11: Axial (left) and transverse (right) velocity profiles at several stations upstream of monolith at $Re = 2.2 \times 10^4$. Markers correspond to experimental data [168].

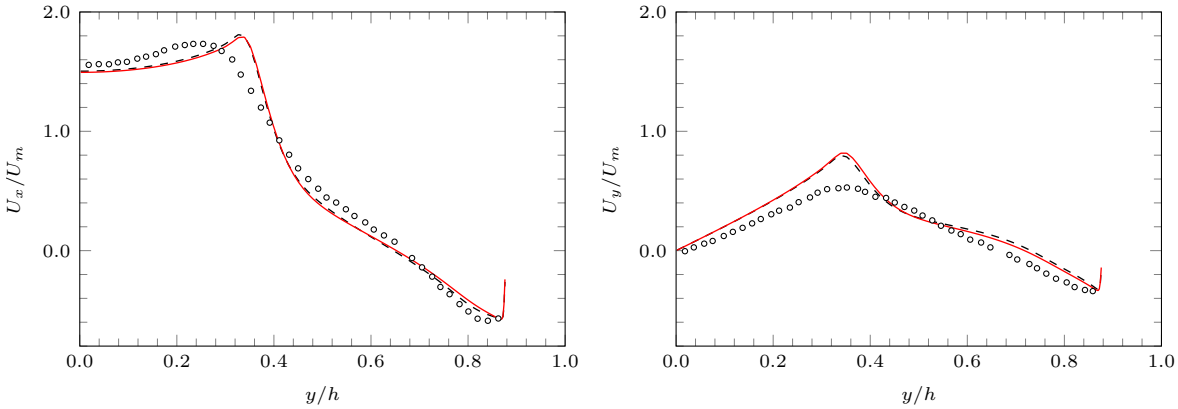

(a) 10.13 mm upstream

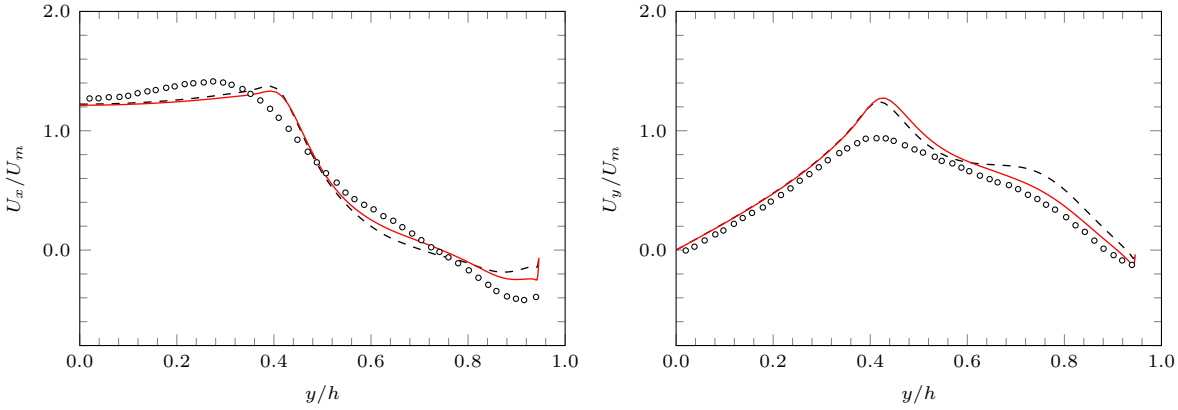

(b) 5.55 mm upstream

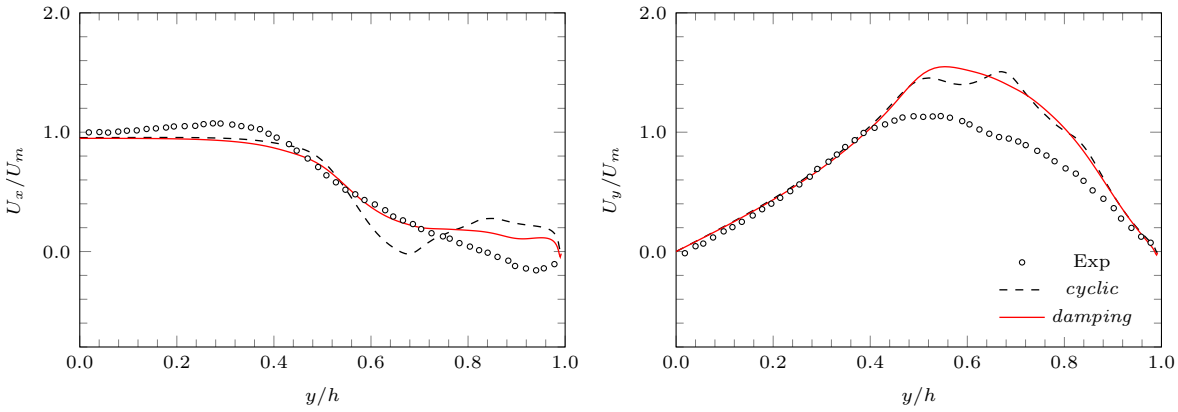

(c) 2.5 mm upstream

Figure D.12: Axial (left) and transverse (right) velocity profiles at several stations upstream of monolith at $Re = 3.0 \times 10^4$. Markers correspond to experimental data [168].

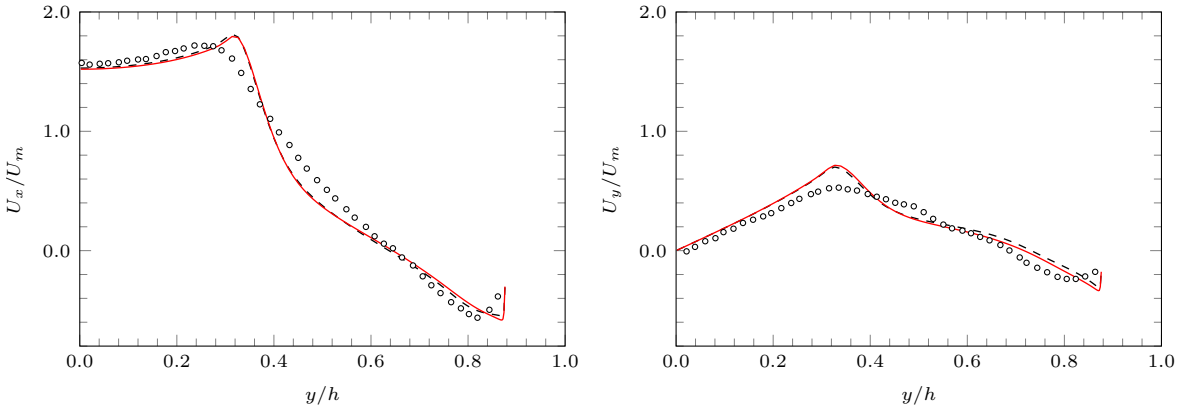

(a) 10.13 mm upstream

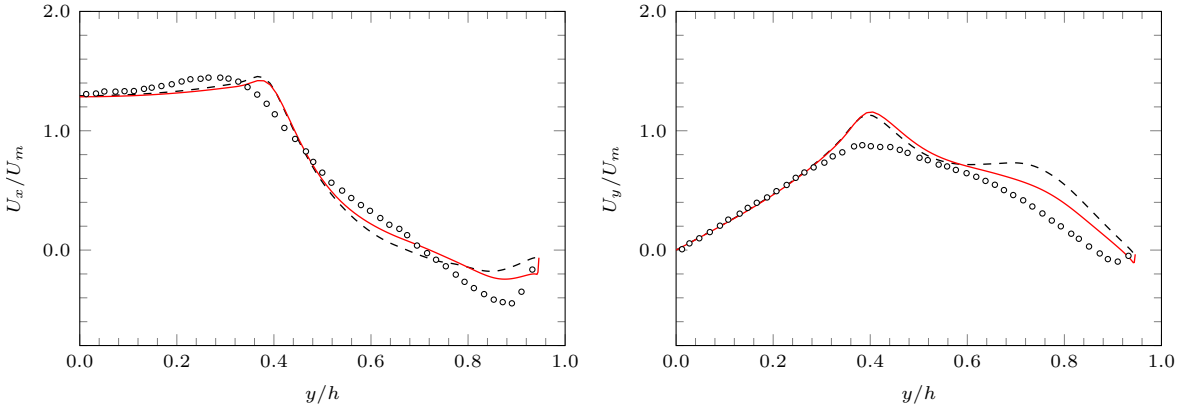

(b) 5.55 mm upstream

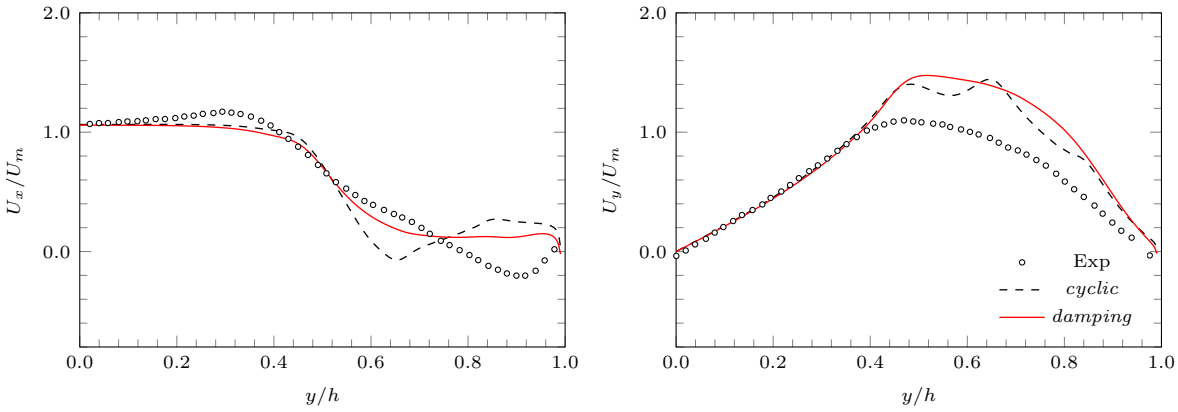

(c) 2.5 mm upstream

Figure D.13: Axial (left) and transverse (right) velocity profiles at several stations upstream of monolith at $Re = 4.2 \times 10^4$. Markers correspond to experimental data [168].

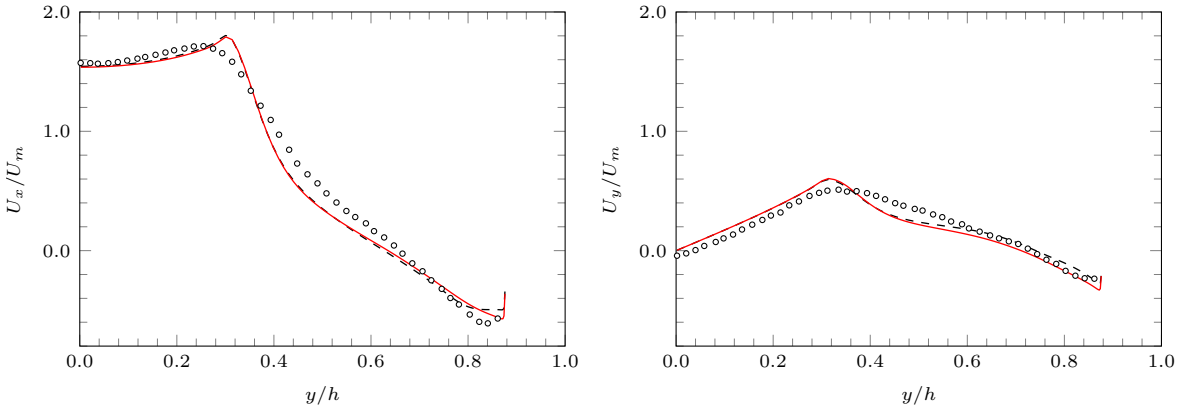

(a) 10.13 mm upstream

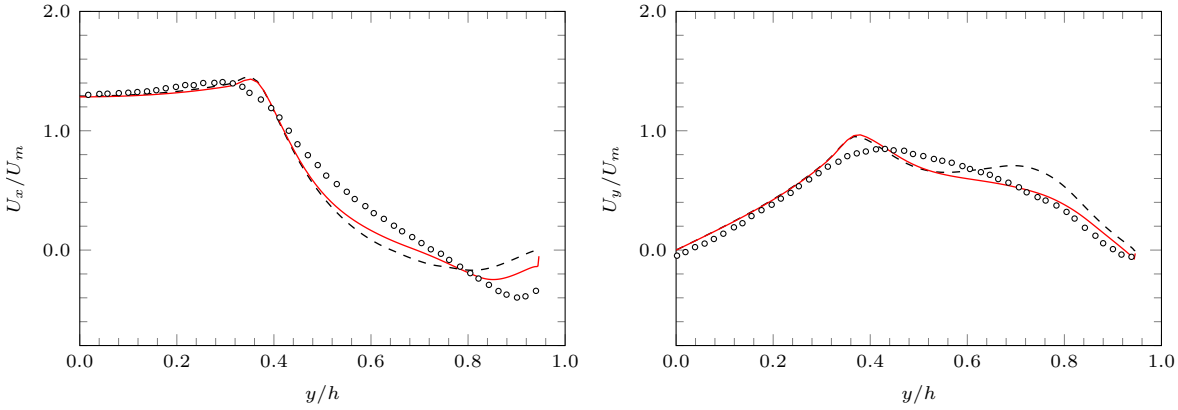

(b) 5.55 mm upstream

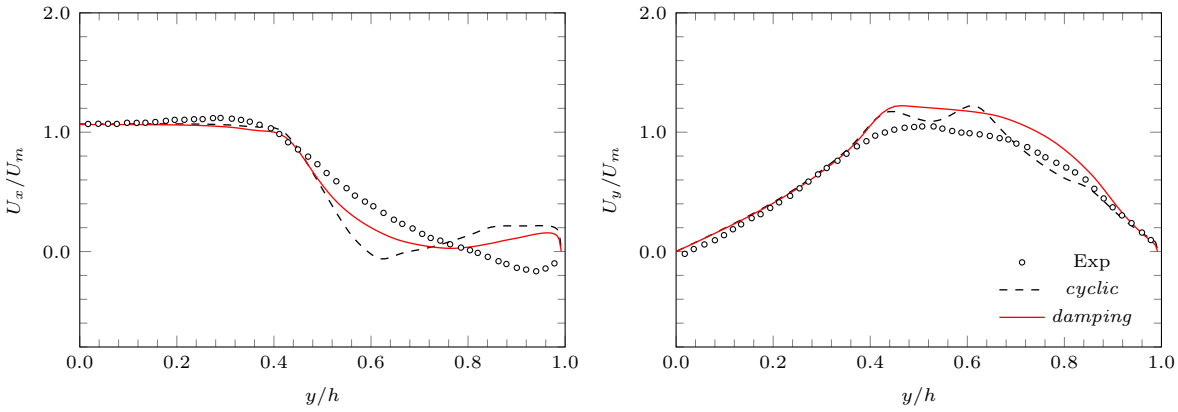

(c) 2.5 mm upstream

Figure D.14: Axial (left) and transverse (right) velocity profiles at several stations upstream of monolith at $Re = 6.0 \times 10^4$. Markers correspond to experimental data [168].

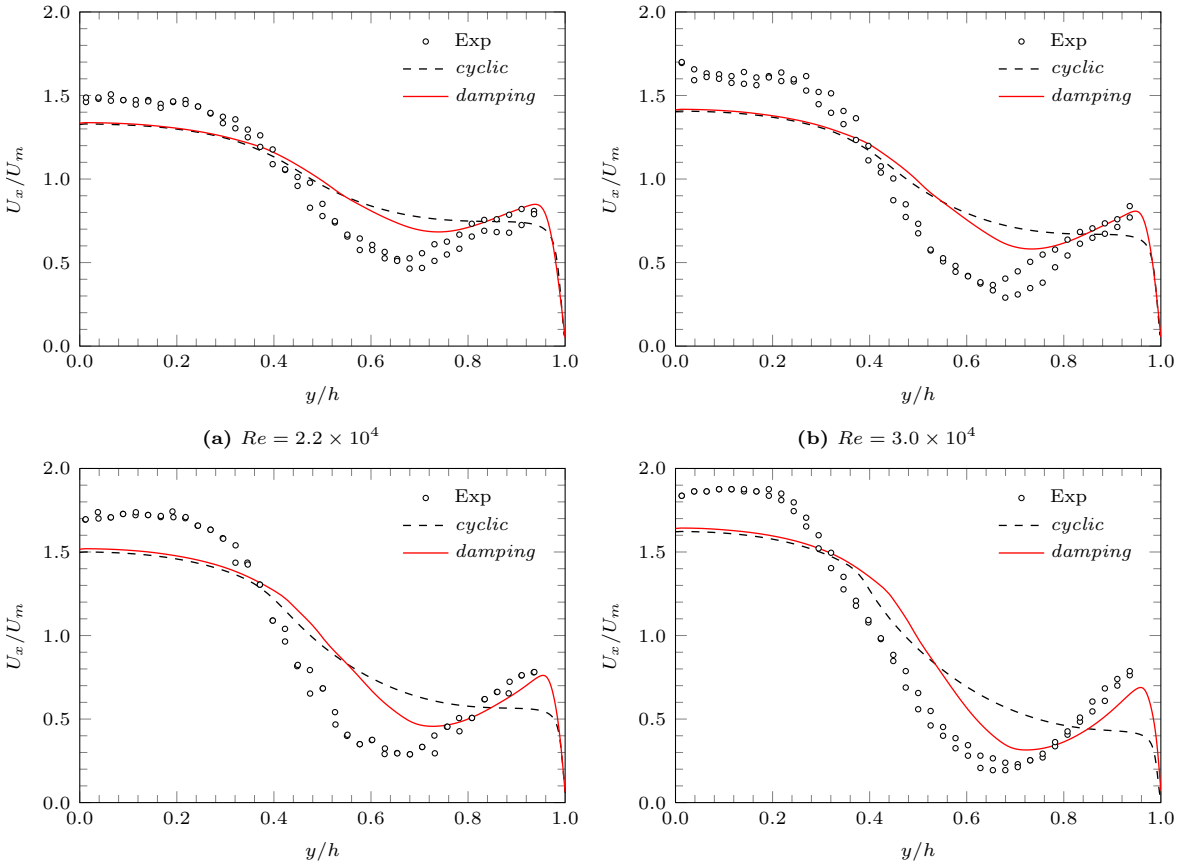

(a) $Re = 2.2 \times 10^4$ **(b)** $Re = 3.0 \times 10^4$

(c) $Re = 4.2 \times 10^4$ **(d)** $Re = 6.0 \times 10^4$

Figure D.15: Axial velocity profile 40 mm downstream of monolith. Markers correspond to experimental data [168].

D.2.2 Monolith length 100 mm

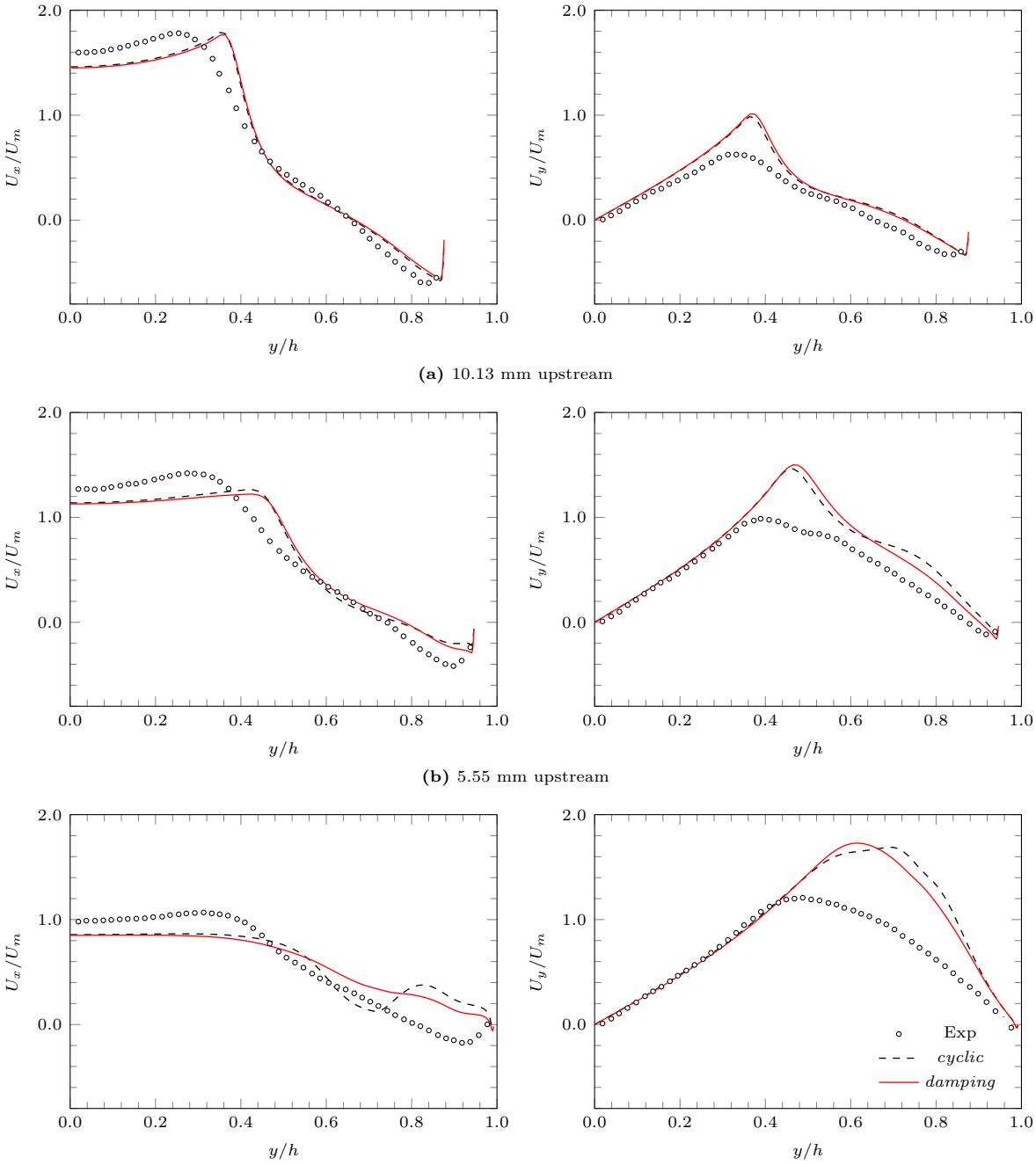

(a) 10.13 mm upstream

(b) 5.55 mm upstream

(c) 2.5 mm upstream

Figure D.16: Axial (left) and transverse (right) velocity profiles at several stations upstream of monolith at $Re = 2.2 \times 10^4$. Markers correspond to experimental data [168].

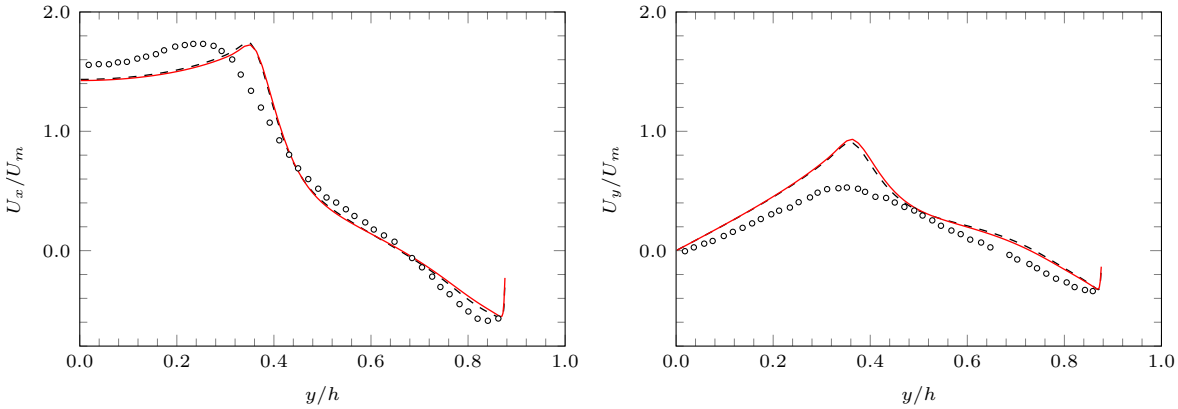

(a) 10.13 mm upstream

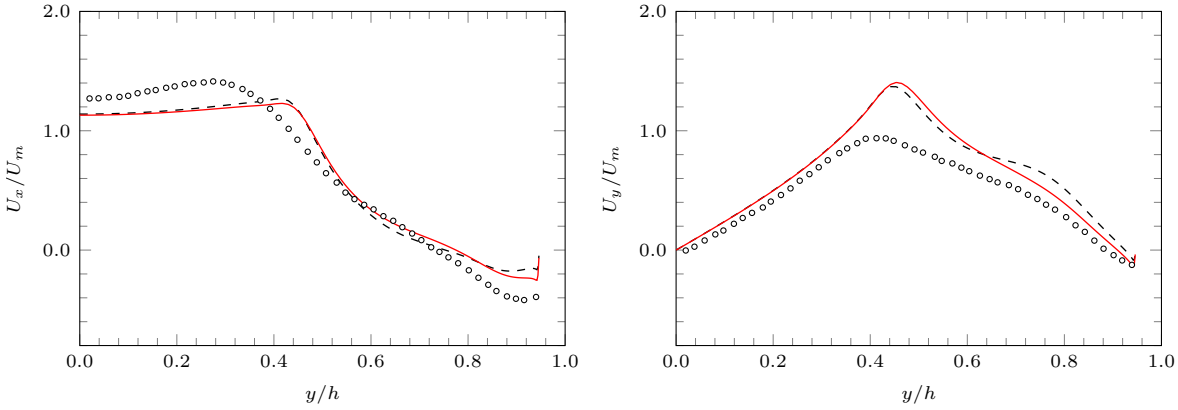

(b) 5.55 mm upstream

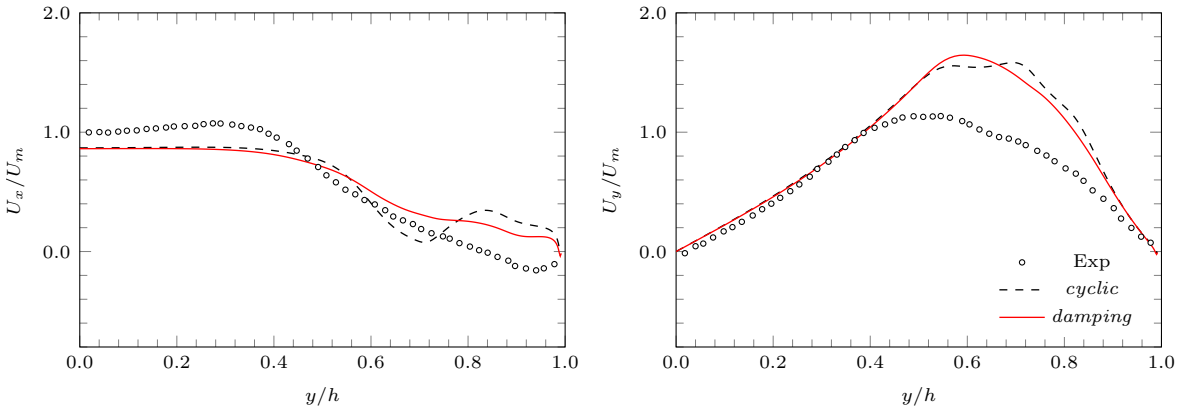

(c) 2.5 mm upstream

Figure D.17: Axial (left) and transverse (right) velocity profiles at several stations upstream of monolith at $Re = 3.0 \times 10^4$. Markers correspond to experimental data [168].

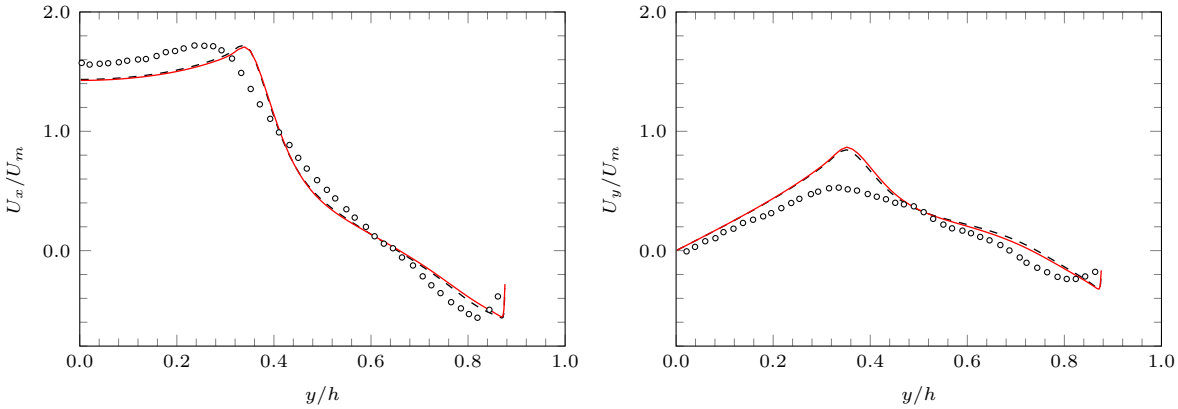

(a) 10.13 mm upstream

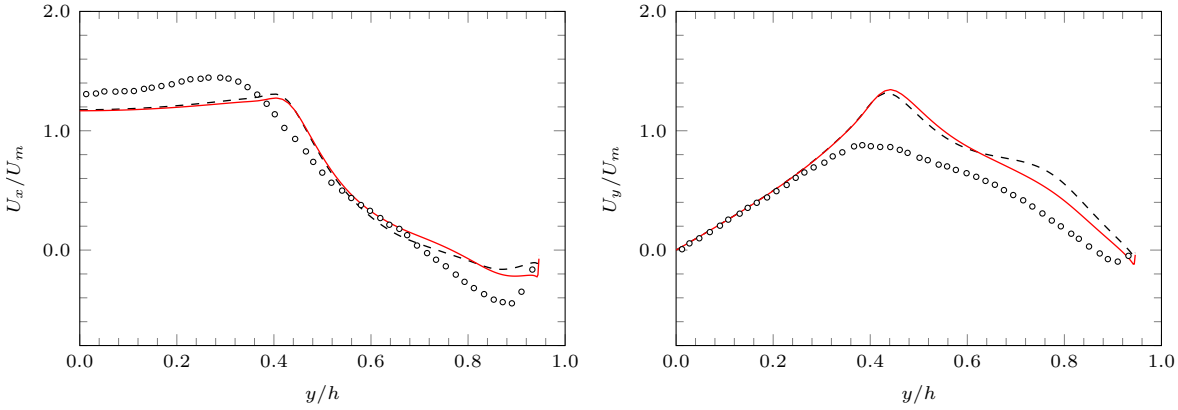

(b) 5.55 mm upstream

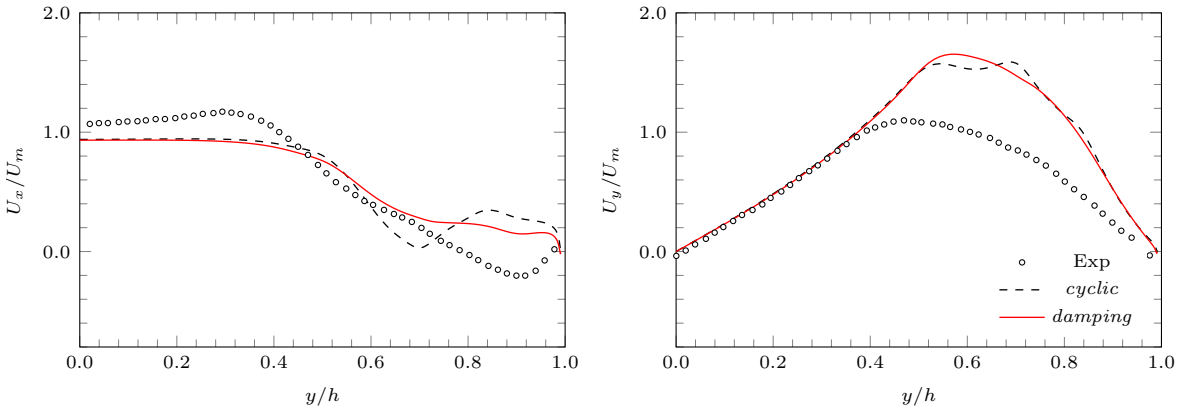

(c) 2.5 mm upstream

Figure D.18: Axial (left) and transverse (right) velocity profiles at several stations upstream of monolith at $Re = 4.2 \times 10^4$. Markers correspond to experimental data [168].

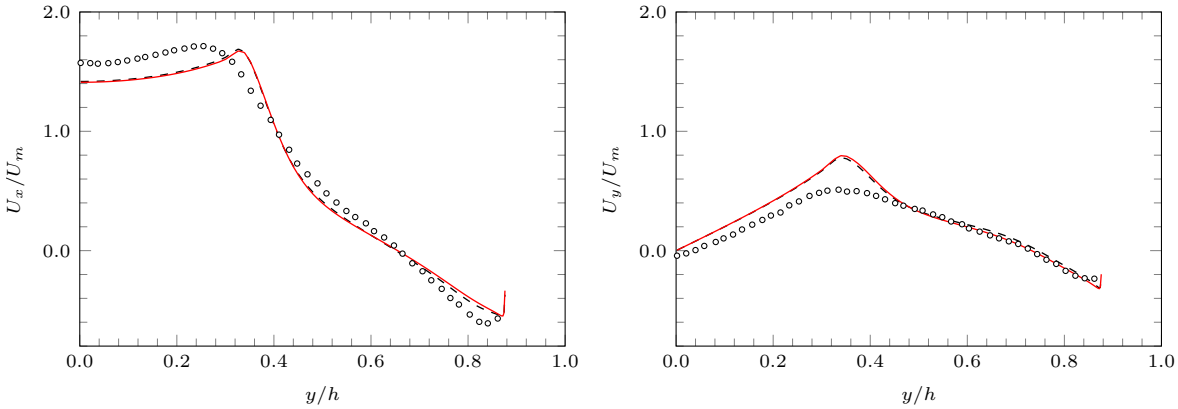

(a) 10.13 mm upstream

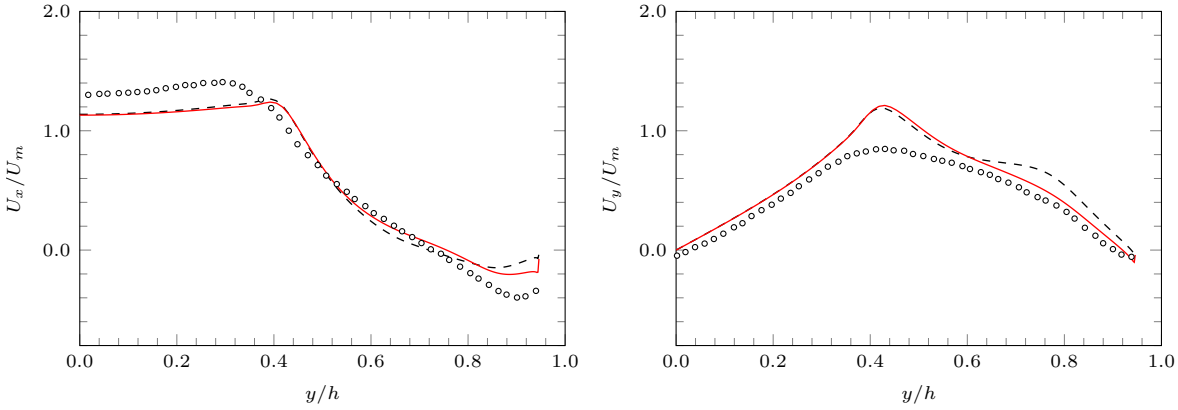

(b) 5.55 mm upstream

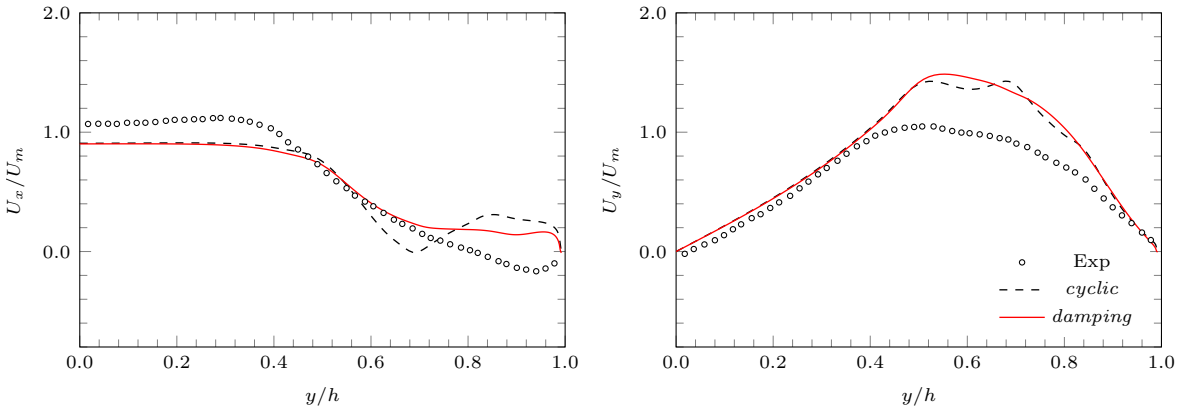

(c) 2.5 mm upstream

Figure D.19: Axial (left) and transverse (right) velocity profiles at several stations upstream of monolith at $Re = 6.0 \times 10^4$. Markers correspond to experimental data [168].

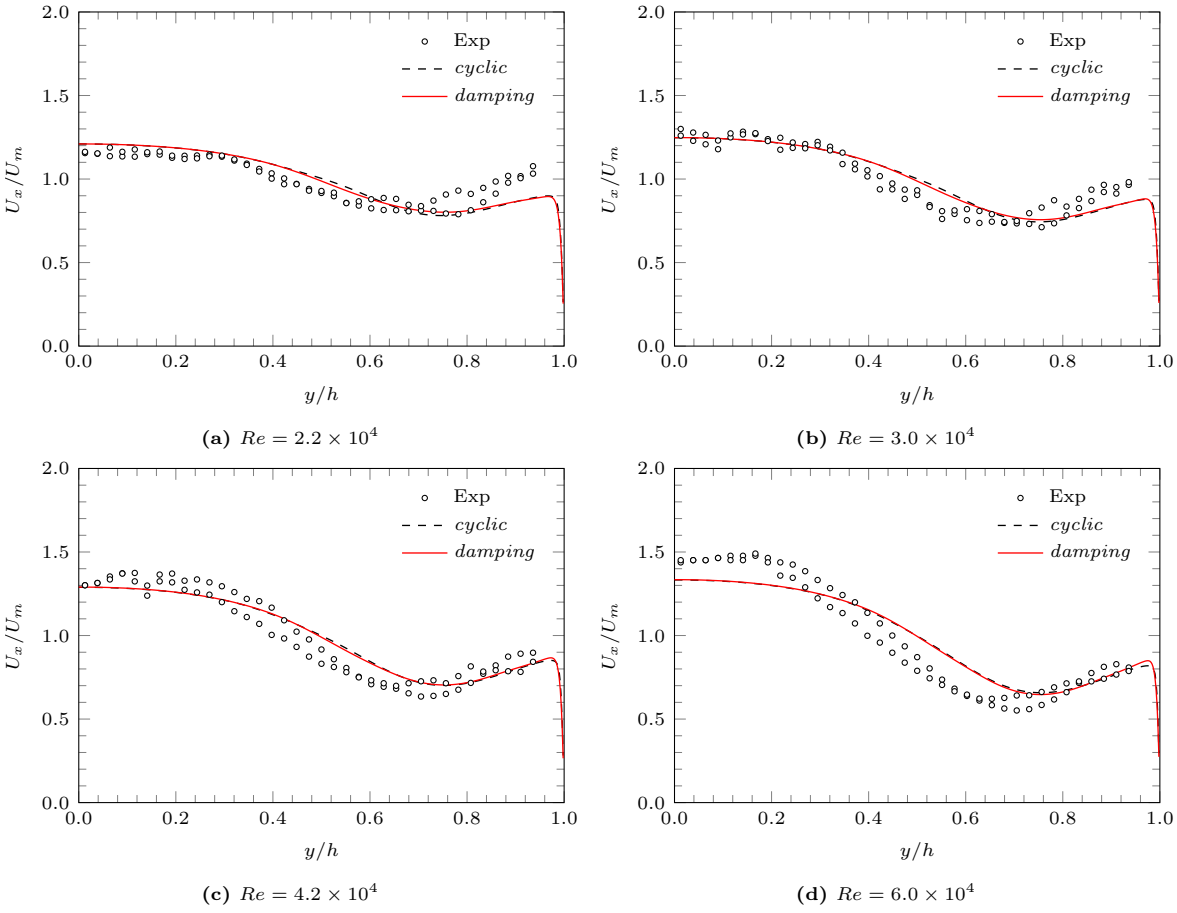

(a) $Re = 2.2 \times 10^4$ **(b)** $Re = 3.0 \times 10^4$

(c) $Re = 4.2 \times 10^4$ **(d)** $Re = 6.0 \times 10^4$

Figure D.20: Axial velocity profile 40 mm downstream of monolith. Markers correspond to experimental data [168].

D.3 Turbulence models comparison

D.3.1 Monolith length 27 mm

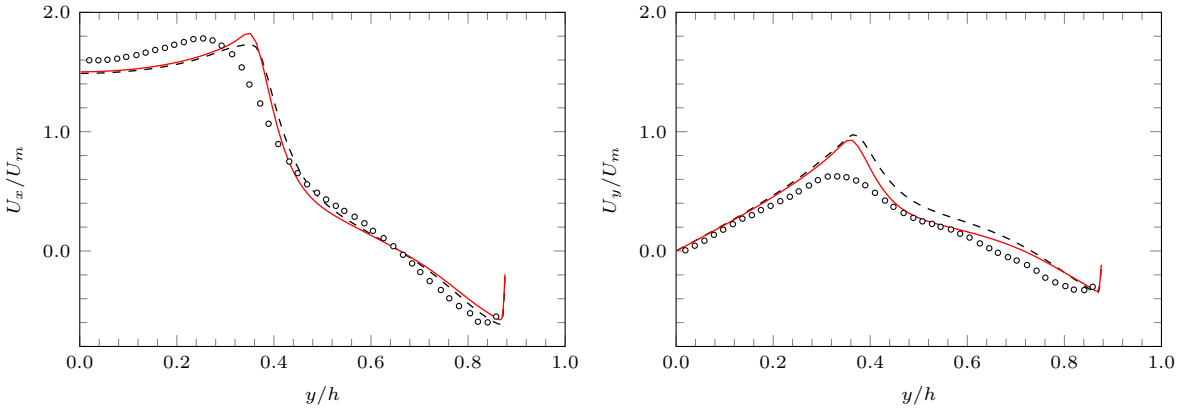

(a) 10.13 mm upstream

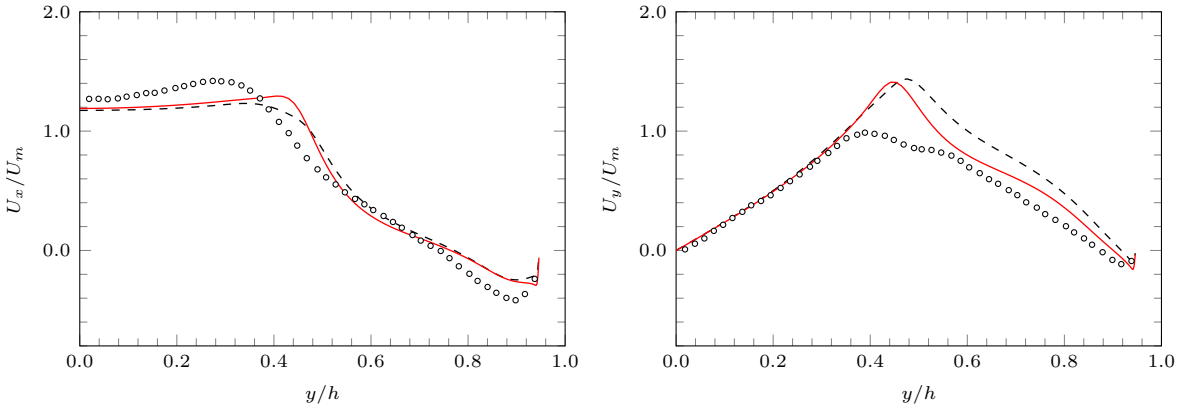

(b) 5.55 mm upstream

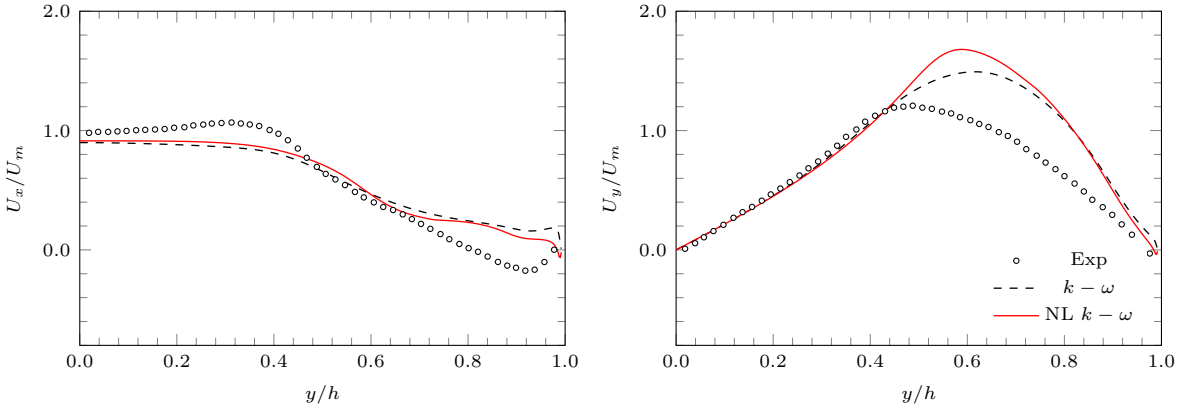

(c) 2.5 mm upstream

Figure D.21: Axial (left) and transverse (right) velocity profiles at several stations upstream of monolith at $Re = 2.2 \times 10^4$. Markers correspond to experimental data [168].

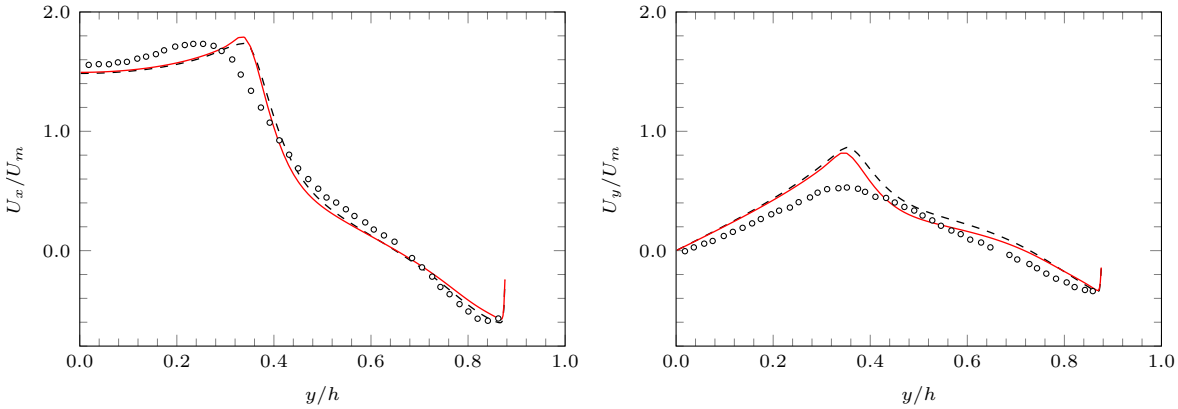

(a) 10.13 mm upstream

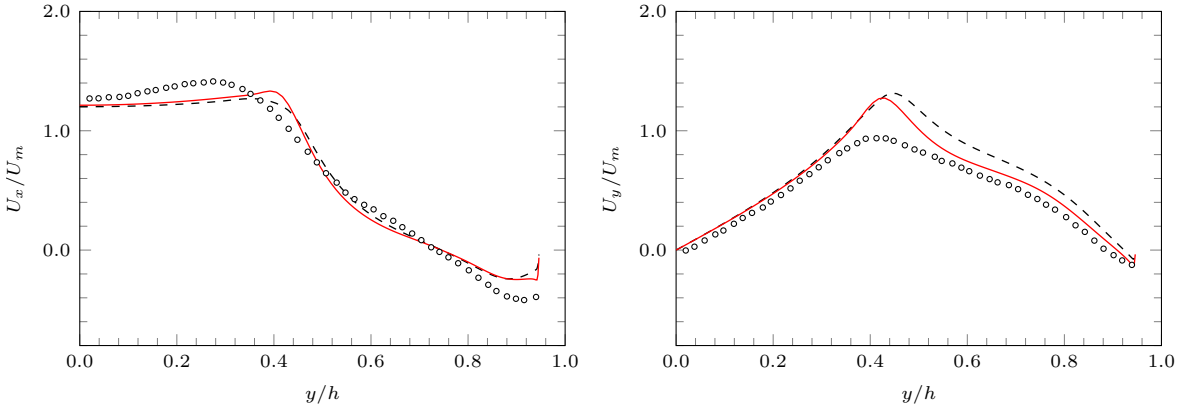

(b) 5.55 mm upstream

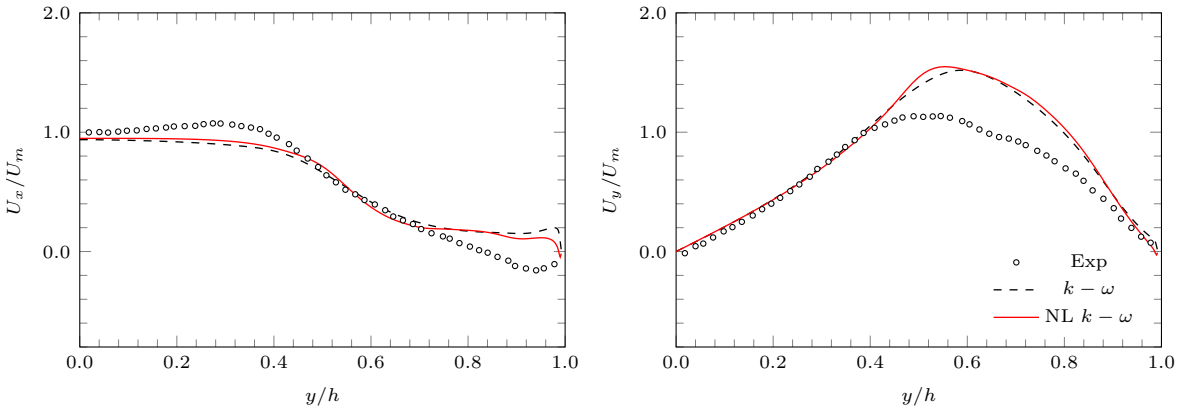

(c) 2.5 mm upstream

Figure D.22: Axial (left) and transverse (right) velocity profiles at several stations upstream of monolith at $Re = 3.0 \times 10^4$. Markers correspond to experimental data [168].

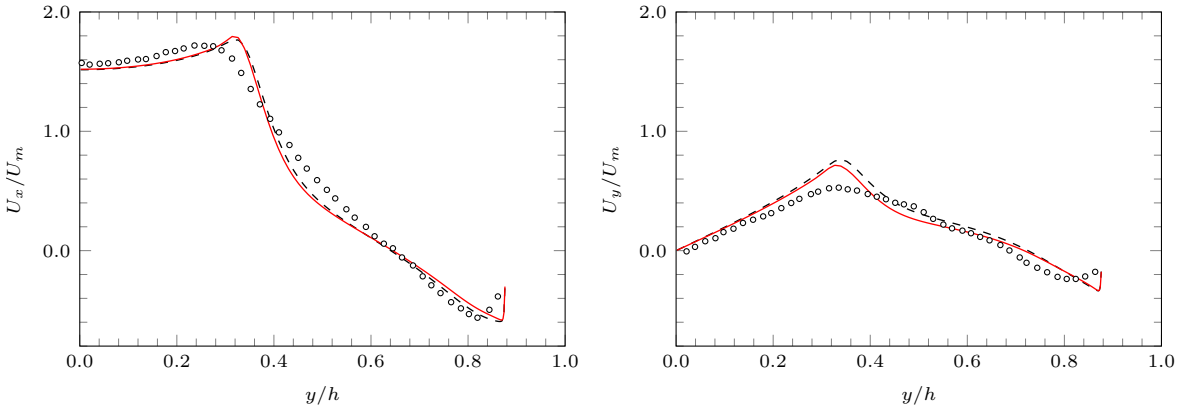

(a) 10.13 mm upstream

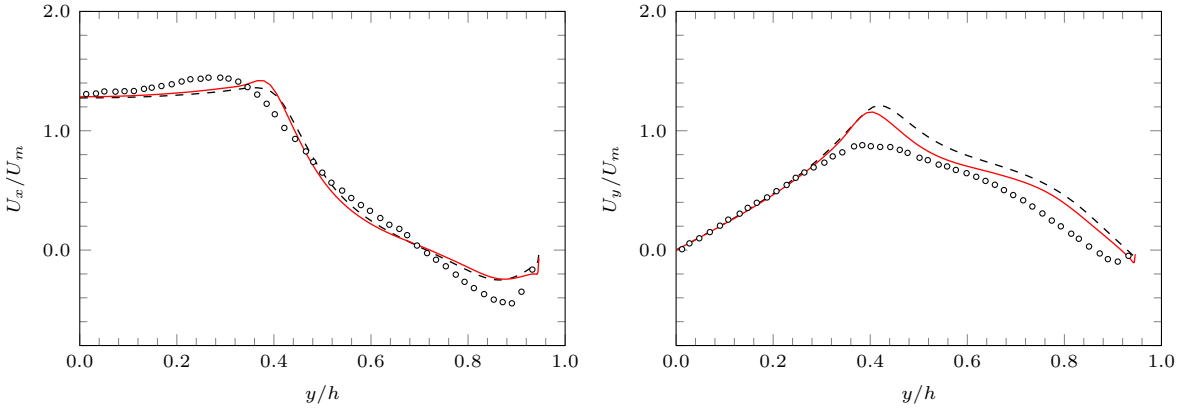

(b) 5.55 mm upstream

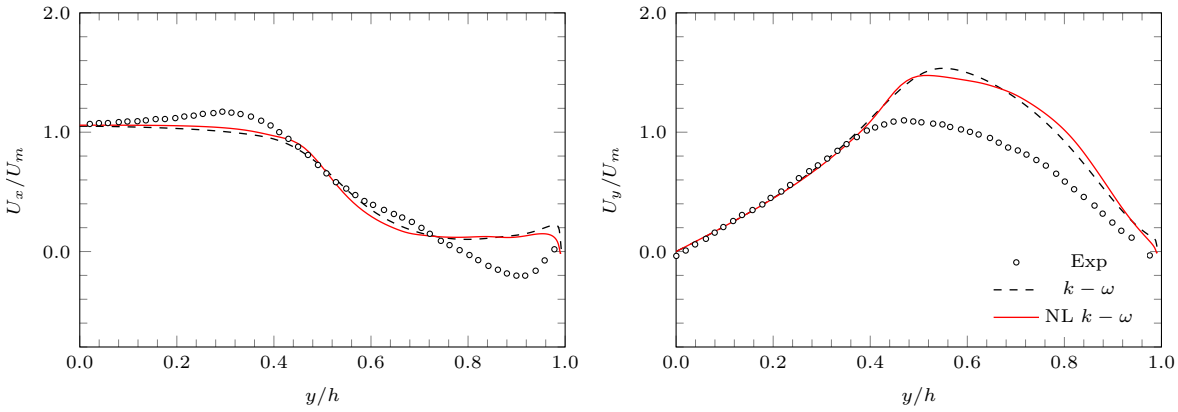

(c) 2.5 mm upstream

Figure D.23: Axial (left) and transverse (right) velocity profiles at several stations upstream of monolith at $Re = 4.2 \times 10^4$. Markers correspond to experimental data [168].

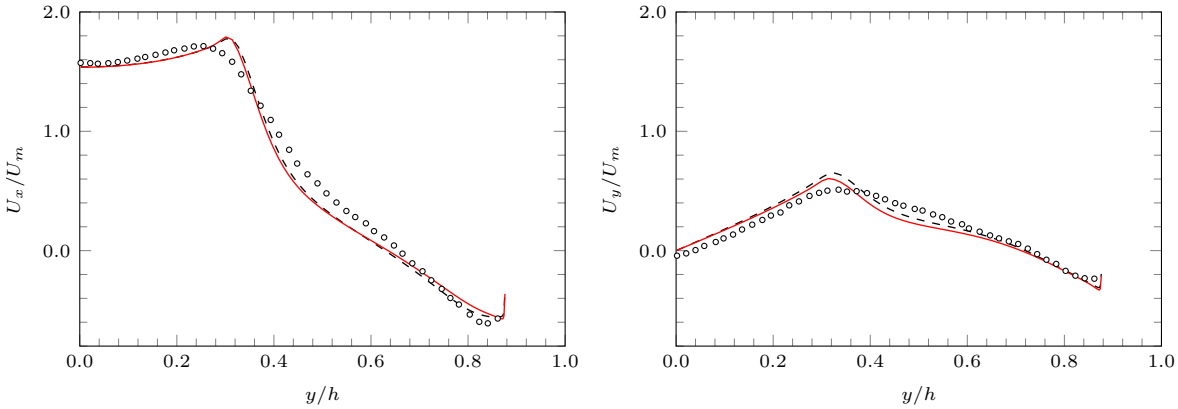

(a) 10.13 mm upstream

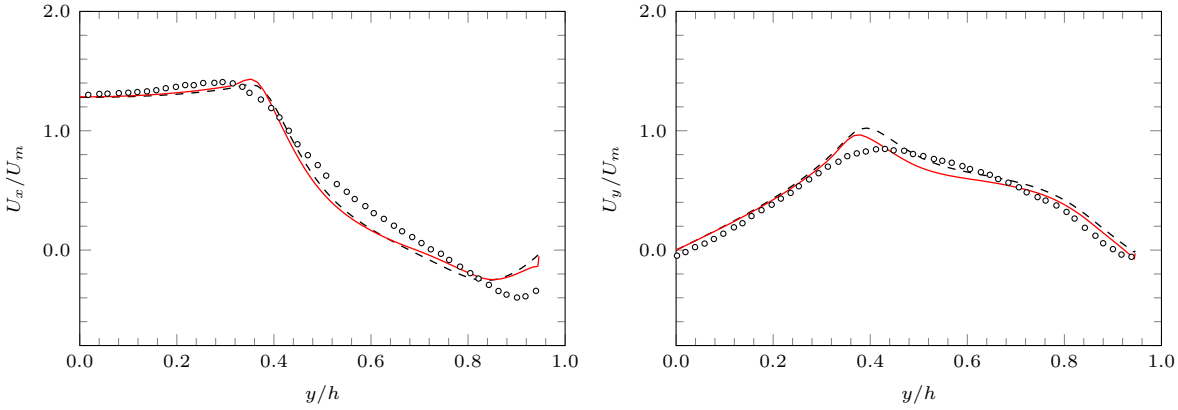

(b) 5.55 mm upstream

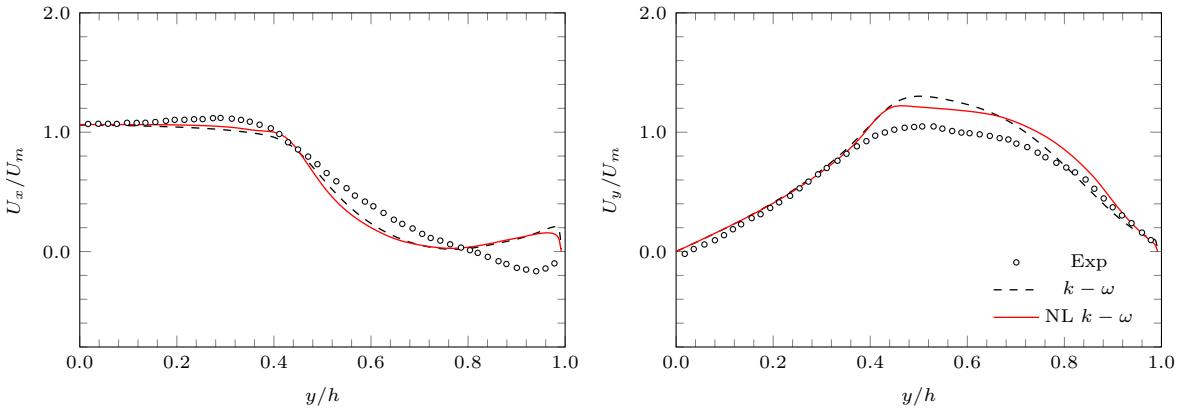

(c) 2.5 mm upstream

Figure D.24: Axial (left) and transverse (right) velocity profiles at several stations upstream of monolith at $Re = 6.0 \times 10^4$. Markers correspond to experimental data [168].

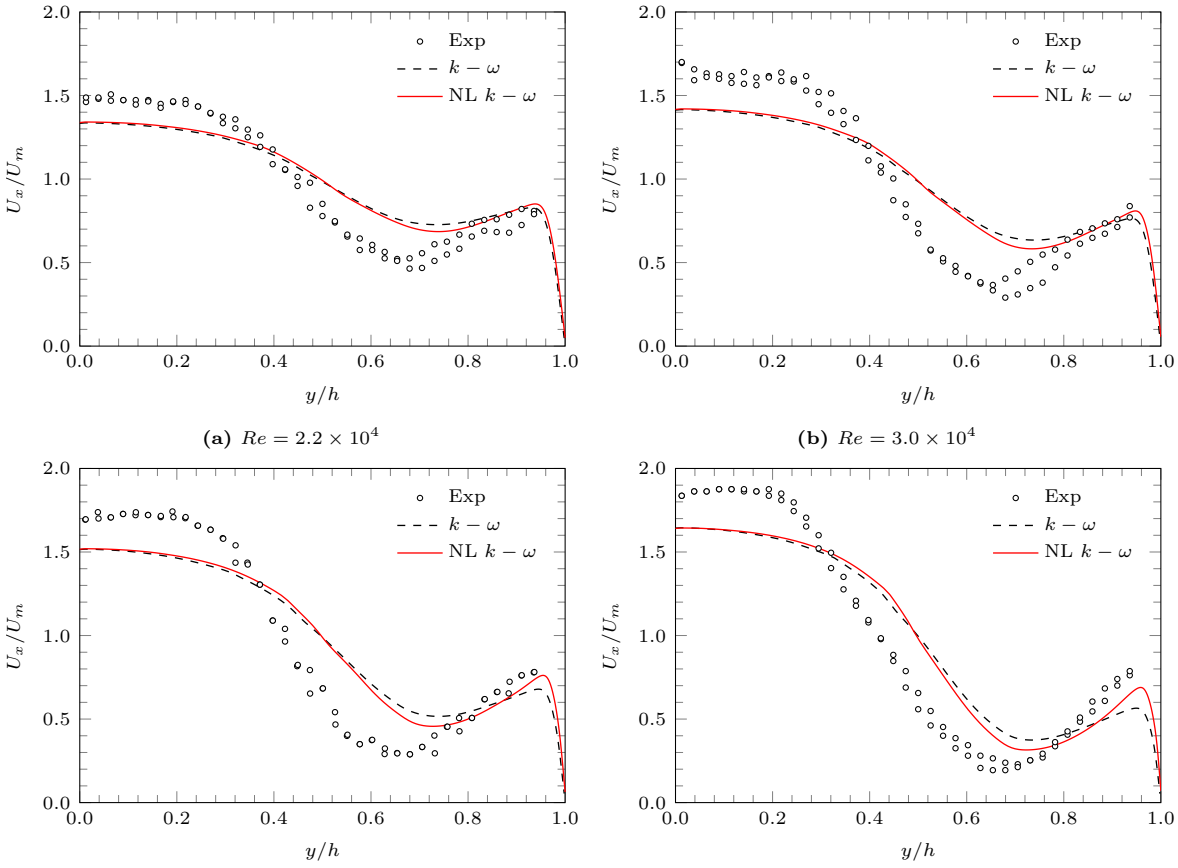

(a) $Re = 2.2 \times 10^4$ **(b)** $Re = 3.0 \times 10^4$

(c) $Re = 4.2 \times 10^4$ **(d)** $Re = 6.0 \times 10^4$

Figure D.25: Axial velocity profile 40 mm downstream of monolith. Markers correspond to experimental data [168].

D.3.2 Monolith length 100 mm

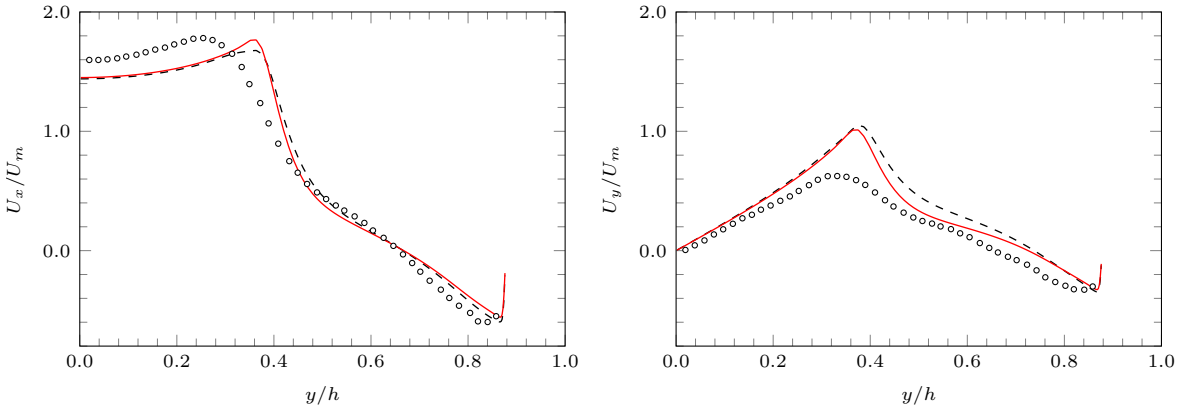

(a) 10.13 mm upstream

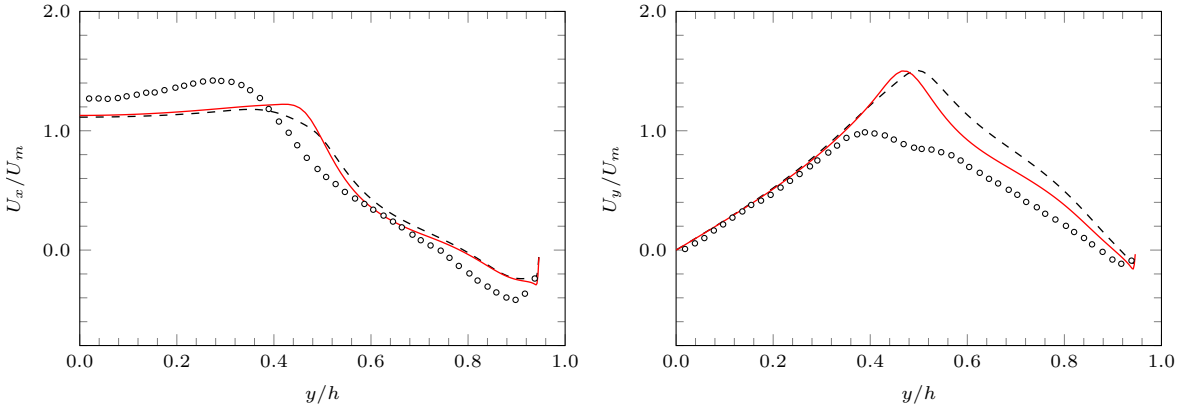

(b) 5.55 mm upstream

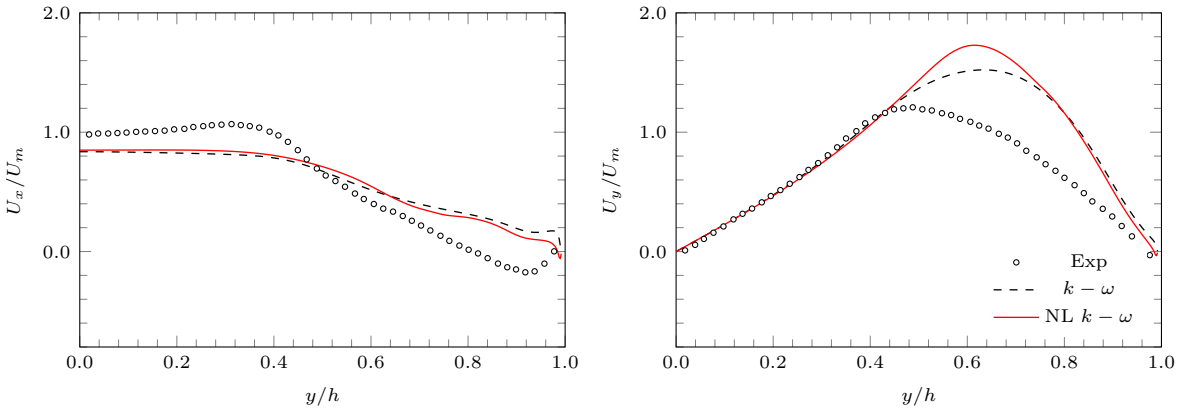

(c) 2.5 mm upstream

Figure D.26: Axial (left) and transverse (right) velocity profiles at several stations upstream of monolith at $Re = 2.2 \times 10^4$. Markers correspond to experimental data [168].

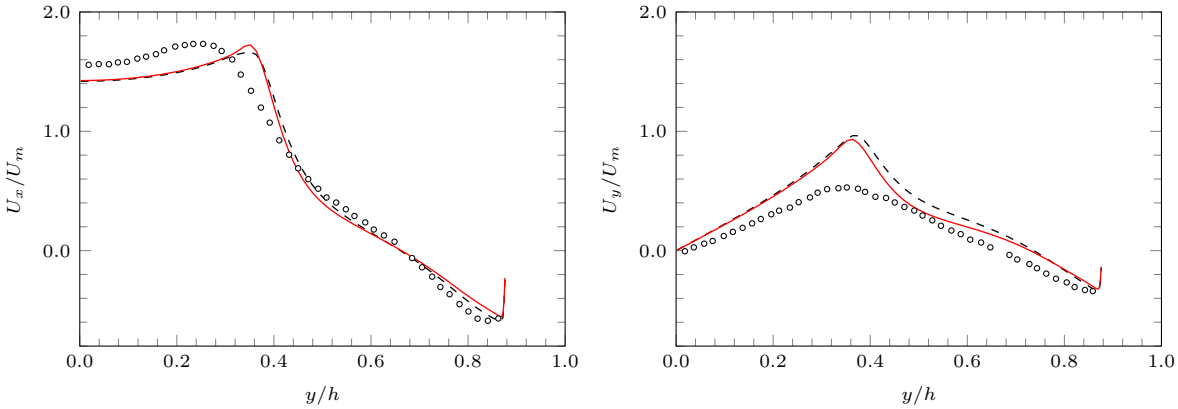

(a) 10.13 mm upstream

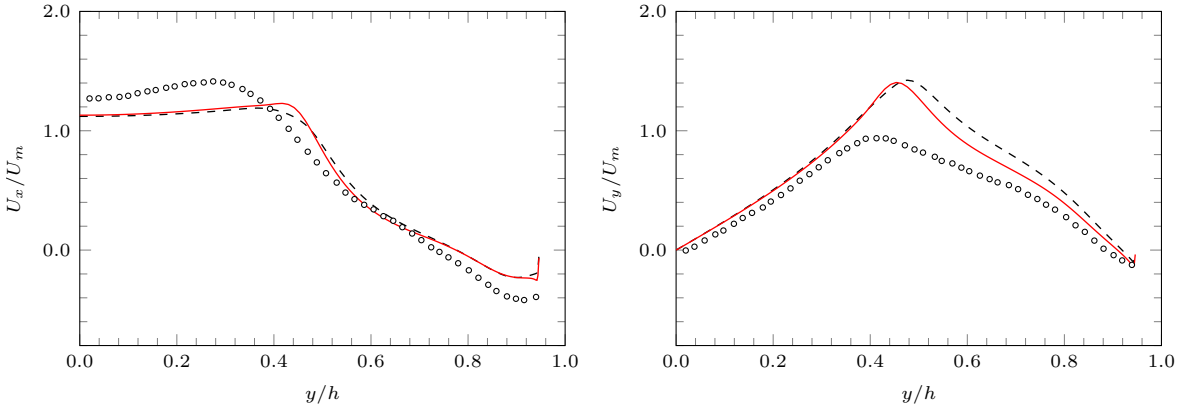

(b) 5.55 mm upstream

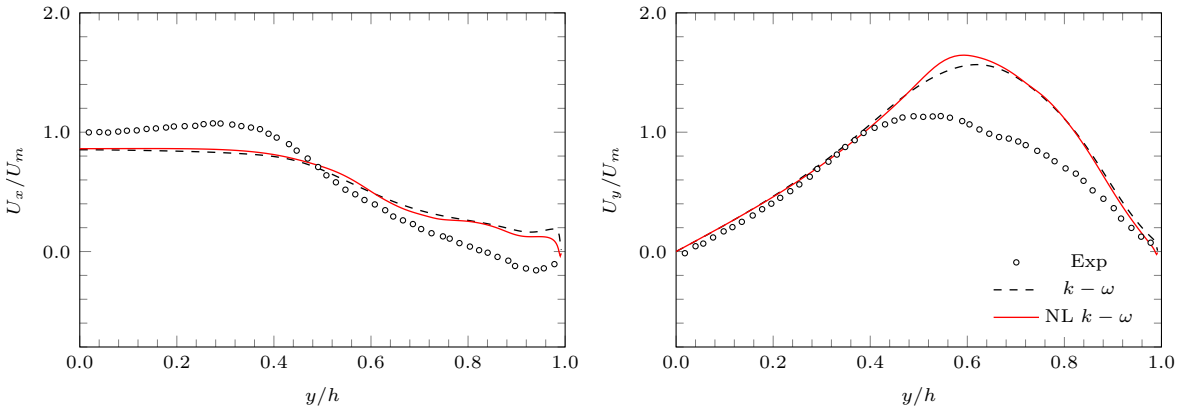

(c) 2.5 mm upstream

Figure D.27: Axial (left) and transverse (right) velocity profiles at several stations upstream of monolith at $Re = 3.0 \times 10^4$. Markers correspond to experimental data [168].

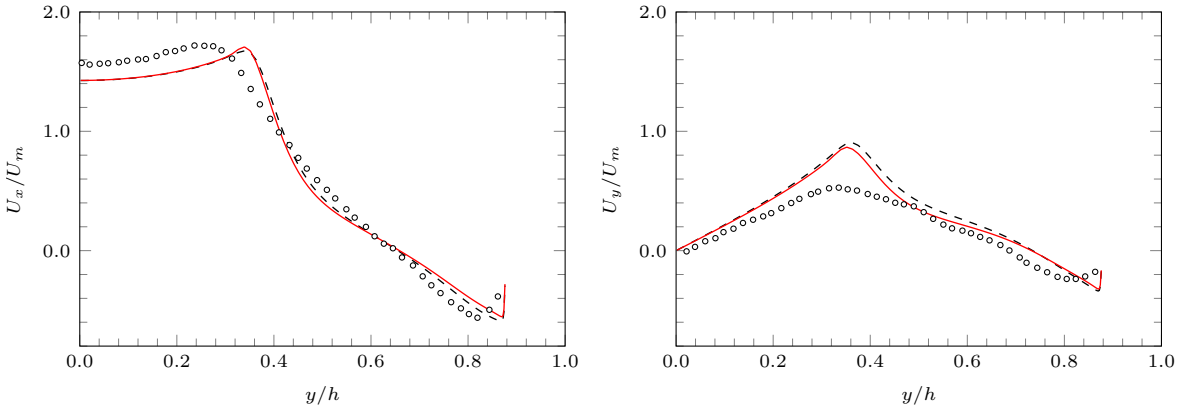

(a) 10.13 mm upstream

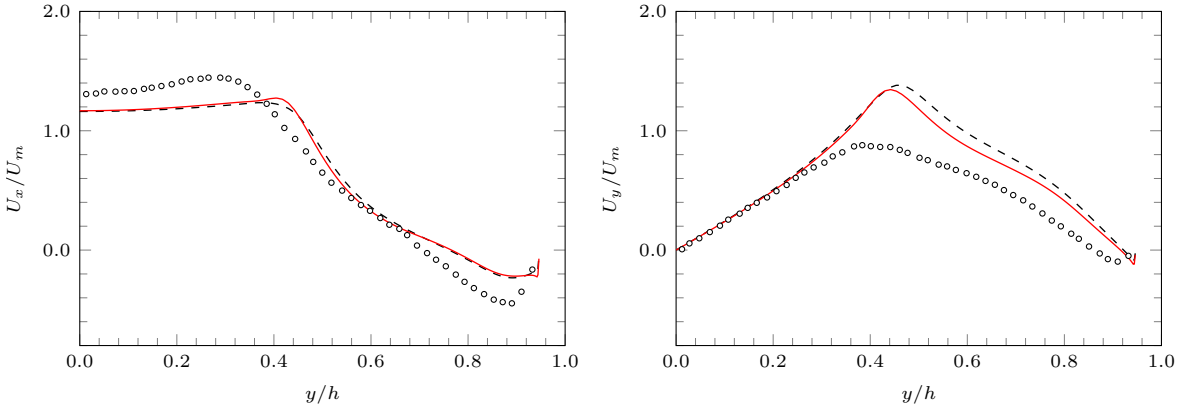

(b) 5.55 mm upstream

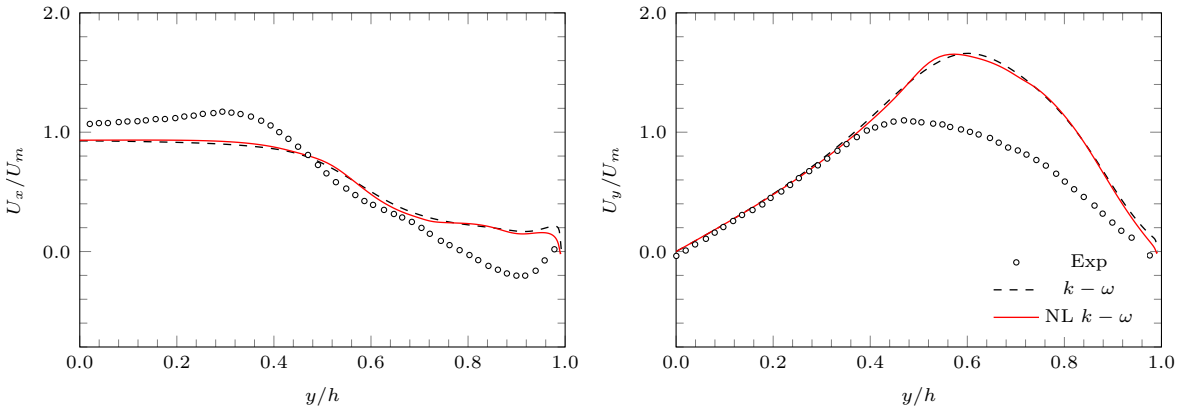

(c) 2.5 mm upstream

Figure D.28: Axial (left) and transverse (right) velocity profiles at several stations upstream of monolith at $Re = 4.2 \times 10^4$. Markers correspond to experimental data [168].

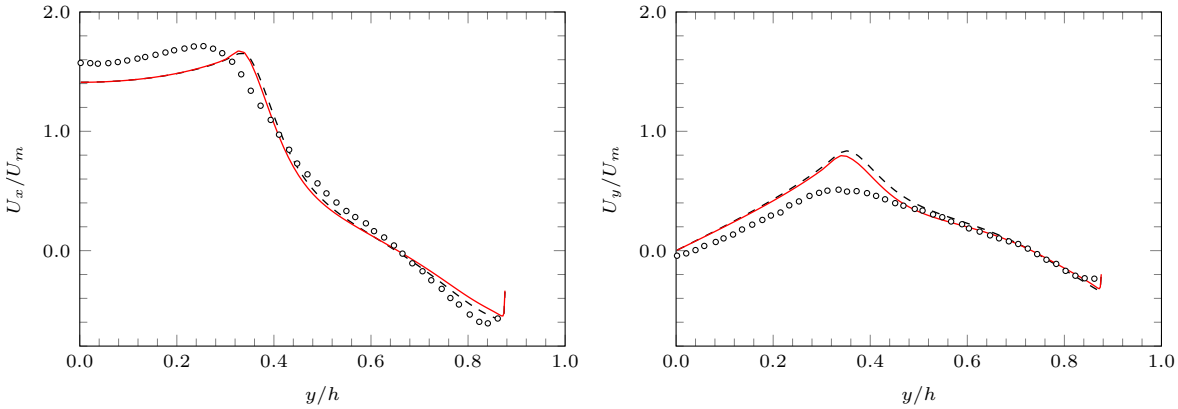

(a) 10.13 mm upstream

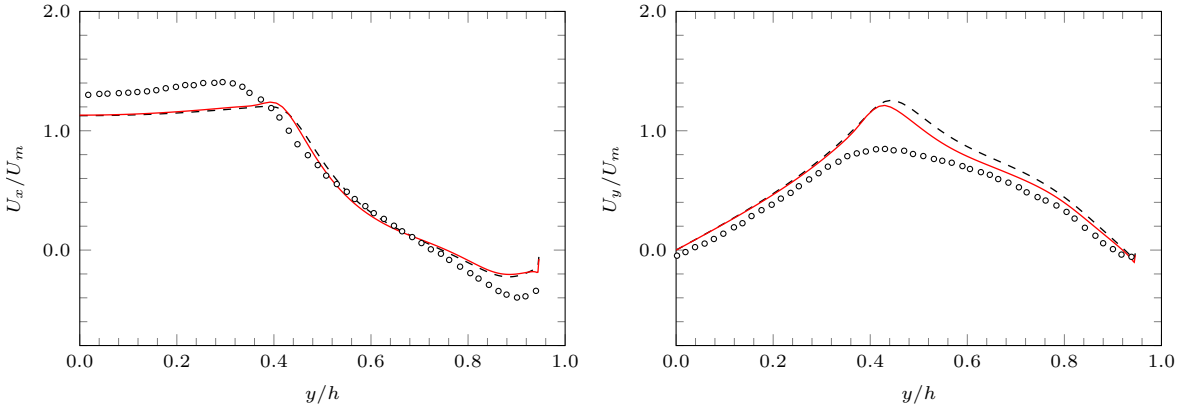

(b) 5.55 mm upstream

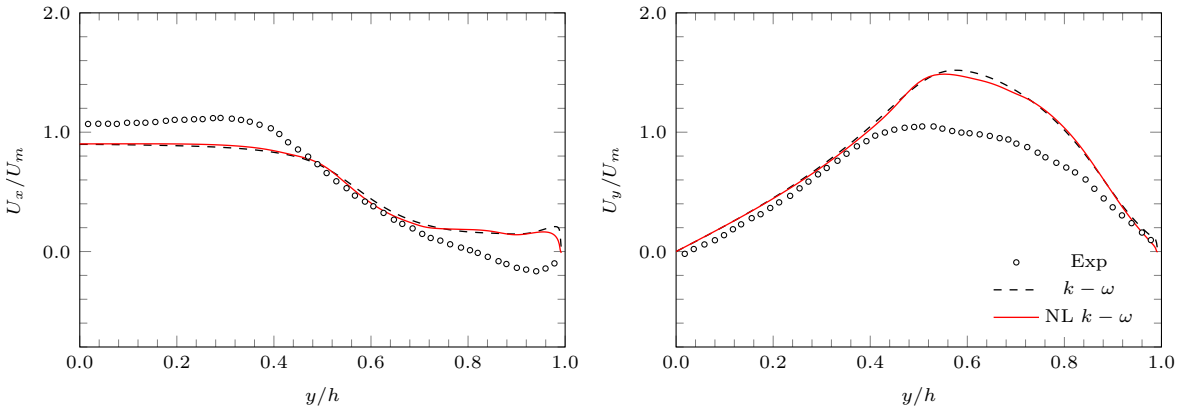

(c) 2.5 mm upstream

Figure D.29: Axial (left) and transverse (right) velocity profiles at several stations upstream of monolith at $Re = 6.0 \times 10^4$. Markers correspond to experimental data [168].

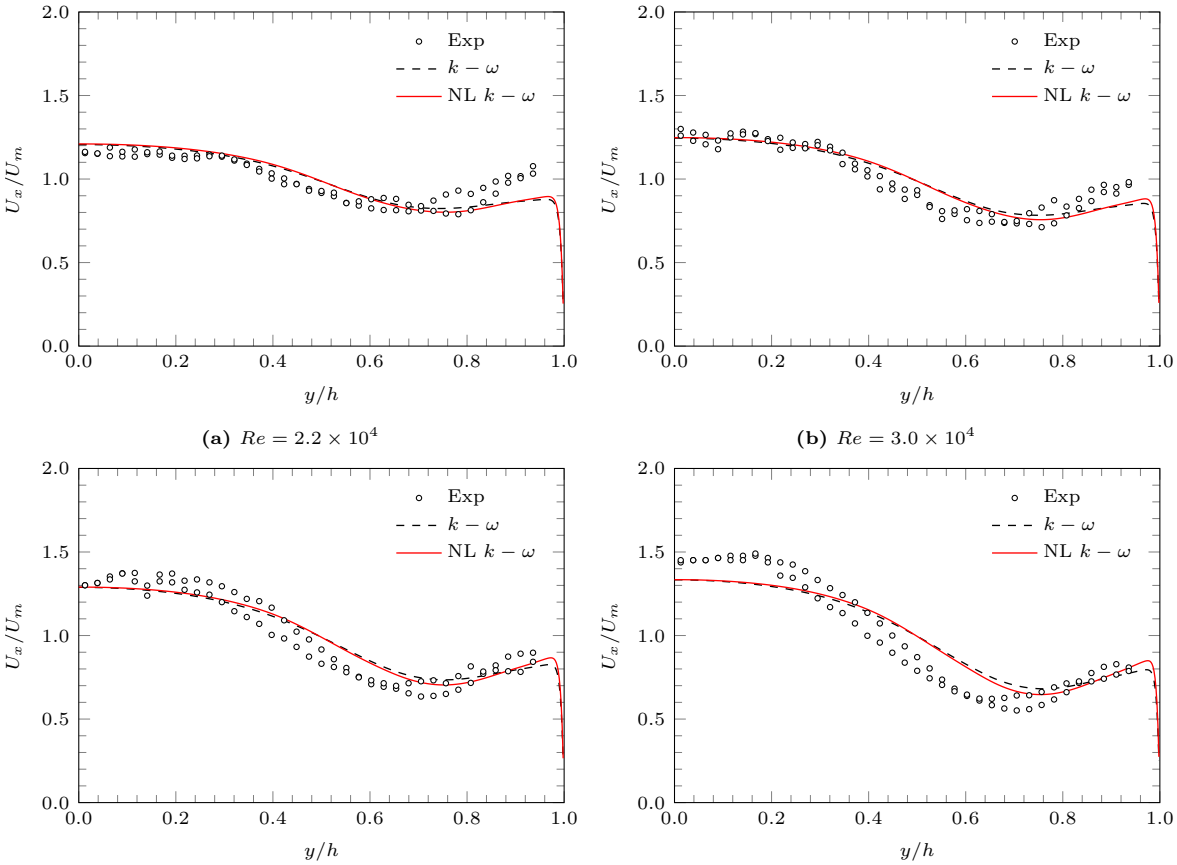

(a) $Re = 2.2 \times 10^4$ **(b)** $Re = 3.0 \times 10^4$

(c) $Re = 4.2 \times 10^4$ **(d)** $Re = 6.0 \times 10^4$

Figure D.30: Axial velocity profile 40 mm downstream of monolith. Markers correspond to experimental data [168].

Appendix E

The NL $k - \omega$ model OpenFOAM implementation

E.1 NLkOmega.H

```
/*---------------------------------------------------------------------------*\
  ========= |
  \\ / F ield | OpenFOAM: The Open Source CFD Toolbox
   \\ / O peration | Website: https://openfoam.org
    \\ / A nd | Copyright (C) 2011-2018 OpenFOAM Foundation
     \\/ M anipulation |
-------------------------------------------------------------------------------
License
    This file is part of OpenFOAM.

    OpenFOAM is free software: you can redistribute it and/or modify it
    under the terms of the GNU General Public License as published by
    the Free Software Foundation, either version 3 of the License, or
    (at your option) any later version.

    OpenFOAM is distributed in the hope that it will be useful, but WITHOUT
    ANY WARRANTY; without even the implied warranty of MERCHANTABILITY or
    FITNESS FOR A PARTICULAR PURPOSE. See the GNU General Public License
    for more details.

    You should have received a copy of the GNU General Public License
    along with OpenFOAM. If not, see <http://www.gnu.org/licenses/>.

Class
    Foam::RASModels::NLkOmega

Description
    A non-linear (NL) k-omega turbulence model

    References:
    \verbatim
      Fadhila, H. et al. (2019)
    \endverbatim

    The default model coefficients are
    \verbatim
        NLkOmegaCoeffs
```

```
                                {
                                    betaStar 0.09;
                                    gamma 0.52;
                                    Comega2 0.072;
                                    sigmaK 0.5;
                                    sigmaOmega 0.5;
                                    Cfm 0.01;
                                    Cfmu 1;
                                    kappa 0.4;
                                    C1 0.92;
                                    C2 0.01;
                                    C3 0.4;
                                    C4 0.18;
                                    C5 1.9;
                                    C6 70;
                                    CL1 10.2;
                                    CL2 8;
                                    CB1 25;
                                    CB2 15;
                                    CV1 160;
                                    CV2 122;
                                }

    \endverbatim

SourceFiles
    NLkOmega.C

\*---------------------------------------------------------------------------*/

#ifndef NLkOmega_H
#define NLkOmega_H

#include "RASModel.H"
#include "nonlinearEddyViscosity.H"

// * * * * * * * * * * * * * * * * * * * * * * * * * * * * * * * * * * * * * //

namespace Foam
{
namespace RASModels
{

/*---------------------------------------------------------------------------*\
                        Class NLkOmega Declaration
\*---------------------------------------------------------------------------*/

template<class BasicTurbulenceModel>
class NLkOmega
:
    public nonlinearEddyViscosity<RASModel<BasicTurbulenceModel>>
{

protected:

    // Protected data

        // Model coefficients

            dimensionedScalar betaStar_;
            dimensionedScalar Comega1_;
            dimensionedScalar Comega2_;
            dimensionedScalar sigmaK_;
            dimensionedScalar sigmaOmega_;

                                            dimensionedScalar Cfm_;
                                            dimensionedScalar Cfmu_;
                                            dimensionedScalar kappa_;

                                            dimensionedScalar C1_;
                                            dimensionedScalar C2_;
                                            dimensionedScalar C3_;
```

```
                                        dimensionedScalar C4_;
                                        dimensionedScalar C5_;
                                        dimensionedScalar C6_;

                                        dimensionedScalar CL1_;
                                        dimensionedScalar CL2_;
                                        dimensionedScalar CB1_;
                                        dimensionedScalar CB2_;
                                        dimensionedScalar CV1_;
                                        dimensionedScalar CV2_;

        // Fields

            volScalarField k_;
            volScalarField omega_;
                                        volScalarField epsilon_;

                                        const volScalarField& y_;

                                        tmp<volScalarField> Ret() const;


    // Protected Member Functions

        virtual void correctNut();

        virtual void correctNonlinearStress(const volTensorField& gradU);

                            tmp<volScalarField> fv1(const volScalarField& Ret)
                                const;

                            tmp<volScalarField> fv2(const volScalarField& Ret)
                                const;

                            tmp<volScalarField> fv3(const volScalarField& Ret)
                                const;

        tmp<volScalarField> fSS() const;

                            tmp<volScalarField> fm
                            (
                                        const volSymmTensorField& S,
                                        const volTensorField& W
                            ) const;

                            tmp<volScalarField> Cmu
                            (
                                        const volSymmTensorField& S,
                                        const volTensorField& W
                            ) const;

                            tmp<volScalarField> scalingTerm() const;

public:

    typedef typename BasicTurbulenceModel::alphaField alphaField;
    typedef typename BasicTurbulenceModel::rhoField rhoField;
    typedef typename BasicTurbulenceModel::transportModel transportModel;


    //- Runtime type information
    TypeName("NLkOmega");


    // Constructors

        //- Construct from components
        NLkOmega
        (
            const alphaField& alpha,
            const rhoField& rho,
```

```
            const volVectorField& U,
            const surfaceScalarField& alphaRhoPhi,
            const surfaceScalarField& phi,
            const transportModel& transport,
            const word& propertiesName = turbulenceModel::propertiesName,
            const word& type = typeName
        );


    //- Destructor
    virtual ~NLkOmega()
    {}


    // Member Functions

        //- Read RASProperties dictionary
        virtual bool read();

        //- Return the effective diffusivity for k
        tmp<volScalarField> DkEff() const
        {
            return tmp<volScalarField>
            (
                new volScalarField
                (
                    "DkEff",
                    sigmaK_*this->nut_ + this->nu()
                )
            );
        }

        //- Return the effective diffusivity for omega
        tmp<volScalarField> DomegaEff() const
        {
            return tmp<volScalarField>
            (
                new volScalarField
                (
                    "DomegaEff",
                    sigmaOmega_*this->nut_ + this->nu()
                )
            );
        }

        //- Return the turbulence kinetic energy
        virtual tmp<volScalarField> k() const
        {
            return k_;
        }

        //- Return the turbulence specific dissipation rate
        virtual tmp<volScalarField> omega() const
        {
            return omega_;
        }

        //- Return the turbulence kinetic energy dissipation rate
        virtual tmp<volScalarField> epsilon() const
        {
            return epsilon_;
        }

        //- Solve the turbulence equations and correct the turbulence viscosity
        virtual void correct();
};
```

```
// * * * * * * * * * * * * * * * * * * * * * * * * * * * * * * * * * * * * //

} // End namespace RASModels
} // End namespace Foam

// * * * * * * * * * * * * * * * * * * * * * * * * * * * * * * * * * * * * //
#ifdef NoRepository
    #include "NLkOmega.C"
#endif

// * * * * * * * * * * * * * * * * * * * * * * * * * * * * * * * * * * * * //

#endif

// ************************************************************************* //
```

E.2 NLkOmega.C

```
/*---------------------------------------------------------------------------*\
  ========= |
  \\ / F ield | OpenFOAM: The Open Source CFD Toolbox
   \\ / O peration | Website: https://openfoam.org
    \\ / A nd | Copyright (C) 2011-2018 OpenFOAM Foundation
     \\/ M anipulation |
-------------------------------------------------------------------------------
License
    This file is part of OpenFOAM.

    OpenFOAM is free software: you can redistribute it and/or modify it
    under the terms of the GNU General Public License as published by
    the Free Software Foundation, either version 3 of the License, or
    (at your option) any later version.

    OpenFOAM is distributed in the hope that it will be useful, but WITHOUT
    ANY WARRANTY; without even the implied warranty of MERCHANTABILITY or
    FITNESS FOR A PARTICULAR PURPOSE. See the GNU General Public License
    for more details.

    You should have received a copy of the GNU General Public License
    along with OpenFOAM. If not, see <http://www.gnu.org/licenses/>.

\*---------------------------------------------------------------------------*/

#include "NLkOmega.H"
#include "fvOptions.H"
#include "bound.H"

// * * * * * * * * * * * * * * * * * * * * * * * * * * * * * * * * * * * * //

namespace Foam
{
namespace RASModels
{

// * * * * * * * * * * * * Protected Member Functions * * * * * * * * * * * //

template<class BasicTurbulenceModel>
tmp<volScalarField> NLkOmega<BasicTurbulenceModel>::Ret() const
{
    return (k_/(this->nu()*(omega_ + this->omegaMin_)));
}

template<class BasicTurbulenceModel>
tmp<volScalarField> NLkOmega<BasicTurbulenceModel>::fv1(const volScalarField& Ret
    ) const
{
    return (1-exp(-pow(Ret,C1_)/C2_));
```

```
}

template<class BasicTurbulenceModel>
tmp<volScalarField> NLkOmega<BasicTurbulenceModel>::fv2(const volScalarField& Ret
    ) const
{
    return (exp(-pow(Ret,C3_)/C4_));
}

template<class BasicTurbulenceModel>
tmp<volScalarField> NLkOmega<BasicTurbulenceModel>::fv3(const volScalarField& Ret
    ) const
{
    return (1-tanh(pow(Ret,C5_)/C6_));
}


template<class BasicTurbulenceModel>
tmp<volScalarField> NLkOmega<BasicTurbulenceModel>::fm
(
                const volSymmTensorField& S,
                const volTensorField& W
) const
{
                volScalarField STilde((1/((omega_ + this->omegaMin_)))*sqrt(2.0)*
                    mag(S));
                volScalarField OmegaTilde((1/((omega_ + this->omegaMin_)))*sqrt
                    (2.0)*mag(W));
                volScalarField M(max(STilde,OmegaTilde));

                return (1/(1+(Cfm_*sqr(M))));

}

template<class BasicTurbulenceModel>
tmp<volScalarField> NLkOmega<BasicTurbulenceModel>::Cmu
(
                const volSymmTensorField& S,
                const volTensorField& W
) const
{
                volScalarField STilde((1/((omega_ + this->omegaMin_)))*sqrt(2.0)*
                    mag(S));
                volScalarField OmegaTilde((1/((omega_ + this->omegaMin_)))*sqrt
                    (2.0)*mag(W));
                volScalarField M(max(STilde,OmegaTilde));
                volScalarField fm(1/(1+(Cfm_*sqr(M))));

                return (min(1.00,Cfmu_*fm));

}

template<class BasicTurbulenceModel>
tmp<volScalarField> NLkOmega<BasicTurbulenceModel>::scalingTerm() const
{
                const volScalarField S2(2.0*magSqr(dev(symm(fvc::grad(this->U_)))))
                    ;

                const volScalarField scalingTerm1 (k_/sqr((max(omega_, sqrt(S2)/
                    kappa_) + this->omegaMin_)));

                return (max(scalingTerm1,dimensionedScalar("ZERO", sqr(dimLength),
                    0.0)));

}


template<class BasicTurbulenceModel>
```

```
void NLkOmega<BasicTurbulenceModel>::correctNut()
{
     correctNonlinearStress(fvc::grad(this->U_));
}


template<class BasicTurbulenceModel>
void NLkOmega<BasicTurbulenceModel>::correctNonlinearStress(const volTensorField&
     gradU)
{

              const volSymmTensorField S(symm(gradU));
    const volTensorField W(skew(gradU));

              const volScalarField CmuEff(Cmu(S,W));

              this->nut_ = k_/(omega_ + this->omegaMin_);
              this->nut_.correctBoundaryConditions();
              fv::options::New(this->mesh_).correct(this->nut_);


    const volScalarField Cbeta1Eff ( min (
                                          min ( (CV1_*fv1(Ret())*fv2(Ret())) ,
                                              CV1_ )
            + min ( (CB1_*fv1(Ret())*fv3(Ret())) , CB1_ )
                            + min ( (CL1_*(1-fv3(Ret()))) , CL1_)
                              , CV1_ )
                    );

              const volScalarField Cbeta2Eff ( min (
                                    min ( (CV2_*fv1(Ret())*fv2(Ret())) , CV2_ )
            + min ( (CB2_*fv1(Ret())*fv3(Ret())) , CB2_ )
                            + min ( (CL2_*(1-fv3(Ret()))), CL2_ )
                              , CV2_ )
                    );

    this->nonlinearStress_ =
    (
    CmuEff * scalingTerm()
         *(
             Cbeta1Eff*dev(innerSqr(S))
           + Cbeta2Eff*twoSymm(S&W)
          )
    );

}

// * * * * * * * * * * * * * * * * * Constructors * * * * * * * * * * * * * * * //

template<class BasicTurbulenceModel>
NLkOmega<BasicTurbulenceModel>::NLkOmega
(
    const alphaField& alpha,
    const rhoField& rho,
    const volVectorField& U,
    const surfaceScalarField& alphaRhoPhi,
    const surfaceScalarField& phi,
    const transportModel& transport,
    const word& propertiesName,
    const word& type
)
:
    nonlinearEddyViscosity<RASModel<BasicTurbulenceModel>>
    (
        type,
        alpha,
        rho,
        U,
        alphaRhoPhi,
```

```
    phi,
    transport,
    propertiesName
),

betaStar_
(
    dimensioned<scalar>::lookupOrAddToDict
    (
        "betaStar",
        this->coeffDict_,
        0.09
    )
),
          Comega1_
          (
                        dimensioned<scalar>::lookupOrAddToDict
                        (
                                      "gamma",
                                      this->coeffDict_,
                                      0.52
                        )
          ),
Comega2_
(
    dimensioned<scalar>::lookupOrAddToDict
    (
        "Comega2",
        this->coeffDict_,
        0.072
    )
),
sigmaK_
(
    dimensioned<scalar>::lookupOrAddToDict
    (
        "sigmaK",
        this->coeffDict_,
        0.5
    )
),
sigmaOmega_
(
    dimensioned<scalar>::lookupOrAddToDict
    (
        "sigmaOmega",
        this->coeffDict_,
        0.5
    )
),
          Cfm_
          (
                        dimensioned<scalar>::lookupOrAddToDict
                        (
                                      "Cfm",
                                      this->coeffDict_,
                                      0.01
                        )
          ),
          Cfmu_
          (
                        dimensioned<scalar>::lookupOrAddToDict
                        (
                                      "Cfmu",
                                      this->coeffDict_,
                                      1.00
                        )
          ),
          kappa_
          (
```

```
                dimensioned<scalar>::lookupOrAddToDict
                (
                        "kappa",
                        this->coeffDict_,
                        0.40
                )
),
C1_
(
                dimensioned<scalar>::lookupOrAddToDict
                (
                        "C1",
                        this->coeffDict_,
                        0.92    )
),
C2_
(
                dimensioned<scalar>::lookupOrAddToDict
                (
                        "C2",
                        this->coeffDict_,
                        0.01
                )
),
C3_
(
                dimensioned<scalar>::lookupOrAddToDict
                (
                        "C3",
                        this->coeffDict_,
                        0.4
                )
),
C4_
(
                dimensioned<scalar>::lookupOrAddToDict
                (
                        "C4",
                        this->coeffDict_,
                        0.18
                )
),
C5_
(
                dimensioned<scalar>::lookupOrAddToDict
                (
                        "C5",
                        this->coeffDict_,
                        1.9
                )
),
C6_
(
                dimensioned<scalar>::lookupOrAddToDict
                (
                        "C6",
                        this->coeffDict_,
                        70
                )
),
CL1_
(
                dimensioned<scalar>::lookupOrAddToDict
                (
                        "CL1",
                        this->coeffDict_,
                        10.20
                )
),
CL2_
```

```
            (
                        dimensioned<scalar>::lookupOrAddToDict
                        (
                                    "CL2",
                                    this->coeffDict_,
                                    8.00
                        )
            ),
            CB1_
            (
                        dimensioned<scalar>::lookupOrAddToDict
                        (
                                    "CB1",
                                    this->coeffDict_,
                                    25.00
                        )
            ),
            CB2_
            (
                        dimensioned<scalar>::lookupOrAddToDict
                        (
                                    "CB2",
                                    this->coeffDict_,
                              15.00
                        )
            ),
            CV1_
            (
                        dimensioned<scalar>::lookupOrAddToDict
                        (
                                    "CV1",
                                    this->coeffDict_,
                                    160.00
                        )
            ),
            CV2_
            (
                        dimensioned<scalar>::lookupOrAddToDict
                        (
                                    "CV2",
                                    this->coeffDict_,
                                    122.00
                        )
            ),
k_
(
    IOobject
    (
        IOobject::groupName("k", alphaRhoPhi.group()),
        this->runTime_.timeName(),
        this->mesh_,
        IOobject::MUST_READ,
        IOobject::AUTO_WRITE
    ),
    this->mesh_
),
omega_
(
    IOobject
    (
        IOobject::groupName("omega", alphaRhoPhi.group()),
        this->runTime_.timeName(),
        this->mesh_,
        IOobject::MUST_READ,
        IOobject::AUTO_WRITE
    ),
    this->mesh_
),
            epsilon_
```

```
    (
        IOobject
        (
            "epsilon",
            this->runTime_.timeName(),
            this->mesh_,
                  IOobject::NO_READ,
                  IOobject::AUTO_WRITE
        ),
       betaStar_*k_*omega_
    ),
                y_(wallDist::New(this->mesh_).y())
{
    bound(k_, this->kMin_);
    bound(omega_, this->omegaMin_);

    if (type == typeName)
    {
        this->printCoeffs(type);
    }
}


// * * * * * * * * * * * * * * * * Member Functions * * * * * * * * * * * * * * * //

template<class BasicTurbulenceModel>
bool NLkOmega<BasicTurbulenceModel>::read()
{
    if (nonlinearEddyViscosity<RASModel<BasicTurbulenceModel>>::read())
    {
        betaStar_.readIfPresent(this->coeffDict());
        Comega1_.readIfPresent(this->coeffDict());
        Comega2_.readIfPresent(this->coeffDict());
        sigmaK_.readIfPresent(this->coeffDict());
        sigmaOmega_.readIfPresent(this->coeffDict());
                              Cfm_.readIfPresent(this->coeffDict());
                              Cfmu_.readIfPresent(this->coeffDict());
                              kappa_.readIfPresent(this->coeffDict());
                              C1_.readIfPresent(this->coeffDict());
                              C2_.readIfPresent(this->coeffDict());
                              C3_.readIfPresent(this->coeffDict());
                              C4_.readIfPresent(this->coeffDict());
                              C5_.readIfPresent(this->coeffDict());
                              C6_.readIfPresent(this->coeffDict());
                              CL1_.readIfPresent(this->coeffDict());
                              CL2_.readIfPresent(this->coeffDict());
                              CB1_.readIfPresent(this->coeffDict());
                              CB2_.readIfPresent(this->coeffDict());
                              CV1_.readIfPresent(this->coeffDict());
                              CV2_.readIfPresent(this->coeffDict());

        return true;
    }
    else
    {
        return false;
    }
}


template<class BasicTurbulenceModel>
void NLkOmega<BasicTurbulenceModel>::correct()
{
    if (!this->turbulence_)
    {
        return;
    }
```

```
// Local references
const alphaField& alpha = this->alpha_;
const rhoField& rho = this->rho_;
const surfaceScalarField& alphaRhoPhi = this->alphaRhoPhi_;
const volVectorField& U = this->U_;
volScalarField& nut = this->nut_;
fv::options& fvOptions(fv::options::New(this->mesh_));

nonlinearEddyViscosity<RASModel<BasicTurbulenceModel>>::correct();

volScalarField divU(fvc::div(fvc::absolute(this->phi(), U)));

tmp<volTensorField> tgradU = fvc::grad(U);

            const volTensorField& gradU = tgradU();

            const volSymmTensorField S(symm(gradU));
            const volTensorField W(skew(gradU));

            const volScalarField Omega(sqrt(2.0)*mag(skew(gradU)));
            const volScalarField S2(2.0*magSqr(dev(symm(gradU))));

            volScalarField STilde((1/((omega_ + this->omegaMin_)))*sqrt(2.0)*
                mag(S));
            volScalarField OmegaTilde((1/((omega_ + this->omegaMin_)))*sqrt
                (2.0)*mag(W));

volScalarField G
(
    this->GName(),
    (nut*(gradU && dev(twoSymm(gradU))))
);

            const volScalarField Pk( (nut*(gradU && dev(twoSymm(gradU)))) - (
                this->nonlinearStress_ && gradU) );


// Update omega and G at the wall
omega_.boundaryFieldRef().updateCoeffs();

// Turbulence specific dissipation rate equation
tmp<fvScalarMatrix> omegaEqn
(
    fvm::ddt(alpha, rho, omega_)
  + fvm::div(alphaRhoPhi, omega_)
  - fvm::laplacian(alpha*rho*(sigmaOmega_*k_/omega_ + this->nu()), omega_)
 ==
    Comega1_*alpha*rho*G*omega_/k_
  - fvm::SuSp(((2.0/3.0)*Comega1_)*alpha*rho*divU, omega_)
  - fvm::Sp(Comega2_*alpha*rho*omega_, omega_)
  + fvOptions(alpha, rho, omega_)
);

omegaEqn.ref().relax();
fvOptions.constrain(omegaEqn.ref());
omegaEqn.ref().boundaryManipulate(omega_.boundaryFieldRef());
solve(omegaEqn);
fvOptions.correct(omega_);
bound(omega_, this->omegaMin_);


// Turbulent kinetic energy equation
tmp<fvScalarMatrix> kEqn
(
    fvm::ddt(alpha, rho, k_)
  + fvm::div(alphaRhoPhi, k_)
  - fvm::laplacian(alpha*rho*(sigmaK_*k_/omega_ + this->nu()), k_)
 ==
```

```
                            min(alpha*rho*Pk,alpha*rho*20*betaStar_*omega_*k_)
      - fvm::SuSp((2.0/3.0)*alpha*rho*divU, k_)
      - fvm::Sp(betaStar_*alpha*rho*omega_, k_)
      + fvOptions(alpha, rho, k_)
    );

    kEqn.ref().relax();
    fvOptions.constrain(kEqn.ref());
    solve(kEqn);
    fvOptions.correct(k_);
    bound(k_, this->kMin_);


              // Update total fluctuation kinetic energy dissipation rate
    epsilon_ = betaStar_*k_*omega_;
    bound(epsilon_, this->epsilonMin_);

    correctNonlinearStress(gradU);

    tgradU.clear();


}


// * * * * * * * * * * * * * * * * * * * * * * * * * * * * * * * * * * * * * * * * * //

} // End namespace RASModels
} // End namespace Foam

// ************************************************************************* //
```

Appendix F

Ethical approval documents

Certificate of Ethical Approval

Applicant:

Hasna Fadhila

Project Title:

Development of a new non-linear eddy-viscosity turbulence model for anisotropic flows

This is to certify that the above named applicant has completed the Coventry University Ethical Approval process and their project has been confirmed and approved as Low Risk

Date of approval:

20 July 2018

Project Reference Number:

P72933

Low Risk Research Ethics Approval

Project Title

Development of a new non-linear eddy-viscosity turbulence model for anisotropic flows

Record of Approval

Principal Investigator

I **request an ethics peer review** and confirm that I have answered all relevant questions in this checklist honestly.	X
I confirm that I will carry out the project in the ways described in this checklist. I will immediately suspend research and request new ethical approval if the project subsequently changes the information I have given in this checklist.	X
I confirm that I, and all members of my research team (if any), have read and agreed to abide by the Code of Research Ethics issued by the relevant national learned society.	X
I confirm that I, and all members of my research team (if any), have read and agreed to abide by the University's Research Ethics, Governance and Integrity Framework.	X

Name: Hasna Fadhila .....

Date: 04/07/2018 .....

Student's Supervisor (if applicable)

I have read this checklist and confirm that it covers all the ethical issues raised by this project fully and frankly. I also confirm that these issues have been discussed with the student and will continue to be reviewed in the course of supervision.

Name: Humberto Medina .....

Date: 20/07/2018 .....

Reviewer (if applicable)

Date of approval by anonymous reviewer: 20/07/2018

Low Risk Research Ethics Approval Checklist

Project Information

Project Ref	P72933
Full name	Hasna Fadhila
Faculty	Faculty of Engineering, Environment and Computing
Department	School of Mechanical, Aerospace and Automotive Engineering
Supervisor	Humberto Medina
Module Code	FTC
EFAAF Number	
Project title	Development of a new non-linear eddy-viscosity turbulence model for anisotropic flows
Date(s)	21/09/2015 - 31/12/2019
Created	04/07/2018 13:36

Project Summary

This PhD project aims to develop a novel anisotropic RANS-based turbulence model suitable for predicting anisotropic turbulence, for example boundary layer separation and transitional effects within the standard computational fluid dynamics (CFD) framework. This involves formulation of the model, calibration of model coefficients, validation with experimental data, and

implementation to a CFD package.

Names of Co-Investigators and their organisational affiliation (place of study/employer)	
Is the project self-funded?	YES
Who is funding the project?	Faculty of Engineering, Environment and Computing
Has the funding been confirmed?	YES
Are you required to use a Professional Code of Ethical Practice appropriate to your discipline?	NO
Have you read the Code?	NO

Project Details

What is the purpose of the project?	The purpose of the project is to improve the prediction of anisotropic turbulence by developing, validating, and implementing a novel anisotropic turbulence model.
What are the planned or desired outcomes?	The planned outcome is a new formulation and implementation of a validated, accurate, robust turbulence model that is suitable for modelling complex fluid flow that involves anisotropic turbulence.
Explain your research design	The planned approach is quantitative: theoretical, mathematical formulation of a new model followed by calibration and validation through simulations using a CFD software.
Outline the principal methods you will use	Method: theoretical, numerical work and computer simulations

Are you proposing to use an external research instrument, validated scale or follow a published research method?	NO
If yes, please give details of what you are using	
Will your research involve consulting individuals who support, or literature, websites or similar material which advocates, any of the following: terrorism, armed struggles, or political, religious or other forms of activism considered illegal under UK law?	NO
Are you dealing with Secondary Data? (e.g. sourcing info from websites, historical documents)	NO
Are you dealing with Primary Data involving people? (e.g. interviews, questionnaires, observations)	NO
Are you dealing with personal or sensitive data?	NO
Will the Personal or Sensitive data be shared with a third party?	
Will the Personal or Sensitive data be shared outside of the European Economic Area ("EEA")?	
Is the project solely desk based? (e.g. involving no laboratory, workshop or off-campus work or other activities which pose significant risks to researchers or participants)	YES
Are there any other ethical issues or risks of harm raised by the study that have not been covered by previous questions?	NO
If yes, please give further details	

Certificate of Ethical Approval

Applicant:

Hasna Fadhila

Project Title:

Turbulence modelling of steady and unsteady planar jets with downstream resistance

This is to certify that the above named applicant has completed the Coventry University Ethical Approval process and their project has been confirmed and approved as Low Risk

Date of approval:

04 February 2016

Project Reference Number:

P41631

Low Risk Research Ethics Approval

Project Title

Turbulence modelling of steady and unsteady planar jets with downstream resistance

Record of Approval

Principal Investigator

I **request an ethics peer review** and confirm that I have answered all relevant questions in this checklist honestly.	X
I confirm that I will carry out the project in the ways described in this checklist. I will immediately suspend research and request new ethical approval if the project subsequently changes the information I have given in this checklist.	X
I confirm that I, and all members of my research team (if any), have read and agreed to abide by the Code of Research Ethics issued by the relevant national learned society.	X
I confirm that I, and all members of my research team (if any), have read and agreed to abide by the University's Research Ethics, Governance and Integrity Framework.	X

Name: Hasna Fadhila.....

Date: 02/02/2016.....

Student's Supervisor (if applicable)

I have read this checklist and confirm that it covers all the ethical issues raised by this project fully and frankly. I also confirm that these issues have been discussed with the student and will continue to be reviewed in the course of supervision.

Name: Humberto Medina .....

Date: 04/02/2016.....

Reviewer (if applicable)

Date of approval by anonymous reviewer: 04/02/2016

Content removed on data protection grounds

Content removed on data protection grounds

Content removed on data protection grounds

Content removed on data protection grounds

Content removed on data protection grounds

Content removed on data protection grounds